622-232

Seasat

Geophysical Data Record (GDR) Users Handbook

Scatterometer

Dale H. Boggs

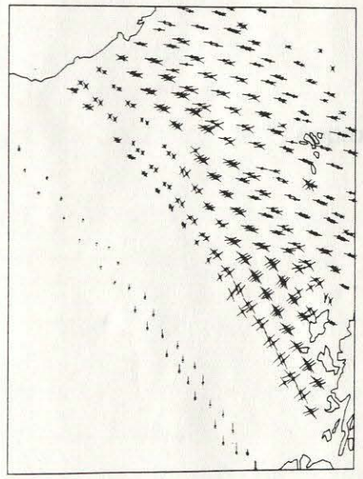

August 1982

National Aeronautics and
Space Administration

Jet Propulsion Laboratory
California Institute of Technology
Pasadena, California

JPL D-129

622-232

Seasat

Geophysical Data Record (GDR) Users Handbook

Scatterometer

Dale H. Boggs

Approved: George H. Born
George H. Born
Geophysical Evaluation Manager

August 1982

National Aeronautics and
Space Administration

Jet Propulsion Laboratory
California Institute of Technology
Pasadena, California

JPL D-129

CONTENTS

Figures

Tables

SECTION 1
INTRODUCTION

1.1 THE SCATTEROMETER AND ITS MEASUREMENTS

The Seasat-A Satellite Scatterometer (SASS) was an active microwave sensor (frequency = 14.6 GHz; λ = 2.1 cm) which was used to remotely sense wind vectors over the oceans. The physical basis for this technique is the Bragg scattering of microwaves from centimeter length capillary ocean waves. The strength of σ^o, the normalized radar cross-section (NRCS) backscatter coefficient measured by the SASS, is a function of the capillary wave amplitude that is itself proportional to the wind speed at the sea surface. Moreover, the backscatter response is anisotropic; wind direction can, therefore, be derived using scatterometer measurements at different azimuths.

1.2 DOCUMENT OVERVIEW

The purpose of this document is to present sufficient information to Seasat scatterometer data users to enable them to understand the contents of and to read the SASS Geophysical Data Record (GDR) tapes produced by the Algorithm Development Facility (ADF) [1,2] at JPL. To this end, the remainder of this document has been divided into the following ten sections. Section 2 describes the project and experiment objectives. For breadth of background and to provide a cross reference, the objectives for all Seasat instruments are included. The Seasat spacecraft, attitude reference system, and scatterometer swaths and Doppler resolution cells (footprints) are described in Section 3. Again, for cross reference, information on all sensors is given. Section 4 describes the data flow for the SASS from the spacecraft through final geophysical data processing. Section 5 is an overview of the sensor file algorithms [3] that compute the basic scatterometer-derived measurement, the radar backscatter coefficient σ^o. Section 6 describes a second phase of SASS sensor file processing that corrects the σ^o measurements -- to the extent possible -- for atmospheric attenuation effects, and also computes high-resolution (5') land/water flags for all σ^o footprint resolution cells.

Geophysical algorithm processing, which operates on the SASS σ^o sensor data to obtain ocean surface wind-vector solutions, is described in Section 7. Included in this discussion is some background on some key decisions that had to be made before GDR wind-vector production could begin; e.g., which σ^o data grouping/wind-solution resolution technique should be used (Doppler cell pairing was chosen), and which σ^o-to-wind-vector model function G-H table should be used. Also presented here is the aliasing phenomenon -- the multiple (usually four) wind-solution directions that arise from the wind-vector retrieval computations due to the bi-harmonic shape of the σ^o-versus-azimuth angle anisotropy characteristic which limits the ability of the σ^o measurement to further resolve the direction component of the solution. Section 8 describes in detail the SASS GDR tape contents and format, including both sensor (σ^o) and geophysical (wind solutions) record types. The basic information necessary to read, unpack, and make use of SASS GDR tape files is included there.

Section 9 contains information that should be of value to almost all SASS data users -- a rather extensive set of both general and specific caveats relating to the SASS-derived wind solutions found on the GDRs. This section is an attempt to answer the important question that will be asked by most users: "How good is this data, and what do I need to be wary of?" With this information, a user should be better able to understand some of the potential pitfalls in the use of the data, as well as be able to define and extract for himself a customized subset of the entire 96-day global data base that can then be more efficiently and intelligently used for his specific investigation(s). At the very least, the reader should be more aware of both the power and the limitations inherent in this unique data set. Section 10 is a "grab-bag" of presumably useful information for users of the scatterometer data. Therein is contained a collection of facts, observations, and helpful and/or practical hints -- relating to the extraction, understanding, and interpretation of the data -- that would otherwise accrue only slowly (and probably with some pain) to the typical user. Section 11 gives a condensed mission operations log.

The remainder of this section provides a brief description of a GDR for initial reference, the time coverage of data taken by each of the Seasat sensors during the mission, the types of SASS GDRs available, with data volume (number of tapes for complete mission, etc.) given for each type, information on where to obtain GDRs, and, finally, a bibliography of general sources of information about the scatterometer and its derived sensor and geophysical measurements.

1.3 DESCRIPTION OF A GDR

The Seasat GDR tapes contain satellite sensor data that has been processed through the sensor and/or geophysical algorithms. Each tape consists of geophysical and (possibly) sensor records (see [3] or Section 5) as well as text (descriptive) records for one of the four sensors processed by the Seasat Project Data Processing System at JPL. (The fifth satellite sensor, the synthetic aperture radar (SAR) is processed independently by another system at JPL.) The contents of the SASS GDR is defined in detail in Section 8.

1.4 GDR RECORD TYPES

GDR text records contain bookkeeping and general information (e.g., system software version pedigree, values of constants used, etc.) relative to the creation of the accompanying data records. There are five types of text records for each sensor. The GDR data records consist of basic geophysical and sensor (in the case of type I scatterometer GDRs -- see Subsection 1.6, below) records for each of the four sensors. Individual GDR tapes contain data from one sensor only; thus the scatterometer data is maintained on a separate set of SASS tapes. In addition to the basic data records, each sensor may have supplemental sensor and/or geophysical records. The scatterometer type I GDRs contain both sensor and geophysical supplemental records.

All of these records -- text and data for each of the four Seasat sensors -- are catalogued for reference in a computer catalogue system at JPL according to time span and data type for all GDRs that have been produced.

1.5 SEASAT DATA COVERAGE IN TIME

The scatterometer was enabled for the first time during the Seasat mission at $18^h19^m50^s$ GMT on July 6 (Day of year 187), 1978. The last telemetry data was taken at $2^h30^m36^s$ GMT on October 10 (Day 283), 1978, which immediately preceded the massive power failure that ended the Seasat mission. Table 1-1 summarizes the engineering unit data that is available at JPL on Master Sensor Data Record (MSDR) tapes (see [2] or Subsection 4.4.3.1) for the four Seasat sensors as well as spacecraft engineering data. The table gives for each instrument the date of data first received, the first date that good science

Table 1-1. Availability of Sensor Data in MSDR Tapes[a]

Mission Duration = 104 days, 6 h, 52 min, 2 s				
Sensor	First Data Date (yr:day:h:min:s)	First Good Science Date (yr:day:h:min:s)	Available Days[b] (day:h:min:s)	Data Gaps in Mission[c] (day:h:min:s)
Engineering (ENG)	78:178:19:38:34	78:178:19:38:34	99:10:44:53 (8,592,293 s)	04:20:07:09 (418,029 s)
Altimeter (ALT)	78:184:14:13:52	78:188:04:21:44	63:11:11:18 (5,483,478 s)	40:17:57:51 (3,526,864 s)
Scatterometer (SASS)	78:187:18:19:50	78:187:18:19:50	90:22:56:17 (7,858,577 s)	13:07:55:45 (1,151,745 s)
Scanning Multichannel Radiometer (SMMR)	78:185:05:27:11	78:185:05:27:11	94:04:24:41 (8,137,481 s)	10:02:27:21 (872,841 s)
Visible and Infrared Radiometer (VIRR)	78:187:09:09:11	78:187:09:09:11	48:00:50:59 (4,150,259 s)	56:06:01:03 (4,860,063 s)

[a]All data not necessarily processed into GDRs for various sensors.

[b]Amount of data at JPL from First Good Science Date to End of Mission.

[c]The sum of all missing or special category data (i.e., standby) from First Data Date to End of Mission. Any data before the First Science Date was regarded as special category data and, therefore, summed in the data gap value.

data was received, the volume of good science data available (at the MSDR level), and data gaps summed for the entire mission.

A complete global set of scatterometer GDRs containing sensor and wind vector data from Day 188, $0^h0^m0^s$ GMT (the last few hours of Day 187 have not been processed) to Day 283, $2^h30^m36^s$ GMT -- an interval of time that includes 96 days -- has been produced and is available. These two times occurred during Seasat orbit revolutions (Revs) 142 and 1502, respectively [4]. Thus, the Seasat scatterometer data set spans approximately 1360 orbit revolutions with orbital period ~100 min. Data does not exist continuously throughout this interval: Table 1-1 indicates that the sum of all missing scatterometer data from the mission interval totals more than 13 full days. A complete data gap summary (with start/stop times) can be found in [5].

1.6 SCATTEROMETER GDR TYPES I, II, AND III

1.6.1 Type I GDRs

The fundamental GDR tapes produced by the ADF scatterometer sensor and geophysical algorithms are the type I GDRs. These tapes contain all records generated during the course of ADF SASS processing -- all text and basic and supplemental sensor and geophysical records. The entire 96-day scatterometer mission data set is contained in chronological order on 381 type I GDR tapes, one-quarter day per tape. (The last day's data (2-1/2 h) requires only one tape.) The GDRs (resident at JPL and NOAA-EDIS -- see Subsection 1.8) are standard 2400-ft length tapes written in the 9-track, 1600-bpi format. The four type I GDR tapes for a given day are organized as follows: the first tape contains data from (approximately) 0^h0^m to 6^h10^m, the second contains data from 6^h0^m to 12^h10^m, and so on.

The 10 minutes of overlap at the end of each GDR are necessary to avoid small gaps in the final data set. Such gaps would result because: (1) wind solutions are generated and written onto GDRs in an order that is chronologically increasing only to within a tolerance of about two minutes due to the nature of the geophysical algorithms' grouping mechanism, and (2) a triangular-shaped region enclosing several minutes of missing data occurs at the beginning of each solution swath due to geophysical processing start-up conditions (see Section 7).

1.6.2 Type II GDRs

Since many users of scatterometer data have no need for the sensor (σ^o) data component (which occupies over 75 percent of the data storage volume), and because 381 tapes is a rather cumbersome volume to deal with, a second set of GDRs containing only text and geophysical -- both basic and supplemental -- records has been created. Each member of this set of 96 type II one-day tapes contains the geophysical data records from the four type I GDRs for a given day. Each of these type II tapes is organized into four chronologically ordered files containing all of the geophysical records extracted from the four successive quarter-day GDRs for that day.

1.6.3 Type III GDRs

The scatterometer supplemental geophysical records, which occur paired with each basic geophysical record on type I and II GDRs, contain sensor data organized according to the grouping scheme required by the SASS geophysical algorithms (see Section 8). As such, these records are also not necessary for many users of scatterometer data. The most condensed set of SASS GDRs -- the type III -- was created by retaining only text and basic geophysical records from the original type I tapes. This set of 48 two-days-per-tape GDRs contains all scatterometer wind solutions derived from the 96 days of data. They are also organized in the obvious chronological manner: each type III GDR consists of eight consecutive files containing the basic geophysical records extracted from eight successive type I GDRs over a two-day period.

1.7 DATA VOLUME ON SCATTEROMETER GDR TAPES

The typical (full) quarter-day type I GDR contains between 430 and 480 basic (and a like number of supplemental) geophysical records, each consisting of 100 ocean-surface wind vector solutions (see Section 8). Thus, a type I GDR contains an average of about 45K wind solutions. (These records, of course, contain many other supporting parameters beyond just the solution vectors.) A SASS GDR basic sensor record contains one minor frame [6,7] of sensor backscatter data; i.e., the 15 backscatter coefficient measurements (σ^os) and related parameters derived from one scatterometer antenna beam illumination pattern of 15 Doppler

resolution cells (see Subsection 3.4.3). A SASS minor frame occurs every 1.89 s; each type I GDR will therefore contain about 11,400 basic sensor records. In addition, each type I GDR contains 109 text records and about 100 supplemental sensor records (containing calibration data).

A type II SASS GDR will therefore contain about 180K wind solutions, 1800 supplemental geophysical records, and 400 text records. A full type III GDR contains approximately .36 million wind solutions; the complete SASS mission yields about 15.9 million solutions (including about 2% repetition due to the GDR file overlap), taking into account all data gaps.

1.8 WHERE TO OBTAIN GDRs

Type I, II, and III GDRs for the entire scatterometer global 96-day mission or for any data subset -- as well as available GDRs for the other Seasat sensors -- can be obtained from the following source:

NOAA Environmental Data and Information Service
National Climatic Center
Satellite Data Services Division
World Weather Building, Room 100
Washington, D.C. 20233

Phone: Commercial (301) 763-8111
FTS 763-8111

This distribution source has the additional capability of providing SASS data subsets on a fixed-region (specified by user) basis for any period of time.

1.9 BIBLIOGRAPHY

There is much about the scatterometer and its derived sensor and geophysical measurements that cannot be included in this document. In an attempt to provide background and source material on the scatterometer instrument, its signal and data processing, the sensor and geophysical algorithms, and data evaluation (via Seasat workshops), the following bibliography is given.

NASA Headquarters, Earth and Ocean Physics Applications Program, Vol. 1, Executive Summary, National Aeronautics and Space Administration, Washington, D.C., Sept. 1972.

Seasat-A Mission Specification, JPL Internal Document 622-4, Pasadena, Calif., May 6, 1977.

Kitsiz, S. N., Seasat Instrument Data Processing System Specifications, Vols. I and II, JPL Internal Document 622-14, Rev. 1, Pasadena, Calif., March 1, 1978.

Born, G.H., Dunne, J.A., and Lame, D.B., "Seasat Mission Overview," Science, Vol. 204, pp. 1405-1406, June 29, 1979.

Brown, J.W., et al., "Seasat Low-Rate Data System," Ibid., pp. 1407-1408.

Wilkerson, J.C., et al., "Surface Observations for the Evaluation of Geophysical Measurements from Seasat," Ibid., pp. 1408-1410.

Jones, W.L., et al., "Seasat Scatterometer: Results of the Gulf of Alaska Workshop," Ibid., pp. 1413-1415.

Grantham, W.L., et al., An Operational Satellite Scatterometer for Wind Vector Measurements Over Oceans, NASA TMX 72672, March 1975.

Grantham, W.L., et al., "The Seasat-A Satellite Scatterometer," IEEE J. Oceanic Eng., Vol. OE-2, No. 2, pp. 200-206, 1977.

Fischer, R.E., "Standard Deviation of Scatterometer Measurements from Space," IEEE Trans. Geosci. Electron., Vol. GE-10, pp. 106-113, April 1972.

Jones, W.L., et al., "Aircraft Measurements of the Microwave Scattering Signature of the Ocean," IEEE J. Oceanic Eng., Vol. OE-2, pp. 52-61, April 1977.

Chan, H.L., and Fung, A.K., "A Theory of Sea Scatter at Large Incidence Angles," J. Geophys. Res., Vol. 82, pp. 3429-3444, 1977.

Dome, G.J., Fung, A.K., and Moore, R.K., "An Empirical Model for Ocean Radar Backscatter and Its Application in Inversion Routine to Estimate Wind Speed and Direction Effects," Proc. URSI Comm. F, La Baule, France, April 28-May 6, 1977.

Bracalente, W.L., Boggs, D.H., Grantham, W.L., and Sweet, J.L., "The SASS Scattering Coefficient σ^o Algorithm," IEEE J. Oceanic Eng., Vol. OE-5, No. 2, pp. 145-154, April 1980.

Johnson, J.W., et al., "Seasat-A Satellite Scatterometer Instrument Evaluation," Ibid., pp. 138-144.

Boggs, D.H., Algorithm Development Facility Scatterometer Sensor Algorithm Specifications, JPL Internal Document 622-231, Pasadena, Calif., May 1981.

Jones, W.L., Wentz, F.J., and Schroeder, L.C., "Algorithm for Inferring Wind Stress from Seasat-A," AIAA J. Spacecraft and Rockets, Vol. 15, No. 6, pp. 368-374, December 1978.

Wentz, F.J., Winvec: Computation of Sea-Surface Friction Velocity and Wind Direction, T.R. 78-001 under JPL contract 954942, January 1978.

Moore, R.K., and Fung, A.K., "Radar Determination of Winds at Sea," IEEE Proc., Vol. 67, No. 11, pp. 1504-1521, 1979.

Born, G.H., Wilkerson, J.C., and Lame, D.B., Seasat Gulf of Alaska Workshop Reports, Vols. I and II, JPL Internal Document 622-101, Pasadena, Calif., 1979.

Barrick, D.W., Seasat Gulf of Alaska Workshop II Report, JPL Internal Document 622-107, Pasadena, Calif., January 1980.

Businger, J., et al., Seasat-JASIN Workshop Report, Vol. I, JPL Publication 80-62, Pasadena, Calif., 1980.

Black, P., and Wilkerson, J.C., Seasat Storms Mini-Workshop Report, JPL Internal Document 622-210, Pasadena, Calif., 1979.

Pierson, W.J., et al., "The Winds of the Comparison Data Set for the Seasat Gulf of Alaska Experiment," IEEE J. Oceanic Eng., Vol. OE-5, No. 2, pp. 169-176, April 1980.

Schroeder, L.C., et al., "The Relationship Between Wind Vector and Normalized Radar Cross Section Used to Derive Seasat-A Satellite Scatterometer Winds," J. Geophys. Res., Vol. 87, No. C5, pp. 3318-3336, April 30, 1982.

Brown, R.A., et al., "Surface Wind Analyses for Seasat," Ibid., pp. 3355-3364.

Jones, W.L., et al., "The Seasat-A Satellite Scatterometer: The Geophysical Evaluation of Remotely Sensed Wind Vector," Ibid., pp. 3297-3317.

Moore, R.K., et al., "Evaluation of Atmospheric Attenuation from SMMR Brightness Temperature for the Seasat-A Satellite Scatterometer," Ibid., pp. 3337-3354.

Wentz, F.J., et al., "Intercomparison of Wind Speeds Inferred by the SASS, Altimeter, and SMMR," Ibid., pp. 3378-3384.

Klose, J.C., Seasat Node Tables and Osculating Orbital Elements, JPL Internal Document 622-215, Pasadena, Calif., December 18, 1979.

Porche, W.D., Detailed Accountability of Seasat Data and Data Gaps, JPL Internal Document 622-221, Pasadena, Calif., September 1980.

Ronai, P., Interim Geophysical Data Record (IGDR) Users Handbook: Initial Version — Scatterometer, JPL Internal Document 622-204, Pasadena, Calif., 15 May 1979.

Boggs, D.H., The Seasat Scatterometer Model Function: The Genesis of SASS1, JPL Internal Document 622-230, Pasadena, Calif., March 3, 1981.

SECTION 2

PROJECT AND EXPERIMENT OBJECTIVES

The Seasat project and experiment objectives outlined here relate directly to the ocean dynamics objectives of the NASA applications program as stated in [8].

2.1 PROJECT OBJECTIVES

The objectives of the Seasat Project [9], a proof-of-concept mission, include demonstration of techniques for global monitoring of oceanographic and surface meteorological phenomena and features, provision of oceanographic data for both application and scientific users, and the determination of key features of an operational ocean dynamics monitoring system.

2.2 EXPERIMENT OBJECTIVES

2.2.1 Scatterometer (SASS)

The objective of this experiment was to provide a closely spaced grid measurement ($\sim$50 km) of ocean-surface wind speed and direction in the range of 4 to $\geq$26 m/s, accurate to $\pm$2 m/s or 10 percent (whichever is greater) in magnitude and $\pm$20 deg in direction.

2.2.2 Radar Altimeter (ALT) and Precision Orbit Determination (POD)

The altimeter experiment utilizes precise satellite-surface range determinations to study phenomena relating to the detailed shape of the marine geoid and departures from that shape resulting from phenomena such as ocean currents, storm surges, and tides. Range precision to $\pm$10 cm on a 1-s average allows global ocean topographic solutions on the submeter level. Pulse signal processing yields significant wave height ($H_{1/3}$) estimates in the range from 1 to 20 m to an accuracy of .5 m or 10 percent, whichever is greater, for use in forecasting models and related scientific studies. A determination of the ocean backscatter coefficient beneath the satellite to within $\pm$1 dB is obtained via ground processing.

The objectives of the POD experiment were to obtain precision orbit determination of the satellite in support of the other experiments, and to evaluate the ultimate accuracy to which the Seasat orbit can be determined.

2.2.3 Scanning Multichannel Microwave Radiometer (SMMR)

The objectives of this experiment include the provision of all-weather global measurements of sea-surface temperature ($\pm$1.5 - 2 K), wind speeds, and, subject to orbit limitations, sea ice coverage. In addition, liquid water and water vapor column content determination obtained by the SMMR is used to calculate path loss and atmospheric refraction corrections for the ALT and SASS.

2.2.4 Visible and Infrared Radiometer (VIRR)

The objective of this instrument was to provide modest-resolution (8 km) feature recognition and cloud position information, clear air-surface temperatures, and cloud-top brightness and temperatures in support of microwave experiments.

2.2.5 Synthetic Aperture Radar (SAR)

The objective of this experiment was to demonstrate the capability of a satellite-borne SAR to obtain high-resolution ocean-surface imagery capable of yielding directional wave spectra in the open ocean, monitoring of coastal features, charting ice fields and leads, iceberg detection, and fishing vessel surveillance, and to obtain land imagery useful in geological, hydrological, and glaciological studies.

SECTION 3

SEASAT SPACECRAFT AND SENSOR DATA SWATHS

3.1 SATELLITE VEHICLE SYSTEM

The Seasat spacecraft consisted of a three-axis-stabilized Lockheed Agena bus carrying a sensor module on which five remote-sensing instruments were mounted (Figure 3-1). Three of the instruments were active radar systems; the other two were radiometers (Table 3-1). Each instrument had its own antenna subsystem.

3.2 ORBIT

The satellite orbit was near-circular, with an inclination of 108 deg, a period of about 101 min, and an altitute of approximately 800 km. For the wide-swath instruments (i.e., SASS, SMMR, and VIRR), 95 percent global coverage was accomplished every 36 h. The ground-track speed was about 6.6 km/s.

3.3 SENSORS

3.3.1 Scatterometer

The physical "observable" measured by the scatterometer is the NRCS backscatter coefficient σ^o. This parameter was not directly "measured" by the SASS, but results only after considerable ground-based computations which include scatterometer-specific calibrations and corrections [3]. The resulting σ^os are then essentially independent of the specific Seasat hardware implementation of the instrument. The backscatter coefficient is actually computed from a form of the radar equation which yields a relationship between σ^o and the quantity most nearly sensed (after some conversions and the application of an averaging technique) by the scatterometer, the mean received backscattered power P_R.

The primary, but not only, use of the sensor backscatter data is as input to the scatterometer geophysical algorithms. These algorithms employ a wind-to-σ^o model function and an inversion mechanism to compute both the 19.5-m-reference-height wind vector and the ocean-surface wind stress vector for the global data set.

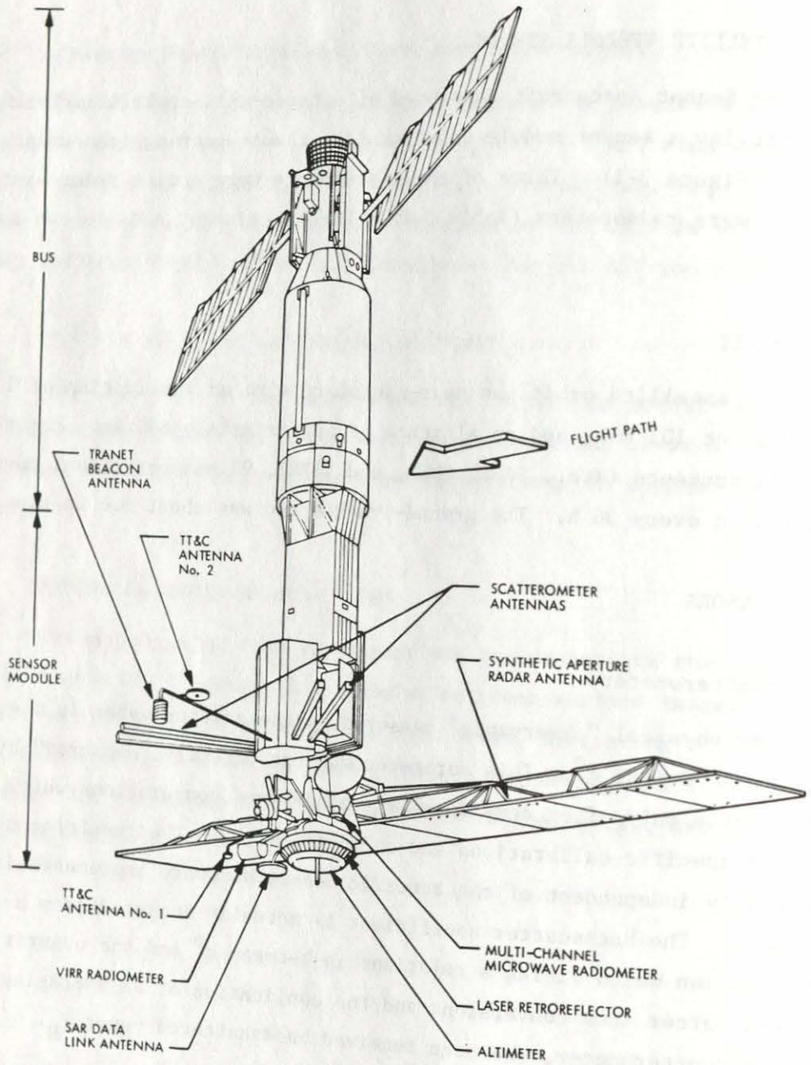

Figure 3-1. Seasat Configuration

Table 3-1. Seasat Remote Sensing Instruments

Instrument	Type	Geophysical Measurement	Sensing Method
Altimeter (ALT)	Active, short-pulse radar	Wave height, altitude above mean sea level surface and wind speed at nadir	Return pulse -- wave form, delay time to midpoint, and backscatter coefficient
Microwave Scatterometer (SASS)	Active	Surface wind speed and direction	Radar backscatter -- increases with wind speed; forward and aft beam data determine direction
Synthetic Aperture Radar (SAR)	Active, imaging	Wave spectra	Radar echo -- range or time delay and frequency shift; forms brightness image
Scanning Multi-channel Microwave Radiometer (SMMR)	Passive	Surface wind speed, sea surface temperature, atmospheric water content	Receives and measures several microwave frequencies, each one sensitive to a particular geophysical parameter
Visible and Infrared Radiometer (VIRR)	Passive, imaging	Sea surface and cloud top mean temperature; ocean, coastal, and atmospheric feature location	Receives and measures visible and infrared emissions

3.3.2 ALT, SMMR, VIRR, and SAR

The basic sensing method and purpose of these four Seasat sensors are summarized in Table 3-1.

3.4 SENSOR COVERAGE

(As SAR instrument data is not part of the ADF processing, sensor coverage for the SAR is not included in this document.)

Coverage characteristics were different for each sensor, depending on sensor pointing, field-of-view, data handling, and, in the case of the SASS, Doppler velocity between the satellite and points instantaneously fixed on the Earth's surface. As the sensors were in fixed alignments with respect to the satellite bus, only a change in satellite position and/or spacecraft attitude orientation could cause a change in sensor coverage.

The swath for each of the five sensors depended on the ground pattern produced by its receiving field-of-view. Figure 3-2 shows the ground pattern and swath for the five sensors. Table 3-2 summarizes the swath widths and positions for each sensor.

3.4.1 Sensor Pointing Angles

3.4.1.1 Attitude Reference System

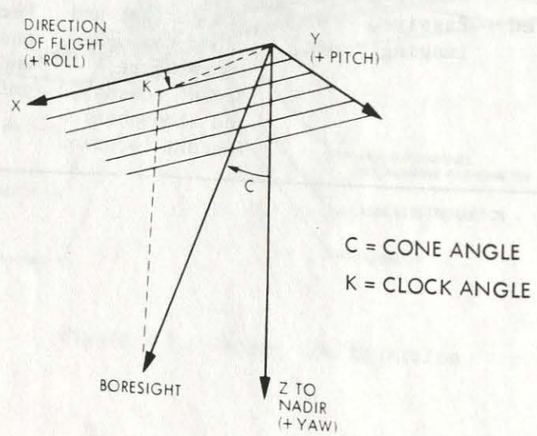

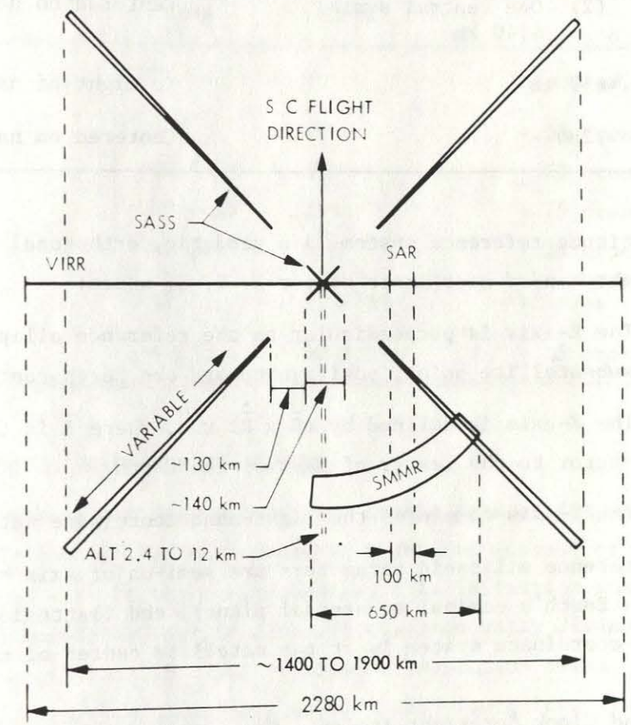

Figure 3-2. Seasat Static Footprint Patterns -- to Scale at 800-km Altitude

Table 3-2. Sensor Coverage

Sensor	Swath	
	Width	Position
ALT	∿2.4 to 12 km depending on sea state	Centered on nadir
SASS	(1) Two 500-750 km swaths (400 km apart)	At either side of nadir
	(2) One central swath, ∿140 km	Centered on nadir
SMMR	∿659 km	To right of nadir
VIRR	∿2280	Centered on nadir

The attitude reference system is a geodetic, orthogonal reference set defined by the right-handed coordinate system X, Y, Z, where:

(1) The Z-axis is perpendicular to the reference ellipsoid at the subsatellite point, positive toward the Earth center.

(2) The X-axis is defined by $(\overline{R} \times \dot{\overline{R}}) \times \overline{Z}$, where $\overline{R}$ is the radius vector to the center of mass of the Earth.

(3) The Y-axis completes the right-hand coordinate set.

The reference ellipsoid parameters are semi-major axis = 6378.137 km (which lies in the Earth's nominal equatorial plane), and flattening = 1/298.257. The origin of the coordinate system is at the satellite center of mass.

3.4.1.2 Cone and Clock Boresight Angles. The instrument boresights (sensor pointing angles) are defined in terms of cone and clock angles as follows:

(1) Cone angle is the angle between the instrument boresight vector and the Z-axis.

(2) Clock angle is the angle between the boresight vector projection in the X-Y plane and the X-axis measured at the spacecraft clockwise looking toward the Earth.

Cross cone (see Table 3-3) is measured from the boresight in a plane containing the boresight and perpendicular to the plane of the cone angle.

Cone and clock angles as well as field-of-view for each instrument are given in Table 3-3.

Table 3-3. Instrument Pointing

Instrument	Angle, deg		Field-of-View, deg
	Cone	Clock	
ALT	0	0	circular, radius = .75
SASS	0-7	45	±.25 cross cone
	19.5-55	135	±.25 cross cone
	19.5-55	225	±.25 cross cone
	19.5-55	315	±.25 cross cone
SMMR	42	133-183	±2 cone
VIRR	51.38	90-270	±.15 cross cone

3.4.2 Sensor Footprints and Swaths

In general, a sensor footprint is the area on the surface of the Earth sensed by one of the instruments at a defined instant or during a period of time. In the case of the scatterometer, this definition must be extended: a full SASS antenna footprint is actually electronically divided by Doppler frequency filtering into 15 distinct Doppler resolution cells. Each of these 15 Doppler cells is then considered to be a SASS footprint. The sensor swath is the track of the sensor footprints swept out by the moving satellite in time. The SASS Doppler footprint cells and the resulting swaths are described in the following subsections.

3.4.3 SASS Swath and Doppler Resolution Footprint Cells

3.4.3.1 Four Dual-Polarized X-Oriented Fan-Beam Antennas. The nominal scatterometer swath ground pattern and incidence angle distribution across the swath are shown in Figure 3-3. Four dual-polarized (vertical (V) and horizontal (H) polarizations) fan-beam antennas were aligned (see Figure 3-1) so that they pointed 45 and 135 deg relative to the spacecraft flight direction (in the orbit plane) to produce an X-shaped illumination pattern on the Earth. In this way a given surface location was first viewed by a forward antenna, and then viewed, somewhere between a few seconds and about three minutes later -- depending on the location's cross-track distance from the subsatellite track -- near-orthogonally by an aft antenna. Thus, σ^o measurements of the same region were provided at two azimuthal angles separated by approximately 90 deg.

3.4.3.2 SASS Operational Modes -- Antenna Sequencing. The illumination pattern for each antenna was active for 1.89-s measurement periods. The 1.89-s measurement interval was repeated continually and contiguously, but a different antenna or polarization was activated for each consecutive sampling period. Each of eight possible SASS science operational modes was associated with a different prescribed antenna/polarization sequence ordered as shown in Table 3-4. All modes were characterized by an antenna switching-cycle period of 7.56 s, during which four antenna-beam/polarization combinations were cycled through. This timing was designed to provide σ^o measurements spaced approximately 50 km apart (footprint area center-to-center distance) in the along-track direction.

Table 3-4 and the antenna beam-number designations in Figure 3-3 show that only modes 1 and 2 yielded the full two-sided SASS swath coverage shown in the figure. Modes 3-8 generated left- or right-side-only half-swath, but double-density, measurement coverage. Inspection of the Seasat data log [5] reveals that mode 1 occurred most frequently during the mission.

The continuous calibrate (instrument calibration data) and standby (instrument essentially "idling") modes shown in Table 3-4 generated no science data. These modes were in effect only rarely during the mission data interval given in Section 1.5.

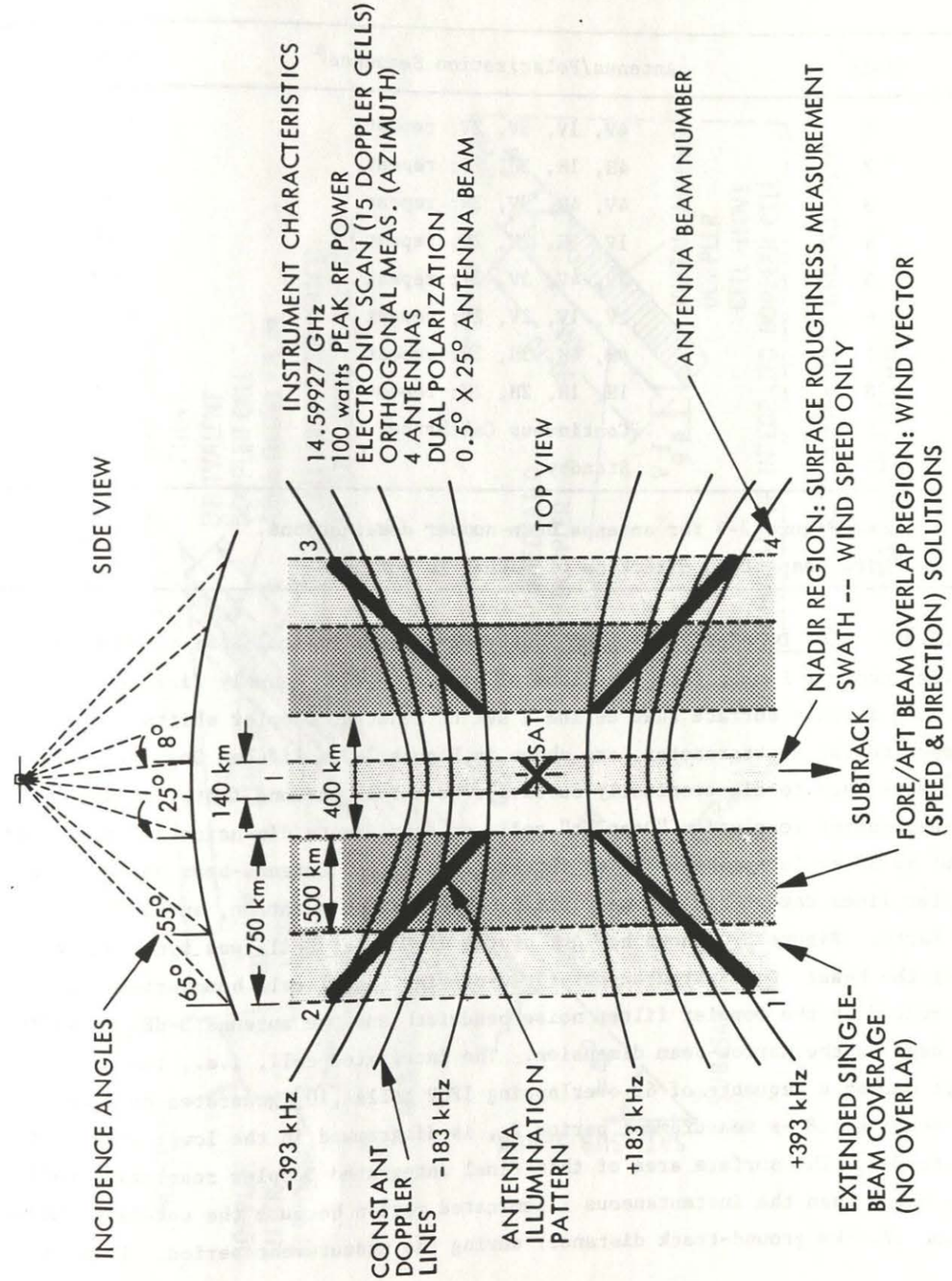

Figure 3-3. Scatterometer Ground Pattern and Swath

Table 3-4. SASS Mode Descriptions

Mode	Antenna/Polarization Sequence[a]	Side[b]
1	4V, 1V, 3V, 2V; repeat	Both
2	4H, 1H, 3H, 2H; repeat	Both
3	4V, 4H, 3V, 3H; repeat	Left
4	1V, 1H, 2V, 2H; repeat	Right
5	4V, 4V, 3V, 3V; repeat	Left
6	1V, 1V, 2V, 2V; repeat	Right
7	4H, 4H, 3H, 3H; repeat	Left
8	1H, 1H, 2H, 2H; repeat	Right
9	Continuous Calibrate	
10	Standby	

[a]See Figure 3-3 for antenna beam-number designations.
[b]With respect to direction of satellite motion.

3.4.3.3 SASS Doppler Resolution Footprint Cells. Typical SASS iso-Doppler surface contour lines, i.e., the loci of points instantaneously fixed on the rotating Earth's surface that define a set of constant Doppler shifts with respect to the scatterometer, are shown in Figure 3-3. Fifteen Doppler filters [10] were used to electronically subdivide each full antenna footprint into 15 measurement resolution "Doppler" cells of approximate dimension 20 km (cross-beam) by 50 km (along-beam). The intersection of the antenna-beam pattern and Doppler lines determined the resolution cell size, orientation, and location on the Earth. Figure 3-4 shows how one of the 15 Doppler cells was synthesized along the beam: the instantaneous-field-of-view (IFOV) cell boundaries were determined by the Doppler filter noise bandwidth and the antenna 3-dB beamwidth (.5 deg) in the narrow-beam dimension. The integrated cell, i.e., the area swept out by a sequence of 61 overlapping IFOV cells [10] generated over the course of a 1.89-s measurement period T_p, is diagrammed in the lower insert of Figure 3-4. The surface area of this final integrated Doppler resolution cell is greater than the instantaneous illuminated region because the satellite moved (about 12.5-km ground-track distance) during the measurement period. Each of

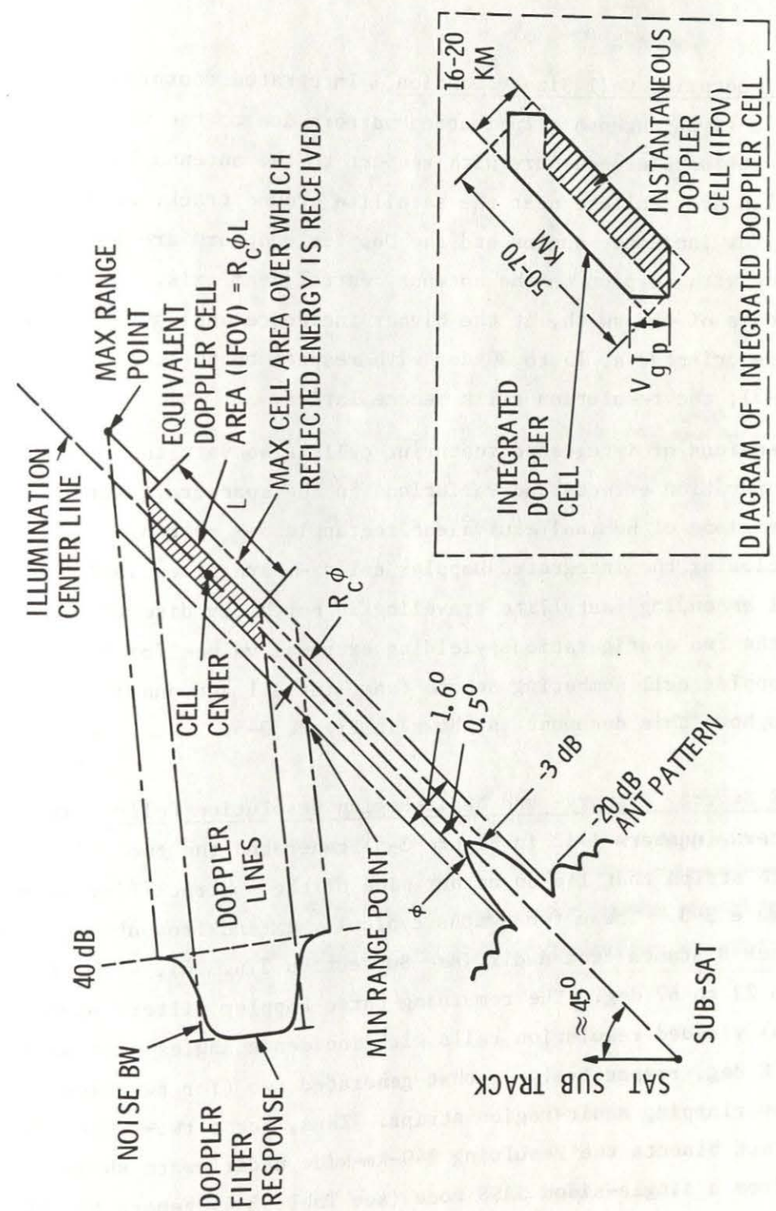

Figure 3-4. Doppler Cell Area as Determined by Antenna Pattern and Filter Response

these integrated Doppler cells is a SASS footprint, and has one σ^o backscatter measurement value associated with it. Of course, all 15 Doppler measurement channels synthesized from one antenna footprint are associated with the same time-tag.

3.4.3.4 Doppler Footprint Cell Size Variation. Integrated footprint cells vary in size along a given antenna illumination pattern due to the variation in the orientation of the Doppler contours with respect to the antenna beam axis direction. The cells are smallest near the satellite ground track, where they are illuminated at low incidence angles and the Doppler contours are rotated approximately 45 deg with respect to the antenna central beam axis. Progressing toward the outer edges of the swath, at the higher incidence angles where the Doppler contours are oriented at 15 to 30 deg with respect to the central beam axis (see Figure 3-3), the resolution cells become larger.

The dimensions of integrated footprint cells also vary throughout an orbit due to Earth rotation effects and variations in the spacecraft attitude and altitude. Dimensions of nominal equivalent rectangles -- rectangles of equivalent area enclosing the integrated Doppler cells -- are given in Table 3-5 for both equatorial ascending (satellite traveling in northerly direction) and descending cases, the two configurations yielding extremal values for these dimensions. The Doppler cell numbering scheme (same for all antennas) used in the table and throughout this document is shown in Figure 3-5.

3.4.3.5 The SASS Swath: Primary- and Nadir-Region Resolution Cells. Twelve of the Doppler filters (numbers 1-12 in Figure 3-5) generated the two primary σ^o measurement swath strips that lie on either side of the subtrack (for two-sided modes) in Figure 3-3. These two swaths typically extend from about 200 to 950 km in cross-track distance from nadir (see Subsection 3.4.3.6), with incidence angles ranging from 22 to 67 deg. The remaining three Doppler filters (numbers 13-15 in Figure 3-5) yielded resolution cells with incidence angles near nadir -- at about 0, 4, and 8 deg, respectively -- that generated two (for two-sided modes) 90-km-wide overlapping nadir-region strips. Thus, for a two-sided mode, the satellite subtrack bisects the resulting 140-km-wide nadir swath shown in Figure 3-3. Data from a single-sided SASS mode (see Table 3-4) generates the

Table 3-5. Minimum and Maximum Dimensions of Integrated Cell Equivalent Rectangles (Values Occur at 0° Latitude)

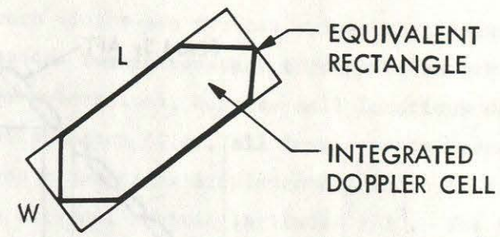

Cell No.	Equator			
	Ascending[a]		Descending[b]	
	W (km)	L (km)	W (km)	L (km)
1	16.2	67.8	16.0	55.9
2	16.5	69.1	16.3	55.2
3	16.9	70.3	16.5	54.0
4	17.3	73.5	16.8	54.0
5	17.8	71.9	17.1	50.2
6	18.4	72.1	17.4	47.5
7	19.0	71.2	17.8	44.0
8	19.7	73.3	18.1	42.2
9	20.4	73.7	18.5	39.2
10	21.2	77.2	18.8	37.6
11	22.1	83.4	19.1	36.7
12	23.0	93.0	19.5	36.5
13	15.7	56.1	15.6	48.7
14	15.6	55.0	15.6	48.0
15	15.6	54.2	15.6	52.8

[a]These are the maximum values that occur during an orbit.

[b]These are the minimum values that occur during an orbit.

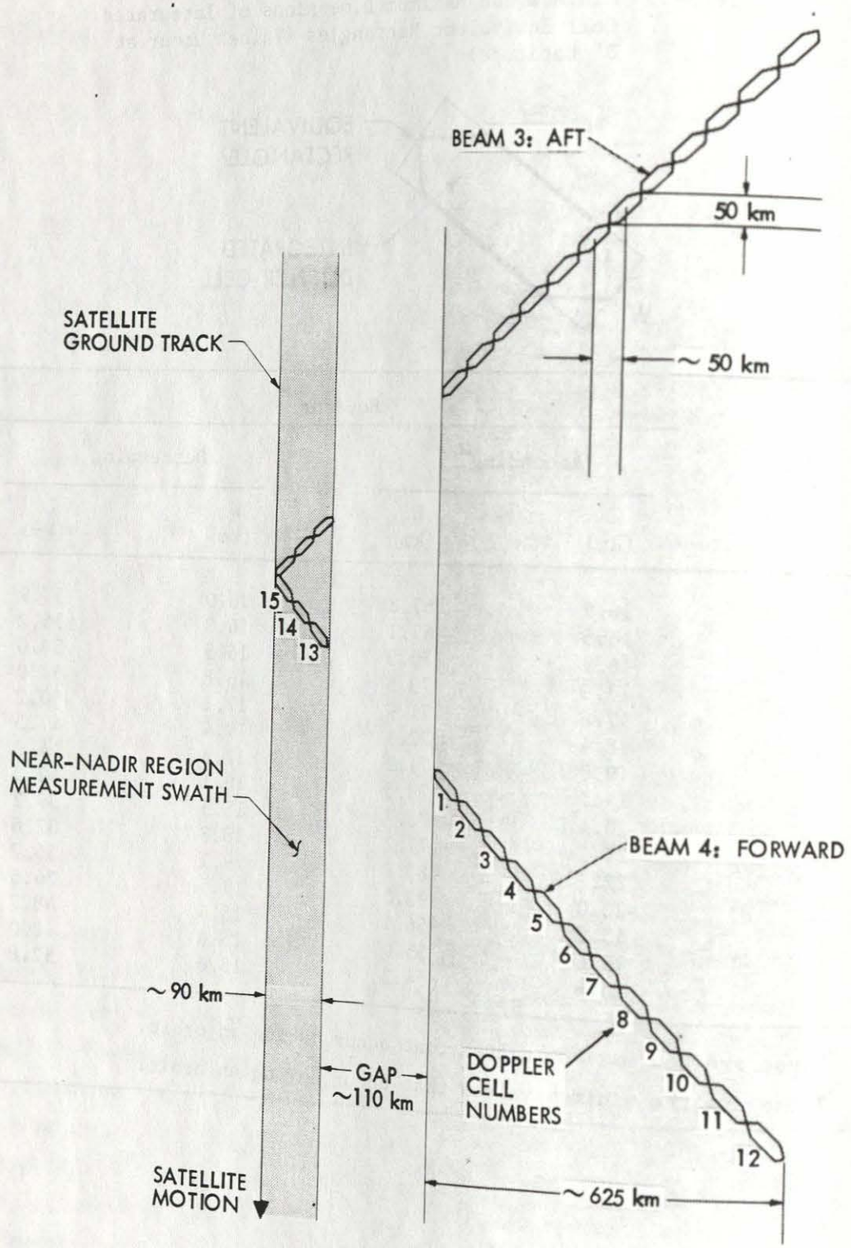

Figure 3-5. SASS Half Swath at Spacecraft Latitudes ±72° (Not to Scale)

nominal half-swath (right-side example) shown in Figure 3-5, with a cell density that is twice that of a double-sided mode.

These swath widths are typical values that occur: neither nadir nor primary swath dimensions remain constant throughout an orbit. Due to in-orbit variations (see next subsection), Doppler cell locations drift in and out from the symmetrical configuration (i.e., all four antenna beams subtending swaths of the same width and cross-track displacement) shown in Figures 3-3 and 3-5, which occurs at the extremal orbital latitudes ±72°. The sensor swath dimensions given in Figure 3-5 also correspond to latitudes ±72°, but the typical wind solution swath dimensions (see below) shown in Figure 3-3 are attained approximately at latitudes ±30°.

A full SASS two-sided mode swath thus consists of one nadir-region strip, within which wind speed (no direction) determinations are made, and the two primary measurement strips on opposite sides of the subtrack, within which wind vector solutions are derived. Since a wind vector determination requires at least two nearly azimuthally orthogonal "views" of roughly the same geographic area, vector solutions are generated only in the regions of fore- and aft-beam overlap, the (typical) 500-km-wide subswaths of the primary measurement strips located on both sides of the spacecraft as shown in Figure 3-3. The two overlap measurement subswaths thus yield a wind vector swath width totalling about 1000 km. The incidence angles corresponding to the overlap measurement regions vary over the approximate range 25-55 deg.

3.4.3.6 Inter-Cell Spacing and Swath-Width Variations. The numbering scheme used for identifying the 15 Doppler cells for each antenna is shown in Figure 3-5 along with nominal half-swath and inter-cell dimensions. The gradual increase in cell size going from nadir to the outer swath-edge is depicted (not to scale). The center-to-center cross- and along-track spacing between Doppler cells is nominally about 50 km. However, because of Earth-rotational/orbit-geometry effects, over a complete orbit the cross-track spacing between the three inner cells varied from 45 to 56 km, and between the outer cells, from 34 to 87 km. The along-track spacing stayed relatively constant at 50 km throughout an orbit.

Small periodic variations in the orientation of the iso-Doppler lines away from symmetry about the subtrack line (see Figure 3-3) occurred throughout an orbit due to Earth rotational effects (maximum value: ±3.5 deg at the equator). These variations caused Doppler cell locations to smoothly drift in and out along the beam pattern from the nominal positions shown in Figure 3-5 as the satellite latitude changed [10]. The Doppler cells from the forward and aft beams moved in opposite directions as the spacecraft traveled in orbit, so that, for example, at the equator where the maximum effect occurred, the swath from one antenna (forward or aft depending on spacecraft direction of travel) was 490 km wide while that of the other antenna was 785 km wide. Thus, the overlap swath in which both wind speed and direction can be derived by the geophysical algorithms had a resulting width determined by the beam with the narrower swath.

The sensor swath configuration and dimensions given in Figure 3-5 and the configuration shown in Figure 3-3 are shown as they would occur at spacecraft latitudes ±72° (the maximum and minimum orbital latitudes), which are the orbit positions where the forward, aft, and wind vector overlap swaths are all symmetric and edge-to-edge co-located with a common 625-km width. These values and other full beam sensor swath widths (not overlay swaths) are given for each antenna at a few representative latitudes in Table 3-6. The maximum swath-width difference between beams is seen to occur at 0° latitude. The resulting wind-vector overlap primary swath width therefore ranges from about 450 km at the equator to about 550 km at the orbital extremities.

Table 3-6. SASS Swath Widths for Each Antenna at Selected Latitudes

Latitude	Swath Width, km			
	Beam 1	Beam 2	Beam 3	Beam 4
±72°	625	625	625	625
+40° Ascending	720	508	720	508
0° Ascending	785	490	785	490
+40° Descending	508	720	508	720
0° Descending	490	785	490	785

The unmatched cells in the outer non-overlapped region of the wider forward or aft swath could actually be used to obtain wind speed information, provided the a priori wind direction is known (or assumed). However, to generate such measurements would require a significant modification to the current ADF geophysical algorithms. Thus, the present GDRs do not contain speed solutions from these portions of the primary swaths that are without orthogonally viewed sensor data.

Figure 3-6 shows one side of a (two-sided) SASS swath that passed over hurricane FICO on July 20, 1978. Seen are the relative location, orientation, and extent of the 15 Doppler resolution cells for beams 1 and 2 that, over a period of several minutes, swept out the nadir and off-nadir swaths. At this part of the orbit, the primary wind-vector solution overlap region is derived from Doppler cells 2-12 (see Figure 3-5) of the compressed beam (beam 1) and cells 1-7 of the expanded beam (beam 2). Two frames of a four-frame calibration sequence (see Subsection 4.5.1) -- which does not generate σ^o measurements -- are evident, including a direct "hit" of the hurricane eye.

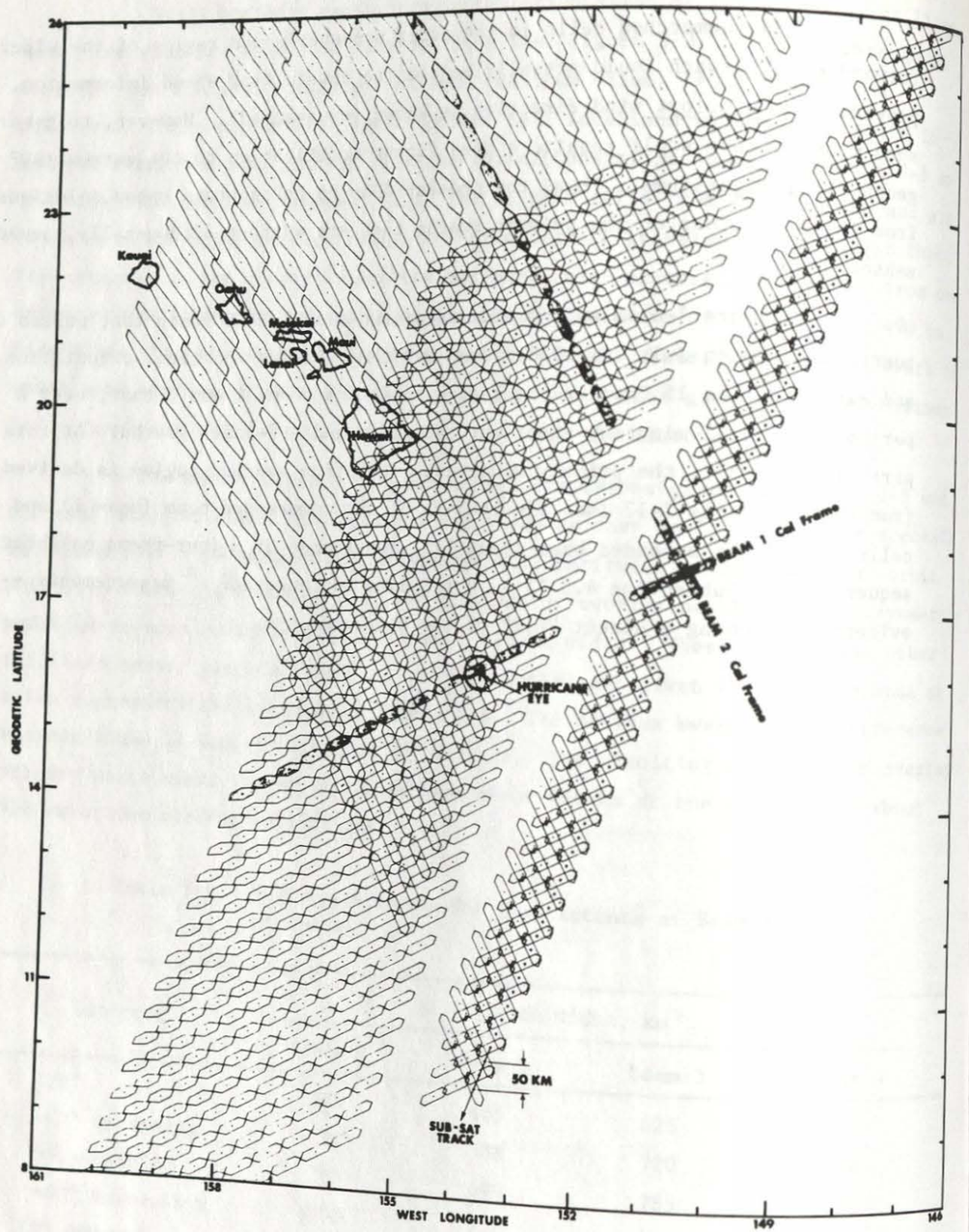

Figure 3-6. Doppler Cell Locations for Beams 1 and 2 Over Hurricane FICO (Rev 331, Day 201)

SECTION 4
SASS DATA FLOW

4.1 ON-BOARD DATA HANDLING

The data collected by the sensors was converted from analog to digital form, except in the case of the SAR. Digitization was achieved by the instruments themselves for the ALT, SASS, and SMMR, and by the satellite data subsystem for the VIRR. All data, with the exception of the SAR instrument, were arranged into block telemetry format.

4.2 SPACECRAFT TELEMETRY

Data was transmitted from the satellite in three separate streams: a 25-kbps real-time stream consisting of instrument data from the ALT, SASS, SMMR, and VIRR, and all engineering subsystem data; an 800-kbps playback stream of recorded real-time data; and a 20-MHz analog SAR instrument data stream which was receivable only in real-time by specially equipped tracking stations.

4.3 RECEPTION AND GROUND TRANSMISSION

Spacecraft data was received and recorded by tracking stations of the Spaceflight Tracking Data Network (STDN), and transmitted to the Goddard Space Flight Center (GSFC). There, data was sorted, merged, time-tagged, and recorded on magnetic tape, which was then shipped to the Instrument Data Processing System (IDPS) at JPL [6].

4.4 INSTRUMENT DATA PROCESSING SYSTEM

The IDPS located at JPL operated on IBM 360/75 systems except for some cataloguing functions that were carried out on a Univac 1108, and later on a Univac 1100/81. The data package received from GSFC consisted of the (non-SAR) sensor and engineering data as well as attitude and orbit determination data. This data was decommutated, organized by major frame, and converted from data numbers to engineering units. Footprint locations were calculated, and data was then formatted into archival-quality MSDR (Master Sensor Data Record) tape files [7] suitable as input for engineering assessment and sensor/geophysical processing programs.

In summary, the primary purpose of the IDPS was the generation -- and cataloguing -- of a complete set of MSDR tape files containing all Seasat instrument data (excluding the SAR) taken during the mission interval (see Table 1-1). An MSDR is a chronologically ordered data file formatted for the utility of further sensor-specific computer processing. The generation of an MSDR by the IDPS began with the extraction of necessary raw telemetry data frames, spacecraft attitude, and orbit ephemeris from the Project Master Data File, Definitive Attitude File, and Definitive Orbit File, respectively (see Subsection 4.4.1). The primary steps in creating an MSDR were: (1) decommutation -- the unpacking of efficiently packed telemetry frames; (2) engineering unit conversion -- the conversion of telemetered numbers to engineering units (volts, degrees, or other units); (3) locating in Earth-fixed coordinates -- the determination of the sensor's field-of-view footprint boresights, footprint cell extent and orientation, slant range, etc.; (4) footprint cell location land/ocean determinations; and (5) formatting.

IDPS processing was the stage immediately preceding the ADF in the overall Seasat data path. The SASS data flow from satellite through the ADF is given schematically in Figure 4-1.

4.4.1 IDPS Input

The IDPS input consisted of data tape files from GSFC. Each set represented a designated 24-h GMT day. The data set comprised three files: the Project Master Data File (PMDF), Definitive Orbit File (DOF), and Definitive Attitude File (DAF).

4.4.1.1 PMDF. The PMDF is a complete record of the Seasat low-rate telemetry stream (25 kbps) that contains all of the playback data received at GSFC, including the low-rate SAR instrument engineering data. It does not contain the high-rate analog SAR data.

The telemetry data stream is positioned within a PMDF tape file in the order in which it was recorded on the satellite (the data is down-linked in reverse order from the way it is recorded). The full 1024-bit Seasat telemetry block [7] is included. There is a minimum of data overlap or redundancy caused by either station redundancy or by the simultaneous recording of the same data on two satellite tape recorders.

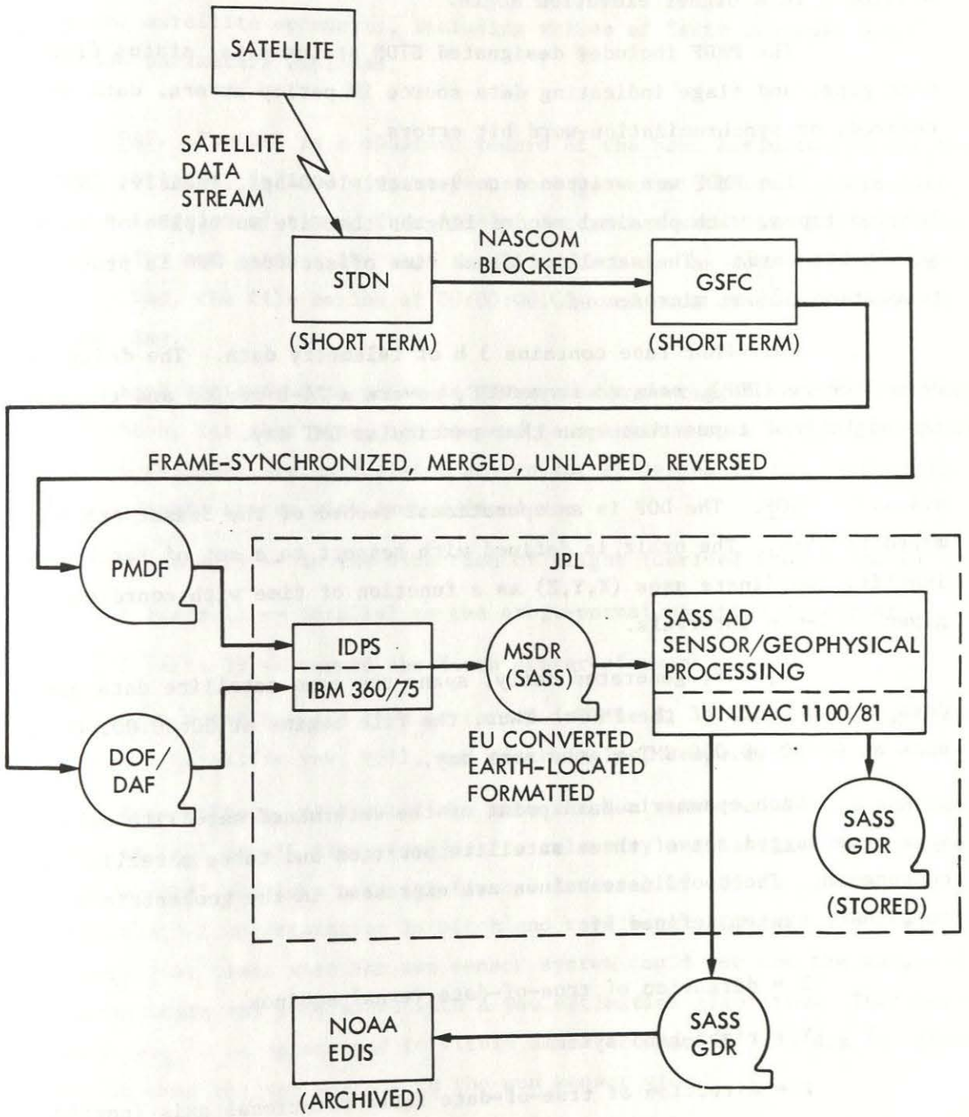

Figure 4-1. SASS Satellite-to-GDR Data Flow

Data received from the STDN sites with NASCOM error indications are not included, but data blocks that are in error are replayed from the station and time-merged onto the PMDF. Redundant data resulting from overlapped STDN coverage was removed by using the criterion of retaining data only from that station with a higher elevation angle.

The PMDF includes designated STDN status bits, status flags to indicate data gaps, and flags indicating data source ID parity errors, data overlap removed, or synchronization-word bit errors.

The PMDF was written onto 9-track, 1600-bpi, (nearly) ANSI-standard-labeled tapes, with physical record lengths that are multiples of both 8-bit bytes and 36-bit words. The satellite clock time offset from UTC is provided to a resolution of one microsecond.

Each PMDF tape contains 3 h of telemetry data. The daily Project Data Package (PDP), relayed from GSFC, covers a 24-h period and therefore contains the eight PMDF tapes that span that particular GMT day.

4.4.1.2 DOF. The DOF is an operational record of the Seasat orbit as determined by GSFC. The orbit is defined with respect to a set of Earth-centered inertial coordinate axes (X,Y,Z) as a function of time with coordinate values given at 1-min intervals.

The DOF, generated daily, spans the same satellite data day as does the contents of the PMDF. Thus, the file begins at 00:00:00.000 GMT and ends at 00:00:00.000 GMT of the next day.

Each ephemeris data point of the determined satellite orbit is given as a time-tagged set of three satellite position and three satellite velocity components. The coordinate values are expressed in the geocentric inertial coordinate system defined by:

X = direction of true-of-date vernal equinox

Y = right-hand system

Z = direction of true-of-date Earth rotational axis (north)

The frequency of the orbit ephemeris points are one per minute, with grid values provided at the exact-minute marks (i.e., 00:00:00.000,

00:01:00.000, ...). The definitive orbit position accuracies, expressed as 3-σ uncertainties, were guaranteed to be no worse than 50 m in the along-track direction and 30 m in both the cross-track and radial directions. The file contains a header record with auxiliary information about the models used to generate the satellite ephemeris, including values of Earth precession and perturbation parameters employed.

4.4.1.3 DAF. The DAF is a complete record of the best estimates of the Seasat spacecraft attitude, defined with respect to a geocentric orbital coordinate system as a function of time. This file of determined satellite attitude was generated daily and spanned the same satellite data day as does the contents of the PMDF. Thus, the file begins at 00:00:00.000 and ends at 24:00:00.000 GMT of the data day.

Each attitude data point is given as a time-tagged set of Euler-angle rotations which, for that time, can be used to transform to a satellite-fixed-alignment coordinate reference system any vector expressed in the geocentric orbital coordinate system with axes defined as:

X (axis 1) -- in the direction of flight (derived from Y and Z)

Y (axis 2) -- parallel to the orbit-normal negative direction

Z (axis 3) -- toward the Earth center-of-mass

The Euler-angle rotations are then performed in the 3, 1, 2 axis order, which corresponds to satellite yaw, roll, and pitch angles, respectively.

Yaw attitude, at those times when the sun sensor could see the sun, and pitch and roll at all times (subject to telemetry availability) were determined with a total absolute accuracy (in a 3-σ sense) of .05 to .23 deg. Similarly, the 3-σ uncertainties in pitch and roll were .305 and .225 deg, respectively. At times when the sun sensor system could not see the sun, the yaw attitude angle was determined with a yaw estimation algorithm. This technique allowed the yaw to be determined to within a 3-σ accuracy of .85 deg for those time periods when the sun was not in the sun sensor view.

The grid-time and frequency of the attitude angle points were selected on 5-s intervals to be sub-synchronous with the DOF data points. That is, the DAF values were provided at integral-minute time grids corresponding to the

DOF, but, in addition, DAF attitudes were provided at eleven other grid points equally spaced between the integral-minute points.

The Definitive Attitude File contains data points at a frequency greater than the DOF frequency so that linear interpolation on the grid values generate errors that are no greater than .02 deg per axis. Each attitude data point in the DAF is accompanied by a coded status flag which, at a minimum, indicates the acceptability, on a per-axis basis, of the telemetry data used to generate that point.

4.4.1.4 Attitude-Orbit Tape. The DOF and DAF are actually maintained as two separate files on a single tape -- the Attitude-Orbit (A-O) tape. The data for each 24-h GMT day is contained on one 9-track, 1600-bpi, ANSI-standard label tape.

4.4.2 IDPS Telemetry Processing

To process telemetry data, it was necessary to read a full DOF file, a full DAF file, and at least one PMDF tape into the IDPS system. The IDPS also required various data sets in the form of look-up tables, which are briefly described below.

4.4.2.1 Required Tables

4.4.2.1.1 Decommutation Tables. The decommutation of the telemetry stream into separate channels required decom tables, consisting of channel numbers versus bit locations within the telemetry block for each of the different sensor and engineering data block types. These tables had provisions for:

(1) Subcoms (i.e., more than one channel per bit location within a block).

(2) Supercoms (i.e., more than one occurrence of a given channel within the same block).

(3) Format changes (i.e., more than one decom map for a given block type, based upon status bits contained within the block).

(4) Split channels (i.e., a channel which consists of nonconsecutive bits).

Items (1) and (2) were required for most block types. Item (3) was required for the ALT block, and item (4) was required for the SMMR antenna position readout channel. Each SASS block contained 64 subcommutated temperature measurements which were read out 8 per block, so that 8 consecutive SASS blocks were needed to sample all 64 measurements.

4.4.2.1.2 EU Tables. The conversion of each telemetry channel from raw binary Data Numbers (DNs) into Engineering Units (EUs) required the use of EU tables. Each table provided channel numbers versus EU coefficients for each of the different block types. These tables had provisions for:

(1) Tenth-order polynomial conversions, using up to 11 coefficients.

(2) Table look-ups, using linear interpolation, for up to 20 pairs of DN versus EU (= 40 input numbers).

(3) Multi-curve special polynomial conversions, where the EU value of one or more other channels is used to convert a given channel's DN value to an EU value.

(4) Own-code conversions using channel-unique conversion techniques.

Items (1) and (2) were required for most block types. Items (3) and (4) were required for some ALT and SASS channels. SASS channels required four different types of special EU conversions, in addition to the standard types (1) and (2). (Only one type of conversion was used for any particular channel.)

4.4.2.1.3 Location Tables. The calculation of instrument boresight directions, Earth-fixed latitudes, longitudes, and other location information relating to sensor footprint areas required various data in the form of look-up tables, with one set of tables per block type. These tables contained the time offset from the start of a data minor frame, and cone and clock angles for each sensor footprint to be calculated. The SASS required special tables such as those containing Doppler-resolution footprint cell center frequencies and bandwidths.

4.4.2.2 Earth Zones. The IDPS flagged each calculated sensor footprint location to indicate whether the footprint fell within a particular zone (i.e., area) fixed on the Earth's surface. Thirteen of these large regions were

established in the northern and southern hemispheres as shown in Figures 4-2 and 4-3. An entire footprint is considered to be in a zone, and therefore flagged, if the center of that footprint falls within the zone. The zone flags were created for the purpose of later extracting data from one or more of the geographical areas and generating Fixed Location Data Record (FLDR) tapes. Footprint data was flagged for the specific zones during the production of the MSDR tapes.

In addition to zone flagging, the IDPS further resolved ALT, SASS, and SMMR footprints with a high-resolution (5'×5') ocean/land discrimination scheme. If a footprint center fell within a specific 5'×5' cell that was all ocean, it was flagged as such; otherwise, it was flagged as land or land/ocean mixed. This first-level land/ocean determination is later refined for all scatterometer Doppler resolution footprint cells during an intermediate stage of SASS ADF processing (see Subsection 6.2) that interrogates an improved land/ocean data base (with the same 5'×5' resolution) with a more exacting discrimination algorithm.

4.4.2.3 Time-Tags. The 40-bit time-tag appearing in each telemetry block was passed on without correction by the IDPS and included as output with each frame of telemetry data. However, the time difference between this telemetry time-tag and the correct UTC time was calculated and supplied by GSFC. The Δ-time correction was included along with the time-tag itself in the MSDR output by the IDPS.

4.4.2.4 Telemetry Block Sort. The telemetry stream was sorted into the following block types:

(1) Altimeter (ALT)

(2) Scatterometer (SASS)

(3) Scanning Multichannel Microwave Radiometer (SMMR)

(4) Visual and Infrared Radiometer (VIRR)

(5) Synthetic Aperture Radar Engineering (SARENG)

(6) Low-Rate-Sampled Engineering (ENGLRS)

(7) Orbit Normal Engineering (ENGORB)

(8) Orbit Adjust Engineering (ENGADJ)

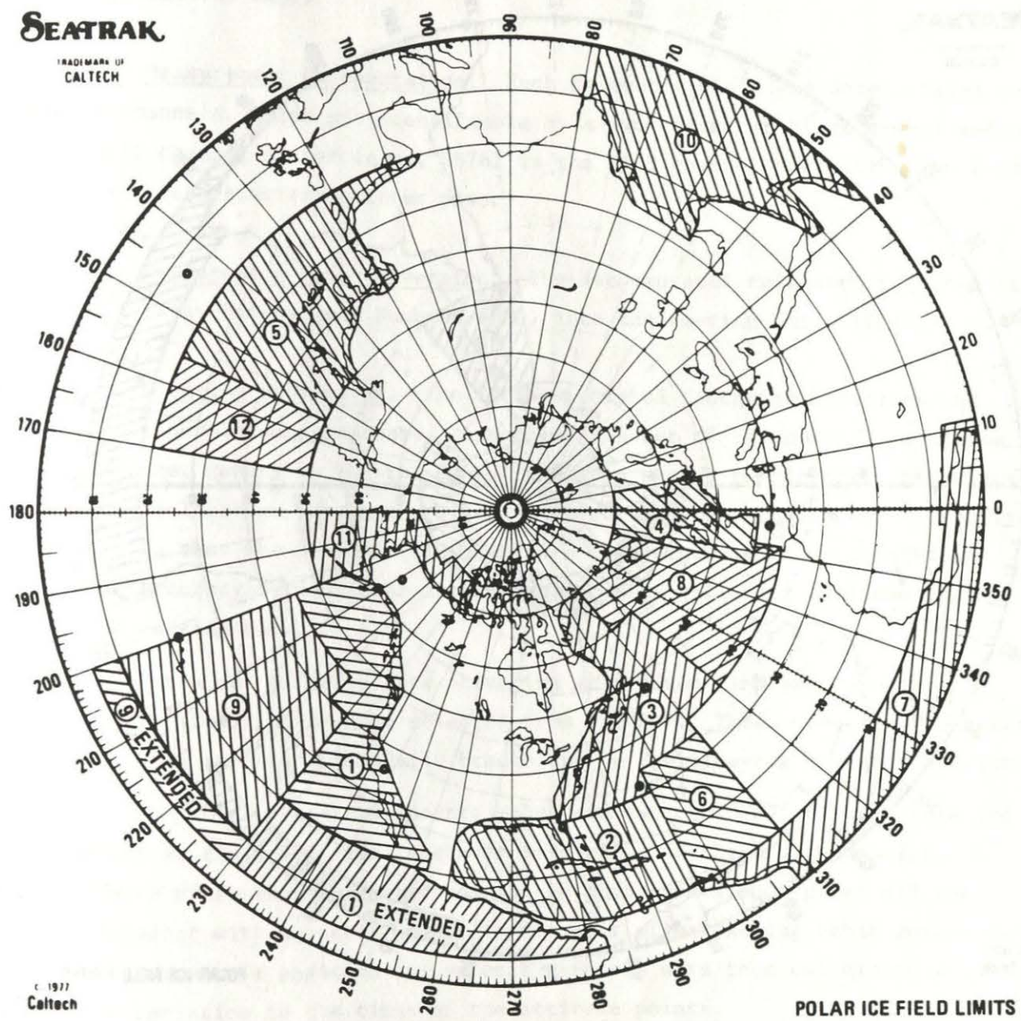

Figure 4-2. MSDR Zones -- North Polar Projection

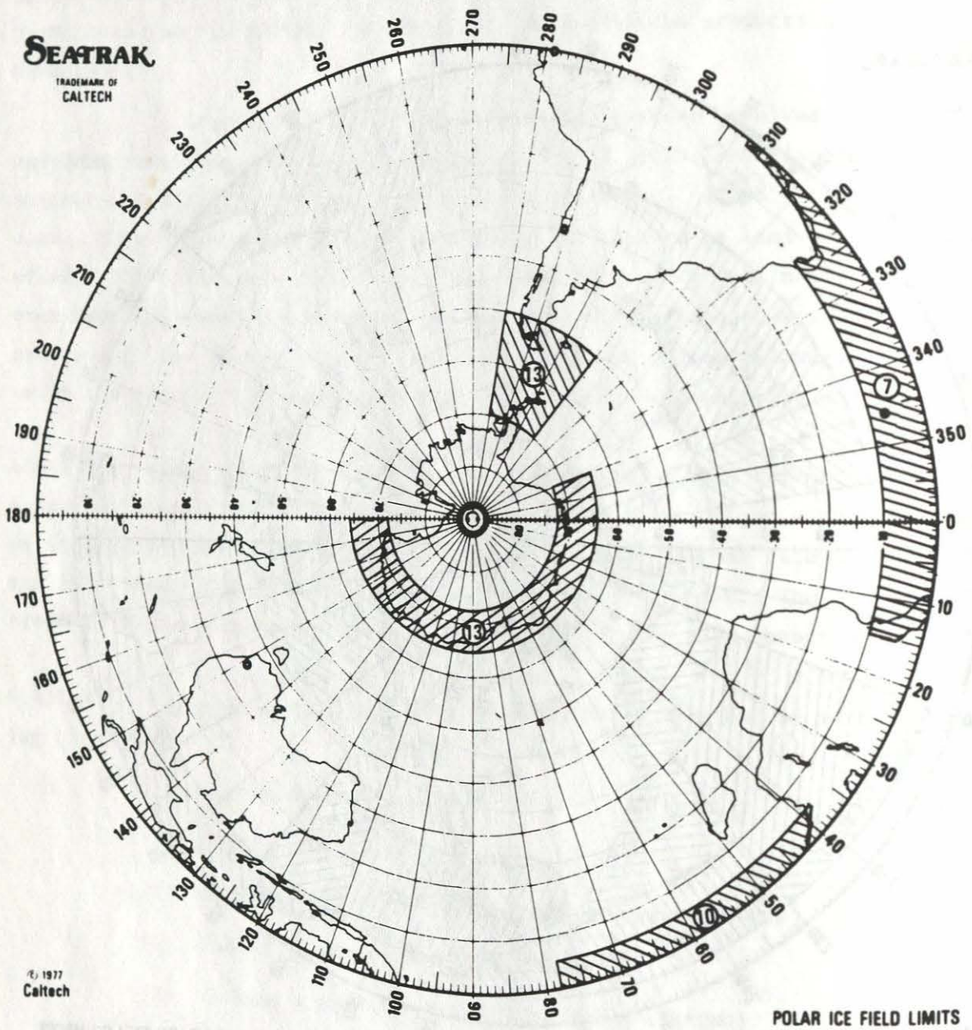

Figure 4-3. MSDR Zones -- South Polar Projection

(9) Ascent Mode Engineering (ENGASC)

(10) Memory Dump

Blocks not containing one of these specified ID values and all Memory Dump and ENGASC blocks were not processed further. A count of these "discarded" blocks was kept.

4.4.2.5 Measurement Decommutation. Each telemetry block was decommutated into separate channels, which are identifiable by a two-character block symbol and a three-digit channel number (e.g., SS761 is the SASS channel containing the time-varying scatterometer transmitter power).

4.4.2.6 Engineering Unit Conversion. The decommutated telemetry required conversion from raw binary Data Numbers (DNs) into Engineering Units (EUs).

4.4.2.7 Location Processing. The IDPS calculated footprint locations and other location-related parameters. Locations consist of Earth-fixed latitudes and longitudes, generally for the center of given sensor footprints. Not every footprint had location parameters directly calculated, but enough were directly calculated so that the remaining intermediate footprints could be located to sufficient accuracy by nonlinear interpolation. The following outlines the general processing flow.

For a set of footprints occurring at a given time-tag, a pair of spacecraft attitude points were selected from the DAF. These were the two points closest in time to -- and nominally bracketing -- the time-tag of the footprints.

For the two attitude points selected, two orbit points were selected from the DOF at the same times, whenever possible. If the attitude points occurred more often than the orbit points, so that an attitude point did not occur coincident with an orbit point, then a pair of bracketing orbit points were selected. Spacecraft position and velocity vectors were then calculated with a spline interpolation to the times of the attitude points.

The latitude and longitude of the geodetic nadir point and the height of the spacecraft above the nadir point were calculated for the times of the two attitude points. These calculations require Greenwich hour angles derived from the DOF and the position vectors.

For the given footprint, the spacecraft-fixed cone and clock angles of the sensor boresight were determined. These angles were obtained by table look-ups for the various instruments. The ALT and SAR have only one boresight direction each; the SMMR and VIRR boresights move with time. The SASS has eight boresight directions, one for each of its antenna/polarization combinations.

Each of the boresight directions was rotated by the spacecraft attitude angles for the two attitude points. Using the pitch, roll, and yaw angles, this transformed all boresight directions from the body-fixed spacecraft coordinate system into the geocentric local orbital coordinate system.

For each attitude-corrected boresight direction, one or more look directions were calculated for the times of the two attitude points. The look directions for the SMMR and VIRR are the attitude-corrected boresight directions. The look direction for the ALT is always directed at the geodetic nadir point. The look direction for the SAR is always given by 90-deg clock and 20.5-deg cone (with respect to geodetic nadir) angles.

The look directions for the SASS required more complicated calculations. Each SASS attitude-corrected antenna boresight results in 30 look directions corresponding to the upper and lower boundaries of each of the 15 scatterometer Doppler resolution cells. The essential calculations performed were:

(1) Calculate the spacecraft's velocity with respect to the rotating Earth's surface.

(2) Calculate the Doppler frequencies corresponding to the upper and lower edges of each Doppler cell. Values of each cell's center frequency and bandwidth were obtained from tables; the upper and lower frequency of each Doppler cell was then calculated by respectively adding or subtracting half the bandwidth to the center frequency.

(3) Calculate the Doppler velocity for the upper and lower edge of each Doppler cell using the Doppler frequencies from (2).

(4) Calculate the squint angle. Each antenna-pair (V and H polarizations) had 10 temperature monitors along its length. Forty total antenna temperatures were subcommutated together in the SASS telemetry blocks (see Subsection 4.4.2.1.1). The squint angle is the key antenna coordinate system angle between the electrical and mechanical boresights of the antenna narrow-beam pattern. Variations in the squint angle about a nominal value due to variations in antenna-beam temperatures were accounted for by a temperature-dependent correction algorithm.

(5) Calculate the look direction of the upper and lower edges of each Doppler cell from the spacecraft and Doppler velocities, the attitude-corrected antenna boresight direction, and the temperature-adjusted squint angle.

The intersection of the look directions and the Earth's surface was then calculated for the given sensor's footprints at the times of the two attitude points. In addition to the resulting footprint center latitudes and longitudes, other location and footprint-extent parameters were calculated for the various sensors. The following location parameters were calculated for each of the 15 SASS Doppler resolution footprint cells and written on the MSDR for each data frame corresponding to a scatterometer telemetry block:

(1) Cell-center latitude and longitude, calculated as the mean of the upper-edge and lower-edge latitudes and longitudes.

(2) Antenna-to-cell-center slant range.

(3) Cell base length, calculated as the distance on the Earth's surface along a direction parallel to the Earth-projected antenna pattern central axis (see Figure 3-4) from the upper edge of the cell to the lower edge.

(4) Angle between the direction of maximum gain in the antenna pattern and the look direction to the center of the cell.

(5) Incidence angle between the look direction to the cell center and the local vertical at that point.

(6) Cone angle at spacecraft from the geodetic nadir point to the cell center.

(7) Azimuth clock angle measured from north at the geodetic nadir point to the cell center.

In addition to these cell-dependent parameters, the IDPS added to each SASS data frame the nadir-point latitude, longitude, and altitude, the pitch, roll, and yaw angles, a sun/no-sun flag, the yaw 1-σ attitude uncertainty (calculated from data on the DAF), the spacecraft velocity azimuth angle from the north, and the along-track velocity component, all of which were interpolated to the footprint time-tag.

4.4.2.8 Zone Flagging. Each calculated footprint location was compared to the zone maps (see Figures 4-2 and 4-3) and flagged accordingly. The footprint latitudes were used to access a latitudinal band of the zone map. (All footprint latitudes on the MSDR are geocentric except for the ALT nadir point, which is geodetic.) The footprint longitude was then compared to each of the longitude pairs for that latitude band to determine whether or not the footprint location falls within the zone.

4.4.2.9 Frame Buildup. Each of the designated block types of the telemetry block sort (Subsection 4.4.2.4), except memory dump and ENGASC blocks, were built up into minor and major frames. A minor frame contains a frame time-tag, a Δ time-tag to correct to UTC, all EU-converted data within the frame, designated location data for the sensor footprints contained within the minor frame, and the zone flags corresponding to these footprints.

For the scatterometer, a major frame consists of eight consecutive minor frames. The first minor frame in a major frame is the minor frame containing the first subcom position for that data type. The last minor frame (No. 8) is the minor frame containing the last subcom position for that data type. A major frame thus consists of enough minor frames to encompass one complete set of subcom data for that data type. The maximum number of subcom positions for any given SASS data type is therefore eight. A major frame contains missing-data indication flags for those minor frames which are missing. The major frame is identical to the minor frame for those data types which do not contain subcoms.

4.4.3 IDPS Output

4.4.3.1 Master Sensor Data Record Tapes. The IDSP produced Master Sensor Data Record (MSDR) tape files that contain satellite data that has been decommutated, converted to engineering units, and Earth-located to the latitude and longitude

of the center of each sensor's boresight. The MSDR is a 9-track, 1600-bpi magnetic tape of archival quality containing typically between 2 and 2-1/2 h of satellite data for all sensors, so that 11-12 consecutive MSDR tapes contain a full day's data. A few minutes of data overlap at the end of each tape precludes the potential loss of varying (instrument-dependent) amounts of sensor data due to the algorithm start-up lag time that accompanies ADF sensor/geophysical processing for the different instruments.

The MSDR contains ALT, SASS, SMMR, VIRR, SARENG, and ENG (including ENGLRS, ENGORB, and ENGADJ) data. Each of these types of data could also be produced on an individual basis on a Sensor Data Record (SDR) tape file.

4.4.3.2 Sensor Data Record Tapes. A Sensor Data Record (SDR) tape file is a complete record of all data processed by the IDPS for a given data type for a given period of time. Thus, a SASS SDR contains all calculated scatterometer data taken from MSDRs for the desired range of time. The tape also contains all coefficients and/or parameters used in calculating these results for the particular data type.

The information contained on an SDR tape is sufficient to allow a user to reconstruct the raw DN data values from the EUs and the complete footprint geometry from the location information. The algorithms for the EU conversions and location processing are the only additional information that a user would need. A complete description of scatterometer SDR tape contents can be found in [7].

A complete set of SASS SDRs covering the mission data interval in a one-tape-per-day ($0^h0^m \rightarrow 24^h10^m$) format exists at JPL.

4.5 SCATTEROMETER FRAME TIMING

4.5.1 Calibration and Science Sequences

A minor frame of SASS data from the SDR (or MSDR) is the time-tagged collection of engineering unit data, footprint locations, and supporting parameters associated with the readings derived from one antenna beam illumination pattern; i.e., a 15-Doppler cell data set. SASS data frames therefore occur nominally every 1.89 s. A SASS instrument science-frame cycle nominally occurs during each 242.05-s interval and consists of 4 consecutive data calibration frames followed by 124 consecutive science frames, occurring in the order

dictated by 31 repetitions of a Table 3-4 mode sequence. Thus, after every group of 124 frames -- about 4 min of data -- science data is interrupted by the presence of 4 calibration frames in the data stream.

This calibration data is in the form of known calibration signal levels applied to the scatterometer receiver. This data was used to determine the current time-varying system gain, which was then used to process the subsequent 124 science data frames. Since measurements leading to σ° backscatter data were not generated during the calibration frames, the SASS sensor data has an X-shaped gap in the (two-sided) swath. The along-track dimension of the gap is evidently given by one or two antenna beam patterns, depending on whether the instrument mode was double- or single-sided, respectively. The subsatellite point moved nearly 1600 km between nominal occurrences of calibration frame sets.

The nominal sequence of 4 calibration frames followed by 124 science frames was interrupted only by (1) the appearance of an uncorrected time regression (see Subsection 4.5.2), (2) missing data frames (i.e., a time gap in the data stream), and (3) a scatterometer mode change. A mode change could occur (and did, hundreds of times during the mission -- a complete SASS mode log is available [5]) at any commanded point in the data stream. Such changes were characterized by the immediate cessation of the science -- or possibly calibration -- frame sequence that was being generated according to the terminated mode's antenna/polarization switching pattern. (If a mode change time occurs anywhere within a 1.89-s frame measurement period (during which time 64 surface samples are being taken -- see Subsection 5.2), that frame is completed before the mode switch is effected.) This is followed at once by the appearance on the SDR of a mode-initializing set of 4 calibration frames; 124 science frames then follow this new-mode calibration data in 31 cycles of the appropriate Table 3-4 switching pattern, unless, of course, this sequence was interrupted by yet another mode change. Successive frame times straddling a mode switch remain 1.89 s apart.

4.5.2 Missing Frames and Time Regressions

Missing data frames do not disturb the 242-s calibration/science frame cycle period; they only cause time-tags on successively appearing frames to differ by some multiple (greater than one) of 1.89 s.

Most time regressions (i.e., time-tags of successive frames not in chronological order) that remained at the IDPS stage of the Seasat data processing path were detected and corrected at that point. Regressions uncorrected by the IDPS were passed through on the MSDRs to the various ADF sensor processors where some abnormal-condition action was taken, depending on the sensor. The response taken by the SASS sensor processor was to re-initialize, that is, to stop processing until the appearance of the next calibration sequence in the scatterometer data stream.

4.6 ADF SENSOR AND GEOPHYSICAL PROCESSING

Algorithms in the form of computer programs are required to process the data from the various sensors into useful sensor and geophysical variables. These algorithms as well as sensor performance and the quality of geophysical results have been, and in some cases continue to be, evaluated by the Seasat sensor managers and experiment teams. The Algorithm Development Facility (ADF) at JPL supports these evaluation tasks by providing the capability for accessing -- on a small or large scale -- the satellite data base, processing the data into geophysical parameters, developing and modifying the computer-code manifestation of the many algorithms used to derive the geophysical parameters, and comparing these parameters to corresponding surface observation data.

When a particular sensor's sensor and geophysical algorithms reached a level of maturity that warranted the generation of GDR tapes containing archival-quality geophysical measurements for that sensor, the ADF provided the capability for such production. The 96-day full mission set of SASS GDR data thus was generated with ADF scatterometer algorithms -- including the key σ°-to-wind-vector model function -- that had undergone extensive development and evaluation. (This is not to say that there exists no room for improvement -- see Section 9.) The SASS GDR algorithms are the culmination of an evolutionary process that included: (1) original design by various team participants, (2) implementation into computer code on the JPL ADF system, (3) several stages of refinement resulting from comparisons with surface "truth" observations and intercomparisons with results from other sensors performed during the Seasat Workshops [11, 12, 13, and 14], and (4) additional algorithm performance evaluations carried on at SASS Experiment Team working sessions.

4.6.1 SASS GDR Sensor Algorithm Processing

The ADF segment of the scatterometer end-to-end data processing system comprises three processing components, the first of which is formed by the SASS σ° sensor file algorithms that are described in the next section. ADF "sensor" files contain data generated by "sensor algorithms"; the sensor file on a SASS GDR is that data contained in all of the σ° basic and supplemental records (see Section 8) and in the associated text header records. In general, such algorithms perform instrument-specific calibrations and corrections, producing as outputs physical "observables" (e.g., σ°s) that are essentially independent of the specific hardware implementation of the instrument. In addition to the measurements of interest, a sensor file contains time-tags, Earth locations, warning flags indicating potential instrument health or data-processing problems, values of all corrections, and instrument mode indicators relating to these measurements.

As shown in the scatterometer ADF processing schematic (Figure 4-4), σ° sensor file computations begin with the reading of a SASS SDR tape file and end with the writing of a GDR σ° sensor file. In the context of the ADF, the SASS σ° algorithms may be viewed as a set of computer (Univac 1100/81) routines forming the first-stage processor whose inputs are: (1) Earth-located SASS EU data from an SDR, (2) a small set of processor control instructions, and (3) a stored table of constant parameters; and whose output is SASS σ° data on a GDR.

4.6.2 SASS GDR Attenuation, Footprint Land/Ocean Resolution, and Geophysical Algorithm Processing

The primary use of the σ° GDR sensor file -- and the σ° data itself -- is as input to the SASS geophysical algorithms. These latter algorithms form a processor that operates on the σ° data to produce the end-product geophysical solutions, the ocean-surface wind vectors. Before this geophysical processing is done, however, the input σ° footprint cell-location first-level land/water flags are refined with a high-resolution (5') land/sea data base, and the σ° measurement values are corrected -- to the extent possible -- for the effects of atmospheric attenuation. As shown in Figure 4-4, this second stage in the ADF SASS computing, which is described in Section 6, is done with a set of algorithms which (1) reads both a SASS "unattenuated" σ° GDR sensor file generated by the first-stage

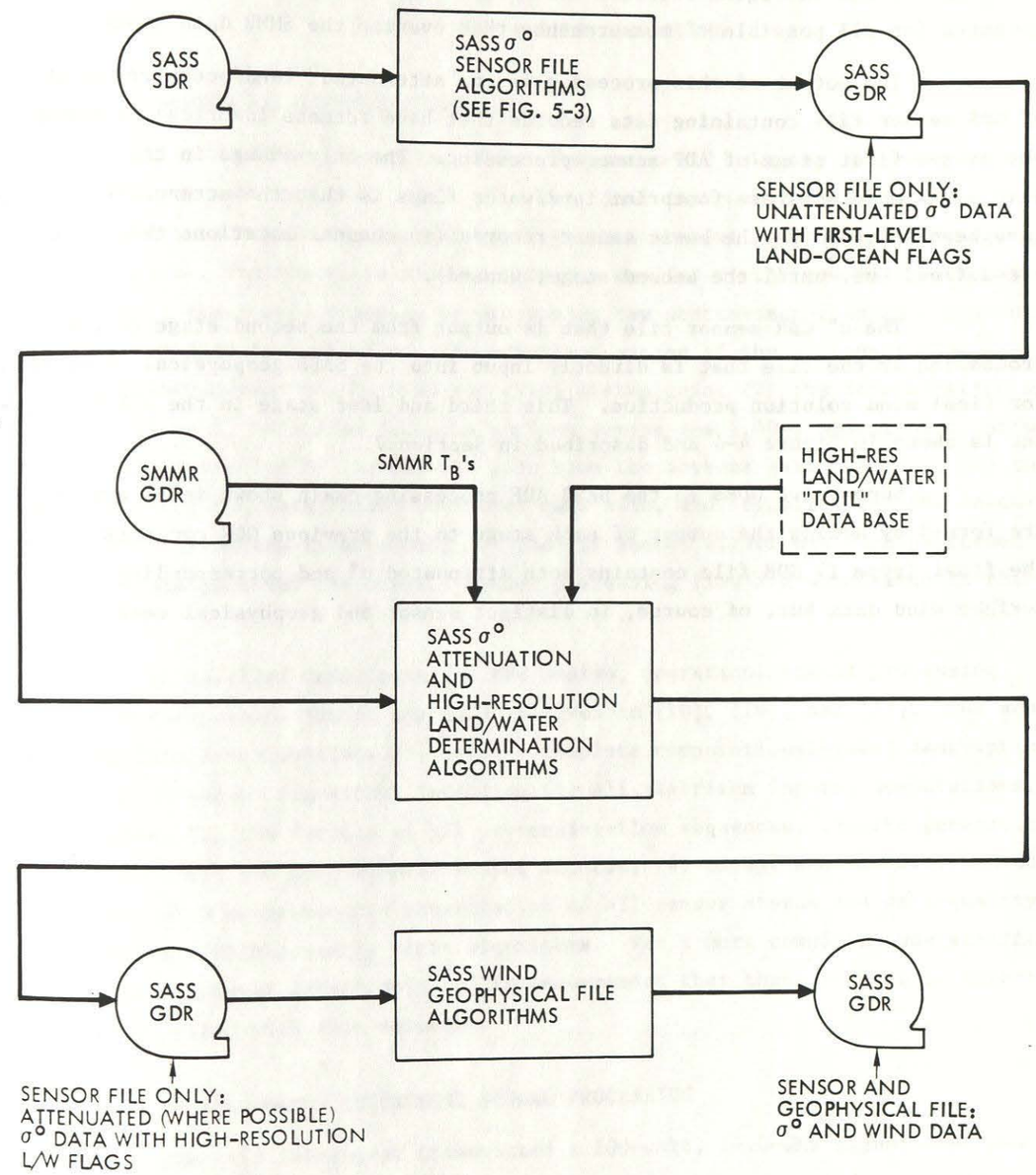

Figure 4-4. Scatterometer ADF Geophysical Data Record (GDR) Sensor (σ°) and Geophysical (Wind Vector) Processing From SDR to Final SASS GDR File

processing and a SMMR GDR brightness temperature (T_B) [15] file, and (2) interrogates the shoreline-location data base. Attenuation corrections are computed for all possible $\sigma°$ measurements that overlap the SMMR data swath.

The output of this processor is an "attenuated" land/ocean resolved $\sigma°$ GDR sensor file containing data records that have formats identical to those out of the first stage of ADF sensor processing. The only change in the GDRs beyond the more accurate footprint land/water flags is that the attenuation values have been appended to the basic sensor records (in channel locations that were pre-defined but, until the second stage, unused).

The $\sigma°$ GDR sensor file that is output from the second stage of ADF processing is the file that is directly input into the SASS geophysical algorithms for final wind solution production. This third and last stage in the ADF processing is shown in Figure 4-4 and described in Section 7.

Successive GDRs in the SASS ADF processing chain shown in Figure 4-4 are formed by adding the output of each stage to the previous GDR contents. Thus, the final (type I) GDR file contains both attenuated $\sigma°$ and corresponding ocean-surface wind data but, of course, in distinct sensor and geophysical records.

SECTION 5
SASS $\sigma°$ SENSOR FILE ALGORITHMS

5.1 SENSOR FILE COMPUTATIONS

The fundamental derived sensor "measurement" taken by the scatterometer is the NRCS backscatter coefficient $\sigma°$. The final instrument-calibrated sensor data and various supporting parameters (e.g., measurement error level and signal-to-noise ratio, instrument-related corrections applied to the computer backscatter coefficient, etc.) were computed by processing raw scatterometer engineering unit and location data from the SDR. The principal stages of the $\sigma°$ computation are (1) the determination of the SASS receiving system gain, (2) the determination of the mean power P_R reflected from the surface during the 1.89-s measurement period, (3) the determination of the antenna gain from the antenna gain function, (4) the calculation of the measurement footprint cell size, and, finally, (5) the calculation of $\sigma°$ from the radar equation. The ADF sensor algorithms that performed these computations and the overall sensor processing flow are summarized in this section.

A detailed description of the design, operation, signal processing, and instrument evaluation of the SASS is given in [10], [16], and [17]. The sensor algorithm specifications [3] offer a complete computational-level description of each SASS sensor algorithm, including (1) all algorithm inputs, computations, and outputs, (2) the details of all processing-flow sequences, (3) the generation of the GDR basic and supplemental sensor records, (4) exceptional-condition handling, and (5) a comprehensive presentation of all sensor status and data-quality flags that are maintained by these algorithms. For a more complete understanding of the scatterometer sensor data, it is recommended that these sources be referred to in conjunction with this document.

5.2 SCATTEROMETER INSTRUMENT SIGNAL PROCESSING

The SASS instrument transmitted a 100-watt, 14.6-GHz signal that was backscattered from the Earth's surface. A square-law detector and gated integrator in the receiver were used to sample the reflected power from a given antenna 64 times during a 1.89-s measurement period. The first three samples reflected from the surface were used to place the receiver-processor in the most

appropriate of four possible gain states. With the proper gain state chosen, the received signal level was certain to be in the linear portion of the square-law detector characteristic. The remaining 61 samples were then processed using the selected gain state. At the end of the 1.89-s period, mean values of the 61 integrated voltage levels were entered into the telemetry data stream for each of the 15 Doppler cells.

The 1.89-s measurement interval was repeated continually, but a different antenna was activated for each consecutive sampling period. Each of the eight possible SASS science operational modes is associated with a different prescribed antenna/polarization sequence ordered as described in Table 3-4. A set of such sequential measurements over a period of time resulted in the ground pattern coverage shown in Figures 3-3 (for a two-sided mode) and 3-6.

A voltage pair was obtained for each of the 15 channels during a science frame period that were measures of (1) the signal reflected from the surface plus system noise V_{SN}, and (2) the system noise V_N only. The determination of this voltage pair is illustrated in Figure 5-1, where a pulse repetition period for one of 61 samples and a simplified diagram of the receiver-processor system for any one of the 15 Doppler channels is shown. The 4.8-ms pulse represents the transmitter-on time. In the period between successive transmitter pulses, the return signal pulse plus noise and the noise itself are individually detected and integrated. A typical output signal from the square-law detector for one of the 15 channels is shown in the figure. At the end of the signal integration period t_g, there results the sample voltage V_{SNN}. The t_g interval is immediately followed by an integration dump; i.e., an integrator zero restart, after which processing over the noise integration period t_n yields the sample voltage V_N. At the end of 61 samples (1.89 s) the mean values V_{SNN} and V_N for all 15 channels, the measured transmitted power, and various housekeeping data and status indicators are entered into the telemetry data stream.

Using the telemetered voltage pair V_{SNN} and V_N, the gain of the receiver obtained from calibration data frames, and known processor integration times, the power reflected from the surface P_R was calculated by the sensor algorithms. P_R results when the measured noise power derived from V_N is subtracted from the measured signal-plus-noise power derived from V_{SN} as shown by Eqs. (3)-(5) of Figure 5-1. This subtraction process allowed accurate signal measurement even when the signal-to-noise ratio (SNR) became as low as -12 dB.

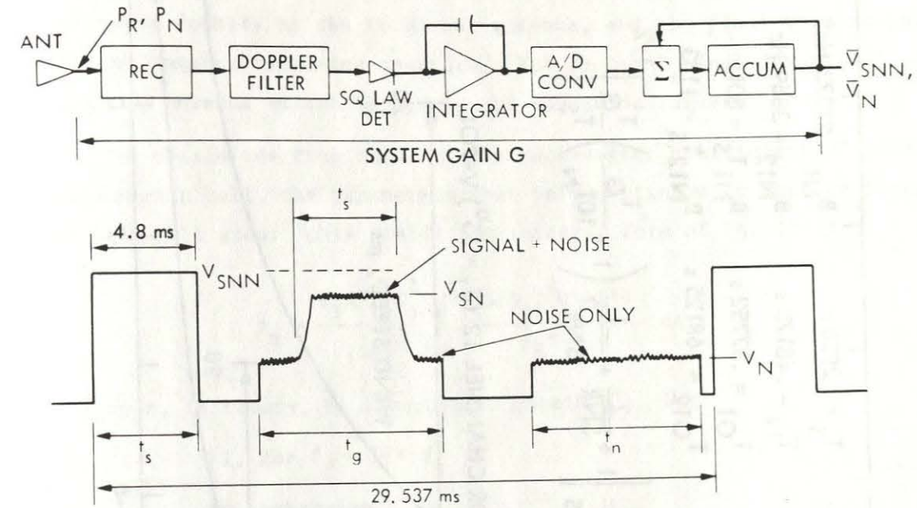

$T_S = 61 \times t_s = .2928$ (ALL CHANNELS)

$T_G = 61 \times t_g = .345$ TO $.69$

$T_N = 61 \times t_n = .4818$ (ALL CHANNELS)

$$\bar{V}_{SNN} = T_S\, G(P_R + P_N) + (T_G - T_S)\, P_N G \qquad (1)$$

$$\bar{V}_{SN} = \bar{V}_{SNN} - \frac{T_G - T_S}{T_N}\, \bar{V}_N \qquad (2)$$

$$P_{SN} = \frac{\bar{V}_{SN}}{T_S G} - \text{SIGNAL + NOISE POWER} \qquad (3)$$

$$P_N = \frac{\bar{V}_N}{T_N G} - \text{NOISE POWER} \qquad (4)$$

$$P_R = \frac{\bar{V}_{SN}}{T_S G} - \frac{\bar{V}_N}{T_N G} - \text{SIGNAL POWER} \qquad (5)$$

WHERE

$$G = \frac{\bar{V}_{SNN} + \bar{V}_N}{P_N (T_G - T_N)} \qquad (6)$$

(OBTAINED DURING CALIBRATION SEQUENCE, WHEN P_N IS KNOWN.)

Figure 5-1. SASS Pulse Repetition Period and Receiver-Processor System

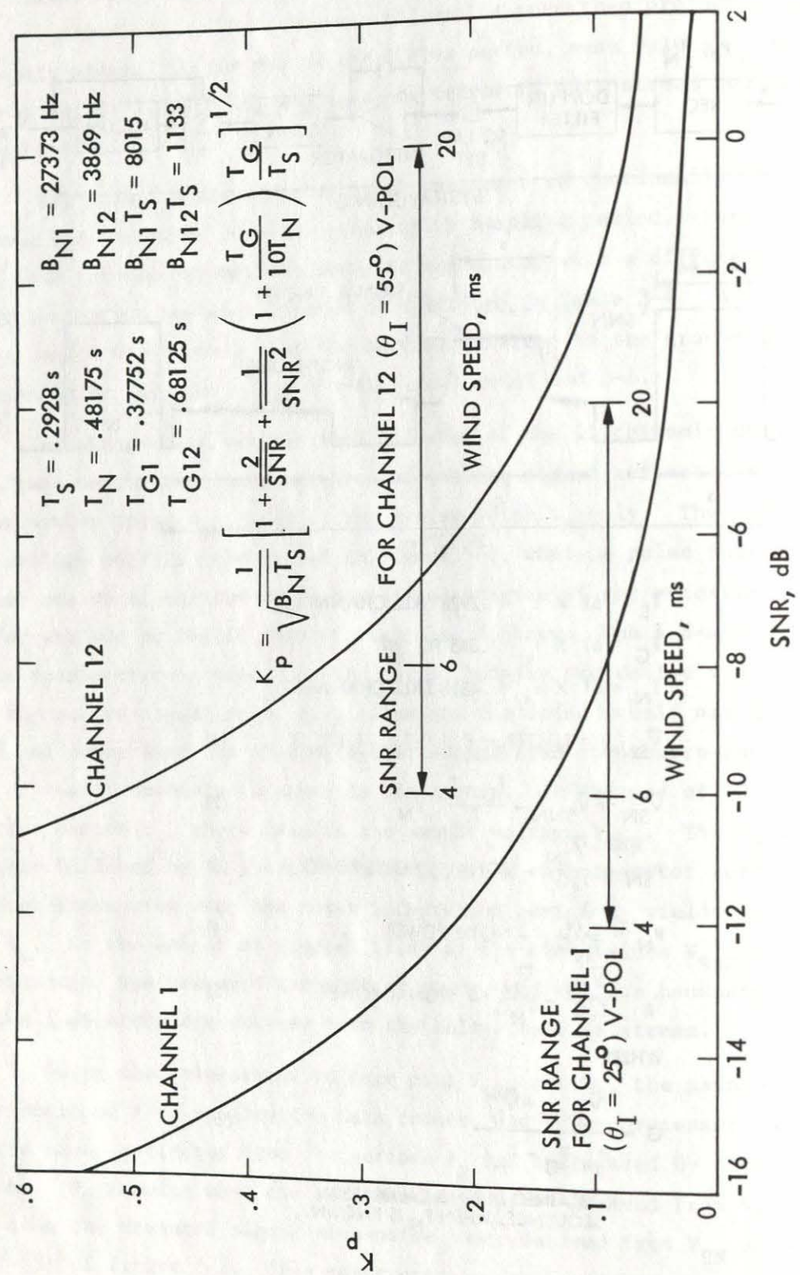

Figure 5-2. Normalized Standard Deviation (K_p) of Received Power Measurement Versus SNR

The terms enclosed in the first three sets of parentheses represent (1) the power density at the surface, (2) the effective radar cross section, and (3) the RF spreading loss, respectively. The product of these three terms represents the power density at the receiving antenna, and the final term in parentheses is the antenna receiving aperture. The factor L_s includes miscellaneous losses such as antenna switching matrix and waveguide losses.

To obtain the true value of the backscatter coefficient $\sigma°$ from a Doppler footprint cell, the parameters that vary continuously must be integrated over the full cell area: this yields the integral form of Eq. (5-1)

$$P_R = \frac{P_T \lambda^2 L_s G_o^2}{(4\pi)^3} \int_A \frac{\left(G/G_o\right)^2 \sigma° h(f)}{R^4}\, dA, \qquad (5\text{-}2)$$

which can then, in theory, be inverted to obtain $\sigma°$. For

$$h(f) = \begin{cases} 1, & \text{for } f_\ell < f < f_u \\ 0, & \text{otherwise} \end{cases}$$

and

$$G_R = G_T = G_o\left(G/G_o\right),$$

where

$f_\ell = f_o - B_N/2$

$f_u = f_o + B_N/2$

B_N = Doppler filter noise bandwidth for particular cell

f_o = Doppler filter center frequency for particular cell

G_o = peak antenna gain

G/G_o = gain loss ratio

and integration cell area defined by $A = LR\phi_A$, where

L = distance on Earth surface from f_ℓ to f_u

ϕ_A = narrow dimension antenna beamwidth in radians,

the integral in Eq. (5-2) can be approximated by assuming that over the integration the integrand variables are constants and are equal to the actual variable values at the center of the area A. Equation (5-2) then reduces to

$$\sigma^\circ = \frac{(4\pi)^3 P_R R^4}{P_T \lambda^2 L_s G_o^2 \left(G/G_o\right)^2 A} \tag{5-3}$$

Here it is assumed that σ°, R, and G/G_o are Doppler cell center values. Inclusion of minor correction factors (that add to the right-hand side of Eq. 5-3) compensates for most of the difference between the approximating equation and the exact integral equation in the calculation of σ°. The constant corrections were determined by a detailed comparison of the values obtained from both forms over a parametric range of conditions. Application of these corrections (see [31]) keeps the error in σ° due to the use of Eq. (5-3) under .1 dB, and allows the calculation of scattering coefficients without the inversion of the integral in Eq. (5-2).

The form (5-3) was used by the SASS sensor algorithms to compute σ° from the received power. Pre-launch measurements of antenna switching matrix and waveguide losses were used for L_s. The peak gain G_o was a constant determined during ground-based antenna pattern measurements, and the relative gain G/G_o was determined from a table lookup as a function of the antenna look direction for each cell. This G/G_o table was also determined from ground-based antenna pattern measurements; it was corrected slightly after analysis of σ° data returned from the Amazon Rain Forest (see Subsection 5.4.2). The SASS-to-cell antenna look angle, slant range R, and other footprint location and extent parameters for each of the 15 Doppler cells were obtained from an SDR file (see Subsection 4.4.2.7) for every SASS frame of data. The integration area A was computed for each cell by a sensor algorithm using some of these parameter values provided on the SDR. Using the measured values of P_R and P_T, σ° could then be obtained for each Doppler channel by evaluating Eq. (5-3) and adding the appropriate correction factor.

5.4 σ° MEASUREMENT ERROR SOURCES

The measurement accuracy [10,16] of σ° was affected primarily by communication noise, attitude pointing uncertainty, instrument processing (e.g., quantization errors and gain uncertainty), and various bias errors. Bias errors

5.4.1.2 Attitude Pointing Uncertainty. The most significant measurement error source after communication noise is attitude pointing uncertainty. Included are roll, pitch, and yaw angle uncertainties, alignment uncertainties due to mechanical and thermal effects, and squint angle uncertainty. Table 5-1 lists the error-slope sensitivities for each of the major sources of pointing uncertainty (e.g.,

Table 5-1. Pointing Uncertainty Sensitivities[a]

θ_I, deg	Error Source	Error Slope σ°, dB/deg	Error Slope θ_I, deg/deg	Error Slope DIST, km/deg
25	Roll	.14	.93	16.8
	Pitch	2.47	.95	17.0
	Yaw	.84	.53	9.7
	Squint	2.04	1.43	25.6
	RSS	.44 dB(10)	.26°	4.7 km
45	Roll	.06	1.02	25.6
	Pitch	.22	1.01	25.5
	Yaw	.03	1.26	31.81
	Squint	.17	1.91	48.2
	RSS	.03 dB(1)	.48°	12.1 km
55	Roll	.01	.87	25.7
	Pitch	.87	.85	25.2
	Yaw	.53	1.31	37.9
	Squint	.8	1.79	52.0
	RSS	.21 dB(5)	.48°	14.0 km

[a] 1-σ Uncertainty:
Roll ≈ .08 deg
Pitch ≈ .11 deg
Yaw ≈ .33 deg
Squint ≈ .1 deg
Mechanical misalignment ≈ 6.9×10^{-3} deg
Thermal misalignment ≈ .02 deg

$\partial\sigma^\circ/\partial(\text{roll})$) at three different incidence angles. Included in the table are uncertainty slopes relating to the calculation of the incidence angle θ_I, and the locating of surface positions (DIST). Thus, the first table entry indicates that for θ_I = 25 deg (channel 1), a 1-deg roll uncertainty will map into a σ° error of .14 dB. These slopes vary slightly throughout the orbit; maximum values are shown. Also included is the total 1-σ RSS error due to these attitude and alignment sources that results from the 1-σ uncertainties listed at the bottom of the table. The values in parentheses in the σ° error column are the errors expressed as normalized standard deviations in percent.

5.4.1.3 Instrument Processing Noise. The instrument processing error that results from processor quantization effects, i.e., the discrete representation of continuously varying parameters, etc., is relatively small compared to the other random measurement errors. A .1-dB 1-σ error-level assessment was made by the sensor algorithms for this source.

5.4.1.4 Total σ° Uncertainty Due to Random Error Sources. For high SNR, corresponding to high wind speeds, the attitude uncertainties dominate the σ° error sources. For low SNR, corresponding to low wind speeds, K_p dominates. Estimates of the 1-σ level for both of these errors were made by the sensor algorithms for all Doppler channels. The total normalized standard deviation (NSD) of σ° measurement error was also then estimated as the RSS of the three random sources, including the .1-dB error assigned to instrument processing.

The total random error that occurred in the measurement of σ° under high SNR conditions is estimated to be less than .47 dB. For worst case SNR conditions occurring at low wind speeds and at the outer edge of the swath, this error approaches 3 dB.

5.4.2 Scatterometer Interbeam Biases

SASS measurements taken during the mission from the Amazon rain forest, a region thought to yield isotropic and polarization-insensitive backscatter, were used in an analysis to determine, to the extent possible, the relative static biases between the four dual-polarized antennas [10]. A sensor algorithm used the resultant table of relatively small corrections to remove these estimated antenna- and polarization-dependent biases. This table is further

separated into nadir- and primary-swath bias corrections. The analysis indicated that any interbeam biases that might remain in the final corrected σ° measurements output to the GDR sensor file are small.

5.5 INSTRUMENT STABILITY: THE SASS NOISE FIGURE

The four calibration frames that occur in the data every four minutes or after a mode change were used by the sensor calibration algorithms to estimate the scatterometer noise figure, as well as to update the current system gain. This computed noise figure provides a tool for evaluating the noise characteristics of the instrument receiver system and overall system stability [16]. Analysis of this noise figure parameter indicates that the receiver noise figure remained stable at its prelaunch calibration value of 5.6 dB during the 96 days of mission data.

5.6 SCATTEROMETER SENSOR FILE PROCESSING

5.6.1 Processing Summary

5.6.1.1 Algorithm Computations. SASS σ° sensor processing from input SDR to the output GDR first-stage sensor file (first box in Figure 4-4) is shown in Figure 5-3 as a schematic of the 12 labeled algorithms and their interfaces, functional flow sequence, and outputs to the GDR. Individual algorithms are identified in the figure by shorthand labels (S-xx) taken from their full numbering scheme designations given in [3]. Three algorithms process calibration data, eight process science data, and one functions as a processor controller.

Data is processed from SDR to GDR on a frame-by-frame basis: after one complete telemetry frame of data has been read from the SDR, unpacked from a byte-oriented to a computer word-oriented format, and otherwise prepared for processing by the input algorithm I-01,* control is passed to the σ° "supervisor"

---

*The input (I-01) and output (O-01) algorithms in Figure 5-3 are considered to be ADF system-level subroutines and not σ° sensor file subroutines.

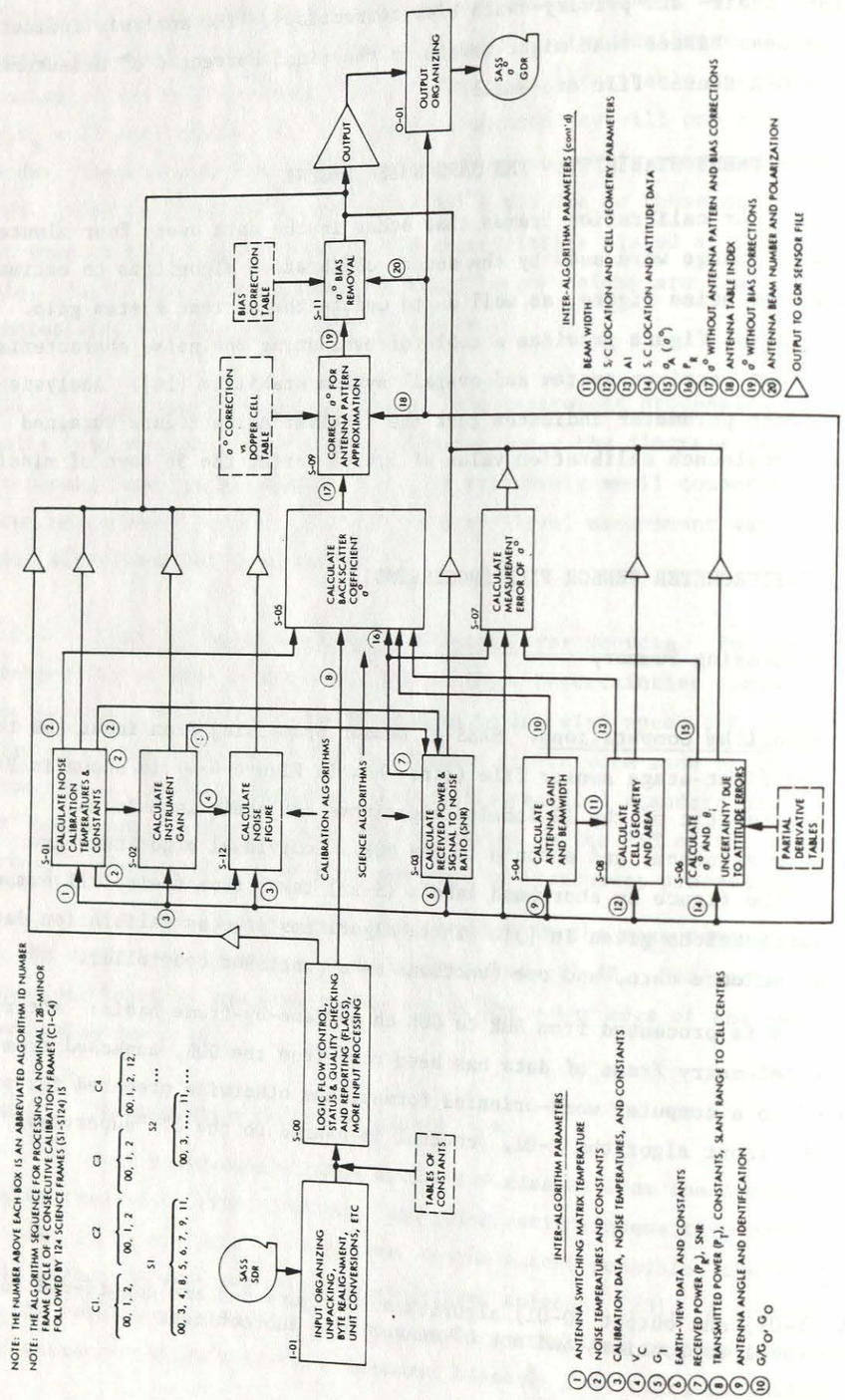

Figure 5-3. Scatterometer ADF GDR σ° Sensor Processing Algorithms

algorithm S-00.* S-00 performs many of the data "housekeeping" functions, such as (1) instrument status and health evaluation; (2) bit error, anomaly, and missing data detection (with corrective action taken, whenever possible); (3) data quality inspection; and (4) status reporting with indicator flags on all of these items.

If the current frame being processed is calibration data, S-00 invokes algorithms S-01, S-02, and S-12. S-01 and S-02 determine the current system gain (see Subsection 5.2), and S-12 performs the receiver noise figure computations at the end of the calibration sequence. If the current frame is science data, then the other eight σ° algorithms (there is no S-10) are invoked in the order shown in Note 2 of Figure 5-3. The received power, antenna gain, cell area, and σ° value are determined by algorithms S-03, S-04, S-08, and S-05, respectively. Estimates of σ° error components and total measurement NSD are computed, and the σ° bias and antenna pattern corrections are applied by algorithms S-06, S-07, S-11, and S-09, respectively.

Some Doppler cell geometry parameters not computed by the IDPS (see Subsection 4.4.2.7), such as the latitude and longitude of the four corners of a rectangular box which approximates a cell's location and extent, are also computed by S-08 for inclusion in the GDR sensor file. These corner locations are used for, among other things, co-locating SASS and SMMR footprint cells and for identifying SASS cells that partially or completely overlay land or ice in the attenuation and ocean/land resolution SASS sensor file processing (Section 6) that follows the σ° computation stage.

5.6.1.2 SASS GDR Sensor Records

5.6.1.2.1 Basic Sensor Record. After an input frame of science data has been processed by the σ° algorithms, the resulting parameters to be saved are collected, organized into a byte-formatted record, and then written as a single data frame onto a GDR sensor file by the output algorithm O-01. This GDR σ° record thus

---

*In the context of the ADF environment, higher level system algorithms not shown in Figure 5-3 control the functioning of S-00.

retains the one antenna beam -- 15-cell data set frame structure described in Subsection 4.5. Numerous intermediate and auxiliary parameters (SNR, various σ° corrections, etc.), as well as footprint location data passed through from the SDR and from algorithm S-08, are also included in this GDR science frame output record. This data unit is the SASS GDR basic sensor record; its contents and format are given in Section 8.

5.6.1.2.2 Supplemental Sensor Record. For each calibration four-frame sequence a separate record containing the resulting system gain, noise figure, and supporting parameters is written onto the GDR sensor file. Each calibration data record appearing on a GDR is therefore nominally followed by 124 consecutive science frame (basic sensor) records. This second record generated by the σ° algorithms is the SASS GDR supplemental sensor record; its contents and format are also given in Section 8.

5.6.1.3 Unavailable Footprint Location Data. Occasionally in the mission data stream, the IDPS was unable to compute Doppler cell Earth-location parameters for SASS science frames even though the corresponding telemetry data was present. Typically, this occurred earlier in the mission when attitude control difficulties caused attitude reference parameters (e.g., yaw) to exceed mission-design performance specifications. This in turn resulted in Doppler cells near the outer edge of the SASS swath having calculated locations that did not intersect the Earth's surface for short bursts of data. Such data frames are flagged on the SDR as having no footprint location information available for all 15 cells (the entire minor frame). For continuity, the SASS sensor algorithms carried the processing of unlocated science frames as far as they could -- to the point of received power P_R and signal-to-noise ratio (S-03) -- with the circumstance appropriately flagged on the output GDR basic sensor record.

5.6.2 Capsule Description of Sensor Algorithms

An algorithm-by-algorithm summary of the function of the 12 computer modules that perform the scatterometer sensor file processing is given below. A detailed description of these algorithms can be found in [3].

5.6.2.1 S-00: Status and Quality Checking. This algorithm is the main controller of the sensor file processing. It checks the various status, science, and housekeeping telemetry channels for proper instrument operation, channel out-of-range conditions, and possible data stream bit errors. It provides status and quality flags on the output records (see Section 8) for use in assessing the quality of the σ° measurements. A subset of these flags is examined by the geophysical processing algorithms to determine whether the quality of particular σ° measurements is too low to warrant their use in computing wind vector solutions. Where possible, the algorithm makes adaptive changes to the processing to avoid errors which would otherwise result because of key detectable bit errors and/or channel out-of-range conditions. It determines when science and/or calibration frames are missing and performs related record-keeping. It provides for continued sensor file processing when some, or even all, of the four calibration frames in a calibration sequence are missing from the data stream.

The algorithm determines the instrument operating mode and attempts to resolve conflicting mode indications. It provides the necessary processing for the continuous calibrate and standby modes. It also performs science frame time filtering, yaw uncertainty override, orbit number calculation, some input data transformations, and sequencing of the other sensor algorithms after determining if an input frame is science or calibration data.

5.6.2.2 S-01: Constants. This calibration algorithm calculates various parameters such as antenna switching matrix (ASM) gains and calibration noise temperatures that are subsequently used by other algorithms. These parameters are recomputed during each calibration sequence using ground calibration and temperature monitoring data, and remain constant over the ensuing 124 science frames until the next calibration sequence.

5.6.2.3 S-02: Gain Calibration. This calibration algorithm determines the instrument gain using data obtained during a calibration period. These gain factors are then used for the subsequent science cycle of 124 frames (or less if a mode change and resultant calibration sequence occur -- see Subsection 4.5.1).

5.6.2.4 S-03: P_R, NP, and SNR. This algorithm determines the value of measured reflected signal power (P_R), measured noise power (NP), signal-to-noise

ratio (SNR), and the mean antenna noise temperature (TAM). These parameters are computed for all 15 Doppler channels in each frame of science data, except for TAM, which is the noise temperature averaged over the 15 channels.

5.6.2.5 S-04: Antenna Factors. This algorithm determines the antenna gain factors and beam width for each frame of science data using lookup tables.

5.6.2.6 S-05: Scattering Coefficient. This algorithm determines the value of the normalized radar cross-section (NRCS) scattering coefficient $\sigma°$ for the 15 Doppler channels. These $\sigma°$s come directly from the radar equation (5-3) and, at this stage, have had no corrections (e.g., antenna pattern) applied.

5.6.2.7 S-06: Attitude Uncertainty Errors. This algorithm determines the uncertainty in the $\sigma°$ measurements, incidence angles θ_I, and cell locations due to uncertainties in the spacecraft attitude pointing angles and mechanical/thermal alignment errors. It also determines the direction of the line along which the cell location errors lie.

5.6.2.8 S-07: Measurement Error. This algorithm determines the measurement error K_p on $\sigma°$ due to communication noise, and the total normalized standard deviation on the measurement of $\sigma°$ combining all sources of error.

5.6.2.9 S-08: Cell Geometry and Area. This algorithm determines the approximate instantaneous field-of-view (IFOV) and total integrated area of the resolution footprint cell for each of the 15 Doppler channels. It also determines the dimensions of the rectangle that overlays, and is equivalent in area to, the total integrated cell. Finally, it determines the corner locations of the larger region defined by the lines of longitude and latitude that describe the minimum rectangle containing the measurement area.

5.6.2.10 S-09: Scattering Coefficient Correction. This algorithm corrects the $\sigma°$s calculated from the radar equation (5-3) for antenna pattern and filter response approximations (see Subsection 5.3). These corrections are obtained from a table and are added to the scattering coefficient values determined by algorithm S-05.

5.6.2.11 S-11: Bias Removal. This algorithm adjusts the scattering coefficient measurements for relative interbeam biases by removing the bias errors determined from bias calibration data (see Subsection 5.4.2). These corrections are obtained from a table and are added to the antenna-pattern-corrected $\sigma°$ values determined by algorithm S-09. These bias-corrected $\sigma°$s are the final instrument-corrected backscatter coefficient measurement values coming out of the first-stage of SASS sensor file processing. At this stage, they have not been corrected for atmospheric attenuation effects.

5.6.2.12 S-12: Noise Figure. This algorithm determines the scatterometer receiver noise figure from calibration data using the y-factor technique.

SECTION 6

SASS σ° ATTENUATION AND FOOTPRINT LAND/OCEAN RESOLUTION PROCESSING

6.1 INTRODUCTION

The SASS σ° sensor data computed as described in Section 5 is without atmospheric attenuation corrections, and the land/ocean resolution flags corresponding to each σ° measurement location pertain only to the center of the associated footprint Doppler cell (see Subsection 4.4.2.2). As shown in Figure 4-4, the σ° measurement values are corrected for attenuation to the extent possible, and the cell-center land/water flags derived by the IDPS are upgraded to include land/water determinations at other points throughout each cell's extended area by a set of algorithms that serve as the second, and final, stage of ADF SASS sensor file processing (see Subsection 4.6.2). The output of this intermediate processing stage is an "attenuated" land/ocean resolved σ° GDR sensor file that is input directly into the wind-retrieval geophysical algorithms. This section describes the refined "TOILing"* that is performed to yield an accurate (ocean, land, or mixed) measurement-type indicator for each σ° footprint cell and the method used to compute attenuation corrections for the σ° data.

6.1.1 SMMR Brightness Temperature (T_B) Data

The SASS attenuation algorithms use SMMR-derived brightness temperature (T_B) data as the basis for computing corrections for the loss suffered by the scatterometer signal due to heavy clouds and precipitation during its round-trip passage through the atmosphere. The SMMR instrument was designed for the purpose of determining a variety of parameters such as sea-surface temperature, wind speed, and atmospheric water vapor and liquid water on a global, nearly all-weather basis [15,20,21]. The instrument measures thermal microwave emission from the Earth at five dual linearly polarized frequencies (6.6, 10.7, 18, 21,

---

*TOIL (Time-Tagged Ocean Ice Land): this acronym is a legacy of the mission data processing requirements planning phase and only "Ocean" and "Land" remain as correct descriptions of the data base used to resolve the Earth's surface. Whatever (surface) "Ice" that was included is incorporated into the static data base as "Land."

and 37 GHz) from which the geophysical parameters may be derived. Before the geophysical quantities can be retrieved from the data, the radiometric antenna temperature measurements must be corrected for a number of antenna pattern effects in order to obtain actual brightness temperature distributions of the observed fields of view (see Figure 3-2 and Table 3-2). For purposes of recovering these geophysical parameters to within desired Seasat mission goals, the rms accuracy requirements on the determined brightness temperatures were less than 1 K, depending on the particular frequency [15]. To achieve these system goals, it was therefore necessary to pay careful attention to the instrument calibration and antenna pattern corrections (APCs).

The SMMR antenna received radiation from all directions as weighted by the antenna patterns, so that radiation received through the sidelobes and cross-polarization lobes needed to be accounted for in order to derive the actual brightness temperatures viewed in the direction of the antenna boresight. The essential problem dealt with by the SMMR APC algorithms was therefore to make the correction for radiation received through the secondary antenna lobes so that the corrected value represented the average T_B over only the main-beam footprint region. Correction for the antenna pattern effects begins with the integral formulation of the antenna temperature equation involving the vector properties of the emitted field and the antenna patterns. The inversion of this integral equation for radiometric data has been done with varying success using such techniques as successive approximation, Fourier transforms, and matrix methods. Matrix and transform methods are useful for processing large volumes of data and lend themselves to smoothing techniques for reducing instabilities in the inversion procedure. In general, a procedure for accurately reconstructing T_B distributions requires a complete set of antenna temperature measurements and large amounts of computation. In any practical situation, such as with the SMMR where large volumes of data needed correcting, a trade-off must be made between the recovered-T_B accuracy requirements and the need for cost- and time-efficient processing of the data set.

6.1.2 Interim Antenna Pattern Correction for SMMR Brightness Temperature Data

The SMMR "full" APC algorithm performs the following four major functions: (1) reformats the antenna scan-oriented data onto regularly spaced

Earth-located grid cells, (2) corrects for cross-polarization coupling, (3) corrects for radiation entering the sidelobes, and (4) arranges the output data into a format suitable for geophysical processing. Functions (2) and (3) are performed as a unit in the algorithm since the cross-polarization and sidelobe characteristics of the antenna patterns are, in principle, inseparable. However, as shown in [15] for reasonably homogeneous areas (such as over open ocean well away from major land areas), the error introduced by neglecting sidelobe effects is not significant and approximate retrievals can be obtained by considering only cross-polarization effects. This approach was taken to develop an earlier "interim" version of the SMMR APC which omitted function (3), above, correcting only for the sidelobes viewing cold space beyond the Earth horizon. In this case the cross-polarization correction or decoupling can be done by simple 2x2 matrix operations on the pairs of horizontal and vertical antenna temperatures for each cell (with the matrix elements computed off-line based on the nominal antenna scan characteristics and the antenna patterns).

The interim-APC T_B's were found (during a mini-workshop conducted by the SASS Evaluation Task Group) to yield SASS $\sigma°$ attenuation corrections that were not substantially degraded over those derived from full-APC T_B's for SMMR data that is located no closer than about two SASS footprint resolution cells away from major land areas. In addition, it developed that an unacceptable delay in the production of the final SASS GDR geophysical data set would have resulted had the SASS attenuation processing (which had to be done before the geophysical processing could begin) awaited the generation of final SMMR full-APC T_B's rather than interim-APC T_B's. (Seasat Project GDR production time schedules for the various sensors required the completion of SASS GDRs considerably before the earliest projected date of completion of SMMR GDR full-APC T_B data.) A management decision was therefore made to do all scatterometer $\sigma°$ attenuation processing with interim-APC brightness temperature data. A set of interim-APC T_B data was thus generated covering the complete SMMR mission time span for the sole purpose of providing input to the SASS sensor data attenuation algorithms described below. Each SASS sensor GDR containing $\sigma°$ data to be "attenuated" by these algorithms was therefore accompanied by a SMMR interim-APC T_B GDR file covering a time interval which, whenever possible, spanned the scatterometer data -- see Figure 4-4.

6.1.3 T_B or Not T_B?

A note of terminology clarification is appropriate. In keeping with Seasat -- and much other -- literature, the term "brightness temperature" or "T_B" used in this subsection (6.1) refers to the SMMR-derived experimental apparent temperature data that results after antenna temperature measurements have undergone APC manipulations. This APC-corrected antenna apparent temperature, which is measured by the radiometer for a given atmospheric condition, is the (measured) brightness temperature of the solid-angle volume seen through the antenna main lobe and thus includes the brightness temperature of the sea surface as well as an atmospheric component. However, in Subsection 6.3, "brightness temperature" and "T_B" will refer only to the brightness temperature of the sea, while the apparent temperature -- whether theoretically modeled as a function of atmospheric and surface conditions or derived from SMMR measurements -- will be denoted T_a. As so defined, T_a and T_B are equivalent only in the case of a lossless atmosphere. It is precisely for the SASS attenuation algorithm that the distinction becomes important: the $\sigma°$ correction for attenuation will be modeled as a function of the difference between the two temperatures.

6.2 SASS $\sigma°$ FOOTPRINT CELL LAND/OCEAN FLAGGING

The downstream SASS geophysical processing must reject from the wind solution retrieval process any $\sigma°$ measurement whose footprint resolution cell region is intersected by any portion of a land mass. Because a SASS resolution cell has an extended area, it would be inadequate to make a use/reject decision based only on the IDPS-provided land/ocean flags since they apply only to the location of the cell center point. These flags are thus upgraded to include land/ocean determinations at each of four additional points per cell located approximately at the extremities of the footprint areas. An understanding of the location of these four points requires the delineation of the relative placement of three juxtaposed footprint cell-related regions.

6.2.1 Doppler Measurement Cell Flagging

Figure 6-1 depicts a typical six-sided integrated Doppler footprint cell (see also Figure 3-4) along with the derived equivalent-area rectangle and the latitude- and longitude-defined rectangular measurement area. The along-beam

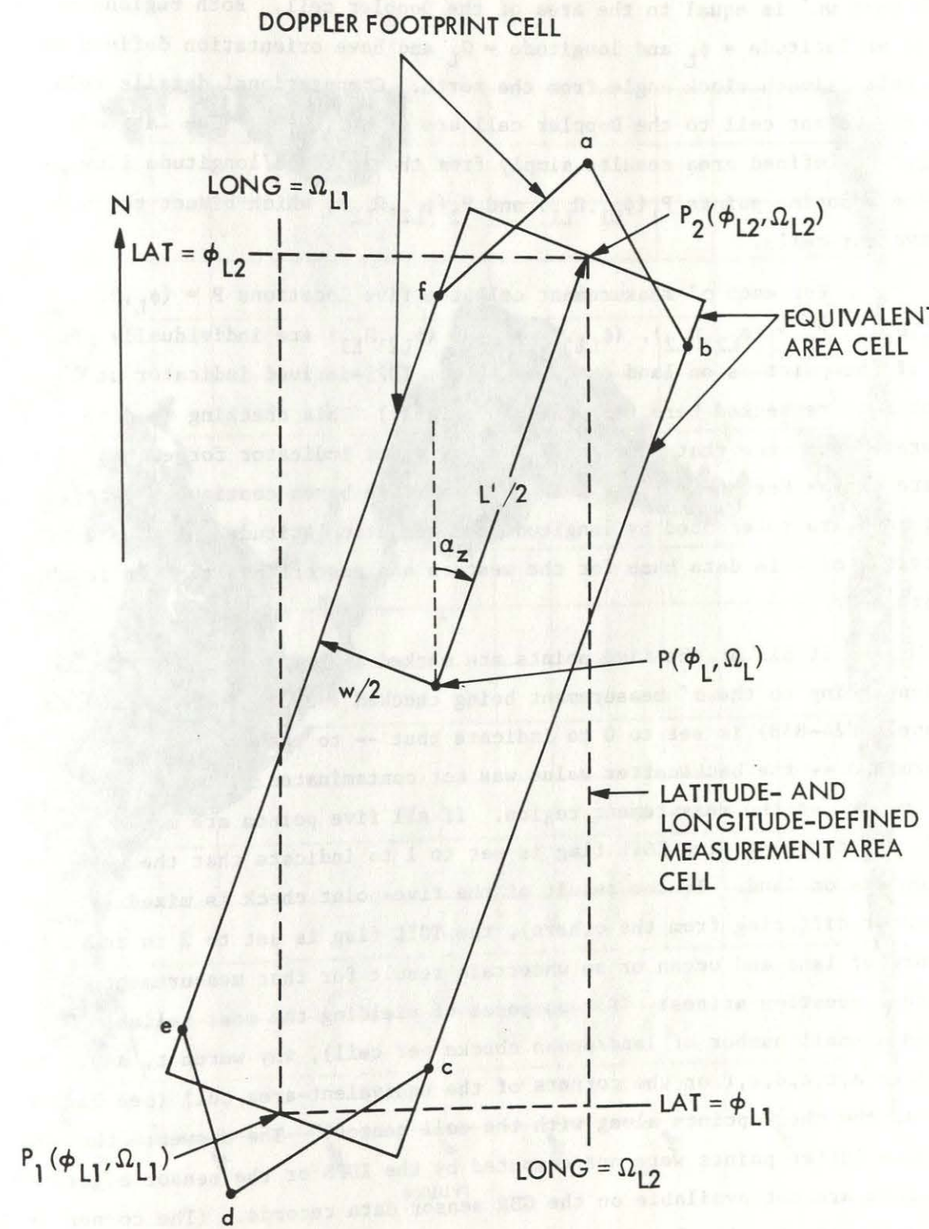

Figure 6-1. Doppler Footprint, Equivalent-Area, and Latitude- and Longitude-Defined Measurement Cells

edges of the equivalent-cell rectangle coincide with the edges of the Doppler cell (with vertices a-b-c-d-e-f) of width w; the length L' of the rectangle is such that wL' is equal to the area of the Doppler cell. Both regions are centered at latitude = ϕ_L and longitude = Ω_L and have orientation defined by α_z, the cell azimuth clock angle from the north. Computational details relating the equivalent cell to the Doppler cell are given in [3]. The latitude- and longitude-defined area results simply from the latitude/longitude lines generated by the opposing points $P_1(\phi_{L1},\Omega_{L1})$ and $P_2(\phi_{L2},\Omega_{L2})$, which bisect the ends of the equivalent cells.

For each $\sigma°$ measurement cell the five locations $P = (\phi_L,\Omega_L)$, $P_1 = (\phi_{L1},\Omega_{L1})$, $P_2 = (\phi_{L2},\Omega_{L2})$, (ϕ_{L1},Ω_{L2}), and (ϕ_{L2},Ω_{L1}) are individually checked to see if the point is on land or water. (The IDPS-derived indicator at the center point P is rechecked here for possible errors.) This checking is done using an accurate data base that contains a land or water indicator for each 1/12 x 1/12-deg square on the Earth's surface. These 5' surface boxes contiguously cover the Earth and are referenced by longitude and geodetic latitude. A graphical representation of this data base for the western and eastern hemispheres is shown in Figure 6-2.

If all of the five points are marked as being ocean, the TOIL flag corresponding to the $\sigma°$ measurement being checked (see Table 8-3, parameter channels 824-838) is set to 0 to indicate that -- to the extent that it could be determined -- the backscatter value was not contaminated by the presence of land in any part of the measurement region. If all five points are marked as being land, the corresponding TOIL flag is set to 1 to indicate that the measurement region was on land. If the result of the five-point check is mixed (at least one indicator differing from the others), the TOIL flag is set to 2 to indicate a mixture of land and ocean or an uncertain result for that measurement cell. An apparent question arises: "For purposes of yielding the most reliable TOIL flag (given a small number of land/ocean checks per cell), why weren't, say, the vertices a,b,c,d,e,f or the corners of the equivalent-area cell (see Figure 6-1) used as the check points along with the cell center?" The answer: the locations of these latter points were not computed by the IDPS or the sensor algorithms and therefore are not available on the GDR sensor data records. (The corner latitudes and longitudes $\phi_{L1},\phi_{L2},\Omega_{L1},\Omega_{L2}$ are contained in channels 120-179 of the SASS Basic Sensor Record -- see Table 8-3.)

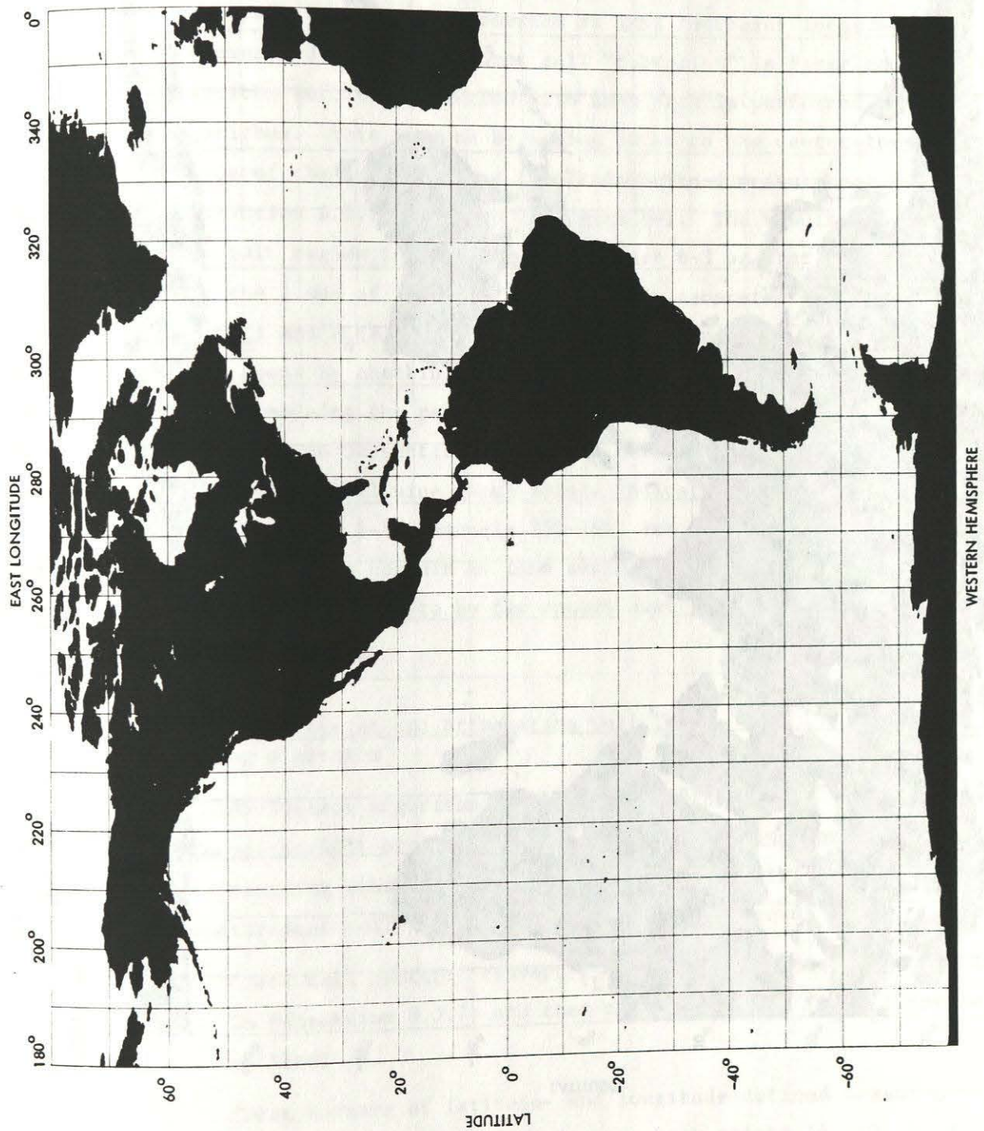

Figure 6-2. CIA World Data Base I Land-Sea TOIL Map From a Discretization by the University of Texas

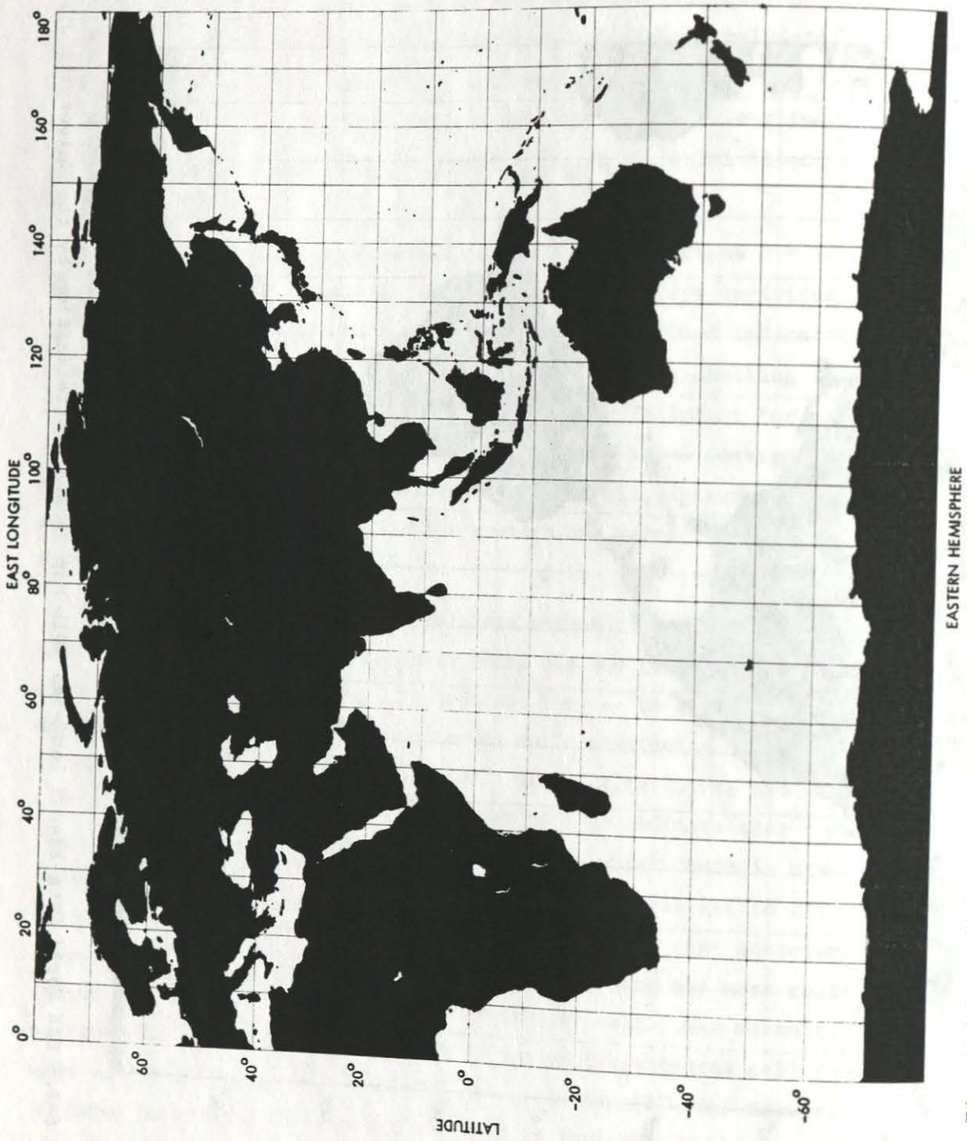

Figure 6-2. CIA World Data Base I Land-Sea TOIL Map From a Discretization by the University of Texas (contd)

6.2.2 Extended Measurement Region Flagging for Attenuation

Attenuation corrections are computed for all $\sigma°$ measurements that (1) overlap the SMMR data swath, and (2) are located far enough away from land. Since ocean T_B computations degrade somewhat as SMMR footprint locations approach a land mass, an expanded SASS measurement cell "footprint" is first computed by the TOILing algorithm before co-location with SMMR data is performed by the attenuation algorithms. This is done by adding 50 km to the center-to-edge distance of each side of the latitude- and longitude-defined measurement region described in Subsection 6.2.1 and shown in Figure 6-1. The resulting expanded SASS attenuation TOIL region is thus shown in Figure 6-3 as that rectangular area enclosed by the lines of latitude and longitude generated by the opposing vertices $P_3(\phi_{L3},\Omega_{L3})$ and $P_4(\phi_{L4},\Omega_{L4})$. This larger attenuation cell is then examined for land/ocean by checking the outer four locations P_3, P_4, (ϕ_{L3},Ω_{L4}), and (ϕ_{L4},Ω_{L3}) and combining the results with that obtained from the inner five check points described in Subsection 6.2.1. As before, this extended SASS cell is marked as all ocean if all nine check points indicate ocean, etc., and the extended TOIL flags (Table 8-3, channels 750-764) are set accordingly. If this expanded region is found to contain no land surface by this test, the corresponding $\sigma°$ footprint cell is deemed to be far enough away from land to be "attenuated" with co-located T_B data.

6.2.3 The SASS Footprint and Attenuation Cell TOIL-Flagging Algorithm

The SASS TOILing algorithm (SS.IG.G-07.00/0/B), which is a component of the SASS attenuation/TOIL processor, performs the following computational steps (refer to preceding subsections for notation and definitions) for each scatterometer measurement cell found in the Basic Sensor Record:

(1) Check cell center: convert ϕ_L to geodetic system (see Eq. (8-1) in Subsection 8.3.7) and then check point $P = (\phi_L,\Omega_L)$ for ocean or land.

(2) Check corners of latitude- and longitude-defined measurement cell: convert ϕ_{Li} to geodetic and then check points (ϕ_{Li},Ω_{Lj}), i=1,2, j=1,2.

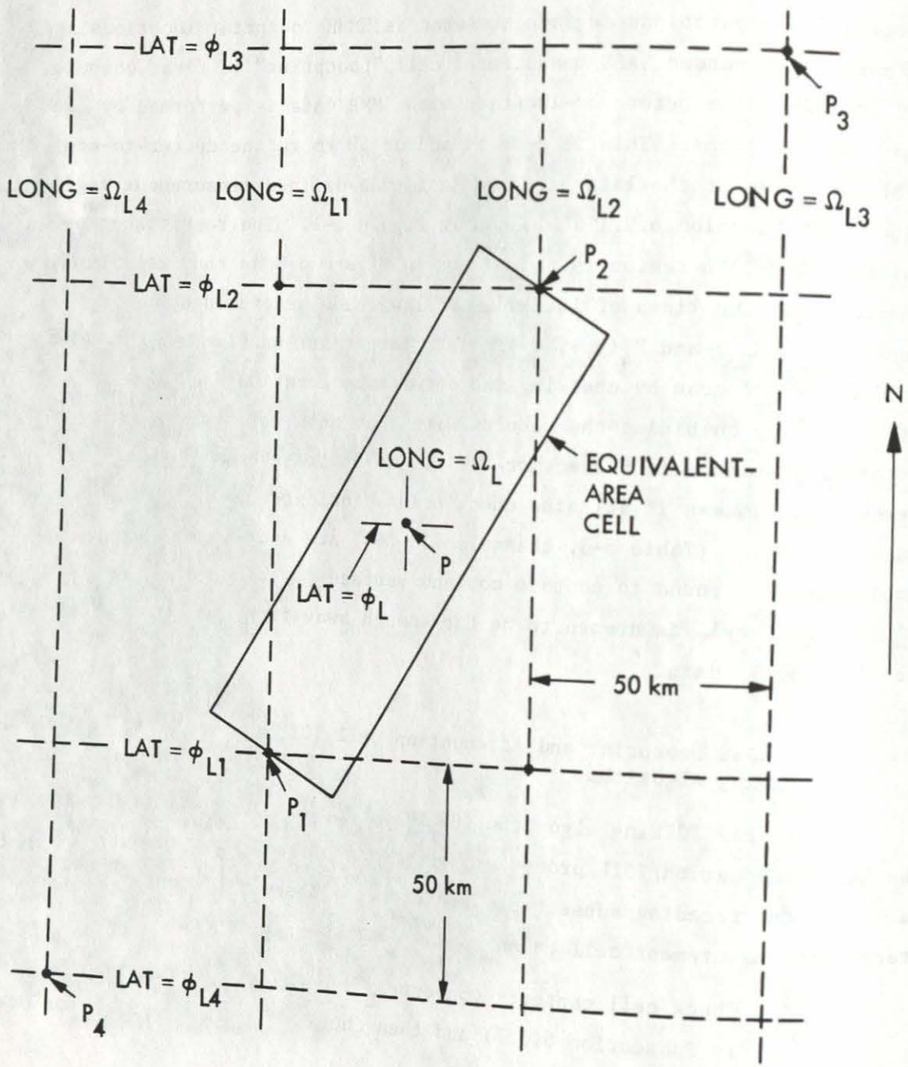

Figure 6-3. SASS TOIL Flagging Geometry (see Figure 6-1)

(3) Set basic TOIL flag (channels 824-838): if results from steps (1) and (2) are all land, or all water, set TOIL flag accordingly (0 = ocean, 1 = land). If results are mixed, set flag = 2 (mixed).

(4) Set extended-cell TOIL flag (XF -- channels 750-764):

(a) Set XF = basic flag. If XF is land or mixed, then quit; otherwise,

(b) Calculate corners of extended cell:

Set $\phi_{L3} = \phi_{L2} + .4545$ deg (50 km)

Set $\phi_{L4} = \phi_{L1} - .4545$ deg

(If $\phi_{L2} < \phi_{L1}$, do the opposite.)

Set $\Omega_{L3} = \Omega_{L2} + .4545/\cos(\phi_L)$

Set $\Omega_{L4} = \Omega_{L1} - .4545/\cos(\phi_L)$

(If Ω_{L1} is east of Ω_{L2}, do the opposite.)

Normalize Ω_{L3} and Ω_{L4} to [0,360) deg.

(c) Check corners: convert ϕ_{Li} to geodetic and then check points (ϕ_{Li},Ω_{Lj}), i=3,4, j=3,4.

If any point is land, set XF=2 (mixed); otherwise stop, leaving XF = basic flag.

Note: If location data is unavailable (see Subsection 5.6.1.3), the flags are all set to 2 (mixed/unknown) for the 15 cells contained in that data frame.

6.3 SASS σ° CORRECTIONS FOR ATTENUATION

In the presence of heavy moisture-laden clouds and precipitation, the scatterometer signal is subject to atmospheric attenuation during the round-trip between antenna and ocean surface. Under this influence an incorrect ocean-surface σ° value will be computed by the sensor algorithms, which will in turn induce an error in derived wind speed. Wherever possible, corrections for this attenuation have been calculated by using the microwave antenna apparent temperature measurements (see Subsection 6.1.3) derived from the SMMR instrument at

18.6 and 37 GHz. These antenna temperatures have been shown to be capable of detecting cloud-top temperatures, and therefore can provide attenuation magnitude and location estimates in a heavy cloud and precipitation environment.

Since the SMMR scanned only the right side of the spacecraft, corrections to σ° data have only been made for the SASS/SMMR overlap portion of the right-side SASS swath (beams 1 and 2). Left-side swath SASS data (beams 3 and 4) have no attenuation corrections applied and may therefore yield wind solutions that significantly underestimate medium to high wind speeds in the presence of higher rain rates. This problem is examined further in Subsection 9.5, where a table of percent wind speed error estimates for various rain rates and incidence angles is provided.

A major problem in correctly estimating the SASS attenuation occurs because (1) the SASS and SMMR footprints on the surface are of different sizes and shapes, and (2) they do not coincide because of different instrument scan patterns. Attenuation estimates are thus based on SMMR observations covering areas much larger than the SASS footprint. Since these areas -- and the SASS footprint itself -- are much larger than most rain cells, errors are inherent in any procedure using SMMR data to correct the SASS signal for attenuation. Such errors would be greatly reduced if the scatterometer and radiometer had coincident footprints and comparable footprint areas. However, even without ideal conditions the SMMR temperature measurements do provide acceptable corrections under low to medium rain rate conditions.

A description of the algorithms used to correct for atmospheric attenuation and their theoretical basis follow. The algorithms were developed by G. Dome and I.J. Birrer of the University of Kansas Remote Sensing Laboratory.

6.3.1 Basis for Use of Radiometer to Estimate Attenuation [22]

A microwave radiometer can be used to determine attenuation between a satellite and the ground because the sensitivity of a radiometer to the change in thermal emission caused by cloud and rain attenuation is much stronger than to the change in emission from the surface caused by change in wind speed. An attenuation that has a relatively small effect on a 14.6-GHz scatterometer measurement of the surface wind causes a rather large increase in the brightness temperature observed at 18 GHz and an even larger increase in that observed at 37 GHz.

The antenna temperature that a radiometer would measure observing the sea without attenuation is equivalent to the sea's brightness temperature T_B (see Subsection 6.1.3), and can be calculated for vertical polarization at the SMMR's constant 49-deg angle of incidence if the sea-surface physical temperature is known. An increase in the observed value above the base-value T_B is an excess temperature caused by attenuation in the atmosphere. The amount of this difference between the total apparent temperature and the brightness temperature of the sea, called the excess brightness temperature, has been determined for various model cloud and rain conditions, as has the attenuation. An empirical relation has been established between the excess temperature at 37 and 18 GHz, and the attenuation at the 14.6-GHz SASS frequency.

The algorithm uses the vertical-polarization 37-GHz SMMR channel to calculate small attenuations and the vertical 18-GHz channel to calculate moderate-to-larger attenuations. The method is based essentially on a model that expresses the antenna apparent temperature in terms of the total atmospheric attenuation and the (known) sea-surface temperature: given SMMR-derived measurements of the apparent temperature, the model can be inverted to yield attenuation. This method has been shown to be reasonably successful, although performance evaluations have been limited due to the difficulty in determining actual attenuations that occurred to compare against.

Radiative transfer theory is briefly outlined here as it applies to the problem. This theory does not take into account atmospheric scattering by particles -- which can yield significant error for larger attenuations at frequencies such that cloud and rain drop diameters become a significant fraction of a wavelength.

6.3.1.1 <u>Modeling of the Antenna Apparent Temperature</u>. The basic radiative transfer equation is [23]

$$\cos\theta \frac{dT_{aj}(z,\theta)}{dz} + \alpha_T(z)T_{aj}(z,\theta) = \alpha_T(z)T_{air}(z) \qquad (6\text{-}1)$$

where

$T_{aj}(z,\theta)$ = apparent temperature for polarization j (V or H) at altitude z and incidence angle θ from the surface normal

$\alpha_T(z)$ = total absorption of the atmosphere at altitude z

$T_{air}(z)$ = air temperature at altitude z

The apparent temperature may be expressed as

$$T_{aj}(z,\theta) = L(z,\theta)T_{aj}(0,\theta) + T_{atm}(z,\theta) \tag{6-2}$$

where the atmospheric transmittance $L(z,\theta)$ is given in terms of the attenuation $\alpha_T(z)$ by

$$L(z,\theta) = \exp\left[-\sec\theta \int_0^z \alpha_T(u)\, du\right] \tag{6-3}$$

and the atmospheric temperature is

$$T_{atm}(z,\theta) = \sec\theta \int_0^z T_{air}(z')\alpha_T(z')\exp\left[-\sec\theta \int_{z'}^z \alpha_T(u)du\right]dz' \tag{6-4}$$

The apparent temperature that would be measured at the surface, $T_{aj}(0,\theta)$, consists of the (sea) surface emission brightness temperature, T_B, and an atmospheric component which is reflected from the target surface, T_r. This surface apparent temperature is then given by

$$T_{aj}(0,\theta) = T_{Bj}(\theta) + T_{rj}(\theta) \tag{6-5}$$

where

$$T_{Bj}(\theta) = \varepsilon_j(\theta)T_S \tag{6-6}$$

$\varepsilon_j(\theta)$ = sea-surface emissivity in the incidence angle direction θ for polarization j

T_S = $T_S(\theta)$ = sea-surface temperature at the location corresponding to the direction θ

$T_{rj}(\theta)$ = reflected sky temperature for polarization j

$$= R_j(\theta)\int_z^0 \alpha_T(z')T_{air}(z')\exp\left[-\sec\theta \int_{z'}^0 \alpha_T(u)du\right]dz' \tag{6-7}$$

where $R_j(\theta) = (1 - \varepsilon_j(\theta))$ is the reflection coefficient for polarization j.

Consequently, the apparent temperature that would be measured by a downward-looking radiometer is given by the relation:

$$T_{aj}(z,\theta) = L(z,\theta)\left[\varepsilon_j(\theta)T_S + T_{rj}(\theta)\right] + T_{atm}(z,\theta) \tag{6-8}$$

The manner in which the individual contributors to the measurement scene combine to yield the apparent temperature is illustrated in Figure 6-4.

The total attenuation in the atmosphere is given by

$$\alpha_T = \alpha_{O_2} + \alpha_{H_2O} + \alpha_{CLOUD} + \alpha_{RAIN} \tag{6-9}$$

The contribution from the first two terms in Equation (6-9), resulting from resonant absorption associated with the O_2 and H_2O molecular components of the atmosphere, is relatively small at the frequencies of the SMMR radiometer (except 21 GHz, which is not used in correcting the SASS). Because these contributions are small and their variations are even smaller, these clear-sky components of the total attenuation may be considered constant in the SASS correction, particularly since their changes are small compared to both the contributions of the other two terms and to the required precision of the SASS measurement. Hence, the correction problem centers on the α_{CLOUD} and α_{RAIN} terms, with particular attention paid to the latter because the effects of clouds are usually too small to significantly affect the performance of the SASS.

Since the absorption is a function of the height above the Earth's surface, L is the integrated value over the height of the atmosphere:

$$L = \exp\left[\frac{R}{h}\int \alpha_T(z)dz\right] \tag{6-10}$$

where R/h is the ratio of range to height that accounts for the path length through the atmosphere at a nadir angle θ from the surface normal: for a flat-Earth assumption, $R/h = \sec\theta$. For the Seasat altitude this remains approximately valid if θ is replaced with θ_i, the SASS incidence angle. The atmospheric absorption is essentially negligible above 30 km and that due to the cloud and rain terms is negligible above 20 km; in fact, for most purposes, it is negligible

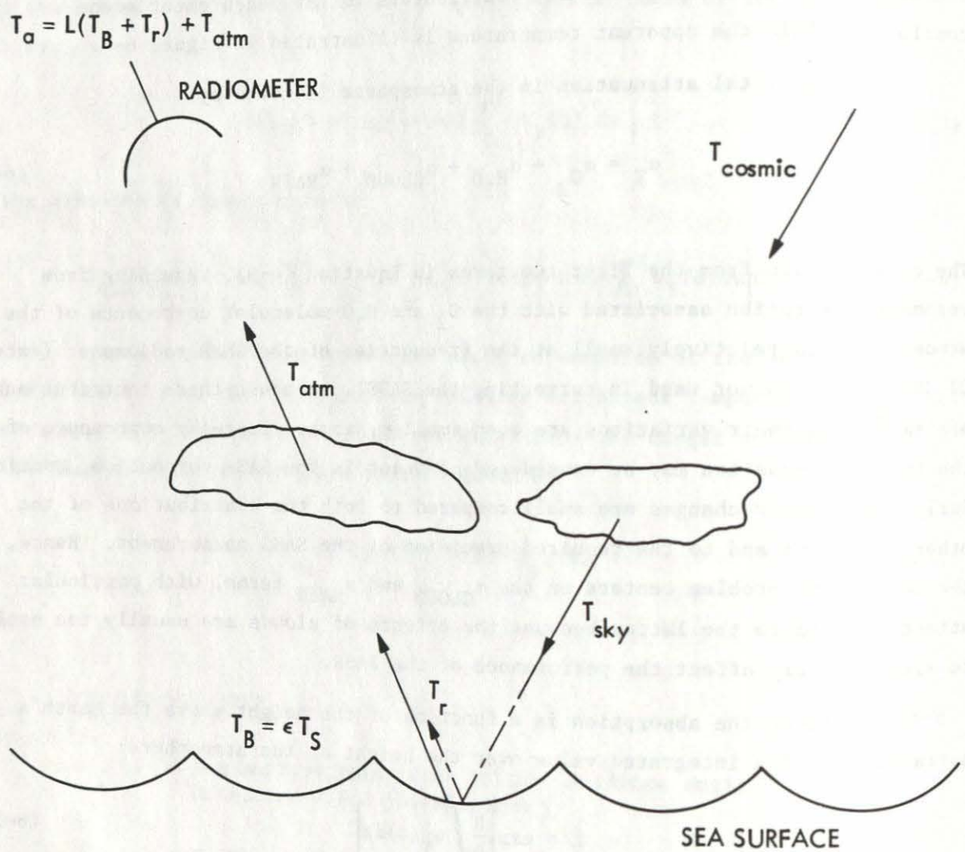

Figure 6-4. Atmospheric Effects on Radiometric Measurements

above 10 km. In the development used here, however, the calculations are carried out to a height of 20 km.

As described in [22], an empirical model developed for cloud absorption by Benoit is

$$\alpha_{CLOUD}(z) = Mf^b \exp(a) \tag{6-11}$$

where

$\alpha_{CLOUD}(z)$ = cloud absorption at height z above the surface, dB/km

M = liquid water content of the cloud, g/m^3

f = propagating frequency, GHz

b = frequency index (for water clouds, b = 1.95; for ice clouds, b = 1.006)

a = temperature coefficient

$= -6.866[1 + .0045(T_{air}(z) - 273)]$ for water clouds

$= -8.261[1 - .01767(T_{air}(z) - 273) - .0004374(T_{air}(z) - 273)^2]$ for ice clouds

$T_{air}(z)$ = air temperature at height z

The form (6-11) and the above coefficient values are used in the atmospheric attenuation algorithm for SASS data.

As indicated in [22], Gunn and East presented a model for rain absorption which is still in use, although numerous papers have been written describing variations in the model coefficients. Their model is represented as

$$\alpha_{RAIN}(z) = KR^p(z) \tag{6-12}$$

where $\alpha_{RAIN}(z)$ (dB/km) is the rain absorption at height z, R(z) (mm/h) is the rainfall rate at height z, and K and p are empirical constants. Medhurst and Ippolito derived values for these constants based on both theory and experiment (see [22]). DeBettencourt (also see [22]) continued this work and developed other values that differed somewhat from those of Medhusrt: values of their

constants as a function of frequency are shown in Figure 6-5. The form (6-12) and the constants from DeBettencourt are used in the development of the rain-absorption component of the atmospheric attenuation algorithm.

The effect that scattering from precipitation droplets has on apparent temperature was studied theoretically by Wu and Fung [24]. It is clear from their work that such scattering lowers the apparent temperature. The effect of a lower apparent temperature, obtained when a model that ignores scattering is used, is an underestimation of the attenuation. However, due to the complexity of the calculations involving scattering, the models used in developing the SASS correction algorithms ignore such scattering. For lesser rain rates, and for rains where the drop sizes are small, the effect of scattering is small and can probably be safely ignored. For higher rain rates the attenuation is large enough to cause the algorithm's computed correction to be invalid whether or not scattering is ignored. (For such high attenuation conditions, the correction algorithm flags its computed results as unreliable and not to be used and, in fact, does not even produce attenuation values in such cases. As discussed later, an attenuation upper-threshold value establishes a maximum level above which no attenuation correction is generated by the algorithm. This cut-off value corresponds to rain rates in the 12- to 15-mm/h range. SASS $\sigma°$ measurements corresponding to these derived out-of-range attenuations are not used for generating wind solutions.) Furthermore, backscatter from the rain to the SASS creates another (unsolved) problem for rain rates above 10 to 12 mm/h, which further renders the inclusion of scattering effects in apparent temperature computations unnecessary. Nevertheless, ignoring scattering effects is bound to cause some underestimating of the attenuation.

The cloud and rain attenuation rate formulations embodied in Equations (6-11) and (6-12) require a knowledge of the variation in rain rate and cloud moisture content as a function of height. Furthermore, the air temperature dependence of the attenuation coefficients requires knowledge of the temperature distribution in the atmosphere. In the study that led to the SASS attenuation algorithm, a series of cloud and rain models was used and a computer program was developed that performed the calculations indicated above. For this effort a standard temperature lapse rate of 7.5 K/km was used. Clearly, a temperature gradient different from this simplistic constant model would probably be found in

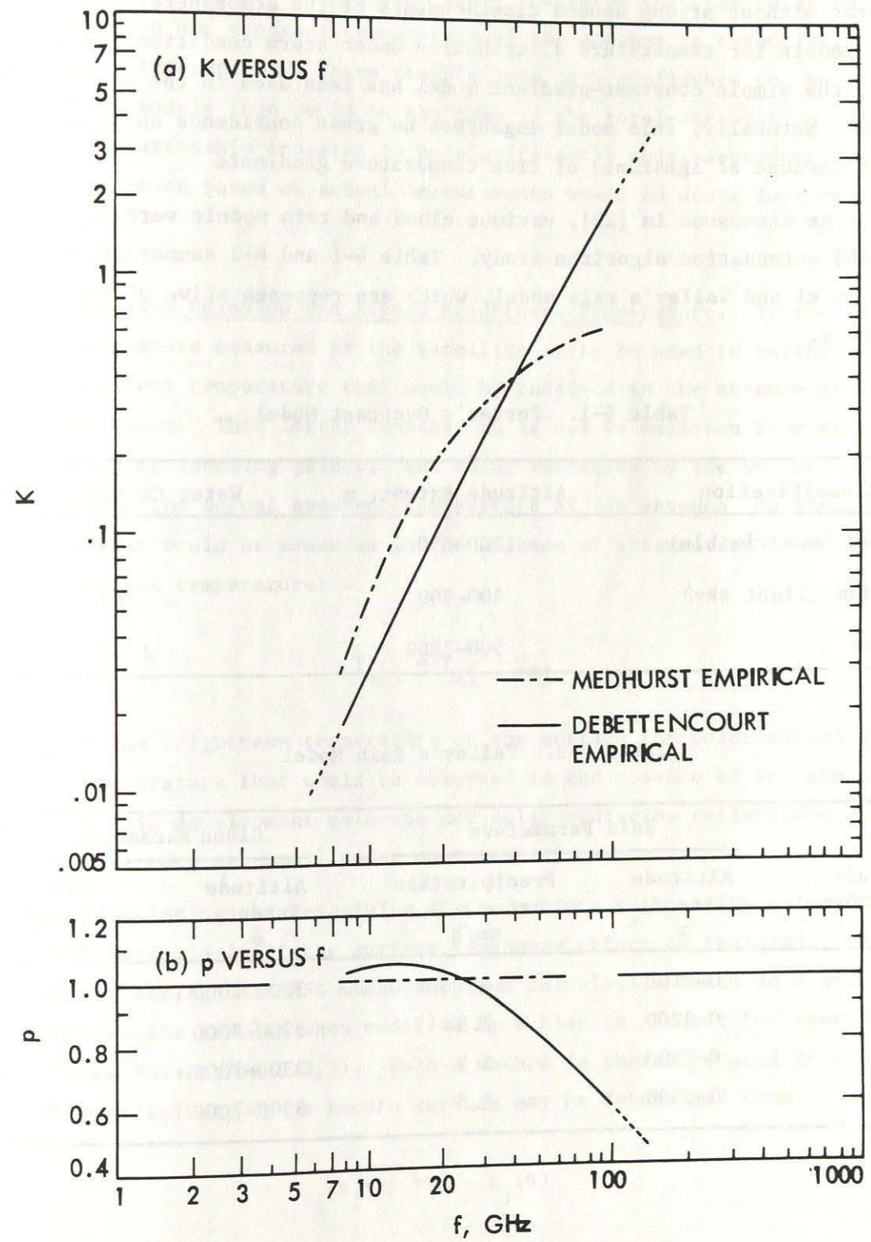

Figure 6-5. Empirical Rainfall Attenuation: $\alpha = KR^p$

a rain storm, and, in fact, it would most likely be dependent upon the storm type. Storms having extreme updrafts would tend to have a more variable gradient than storms without strong upward displacements of the atmosphere, etc. Since suitable models for temperature distribution under storm conditions do not appear to exist, the simple constant-gradient model has been used in the attenuation algorithm. Naturally, this model engenders no great confidence as it was chosen primarily because of ignorance of true temperature gradients.

As discussed in [22], various cloud and rain models were considered in the SASS attenuation algorithm study. Table 6-1 and 6-2 summarize Porter's overcast model and Valley's rain model, which are representative of those used in the study.

Table 6-1. Porter's Overcast Model

Classification	Altitude Extent, m	Water Content, g/m^3
Light (sun visible)	300-650	.33
Medium (light sky)	400-900	.67
Heavy	500-3200	1.00

Table 6-2. Valley's Rain Model

	Rain Parameters		Cloud Parameters	
Updraft Condition, m/s	Altitude Extent, m	Precipitation at z = 0, mm/h	Altitude Extent, m	Water Content, g/m^3
.4	0-3100	10.3	3100-7000	.30
.3	0-3200	7.9	3200-7000	.25
.2	0-3300	5.2	3300-7000	.15
.1	0-3500	2.8	3500-7000	.10

These cloud and rain models are necessarily somewhat simplistic. However, the results of the simulation study indicated that the relation between total attenuation and apparent temperature at the antenna is essentially cloud- and rain-model independent. These results lend more confidence to the use of the simplified models than would be the case if the total-attenuation/apparent-temperature relationship appeared to be significantly model-dependent. Nevertheless, validation based on actual measurements would no doubt improve confidence in the results.

6.3.1.2 Surface Emission and Excess Brightness Temperature. If the antenna apparent temperature measured at the satellite is to be used to estimate attenuation, the apparent temperature that would be received in the absence of attenuation must be known. This latter temperature is due to emission from the surface and scattering of incoming galactic and solar radiation by the surface. The difference between the actual apparent temperature of the antenna and the apparent temperature that would be measured in the absence of attenuation is called the excess brightness temperature:

$$T_{exj} = T_{aj} - T_{Bj} \tag{6-13}$$

where T_{Bj} is the brightness temperature of the surface for polarization index j and is the temperature that would be observed in the absence of any atmospheric effects. In this development galactic and solar radiation reflections will be ignored because they are small under most conditions.

Calculating the emissivity of the surface $\varepsilon_j(\theta)$ of Equation (6-6) can be complex, particularly if the surface roughness effect is included. For the purpose of correcting the SASS measurement, a calculation based on a smooth surface gives adequate results when modified by a bias to account for average surface roughness (see Subsection 6.3.3). Such a method is therefore used in the algorithms. The emissivity for a smooth surface may be determined from

$$\varepsilon_j(\theta) = 1 - R_j(\theta) \tag{6-14}$$

where the subscript j refers to the polarization and $R_j(\theta)$ is the Fresnel reflection coefficient.

Sea-surface brightness temperatures are less sensitive to surface roughness for vertical polarization than for horizontal polarization; this is particularly true at incidence angle $\theta = 49$ deg, where the roughness dependence of the vertically polarized signal is a minimum. This is why the 49-deg angle of incidence was chosen for the SMMR. Because of the relative sensitivities, only vertically polarized brightness temperatures are used in the SASS attenuation determination.

The vertical-polarization Fresnel reflection coefficient is given by the well-known relation:

$$R_v(\theta) = \frac{\varepsilon_r \mu_r \cos\theta - \sqrt{\varepsilon_r \mu_r - \sin^2\theta}}{\varepsilon_r \mu_r \cos\theta + \sqrt{\varepsilon_r \mu_r - \sin^2\theta}} \tag{6-15}$$

where ε_r is the complex-valued relative permittivity of sea water given by

$$\varepsilon_r = \varepsilon' - i\varepsilon'' \tag{6-16}$$

where ε' and ε'' are the real and imaginary parts, and μ_r is the relative permeability (essentially unity).

To calculate the reflection coefficient for sea water, one needs to have an appropriate expression for ε_r. A common expression is that due to Debye (see [22]):

$$\varepsilon_r(T_S,S) = \varepsilon_\infty + \frac{\varepsilon_s - \varepsilon_\infty}{1 + \left[i\omega\tau(T_S,S)\right]^{1-\delta}} - i\,\frac{\sigma}{\omega\varepsilon_0} \tag{6-17}$$

where ω = radar angular frequency; ε_∞ = relative permittivity at infinite frequency; ε_s = relative static permittivity; τ = relaxation time; σ = conductivity; δ is an empirical parameter describing the distribution of relaxation times; ε_0 is the permittivity of free space (8.84×10^{-12}); T_S is the physical temperature of the water; and S is the salinity of the water. The relationships between the constants ε_s, τ, and σ and the temperature and salinity are quite

involved: details are given in such references as Klein and Swift (see [22]). These relations were used in the simulation study to develop the excess brightness temperature versus attenuation dependence.

The permittivity and, consequently, the emissivity are thus functions of sea-surface temperature T_S; the brightness temperature is the product of the emissivity and T_S (Equation 6-6). The brightness temperature of the surface T_B does not increase linearly with physical temperature T_S: depending on frequency, T_B may either increase or decrease as the physical temperature increases. This sensitivity remains nearly flat for frequencies in the vicinity of 10 GHz, but the effect of physical temperature on T_B increases for frequencies higher or lower than this value. Since the 18- and 37-GHz brightness temperature channels are used in determining T_{ex}, the variation of the emissivity with sea-surface temperature must be taken into account.

6.3.2 Simulations of Relation Between Attenuation and Excess Brightness Temperature

Computer simulations using the programs developed by Wu and Fung (see [22]) were made to determine the relationship between attenuation at 14.6 GHz (frequency of the SASS) and excess brightness temperatures at 18 and 37 GHz (frequencies of the SMMR). Some results showing points for the Porter and Kreiss cloud models and the Valley rain model (see Tables 6-1 and 6-2) are given in Figures 6-6 and 6-7. For a more complete discussion of models used in the study, see Dome [23,25]: curves are presented in [23] which show all the points for the different models discussed by Dome.

The results of the simulations shown in Figures 6-6 and 6-7 and the other points given in [23] indicate that the observed relationship between the total attenuation and the excess brightness temperature at $\theta = 49$ deg may be empirically modeled by the form

$$\alpha(T_S,f) = a_1(T_S,f)T_{ex} + a_2(T_S,f)T_{ex}^2 + a_3(T_S,f)T_{ex}^3 \tag{6-18}$$

where a_1, a_2, and a_3 are temperature- and frequency-dependent empirical constants determined by regression on the points obtained in the simulations. Because (1) the attenuations for which the 10.69-GHz SMMR channel frequency is sensitive are

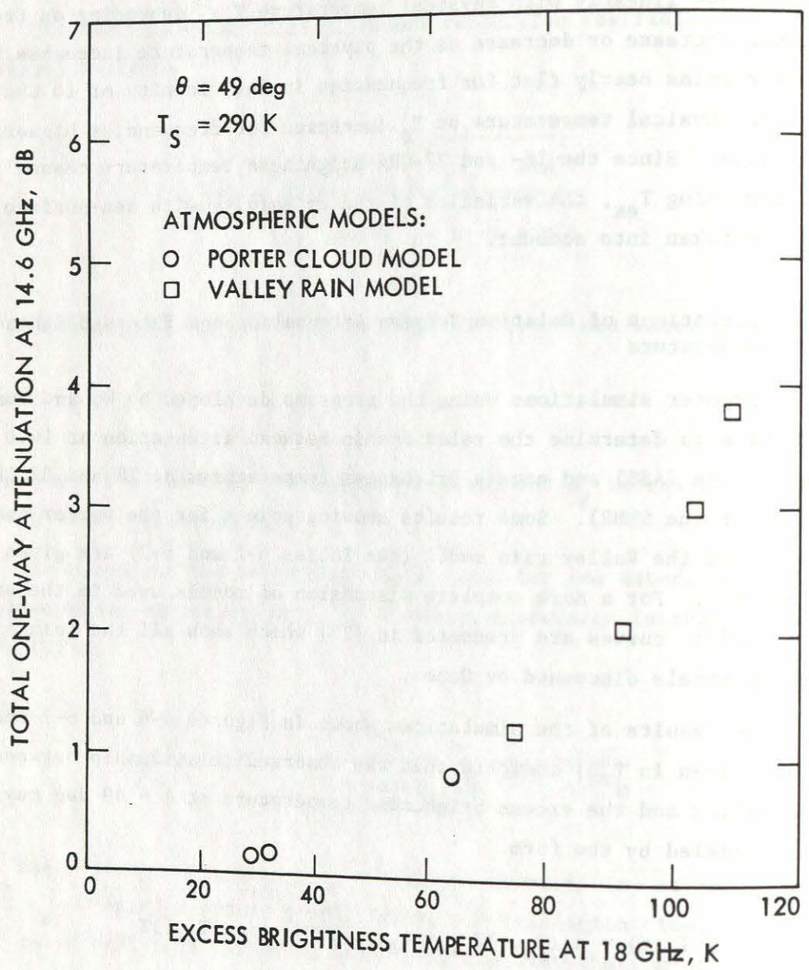

Figure 6-6. Total One-Way Atmospheric Attenuation at 14.6 GHz Versus Excess Brightness Temperature at 18 GHz

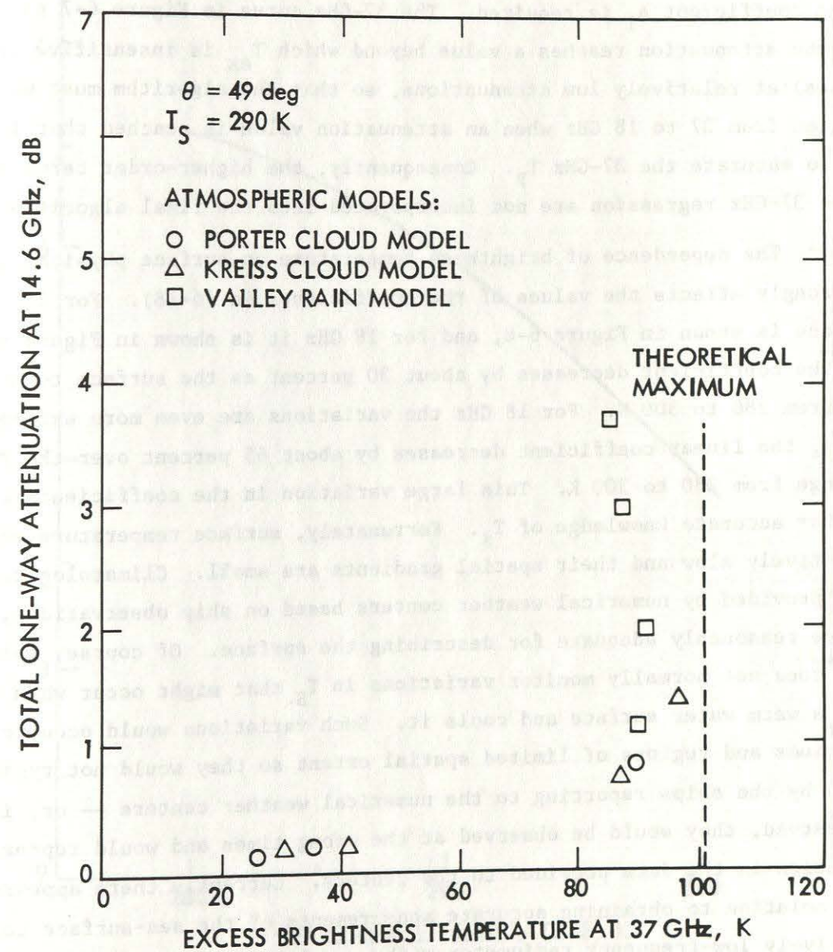

Figure 6-7. Total One-Way Atmospheric Attenuation at 14.6 GHz Versus Excess Brightness Temperature at 37 GHz

so large that the scatterometer signal in such an environment is likely to be corrupted by rain backscatter, and (2) the footprint size for the 10.69-GHz radiometer channel is so large (see Subsection 6.3.4) that there is little chance of finding constant attenuation conditions across such a footprint, the 10.69-GHz channel is not used in the attenuation algorithm. Consequently, the 18- and 37-GHz radiometer channels exclusively are used in determining the SASS attenuations. At 18 GHz all three terms of (6-18) must be used; but at 37 GHz, the usable region of the curve is adequately described by a linear relation, so that only the coefficient a_1 is required. The 37-GHz curve in Figure 6-7 saturates (i.e., the attenuation reaches a value beyond which T_{ex} is insensitive to further increases) at relatively low attenuations, so that the algorithm must make a transition from 37 to 18 GHz when an attenuation value is reached that is high enough to saturate the 37-GHz T_B. Consequently, the higher-order terms resulting from the 37-GHz regression are not incorporated into the final algorithm.

The dependence of brightness temperature on surface physical temperature strongly affects the values of the coefficients in (6-18). For 37 GHz this dependence is shown in Figure 6-8, and for 18 GHz it is shown in Figure 6-9. At 37 GHz the coefficient decreases by about 30 percent as the surface temperature ranges from 280 to 300 K. For 18 GHz the variations are even more extreme; for instance, the linear coefficient decreases by about 65 percent over the temperature range from 280 to 300 K. This large variation in the coefficients creates a need for accurate knowledge of T_S. Fortunately, surface temperature variations are relatively slow and their spatial gradients are small. Climatological data, or data provided by numerical weather centers based on ship observations, are therefore reasonably adequate for describing the surface. Of course, this type of data does not normally monitor variations in T_S that might occur when rain strikes a warm water surface and cools it. Such variations would occur over short time periods and regions of limited spatial extent so they would not typically be observed by the ships reporting to the numerical weather centers -- or, if they were observed, they would be observed at the wrong times and would represent a perturbation in the data provided to the centers. Currently there appears to be no good solution to obtaining accurate measurements of the sea-surface temperatures. (A relatively low-frequency radiometer with a small surface footprint might be adequate for such a purpose because such a radiometer would be much less affected by the atmosphere.)

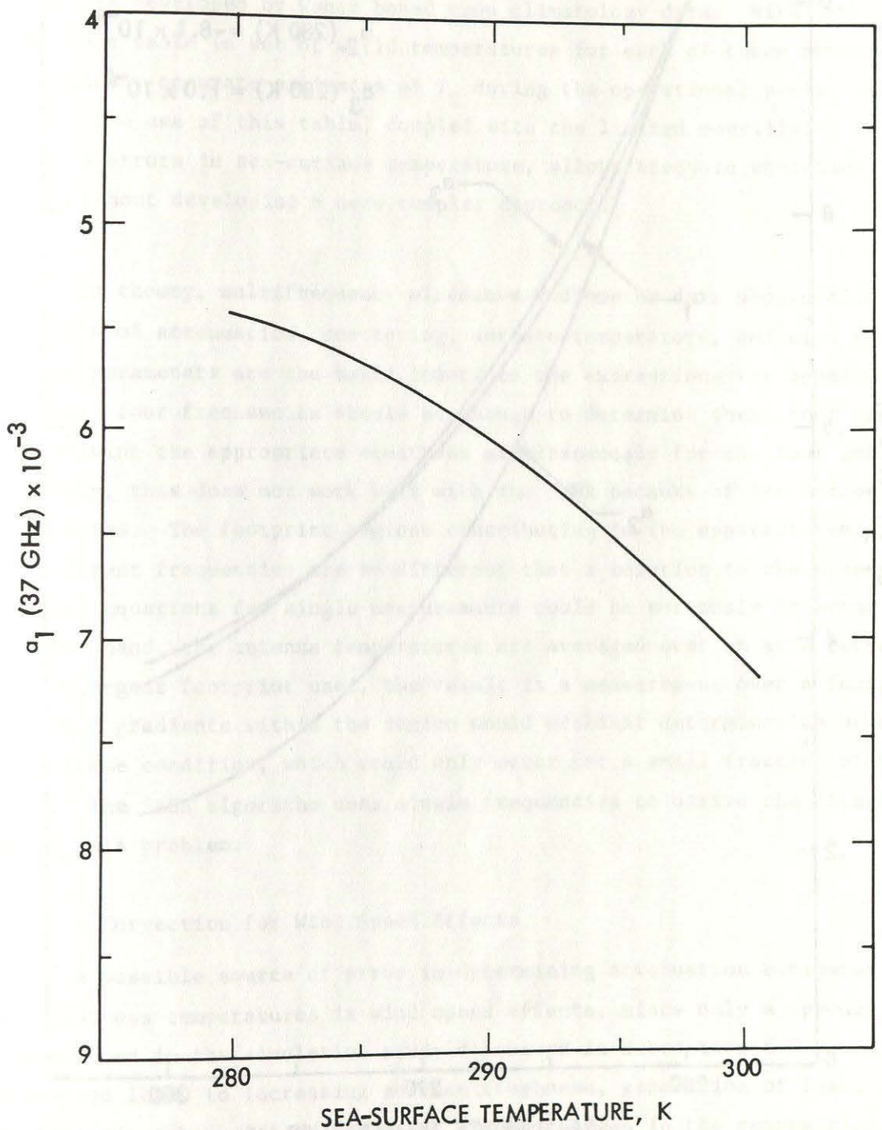

Figure 6-8. Temperature Dependence of a_1 Coefficient for 37 GHz

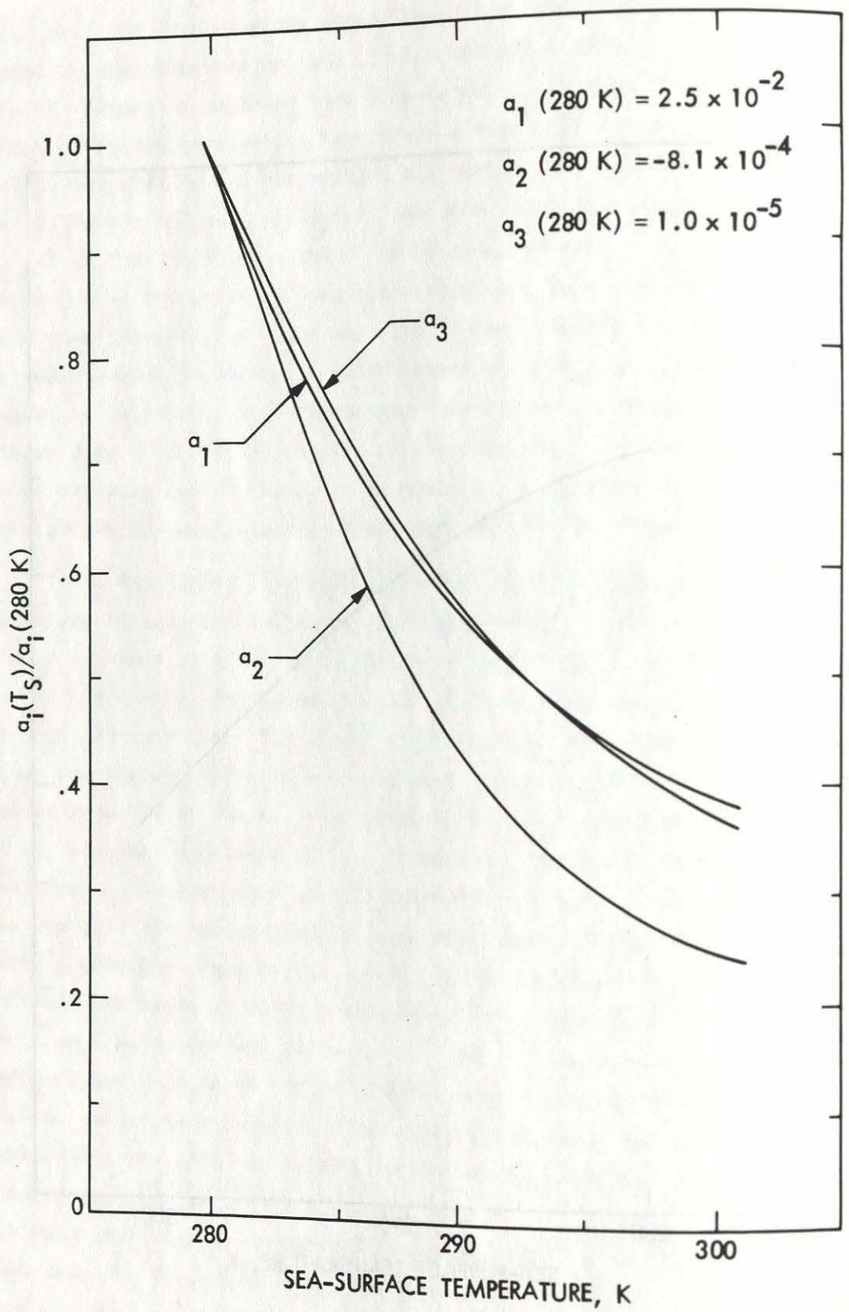

Figure 6-9. Temperature Dependence of Normalized (to 280 K) a_i Coefficients for 18 GHz

Since the Seasat satellite was operational for only slightly longer than three months, a straightforward approach for determining sea-surface temperature for the attenuation algorithm was agreed upon. A single look-up table (see Table 6-3) was developed by Wentz based upon climatology data. With linear interpolation, this table (a set of world temperatures for each of three months) provides reasonably accurate estimates of T_S during the operational period of the satellite. The use of this table, coupled with the limited sensitivity of the algorithm to errors in sea-surface temperature, allows adequate operation of the algorithm without developing a more complex approach.

In theory, multifrequency microwave radiometer data should allow the determination of attenuation, scattering, surface temperature, and wind speed since these parameters are the basic inputs to the expressions for apparent temperature: four frequencies should be enough to determine these four parameters by solving the appropriate equations simultaneously for the four unknowns. Unfortunately, this does not work well with the SMMR because of its different footprint sizes. The footprint regions contributing to the apparent temperatures at the different frequencies are so different that a solution to the proposed simultaneous equations for single measurements could be seriously in error. If, on the other hand, the antenna temperatures are averaged over an area corresponding to the largest footprint used, the result is a measurement over a footprint so large that gradients within the region would prohibit determination of any kind of extreme condition, which would only occur for a small fraction of the footprint. The SASS algorithm uses single frequencies to derive the attenuation because of this problem.

6.3.3 A Correction for Wind Speed Effects

A possible source of error in determining attenuation estimates from excess brightness temperatures is wind speed effects, since only a specular surface was assumed in the simulation study discussed in Subsection 6.3.2. Increasing wind speed leads to increasing surface roughness, generation of foam, and then to larger patches of foam coverage. These changes in the composition of the sea surface can be characterized as an increase in the surface emissivity. A nominal value of .0015 has been reported for the increase in emissivity ε resulting

from each 1-m/s increase in wind speed, over the frequency range of interest for vertical polarization at the SMMR incidence angle of 49 deg, by Wentz in private communication (see [23]).

Intuitively, any errors in the attenuation estimate arising from wind speed effects should be minimal at 37 GHz, since a relatively large change in excess brightness is needed for a small change in attenuation as seen in Figure 6-7. Sizable errors, if they exist, would occur only with the 18-GHz channel. Such possible errors were examined [23] by again performing simulations of the type discussed in Subsection 6.3.2 to determine values of the apparent temperature using emissivity values corresponding to wind speeds of 0, 10, 20, and 30 m/s. From the resulting apparent temperatures, excess brightnesses were calculated with respect to the brightness temperature of a specular surface as before. These values of excess brightness (derived again from an assumed sea-surface temperature of 290 K) are shown for the different wind speeds in Figure 6-10 as a function of the true excess brightness that would result from a specular (no wind) surface. The absolute error resulting in excess brightness is seen to decrease as the excess brightness temperature increases. Such behavior is expected since less of the surface contribution is observed by the radiometer as the atmospheric transmittance becomes less. To illustrate how these errors affect the computed attenuation, Figure 6-10 has a double scale that includes the one-way attenuation at θ=49 deg. For a given surface wind speed, an attenuation estimate error increases with increasing excess brightness.

To reduce the observed error in computed attenuations that would result if surface-roughness effects were ignored, a constant 10-m/s wind speed sea-surface condition is assumed instead of a purely specular condition. With this assumption, there results the final biased form for the excess brightness at θ=49 deg and vertical polarization [23] (c.f., Equations 6-6 and 6-13):

$$T_{ex} = T_a - (\varepsilon_{sp} + .015)\, T_S \qquad (6\text{-}19)$$

where ε_{sp} is the emissivity for a smooth specular surface described in Subsection 6.3.1.2. As in the previous specular case, relationships of the form (6-18) between the attenuation at 14.6 GHz and the vertically polarized excess brightness temperatures at 18 and 37 GHz given by (6-19) have been determined and are given in [23]. In fact, the coefficients a_1 shown in Figure 6-8 and a_1, a_2, a_3

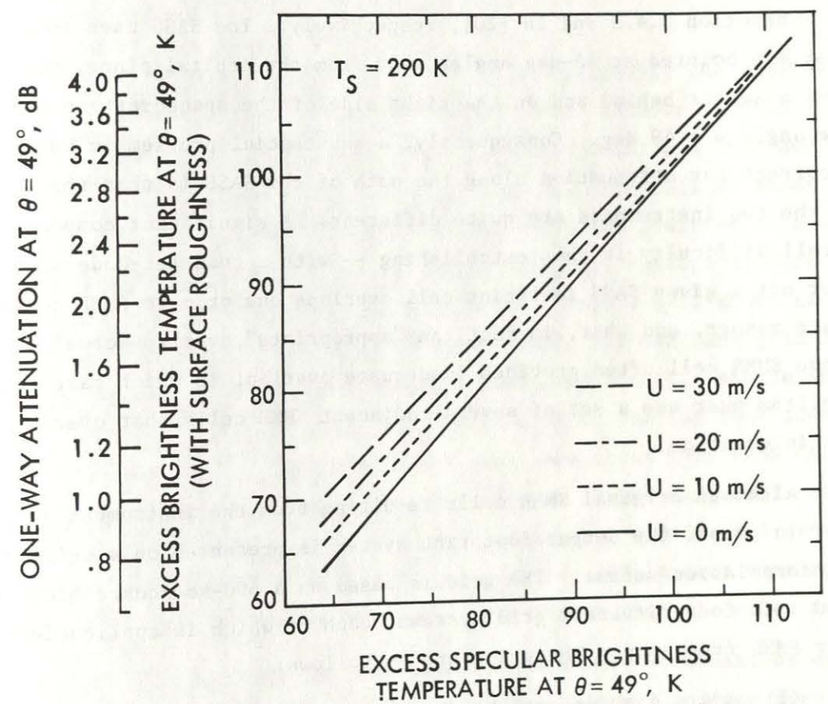

Figure 6-10. Errors in Attenuation and Actual Excess Brightness Temperature for an Assumed No-Wind Surface

shown in Figure 6-9 for 37 and 18 GHz, respectively, as a function of sea-surface temperature are those coefficient values that resulted from a regression on the 10-m/s surface-wind-speed simulation. Thus, these coefficient values used in the form (6-18), along with excess brightness temperatures given by (6-19), form the computational basis of the SASS attenuation algorithm. Through the use of the 10-m/s bias form (6-19) and the associated coefficient values, errors induced by surface roughness due to average winds are considerably reduced.

6.3.4 SASS and SMMR Footprint Relative Geometry

Geometric details for SASS and SMMR swaths and footprint cells are given in Subsection 3.4.3 and in [20], respectively. The SASS uses four fan beams that are pointed at 45-deg angles away from the orbital plane, whereas the SMMR scans a sector behind and on the right side of the spacecraft at the constant incidence angle $\theta = 49$ deg. Consequently, a substantial problem in using SMMR data to correct for attenuation along the path of the SASS is that the scan patterns of the two instruments are quite different. A significant component of this overall difficulty is thus establishing -- with a computer-code algorithm -- whether or not a given SASS footprint cell overlaps one or more SMMR cells in an appropriate manner, and what, in fact, an "appropriate" overlap actually is. Indeed, one SMMR cell often provides inadequate overlap, in which case any reasonable algorithm must use a set of several adjacent SMMR cells that overlap the SASS cell in question.

Although original SMMR cells resulting from the instrument scan are elliptical in shape, the output footprint system is presented on a uniform grid with an interpolation scheme. The grid is based on a 600-km square block that is subdivided into four different grid systems, each of which is applicable to a particular SMMR frequency. The grids are as follows:

(1) A 4 × 4 grid; each block is 150 × 150 km. Antenna apparent temperatures are obtained in this grid for 6.63 GHz from a single measurement (or, at least, equivalent to a single measurement by interpolation), and for the other SMMR frequencies by averaging over the area of the grid.

(2) A 7 × 7 grid; each block is 85.7 × 85.7 km. Antenna apparent temperatures are obtained in this grid for 10.69 GHz from the equivalent of a single measurement, and averages are used for the higher SMMR frequencies (18, 21, and 37 GHz) by averaging over the area of the grid.

(3) An 11 × 11 grid; each block is 54.5 × 54.5 km. Antenna apparent temperatures are obtained in this grid for 18 and 21 GHz from essentially a single measurement, and an average over the grid is used for 37 GHz.

(4) A 22 × 22 grid; each block is 27.3 × 27.3 km. Antenna apparent temperatures are obtained in this grid only for 37 GHz.

Figure 6-11 illustrates the gridding system.

The nominal size of the SASS cell is approximately the same as that of SMMR grid 3, corresponding to the 18-GHz SMMR cell. However, a SASS cell is considerably longer than it is wide (nominal length: 50 km) and thus neither completely fills nor is completely filled by a grid 3 SMMR cell as shown in Figure 6-12. Due to the SASS and SMMR scan differences, the position of a SASS cell center relative to the positions of the nearby SMMR cell centers differs as a function of time in orbit and from orbit to orbit. Figure 6-12 shows two examples of the many possible overlap patterns between a SASS cell and SMMR grid 3 and grid 4 cells. A SASS cell may be completely contained within a single SMMR 18-GHz cell, but it is also possible for a SASS cell to overlap four such cells. In any case, it is clear from the different cell geometries that SASS cell overlap with four different SMMR cells is never uniform. Since SASS cells are basically oriented lengthwise along SMMR cell diagonals, a SASS cell centered exactly at the intersection of four SMMR cells would contain more overlap area in the two SMMR cells through which its longer axis passes than the other two.

Since precipitation is the cause of the severe attenuations encountered by SASS, and since precipitation rates are seldom, if ever, uniform over the area of a single grid 3 (18 GHz) SMMR cell, any determination of attenuation using even just one grid 3 cell will most likely be somewhat in error. Naturally, the attenuation determination will be further degraded because of the SASS/SMMR cell-overlap problem indicated above and in Figure 6-12. Clearly, the attenuation algorithm should in some way use measurements from more than one SMMR cell to calculate a SASS $\sigma°$ correction. Unfortunately for attenuation calculations, four contiguous SMMR grid 4 cells cover an area greater than 100 km^2, so that for

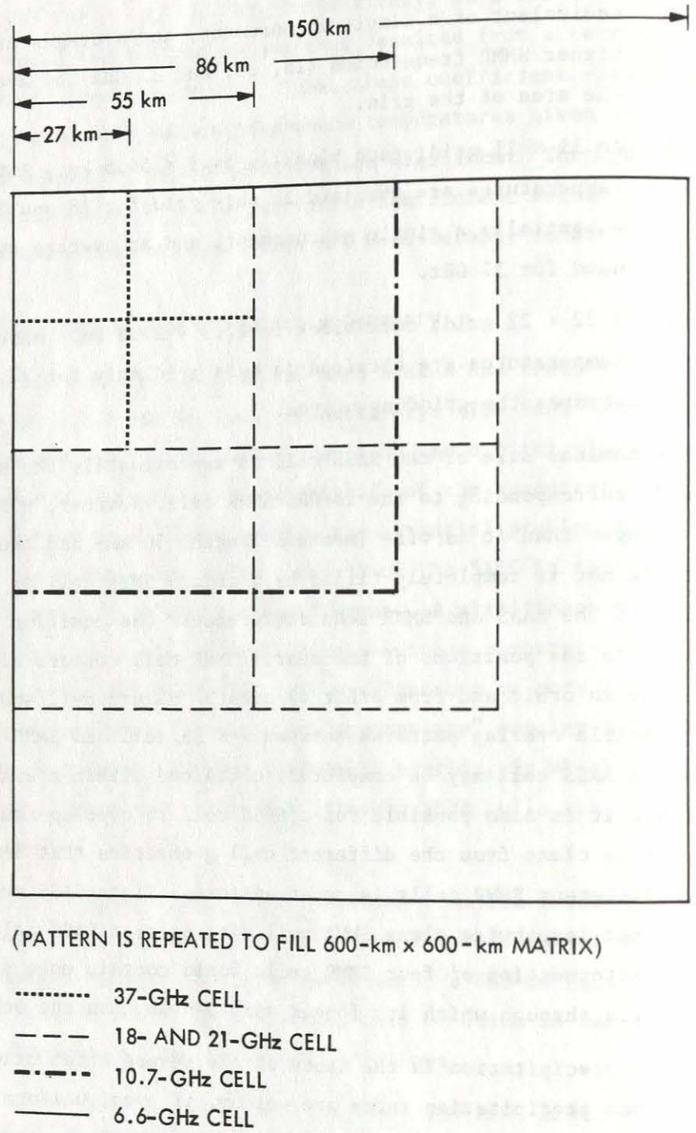

Figure 6-11. SMMR Gridding Pattern

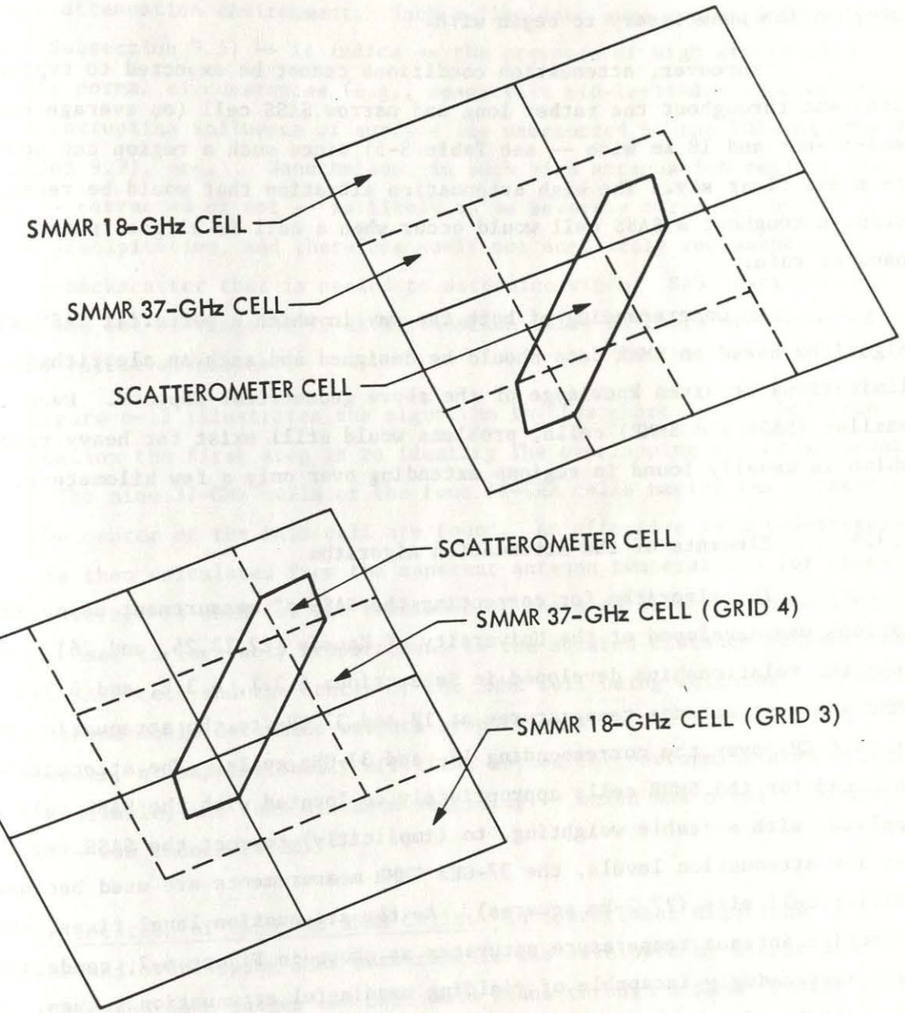

Figure 6-12. Sample Overlaps of SMMR and Scatterometer Cells

typical precipitation patterns there is little chance that uniform attenuation will occur over this region. Perhaps the only situation where uniform attenuation could be expected over such a large area is the rather benign clear-sky/light-cloud case where the attenuation level is small enough to make a σ° correction computation unnecessary to begin with.

Moreover, attenuation conditions cannot be expected to typically remain constant throughout the rather long and narrow SASS cell (on average about 60 km end-to-end and 18 km wide -- see Table 3-5) since such a region can span both rain and clear sky. The high attenuation situation that would be reasonably constant throughout a SASS cell would occur when a cell is aligned parallel to a band of rain.

An understanding of both the way in which a potential SASS attenuation algorithm based on SMMR data should be designed and such an algorithm's inherent limitations requires knowledge of the above geometrical aspects. Even with much smaller (SASS and SMMR) cells, problems would still exist for heavy rainfall, which is usually found in regions extending over only a few kilometers.

6.3.5 Elements of the Attenuation Algorithm

The algorithm for correcting the SASS σ° measurement using SMMR observations was developed at the University of Kansas [22,23,25, and 26]. The method uses the relationships developed in Subsections 6.3.1, 6.3.2, and 6.3.3 to relate SMMR apparent antenna temperatures at 18 and 37 GHz to the attenuation suffered at 14.6 GHz over the corresponding 18- and 37-GHz cells. The attenuation value obtained for the SMMR cells appropriately co-located with the SASS cell is then applied, with suitable weighting, to (implicitly) correct the SASS received power. For low attenuation levels, the 37-GHz SMMR measurements are used because of the smaller cell size (27.3-km squares). As the attenuation level rises, the 37-GHz effective antenna temperature saturates as shown in Figure 6-7, rendering such data increasingly incapable of yielding meaningful attenuation values. Thus, as the calculated attenuation reaches a certain level, the algorithm switches from the use of 37-GHz channel data to 18-GHz data.

When the attenuation computed from 18-GHz measurements increases beyond another threshold level that is assumed by the algorithm to be the largest value that can be reasonably determined using SMMR data, the large flag-value

99.99 dB is inserted into the attenuation channel. This flag value indicates to the user and to the downstream geophysical wind-retrieval processor that σ° corrections cannot be computed with useful accuracy with the present algorithm in such a higher attenuation environment. Such a flag does give useful information however (see Subsection 9.5) -- it indicates the presence of high attenuation activity under normal circumstances (e.g., spacecraft mid-latitudes removed from the possible corrupting influence of surface ice undetected by the TOILing process (see Subsection 9.9), etc.). Nonetheless, in such high attenuation regions the SASS signal -- corrected or not -- is likely to be severely corrupted by backscatter from precipitation, and therefore would not accurately represent the ocean-surface backscatter that is needed to determine winds. SASS data that is flagged with the out-of-range 99.99-dB attenuation value is therefore rejected from the wind retrieval process.

Figure 6-13 illustrates the algorithm in flow chart form. For each SASS cell location the first step is to identify the overlapping and/or adjacent SMMR cells. The nine 37-GHz cells or the four 18-GHz cells having the closest centers to the center of the SASS cell are found. An effective weighted-average temperature is then calculated from the apparent antenna temperatures for these cells: this average is used for the remainder of the algorithm's computations. The weighting used is inversely proportional to the squared distance between the center of the SASS cell and the center of the SMMR cell being weighted. (A more appropriate scheme would determine weights proportional to the areas of cell overlap. However, a computationally efficient method for performing area weighting was not available, and thus distance weighting -- which was straightforward to implement -- was incorporated.)

6.3.5.1 <u>Co-location of SASS and SMMR Cells</u>. An operational algorithm to co-locate SASS and overlapping SMMR measurements was developed by Birrer and Dome [27]. This approach passes the SASS data scans through a SMMR "vector space" generated by forming two storage matrices containing three consecutive 600- × 600-km SMMR data blocks. Separate matrices are used for 18- and 37-GHz data to eliminate unnecessary computer storage. These matrices are referenced through (i,j,k) coordinates. The i-index corresponds to grid rows in the along-track direction of the data vector. Cross-track elements of the data vector are referenced through the j-index, and the k-index represents the data elements: latitude, longitude, and apparent antenna temperature.

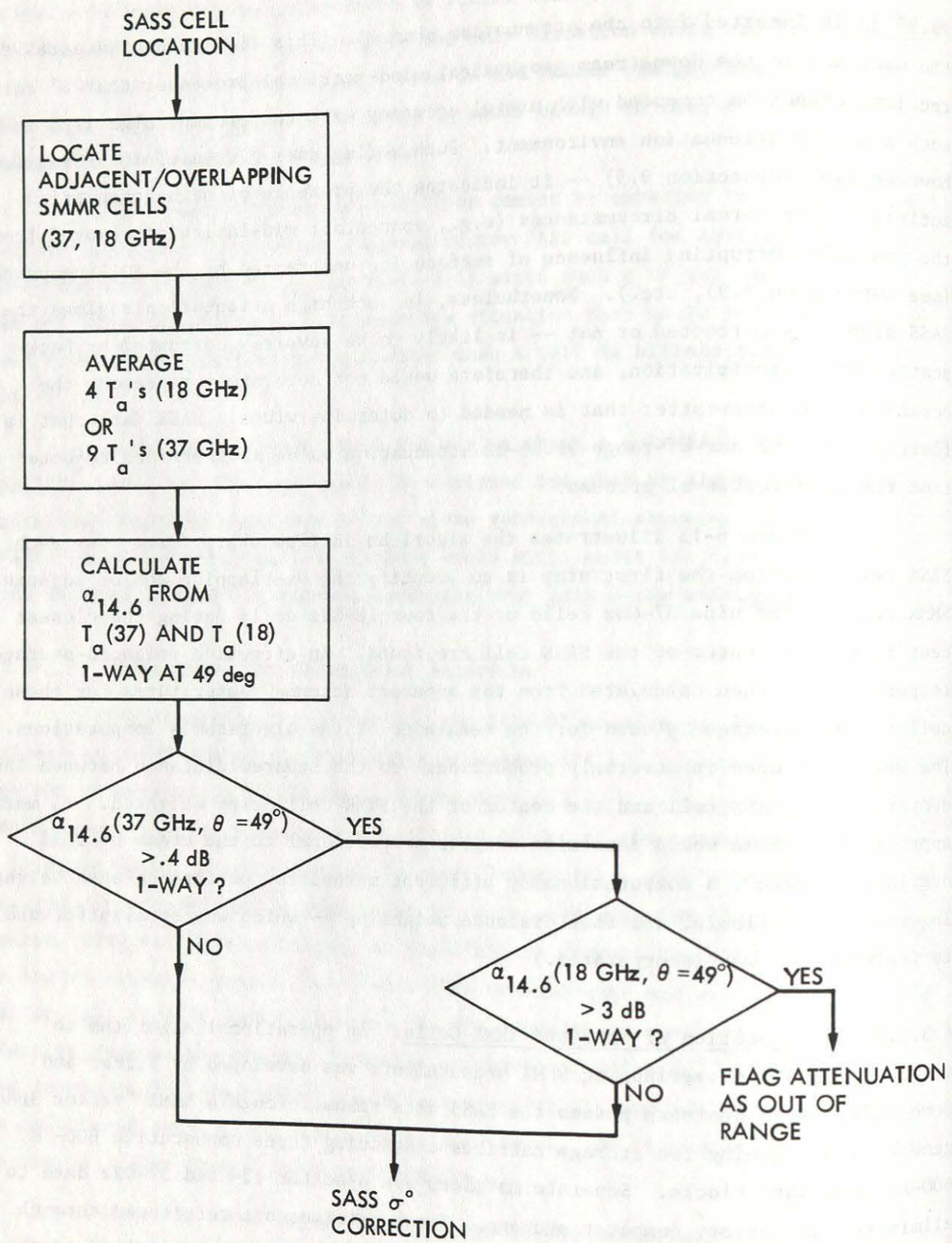

Figure 6-13. SASS Attenuation Algorithm Flow Chart

The co-location process begins once a SASS data scan is known to overlap the SMMR space by comparing the SASS and SMMR time-tags. At this point, a search is initiated to locate the best 37-GHz cell, grid 4, referenced as (i_{15}, j_{15}), which is a minimum distance from the nadir SASS cell.

For the remaining 14 cells in a SASS data frame, distance d is computed from the nadir SASS cell to a specific cell n. This distance and an angle ψ, formed between satellite subtrack and SASS beam, are used to estimate the 37-GHz cell (i_n, j_n), nearest the center of the desired SASS cell, by the relations:

$$i_n = i_{15} + \left(d/r_{37}\right) \cos\psi \tag{6-20}$$

$$j_n = j_{15} + \left(d/r_{37}\right) \cos\psi \tag{6-21}$$

where r_{37} is the resolution cell size at 37 GHz. The geometry used to determine the other SASS cells is illustrated in Figure 6-14. Since the 37-GHz resolution cell is $\sim$ 27 × 27 km, a 3 × 3 submatrix of 37-GHz measurements is specified to insure complete overlap of the SASS cell (see Figure 6-12).

To guarantee that the coordinates (i_n, j_n) are the best match to the SASS cell, the 3 × 3 SMMR submatrix selected about these coordinates is then searched to locate the 37-GHz cell nearest the SASS cell center. If the initial guess is incorrect, a new center point is designated $(i_{n(best)}, j_{n(best)})$, and the final 3 × 3 submatrix is formed.

Since the SMMR grids for different frequencies cover the same 600- × 600-km surface region, the overlapping submatrix for the 18-GHz channel, or any other channel, may be determined without searching. Two opposite corner points of the 37-GHz submatrix designated as (i_4, j_4) can be simply decoded into two potential corner points for any frequency (i_ℓ, j_ℓ) as follows:

$$i_\ell = \left(i_4 - 1\right) n_\ell / 22 + 1 \tag{6-22}$$

$$j_\ell = \left(j_4 - 1\right) n_\ell / 22 + 1 \tag{6-23}$$

where ℓ is the best grid code for a specific frequency, and n_ℓ is the number of rows (or columns) for the frequency grid. This decoding will specify at most a

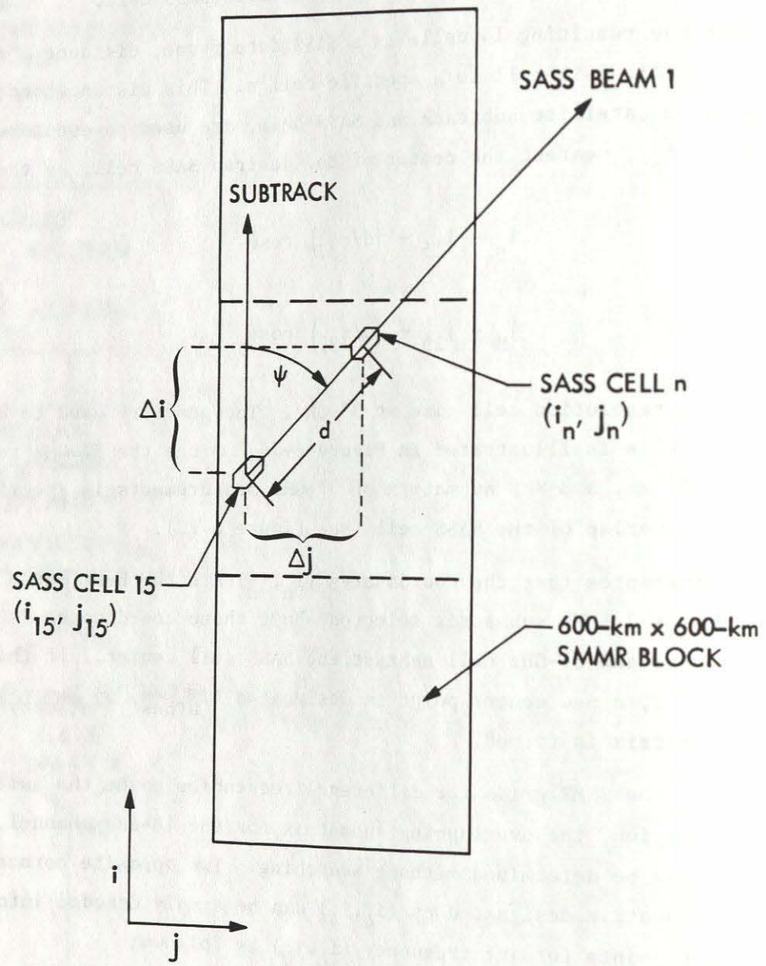

Figure 6-14. Illustration of SASS Cell Positioning in SMMR "Vector Space"

2 × 2 submatrix at other frequencies. However, due to the larger resolution cells, these potential submatrices may degenerate into either 2 × 1, 1 × 2, or 1 × 1 submatrices.

6.3.5.2 Calculations Following Cell Co-location. The next step after co-location processing is to calculate the excess brightness temperature at both 37 and 18 GHz using (1) the sea-surface temperature obtained from Table 6-3, (2) the average effective antenna temperature computed at both frequencies, and (3) the wind-speed-effect adjusted form (6-19). Following this, the attenuation at the SASS frequency 14.6 GHz is computed for both 37- and 18-GHz channels using Equation (6-18) with appropriate coefficient values. Decision logic is then executed to determine which radiometer channel should be used for the final attenuation value (see Figure 6-13).

If $\alpha_{14.6}$, the one-way attenuation at 14.6 GHz and 49-deg angle of incidence, computed for the 37-GHz channel is not greater than .4 dB, this 37-GHz value is used. If this 37-GHz computed attenuation exceeds .4 dB, the algorithm switches to the 18-GHz channel, and then performs another test. If the computed attenuation $\alpha_{14.6}$ indicated by the 18-GHz channel does not exceed 3 dB (again, one-way at 49 deg), this 18-GHz value is used. Finally, if this 18-GHz computed attenuation exceeds 3 dB, the attenuation correction for the SASS measurement is flagged as out of range as described above.

The initial version from which this algorithm was derived [26] used a weighted average of the attenuations obtained from the 37-, 18-, and 10.7-GHz SMMR channels. This earlier scheme was not used to correct SASS data because it requires using the larger 10.7-GHz cell (grid 2, 86 km). The present algorithm allows for the use of the finest possible SMMR resolution consistent with adequate measurement of attenuation without SMMR channel saturation.

All attenuations discussed until this point have referred to the total loss experienced by a signal on its path through the atmosphere. The total attenuation can be resolved into two natural components. The "clear-air" attenuation component is that baseline signal loss incurred over the path through minimally attenuating clear-air. This component is an estimable constant of the system that is always present. The remainder of the attenuation is that part of the radar signal loss that exceeds the clear-air attenuation. While this latter

component must be nonnegative by definition, it may have a magnitude -- particularly as computed by an attenuation algorithm -- as small as zero. For developmental reasons, the model function used to retrieve winds from SASS $\sigma°$ data (G-H table -- see Subsection 7.3.3) has an approximate clear-air component of the attenuation already implicitly "built in." To avoid having this part of the (estimated) attenuation effectively included twice in the final wind solutions, it is subtracted out of the total attenuation computed by the present algorithm. This is done by setting

$$\alpha_{14.6}\left(\theta_I=49°\right) = \alpha_{14.6}^{total}\left(\theta_I=49°\right) - \alpha_{ca} \qquad (6\text{-}24)$$

where α_{ca} = .14 dB is the nominal value assumed for the one-way clear-air attenuation at the incidence angle θ_I=49° and the SASS frequency 14.6 GHz. $\alpha_{14.6}(\theta_I=49°)$ is then the estimated clear-air-excess one-way attenuation at θ_I=49° and 14.6 GHz.

To use $\alpha_{14.6}(\theta_I=49°)$ to correct for the atmospheric effects beyond clear air that are observed by the SASS, the estimate must be adjusted to account for the two-way path loss experienced at the particular SASS Doppler measurement cell incidence angle θ_I. This adjustment is obtained by using the relation

$$\alpha_{SASS}\left(\theta_I\right) = 2\alpha\left(\theta_I=49°\right)\frac{\cos 49°}{\cos\left(\theta_I\right)} \qquad (6\text{-}25)$$

6.3.6 Computation of the Attenuation Correction

The basic computational steps involved in a SASS attenuation calculation (omitting details of co-location and weighting to find SMMR effective T_a's -- see Subsection 6.3.5) follow. For a given SASS cell at incidence angle θ_I:

(1) Co-locate to obtain SMMR 37- and 18-GHz cells that overlap the SASS cell.

(2) Perform weighted average to get effective SMMR $T_a(37)$ and $T_a(18)$ corresponding to SASS cell.

(3) Given latitude (ϕ), longitude (Ω), and time (t) of SASS cell and Table 6-3, use linear interpolation in all three variables to obtain the sea-surface temperature T_S at (ϕ,Ω,t) in kelvins (after adding 273°.16). Table 6-3 contains sea-surface temperatures at 10-deg latitude increments, 30-deg longitude increments, and 1-month time increments.

(4) Compute sea-surface brightness temperature T_B (see Subsection 6.3.1):

For 18 GHz:

$T_B = 155.7$, if $T_S \le 285°$

$T_B = .15(T_S - 285) + 155.7$, if $285° < T_S \le 291°$

$T_B = .31(T_S - 291) + 156.6$, if $291° < T_S$

For 37 GHz:

$T_B = -.372(T_S - 279.3) + 180.84$, if $T_S \le 288°$

$T_B = -.2(T_S - 288) + 177.6$, if $288° < T_S \le 294°$

$T_B = -.052(T_S - 294) + 176.4$, if $294° < T_S$

(5) Using T_a, T_S, and T_B, above, compute excess brightness temperature T_{ex} at θ_I=49°, vertical polarization, and a constant 10-m/s surface wind for both 18 and 37 GHz (see Equations 6-6 and 6-19):

$$T_{ex} = T_a - T_B - .015T_S$$

(6) Compute the coefficients a_1,a_2,a_3 in Equation (6-18):

For 18 GHz:

$$a_1 = 3.25916 - .0216155T_S + 3.595\times10^{-5}T_S^2$$

$$a_2 = -.131152 + .000871T_S - 1.4485\times10^{-6}T_S^2$$

$$a_3 = .0014378 - 9.5345\times10^{-6}T_S + 1.585\times10^{-8}T_S^2$$

Table 6-3. Global Sea-Surface Temperatures Used for Attenuation Processing, deg C

	E Long, deg → / Lat, deg →	-65	-55	-45	-35	-25	-15	-5	5	15	25	35	45	55	65
JUL 1	15	.0,	.0,	5.6,	15.0,	18.0,	20.5,	24.0,	25.6,	-25.3,	-24.6,	20.0,	18.0,	14.0,	12.0
	45	.0,	.0,	6.3,	14.3,	21.0,	23.5,	24.6,	25.0,	24.2,	26.1,	20.0,	18.0,	-9.0,	12.0
	75	.0,	1.0,	1.2,	14.3,	19.5,	23.6,	26.5,	27.2,	27.0,	26.2,	-21.3,	-16.3,	-8.3,	-9.5
	105	.0,	2.0,	7.0,	14.0,	19.9,	24.2,	27.0,	28.0,	28.0,	26.3,	-22.7,	-14.7,	-6.0,	-8.3
	135	.0,	2.0,	8.4,	14.0,	-20.2,	24.0,	26.3,	26.5,	29.0,	27.5,	24.0,	13.0,	4.0,	-5.8
	165	.0,	4.0,	8.6,	14.0,	20.5,	24.5,	27.6,	29.0,	28.7,	27.3,	22.5,	12.7,	2.0,	-4.5
	195	.0,	4.0,	8.6,	14.0,	20.8,	26.2,	28.0,	28.0,	27.0,	25.5,	21.4,	13.3,	4.8,	2.0
	225	.0,	4.0,	8.0,	14.0,	21.3,	25.5,	27.0,	27.0,	26.0,	22.0,	18.0,	10.3,	8.0,	-3.0
	255	.0,	4.0,	8.0,	14.0,	20.0,	22.8,	24.0,	25.9,	27.7,	25.9,	-21.9,	-14.2,	9.0,	4.0
	285	.0,	4.0,	8.0,	14.0,	17.0,	19.6,	21.0,	26.8,	27.8,	27.7,	25.8,	18.0,	9.0,	4.0
	315	.0,	2.0,	7.0,	14.0,	21.0,	24.3,	26.2,	27.0,	26.4,	26.2,	24.0,	18.0,	9.0,	4.0
	345	.0,	.0,	6.0,	14.3,	20.0,	22.5,	24.5,	26.3,	26.3,	23.0,	21.0,	18.0,	13.0,	10.0
AUG 1	15	.0,	.0,	4.9,	13.0,	16.5,	18.6,	22.4,	24.0,	-25.7,	-25.7,	22.0,	18.0,	15.0,	10.0
	45	.0,	.0,	4.4,	14.8,	20.5,	23.3,	24.0,	24.8,	24.5,	27.0,	22.0,	18.0,	-13.8,	10.0
	75	.0,	.0,	6.3,	12.7,	18.6,	23.3,	26.4,	26.5,	27.0,	-23.2,	-17.0,	-12.5,	-8.3
	105	.0,	.0,	6.5,	13.0,	18.7,	23.7,	26.7,	28.0,	28.0,	-24.3,	-16.0,	-11.3,	-7.4
	135	.0,	1.0,	7.5,	12.8,	-19.1,	23.8,	26.8,	28.7,	29.0,	28.2,	25.5,	15.0,	10.0,	-5.6
	165	.0,	2.0,	8.8,	14.0,	19.5,	25.4,	28.8,	29.2,	28.8,	27.8,	24.7,	15.0,	10.0,	-4.8
	195	.0,	2.0,	8.0,	14.0,	20.0,	26.0,	27.8,	28.0,	27.2,	26.0,	22.3,	15.0,	8.8,	3.0
	225	.0,	2.0,	8.0,	14.0,	20.5,	25.0,	25.7,	26.5,	27.2,	22.7,	19.0,	15.4,	12.0,	3.0
	255	.0,	2.0,	8.0,	14.4,	19.5,	22.0,	23.0,	26.0,	27.8,	25.9,	-22.0,	-15.7,	12.0,	3.0
	285	.0,	2.0,	8.0,	13.0,	16.3,	18.3,	20.9,	26.0,	28.0,	27.5,	24.9,	16.0,	12.0,	3.0
	315	.0,	1.0,	6.5,	14.4,	20.0,	23.5,	25.5,	27.0,	26.7,	26.0,	24.5,	17.5,	8.0,	3.0
	345	.0,	.0,	4.4,	13.0,	18.9,	21.7,	23.6,	25.3,	26.8,	24.4,	21.3,	17.7,	13.0,	6.0
SEP 1 (1978)	15	.0,	.0,	5.0,	13.3,	16.0,	18.0,	22.3,	24.3,	-26.3,	-24.9,	21.0,	16.7,	12.7,	9.0
	45	.0,	.0,	4.8,	15.3,	21.0,	23.8,	24.9,	25.3,	26.2,	26.0,	22.0,	18.0,	-12.4,	9.0
	75	.0,	1.0,	7.0,	13.0,	15.0,	23.5,	26.5,	27.0,	27.0,	27.0,	-22.6,	-16.8,	-12.0,	-7.8
	105	.0,	1.0,	7.0,	13.0,	19.0,	23.8,	26.8,	27.9,	28.0,	28.0,	-23.8,	-14.5,	-11.7,	-7.2
	135	.0,	2.4,	8.4,	12.9,	-19.7,	24.5,	26.8,	28.9,	29.0,	28.0,	24.4,	13.3,	11.3,	-5.9
	165	.0,	2.4,	8.5,	12.0,	20.4,	25.0,	27.5,	29.3,	28.8,	27.8,	23.5,	12.4,	11.3,	-5.3
	195	.0,	3.0,	8.0,	13.3,	20.5,	26.0,	28.0,	28.0,	27.2,	25.2,	22.4,	13.3,	10.0,	4.0
	225	.0,	2.4,	8.0,	13.5,	20.5,	25.0,	26.0,	26.6,	26.8,	23.0,	19.0,	15.6,	14.0,	4.0
	255	.0,	3.0,	8.0,	13.3,	19.2,	22.2,	22.7,	25.2,	28.0,	25.4,	-21.8,	-14.3,	6.0,	4.0
	285	.0,	3.0,	7.2,	12.3,	15.5,	17.5,	20.0,	25.5,	28.0,	27.5,	24.6,	13.0,	6.0,	4.0
	315	.0,	.5,	6.0,	14.0,	19.5,	23.7,	25.4,	27.1,	27.2,	25.9,	24.0,	17.0,	8.0,	4.0
	345	.0,	.0,	5.4,	13.1,	17.9,	21.7,	23.5,	25.3,	26.4,	23.8,	21.5,	17.6,	12.0,	6.0

For 37 GHz:

$$a_1 = .257296 - .0016475T_S + 2.693\times10^{-6}T_S^2$$

$$a_2 = a_3 = 0$$

(7) Compute the one-way attenuation α at the SASS frequency 14.6 GHz and at the incidence angle θ_I=49° using the 18- and 37-GHz excess brightness temperatures and coefficients a_1, a_2, a_3 given above, and Equation (6-18):

$$\alpha(18) = \sum_{i=1}^{3} a_i(18)T_{ex}^i(18)$$

$$\alpha(37) = a_1(37)T_{ex}(37)$$

(8) Perform attenuation-level decision tree:

If $\alpha(37) \leq .4$ dB, set α, the final one-way attenuation at SASS frequency 14.6 GHz and incidence angle θ_I=49°, equal to $\alpha(37)$.

If $\alpha(37) > .4$ dB and $\alpha(18) \leq 3$ dB with $\alpha(18) < \alpha(37)$, set $\alpha = \alpha(37)$.

If $\alpha(37) > .4$ dB and $\alpha(18) \leq 3$ dB with $\alpha(18) \geq \alpha(37)$, set $\alpha = \alpha(18)$.

If $\alpha(37) > .4$ dB and $\alpha(18) > 3$ dB, flag α as out of range.

(9) Using previous α (from step 8) and Equation (6-24), compute the excess-of-clear-air attenuation (one-way, 14.6 GHz, θ_I=49°):

$$\alpha = \alpha_{prev} - .14$$

(10) Use Equation (6-25) and α from step (9) to compute the final two-way attenuation experienced at a SASS incidence angle θ_I:

$$\alpha = \frac{1.312}{\cos(\theta_I)}\alpha_{prev}$$

(11) Set minimum computed SASS attenuation at .01 dB as an attenuation-was-computed flag:

$$\alpha = \max\left(\alpha_{prev}, .01\right)$$

(12) If α from step (8) was determined to be out of range, flag the final SASS attenuation with the value α = 99.99.

SECTION 7

SASS WIND VECTOR GEOPHYSICAL ALGORITHM PROCESSING

7.1 OVERVIEW OF THE SASS GDR WIND VECTOR ALGORITHM

The SASS geophysical algorithm computes the sea-surface wind speed and direction from scatterometer $\sigma°$ measurements derived from the sensor algorithms (see Section 5). The backscatter coefficients that are input to this geophysical processor have been corrected for attenuation through the atmosphere to the extent possible (see Section 6). The overall geophysical algorithm consists of three modular components: cell pairing, least-squares estimator, and wind-to-$\sigma°$ model function table.

7.1.1 Geophysical Model Function Morphology

The SASS geophysical algorithm computes the 19.5-m neutral stability wind speed and direction (see Subsection 9.4) for the average location and time at which the $\sigma°$ measurements were taken. The neutral stability wind is defined as the wind speed that would result from a given friction velocity, u*, if the atmosphere were neutrally stratified (air and sea-surface temperature equal) with an adiabatic lapse rate. Thus the neutral stability wind speed is uniquely defined by the friction speed at the sea surface rather than the actual wind at the reference 19.5-m elevation. The physical mechanism upon which the measurement is based for primary-swath (off-nadir) incidence angles; i.e., $\theta_I \gtrsim 20°$, is the Bragg scattering of microwave energy from centimeter-length capillary ocean waves created by the action of surface wind [28]. The strength of the backscatter measurement $\sigma°$ is proportional to the capillary wave amplitude, which is assumed to be in equilibrium with the wind friction speed u*. In addition, the backscatter response is anisotropic for off-nadir incidence angles; wind direction can therefore be derived from radar measurements taken at different azimuths.

The predominant physical basis for measurement sensitivity to wind at nadir and near-nadir incidence angles is specular reflection [29]. A single functional form relating backscatter to wind over the entire range of Seasat scatterometer incidence angles, $0° \leq \theta_I < 70°$, was developed by Wentz [30] and summarized by Jones, Wentz, and Schroeder [31]. This model function relationship is a unification of a Bragg-scattering model component that is dominant over non-nadir incidence angles, and a specular (geometric optics) component that is dominant

over near-nadir incidence angles. The overall model function derives as the sum of the two components in a splining procedure that preserves function and first-derivative continuity at the transition point $\theta_I = 30°$, and is therefore applicable over the whole SASS swath.

This total model is seen to yield values of $\sigma°$ that remain essentially constant under any variation in the measurement azimuth angle or wind direction when the incidence angle is fixed at a nadir-swath value. This insensitivity reflects the fact that the backscatter coefficient is effectively independent of the azimuth at incidence angles less than about ten degrees [38]. Wind direction is therefore not determinable for the SASS nadir swath (see Figure 3-3 and Subsection 3.4.3.5): the general speed-and-direction model function form is nonetheless used to derive nadir-swath solutions consisting only of speed by constraining the a priori wind direction during nadir processing to be (arbitrarily) blowing from the north. In this way, the same model form and computational schema can be used to generate both nadir- and primary-swath solutions.

A table form -- also formulated by Wentz [33] -- of this total backscatter model function is used in the GDR wind processing (see Subsection 7.3.3) to increase computational efficiency. The varying sensitivity to azimuth as a function of incidence angle (as well as other model characteristics) becomes evident upon examination of the table (see Table 7-1) entries or Figure 3a-h of [32].

7.1.2 Sensor Data Grouping: Pairing and Binning

Before the wind vector algorithm can "invert" input sensor data into wind solutions, somewhat complex time/space re-ordering of the input data must be performed. As described in Subsection 5.6 and elsewhere, SASS $\sigma°$ sensor record data is ordered as the data is received from the spacecraft; i.e., one (minor frame) record contains 15 $\sigma°$ Doppler measurements derived from a single antenna illumination pattern extending hundreds of kilometers along the Earth's surface. A unit of geophysical processing producing a wind solution requires a small input set of $\sigma°$ measurements that are nearly coincident in space and time with (for primary-swath solutions) "orthogonality" -- that is, the presence in the set of at least one measurement from each of the forward and aft beams -- satisfied. The mapping between the incoming data structure and that required is provided by the cell grouping front-end stage of the geophysical algorithm.

Two distinct data grouping options were developed for use in the geophysical processing. In the binning option, the data swath area is broken into a square grid pattern with surface region bin sizes selectable in the range from .5° to 2°. The bins have contiguous boundaries formed by appropriate latitude and longitude lines. All $\sigma°$ measurements whose cell centers fall within a given grid square are provided as input to the wind vector estimation component of the algorithm. A single wind solution (which includes up to four alias speeds and directions for a primary-swath bin -- see Subsections 7.4.1 and 7.4.5) results from processing all the sensor data falling within the bin -- providing the orthogonality condition is satisfied. The time-tag and location of the output solution are defined (somewhat arbitrarily) as the centroids of the times and locations of the input $\sigma°$ measurements contained in the solution bin. Much of the wind data examined in the Seasat workshops [11,12,13] was produced with this grouping option, with bin sizes of .5° and 1°.

7.1.2.1 Cell Pairing. The other sensor data grouping option developed for geophysical processing is cell pairing, the scheme used to generate the GDR winds. With this method, a $\sigma°$ measurement cell from the forward beam is paired with a nearby aft beam cell if the (cell center-to-center) surface distance between the two cells is less than a given separation-distance tolerance. (Of course, only sensor data from one satellite pass at a time is considered in this pairing procedure as well as in the binning scheme above: data taken over the same region, but from different orbits, are not matched together.) A single (multiply-aliased) wind solution is then computed based upon this pair of measurements. There are two distance tolerances: 37 km is used for the single-sided double-density instrument modes 3 through 8 (see Table 3-4), while 50 km is used for the double-sided, single-density modes 1 and 2. A discussion of the tradeoff study and rationale behind the choice of these particular pairing maximum-distance criteria for GDR data production is given in Section IV.B of [13].

It is important to be aware of the partial redundancy of data-usage inherent in this cell pairing mechanism: a single given aft cell (primary swath) can be paired with up to six distinct forward cells, or vice versa with a single forward cell. The resulting set of up to six wind solutions, whose mutual separation distances would be less than either 37 or 50 km (depending on the mode), can be considered to be essentially independent scatterometer-derived wind

measurements taken at slightly different surface locations. (It could certainly be argued, however, that such a set of solutions might not be as "independent" as a similar set derived from pairs of $\sigma°$ measurements with no common members.) The number of such solutions evolving from a set of $\sigma°$ pairs sharing a common element ranges from one to six -- with two and three occurring most frequently, and six only rarely -- depending on local inter-cell distances for both forward and aft beams. These distances in turn are functions of location in orbit, incidence angle, and swath side (see Subsection 3.4.3.6). A more detailed discussion of the GDR cell-pairing algorithm component is given in Subsection 7.2.

7.1.2.2 Rationale for Choice of Cell Pairing for Data-Grouping Technique. The use of fore-and-aft pairs of $\sigma°$ measurements as the standard grouping technique for all SASS GDR wind solutions was recommended in an unpublished 1979 LaRC memorandum (L.C. Schroeder), and agreed upon by the SASS Evaluation Task Group at a February 1980 meeting in Boulder, Colorado. This choice was motivated primarily by the following considerations:

(1) Evaluation of SASS performance in important high-gradient situations such as hurricanes and storms was found to be aided by high-resolution data (see First Storms Mini-Workshop Report [14]). The cell-pairing mode clearly generates maximum resolution solutions. (Mixed-mode grouping; i.e., pairing at certain mission epochs -- such as at storm times -- and binning at other times, was determined not to be a viable option for GDR production because of time and fiscal constraints.)

(2) The implementation of the SASS supplemental geophysical record (see Section 8) was significantly simplified by the pairing-mode choice, since pairing always yields a constant number of sensor data elements (two) per solution, whereas binning yields a variable -- and unpredictable -- number. Due to time constraints, such a record would not have been generated and put on the GDR tapes had binning been chosen.

(3) The model function (see Subsection 7.3) was considered to be still under development, and SASS/surface-truth wind data sets were expected to be used in future comparison and model-upgrade efforts. Access to the highest possible resolution SASS-derived winds was strongly preferred for such work.

7.1.2.3 Solution Spatial Patterns Resulting From GDR Cell-Pairing. As a result of the pairing option and the manner in which a single $\sigma°$ measurement can enter into the generation of more than one solution, GDR winds often fall into spatial patterns that are typical -- and therefore recognizable -- for given instrument modes. Solutions resulting from the dual-polarization (V and H), double-density modes 3 and 4 commonly occur in a tightly clustered group of three (with the individual solutions in the cluster sometimes located just a few kilometers apart); where the first member of the triple derives from the measurement-pair type $\{(\sigma°_V)_{fore}, (\sigma°_V)_{aft}\}$, the last from the pair $\{(\sigma°_H)_{fore}, (\sigma°_H)_{aft}\}$, and the middle from either $\{(\sigma°_V)_{fore}, (\sigma°_H)_{aft}\}$ or $\{(\sigma°_H)_{fore}, (\sigma°_V)_{aft}\}$. The three solution locations are generally aligned approximately parallel to the spacecraft groundtrack, and the ordering implied here is with respect to the direction of flight. For the single-polarized, double-density measurement modes 5,6,7, and 8, solutions again often occur as closely grouped triples, except that they now derive from like-polarized (either V or H) $\sigma°$ pairs. For the single-polarization, single-density modes 1 and 2, GDR solutions typically do not occur in a repeating cluster pattern as they tend to be more locally isolated.

As with the binning option, the time, location, and incidence angle of a wind solution derived from cell pairing are defined in terms of the midpoint (centroid) of the corresponding sensor data parameters; e.g., $\theta_I(\text{solution}) \equiv [\theta_I(\sigma°_1) + \theta_I(\sigma°_2)]/2$ for the measurement pair $(\sigma°_1, \sigma°_2)$. This means that a GDR solution time-tag can range from being a few seconds to as much as nearly two minutes removed from the actual times that the two participating $\sigma°$ measurements were taken since such measurements can occur up to four minutes apart (see Subsection 3.4.3.1).

7.1.2.4 Nadir Solution Binning. Nadir-swath solutions (speed only) are derived from Doppler cells 14 and 15 (see Subsection 3.4.3.5) and, independent of the primary-swath grouping choice, are always generated from binned data. GDR nadir solutions result from .5° latitude/longitude bins -- a choice yielding nadir-solution resolution that is consistent with the average primary-swath resolution resulting from pairing. Nadir solutions therefore result from bins containing one

two, or more $\sigma°$ measurements from one, two, or more antenna beams (orthogonality not necessary) in an unpredictable manner. (A solution with $\theta_I \gtrsim 0°$ can result from a bin containing Doppler cell-15 measurements taken from opposite-sided beams (e.g., beams 1 and 4) since such data is sometimes nearly co-located.) Because of the variable number of $\sigma°$'s contained in nadir bins, some of the information contained in the GDR supplemental geophysical records pertaining to nadir solutions is meaningless (see Section 8). Nadir-swath Doppler cell 13 ($\theta_I \approx 8°$) is not processed in the GDR wind algorithm.

7.1.3 Sensor Data Prefiltering for Geophysical Processing

The geophysical algorithm must screen out sensor data that would yield obviously erroneous wind solutions. The scatterometer sensor algorithms generate a considerable number of flags for each minor frame of data that, taken together, provide for the continuing evaluation of overall instrument health and status, and current data quality (see Section 3 of [3]). Not all $\sigma°$ data quality attributes covered by these flags are such that an "on" flag condition (denoting a potential problem) is sufficient reason to rule out the use of the associated $\sigma°$ in the computation of wind solutions. Both nadir- and primary-swath wind solutions are therefore computed, or not computed, on the basis of a nine-flag subset of the total set of flags contained in a GDR sensor frame record. If any one or more of these nine flags is on, the corresponding $\sigma°$ measurement is rejected from consideration for wind computation. In addition, wind solutions are not derived from a particular $\sigma°$ if any of several other circumstances occur; e.g., $\sigma°$'s are not used if they have been designated as anything other than "all ocean" in the TOILing process described in Subsection 6.2. All flag-settings/conditions under which $\sigma°$'s are rejected from further geophysical processing are described in Subsection 9.8. This screening process occurs during the first-stage pairing/binning component of the processing.

7.2 CELL PAIRING ALGORITHM

The SASS cell pairing/grouping component of the geophysical processor (ADF subroutine-level algorithms SS.IG.G-10.00/4/D and SS.IG.G-10.01/4/C) performs the functions of (computer storage) buffering and grouping measurements from individual SASS Doppler cells, and passing selected measurement groups on to the wind vector estimation routines. Algorithm SS.IG.G-10.00/4/D (G-10.00) performs

data validation (including prefiltering -- see Subsection 7.1.3), buffer management, and pointer setup. When buffer space is needed, a pointer (indicator) is passed to SS.IG.G-10.01/4/C (G-10.00), which then selects the appropriate measurements to be grouped with the one indicated by the pointer, reformats the group of measurements to be compatible with the wind estimation routines, and calls the latter.

7.2.1 Data Buffering

Data buffering is fairly tightly optimized, taking advantage of knowledge of the SASS measurement pattern. Since fore-beam data must be buffered until corresponding aft-beam data become available, the buffering is non-symmetrical: the buffering is controlled by the arrival of fore-beam data only. Buffers have (conceptually) a trapezoidal shape. In modes 1 and 2 (single-density, double-sided) there are buffers that can contain from 12 cell-1 measurements to 39 cell-12 measurements for each forward beam. In other modes the buffers can contain twice as many measurements for a given cell, but for one side only. This is estimated to be the largest number of buffers needed for the various modes for the maximal case of all possible data being present and of acceptable quality. In this case, matching aft-beam data becomes available just before a fore-beam buffer needs to be re-used. A little extra memory space is available to allow the binning mode of data grouping to be invoked. Buffers for aft-beam data have the same characteristics as for fore-beam data, but provide more space than is actually needed since aft measurements do not need to be kept in buffers for very long (in terms of spacecraft ground-track time).

7.2.2 Pair Pointer Setup

Algorithm G-10.00 performs all buffer management and pointer setup operations. In the cell-pairing mode, each incoming aft-beam measurement is compared with the fore-beam measurements currently in the buffer for the same side. To save time, only the subset of fore-beam measurements that could potentially yield pairs is examined; e.g., aft-cell 1 is not compared with fore-cells 8-12, since they could never yield a pair match within a reasonable distance. Every fore cell located within the pre-set distance tolerance of 37 km (modes 3 through 8) or 50 km (modes 1 and 2) of the aft cell is entered into a list, together with the separation miss distance. For this purpose, distances are

defined cell center to cell center. After all fore cells have been checked, the list members are sorted according to increasing distance from the given aft cell. Two-way pointers are then established between the buffer containing the aft measurement and the buffer containing each fore measurement in the sorted list, subject to the following conditions:

(1) If a fore measurement already has pointers to six aft measurements, no new pointers are established.

(2) No more than six pointers are established for each aft measurement.

(3) Pointers are established in order of increasing distance.

(4) No pointers are established for pairs beyond the distance tolerance (37 or 50 km).

(5) No pointers are established when operating in the binning mode.

Because of restriction (1), above, the algorithm would quite often be unable to select the best (i.e., closest) pairs if the distance tolerances were set much higher than the chosen values of 50 km for modes 1 and 2, and 37 km for the other modes. If no pointers are established for an aft measurement, a cell- and beam-dependent counter is incremented. Separate counters are used for record-keeping corresponding to restrictions (1) and (4). (In the summary printout that appears at the end of each geophysical processor computer "run" hardcopy, these counters are printed with the labels "aft - no room" and "aft - no match," respectively.) If significant numbers of aft-cell measurements were lost because of restriction (1), it would be an indication that the distance tolerances had been chosen too large; if lost because of restriction (4), it would be an indication that they are too small, except for the large number of measurements from cell 1 and cells 7-12 that are routinely lost due to lack of fore- and aft-beam overlap coverage (particularly near the equator -- see Subsection 3.4.3), and for all cells associated with processor start-up after a data gap or a large land mass. See section IV.B of [13] for further considerations in the choice of the pairing-distance tolerances.

When the buffer management logic indicates that a forward-beam buffer space needs to be re-used, a pointer to that space is passed to algorithm G-10.01, and the measurement contained in that space is grouped as appropriate and passed

on to the wind retrieval algorithms. All pointers to that space are then cleared, and the space is re-used.

7.2.3 Pair Generation

Except for the restrictions discussed in Subsection 7.2.2, the actual selection of measurements to be grouped is done by algorithm G-10.01. G-10.01 can operate in either the pairing or binning mode. In the pairing mode, operation is as follows:

(1) The fore measurement indicated by G-10.00 is selected.

(2) Distances from the selected fore measurement to up to six aft measurements, indicated by pointers, are calculated and entered into a list.

(3) The list is sorted by distance.

(4) The nearest aft measurement is paired with the fore measurement and passed on to the wind estimation routines.

(5) The remaining aft measurements are examined: if the fore measurement currently being processed is the nearest fore measurement to an aft measurement, the pair is passed on for wind processing.

Note that this has the following effects:

(1) Every fore measurement is paired with at least one aft measurement, if there is a candidate within the distance tolerance. The first aft measurement selected will always be the nearest one to the fore measurement.

(2) Every aft measurement is paired with at least one fore measurement, if there is one located within the distance tolerance, noting restriction (1) in Subsection 7.2.2.

(3) An aft measurement may be paired with several fore measurements in addition to the nearest. This can happen because the aft measurement is the best match for each of several fore measurements.

7.2.4 Binning (Nadir)

Nadir cells 14 and 15 are processed independently, using a single circular buffer with space for containing 42 measurements. No distinction is made between fore and aft, or instrument mode. Nadir cells are always processed in the binning mode; the GDR production bin size chosen is .5°. Cell 13 is never processed.

When operating in the binning mode (primary or nadir swath), all pointer setup (with associated restrictions) is bypassed. When G-10.00 must re-use a fore-buffer space, a pointer to that space is passed to G-10.01. A bin identifier is calculated as a pair of integers obtained by dividing the fore-measurement latitude and longitude by the bin size, and truncating any fractional part. All fore and aft buffers are then searched for measurements having the same bin identifier. All such measurements are then grouped together and processed. The buffer spaces they occupied are then marked available for re-use.

7.2.5 Time Tolerance Control for Pairing

An adjustable processor parameter array (TTOL) allows for the designation of a set of time difference tolerances, with a distinct value possible for each cell number. If a fore measurement and an aft measurement differ in time by more than the tolerance value corresponding to the cell number, the measurements are not candidates for pairing. This prevents measurements from separate orbits from being paired together in the event that a large data gap prevented the older measurement from being overwritten with more recent data. The array values currently in use range from 100 seconds for cell 1 to 320 seconds for cell 12. One array value (TTOL(12)) is also used as a time-regression threshold. If a time gap or regression larger than this occurs, all data currently in buffers are processed to the extent possible; the program is then re-initialized.

7.2.6 Mode Change Processing

In the event of a mode change, special processing is required (unless the only effect of the change is a change in polarization). If the change is from mode 1 or 2 (both sides active) to mode 3-8 (one side active), previous data from the newly inactive side is processed to the extent possible, since no further pair matches will occur (if the mode switches back after less than about 4 minutes,

some potential matches will be lost). This purging of the old-mode data is required since the new mode will generate twice as many measurements per unit time on the single active side, and buffer space must be re-allocated accordingly. The same action is taken if the mode change is from one side active to another side active.

If the change is from one side active to both sides active, more complicated action is required. For a short time (about 4 minutes), more fore measurements may have to be held than there is space available for them. This problem is most severe when the incoming data is complete (no gaps) and clean (no data dropped in screening/validation routine), for then the buffers are nearly full of not-yet-matched data. This situation is handled as follows:

(1) Data too old for further pairing is processed and purged.

(2) If the previous mode had both (V and H) polarizations active, data with polarization opposite to the current mode is deleted.

(3) If the previous mode had only one polarization active, adjacent fore measurements for a given cell are averaged together in pairs, producing a 2:1 space reduction. Candidate pairs separated in time by more than a tolerance of 3.9 seconds are not averaged together.

(4) Deletion or averaging of points is done only to the extent required to produce needed buffer space. When the required space is available, the buffers are compressed and switched to a both-sides mode. These procedures result in a small amount of data having resolution "degraded" so that it becomes equivalent to the normal resolution for modes 1 and 2.

7.3 SASS1 GEOPHYSICAL MODEL FUNCTION

7.3.1 Introduction to Model Relationship

The fundamental assumption employed to establish a usable relationship between the speed and direction of surface wind and the backscatter signal is that the latter can be expressed as a function of only four variables: the ocean-surface wind magnitude U, the incidence angle of the radar at the sea surface θ_I,

the wind direction relative to the azimuthal pointing direction of the radar beam χ, and the polarization type -- V or H -- of the incident radiation ε:

$$\sigma^\circ = f(U, \theta_I, \chi, \varepsilon) \tag{7-1}$$

The extent to which this assumption is true remains a matter of some debate and will surely continue to be a topic of ongoing research. Important work in ocean backscatter modeling and its application to (Seasat) surface wind vector retrieval is reported in [31,34,35,52].

In the meantime, a relatively simple form of (7-1) has been used for the geophysical processing of Seasat scatterometer data. If the normalized radar cross section σ° is expressed in logarithmic bel units and the logarithm of the wind speed (in m/s) is used, the dependence assumed has the form

$$\sigma^\circ = G(\theta_I, \chi, \varepsilon) + H(\theta_I, \chi, \varepsilon) \log_{10} U \tag{7-2}$$

where G and H are given by stored coefficient tables for V and H polarizations and incremental values of incidence and relative azimuth angles (see Subsection 7.1.1). The coefficients in the so-called G and H tables are tabulated for incidence angles θ_I from 0° to 70° in 2° steps and for relative azimuth angles χ from 0° to 180° in 10° steps.

7.3.2 Definition of Model Function Variables θ_I and χ

The incidence angle θ_I and the relative azimuth angle χ as used in Eq. (7-2) and elsewhere in this document are defined at the Earth surface location; i.e., at the Doppler resolution cell center point (see Figure 3-4 or the point P in Figures 6-1 or 6-3), of a particular σ° measurement. Thus, these model variables are defined out at the measurement location within the antenna illumination region and not, for example, at the spacecraft subsatellite nadir point. θ_I is therefore the acute angle formed between the radar incident vector for the given Doppler cell (determined as the current look direction from the antenna to that cell -- see Subsection 4.4.2.7) and the local surface vertical defined at the measurement location -- see Figure 3-3. For the SASS configuration θ_I ranges from 0° (nadir-looking) to a nominal maximum of less than 70° at the outer edge of a swath.

The relative wind azimuth angle χ (sometimes called the aspect angle) is defined as the wind direction relative to the radar azimuthal clock angle ϕ measured from the north, and measured at the σ° measurement site. The radar azimuth clock angle ϕ defined at the measurement location is, in general, not the same as the radar azimuth clock angle K described in Subsections 3.4.1 and 4.4.2.7, which is defined to be measured from the north at the subsatellite point. The spherical triangle diagram below -- representing a region on the face of the oblate Earth -- illustrates the two clock angles and the difference between them for a footprint location that is east of the subsatellite point: the lines of longitude with respect to which each angle is measured are parallel only at the equator.

Unfortunately, the nadir-relative azimuths K computed by the IDPS and supplied on the MSDR files (see Subsection 4.4.3) were erroneously used as arguments to the model function during the actual geophysical processing that generated the GDR wind solution data set. The net effect of incorrectly using K instead of ϕ for the wind inversion process has been analyzed in detail and is discussed at length in Subsection 9.2, where solution direction correction tables are supplied. Because of the relatively small effect, it will probably not be necessary to apply such corrections to the GDR data for most purposes.

For present purposes and throughout this document, the wind direction γ is defined with the meteorological convention; i.e., γ is in the "out-of" sense and is measured clockwise from the north in the range $0° \le \gamma \le 360°$. Thus,

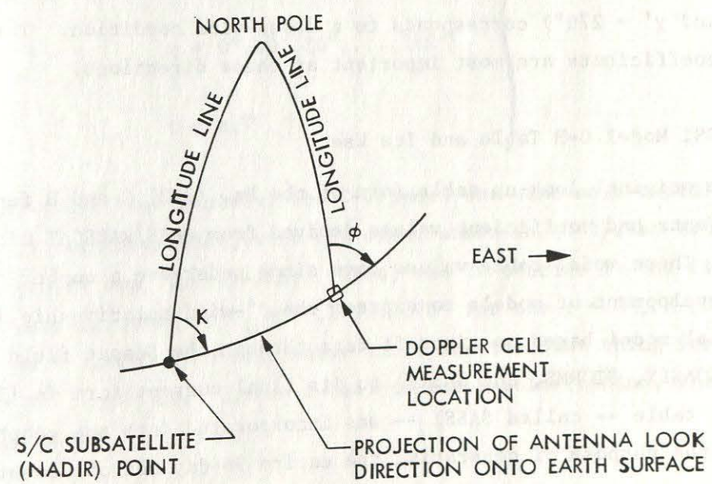

if $\gamma = 45°$, the wind is blowing out of the northeast. The functions G and H and $\sigma°$ itself in Eq. (7-2) are assumed to be dependent upon the wind direction γ and the scatterometer azimuth look angle ϕ only through the difference $\chi' = \gamma - \phi$ over the entire 0° - 360° range of both γ and ϕ [36]. In addition, G and H are assumed to be even functions of χ' about $\chi' = 0°$ and to vary harmonically with maxima occurring at $\chi' = 0°$ and $\chi' = 180°$ and minima occurring at $\chi' = 90°$ and $\chi' = 270°$ [32]. The azimuthal dependence of the functions and $\sigma°$ itself can therefore be expressed over the complete range of wind and antenna look directions by the wind relative azimuth direction χ defined as

$$\left.\begin{aligned} \chi &= \gamma - \phi, && \text{for } 0° \le \gamma - \phi < 180° \\ \chi &= 360° - (\gamma - \phi), && \text{for } 180° \le \gamma - \phi < 360° \end{aligned}\right\} \qquad (7\text{-}3)$$

(If $\gamma - \phi$ is negative, 360° is added before operation (7-3) is performed.) The relative wind direction χ that results from Eq. (7-3) has an operational range of $0° \le \chi \le 180°$: it is this parameter that is the independent variable in the model relationship (7-2). Correspondingly, the table representation (see Table 7-1) of the G and H functions in Eq. (7-2) was constructed for use in geophysical processing as a function of χ over the half-interval $0° \le \chi \le 180°$. Note that (1) $\chi = 0°$ corresponds to an "upwind" condition, i.e., the antenna look direction is directly "into" the wind; (2) $\chi = 180°$ corresponds to a "downwind" condition, i.e., the antenna is pointing in the same direction that the wind is blowing; and (3) $\chi = 90°$ (and $\chi' = 270°$) corresponds to a cross-wind condition. The values of the table coefficients are most important at these directions.

7.3.3 SASS1 Model G-H Table and Its Use

The original look-up table form of the Eq. (7-2) G and H functions developed by Wentz had coefficient values derived from AAFE/RADSCAT aircraft $\sigma°$ measurements. These model table values have since undergone a number of refinements: the development of models to express the $\sigma°$-wind relationship is traced from the initial model based on aircraft data through the Seasat field validation experiments (GOASEX, STORMS, and JASIN) to its final current form in [32]. This last G-H model table -- called SASS1 -- was incorporated into the geophysical processor for the purpose of generating the entire 96-day set of Seasat GDR wind

solutions. The SASS1 model function is a composite of several models that were developed before and immediately after the JASIN workshop [13,37]; its assessment can be found in [13,32,38]. A description of the synthesis of SASS1 from its immediate progenitors and an outline of their origination are contained in [39].

The form (7-2) evidently yields a three-parameter family of straight lines in log $\sigma°$ - log U coordinates with slopes equal to $H(\theta_I,\chi,\varepsilon)$ and $\sigma°$ intercepts corresponding to unit wind speed given by $G(\theta_I,\chi,\varepsilon)$. As noted in Subsection 7.3.2, θ_I and χ need only vary from 0° to 70° and 0° to 180°, respectively, for operational use of the model function. The G-H table coefficients corresponding to Eq. (7-2) are therefore tabulated at nineteen 10°-increment (0°,10°,...,180°) χ values and at thirty-six 2°-increment θ_I values for each of the two polarizations; the resulting G and H tables together total 2736 tabular values.

The SASS1 model G-H table coefficients are given in Table 7-1. The complete array of numbers is a function of θ_I, χ, the polarization index ε, and the G-H table index (= G or H). As used with Eq. (7-2), the assumed units in the table are degrees for the angles, m/s for the 19.5 neutral stability wind speed U, and bels (10 decibels) for the backscatter coefficient $\sigma°$. The tabular values of the four table index parameters are:

$$\left.\begin{aligned} \theta_I &= 0°,2°,4°,\ldots,70° \\ \text{G-H} &= \text{G,H} \\ \chi &= 0°,10°,20°,\ldots,180° \\ \varepsilon &= \text{H,V} \end{aligned}\right\} \qquad (7\text{-}4)$$

The θ_I index varies most rapidly, the G-H index the next most rapidly, χ next, and the H or V indicator last, with the order shown in (7-4), as Table 7-1 is read left-to-right and line-by-line. Thus, the 36 entries in the first three lines correspond in order to $\theta_I = 0°,2°,\ldots,70°$ for the $\chi = 0°$, H-polarization portion of the G table. The next three lines are the same thing for the H table. The first half of the table (lines 1-114) is for H-polarization, the second half for V-polarization.

Table 7-1. SASS1 G-H Table

```
MODELDECKS(1).SASS1-MAY9
 1    1.710 1.689 1.626 1.387 1.076  .778  .474  .126 -.250 -.636-1.016-1.371 }G
 2   -1.686-1.943-2.182-2.423-2.665-2.904-3.139-3.368-3.588-3.797-3.994-4.176 }
 3   -4.341-4.487-4.612-4.713-4.782-4.825-4.857-4.882-4.904-4.923-4.939-4.952 } x=0°
 4    -.576 -.565 -.533 -.390 -.204 -.033  .134  .330  .542  .756  .956 1.130 }H
 5    1.264 1.343 1.409 1.483 1.564 1.649 1.735 1.823 1.908 1.990 2.066 2.135 }
 6    2.193 2.241 2.275 2.293 2.296 2.296 2.296 2.296 2.296 2.296 2.296 2.296 }
 7    1.710 1.689 1.626 1.388 1.078  .780  .476  .126 -.253 -.642-1.025-1.384 }G
 8   -1.701-1.959-2.198-2.439-2.679-2.917-3.151-3.378-3.596-3.805-4.002-4.184 }
 9   -4.349-4.495-4.619-4.721-4.790-4.833-4.865-4.891-4.912-4.928-4.939-4.945 } x=10°
10    -.576 -.566 -.534 -.391 -.207 -.038  .129  .326  .539  .754  .957 1.133 }H
11    1.268 1.348 1.415 1.490 1.570 1.655 1.741 1.827 1.912 1.994 2.070 2.138 }
12    2.197 2.244 2.278 2.296 2.299 2.300 2.300 2.300 2.300 2.300 2.300 2.300 }
13    1.710 1.689 1.627 1.390 1.082  .785  .481  .126 -.261 -.661-1.054-1.422
14   -1.746-2.006-2.246-2.487-2.725-2.960-3.190-3.413-3.626-3.834-4.030-4.210
15   -4.373-4.517-4.640-4.740-4.807-4.850-4.881-4.906-4.926-4.941-4.951-4.956
16    -.576 -.566 -.537 -.397 -.218 -.052  .110  .308  .525  .747  .957 1.141
17    1.281 1.363 1.433 1.509 1.590 1.674 1.759 1.844 1.926 2.008 2.083 2.150
18    2.208 2.254 2.286 2.303 2.306 2.306 2.305 2.305 2.303 2.303 2.303 2.303
19    1.710 1.690 1.627 1.392 1.085  .790  .484  .121 -.278 -.692-1.100-1.481
20   -1.815-2.080-2.324-2.566-2.805-3.038-3.265-3.484-3.693-3.897-4.088-4.264
21   -4.422-4.561-4.678-4.772-4.834-4.873-4.900-4.920-4.935-4.945-4.950-4.950
22    -.576 -.567 -.539 -.403 -.228 -.068  .091  .290  .513  .742  .961 1.153
23    1.300 1.386 1.462 1.542 1.624 1.708 1.793 1.876 1.957 2.036 2.109 2.174
24    2.229 2.273 2.302 2.316 2.316 2.314 2.311 2.308 2.303 2.303 2.303 2.303
25    1.710 1.690 1.628 1.393 1.087  .792  .483  .111 -.302 -.732-1.157-1.554
26   -1.900-2.173-2.427-2.675-2.918-3.154-3.382-3.601-3.809-4.007-4.192-4.360
27   -4.512-4.643-4.753-4.840-4.895-4.928-4.950-4.963-4.970-4.971-4.966-4.955
28    -.576 -.568 -.542 -.409 -.238 -.083  .073  .274  .502  .739  .966 1.167
29    1.322 1.414 1.499 1.585 1.671 1.758 1.844 1.927 2.008 2.084 2.154 2.217
30    2.269 2.309 2.336 2.346 2.343 2.338 2.332 2.325 2.317 2.317 2.317 2.317
31    1.710 1.690 1.628 1.394 1.088  .791  .479  .098 -.328 -.774-1.215-1.629
32   -1.990-2.274-2.543-2.804-3.056-3.300-3.535-3.759-3.971-4.166-4.348-4.513
33   -4.660-4.788-4.894-4.977-5.029-5.058-5.078-5.089-5.094-5.093-5.086-5.073
34    -.576 -.568 -.543 -.413 -.245 -.092  .063  .266  .498  .741  .975 1.183
35    1.346 1.445 1.540 1.635 1.728 1.819 1.909 1.995 2.077 2.153 2.222 2.283
36    2.334 2.374 2.401 2.412 2.409 2.402 2.395 2.386 2.377 2.377 2.377 2.377
37    1.710 1.690 1.628 1.394 1.088  .790  .474  .085 -.352 -.812-1.269-1.697
38   -2.073-2.370-2.657-2.934-3.201-3.458-3.703-3.936-4.156-4.357-4.542-4.711
39   -4.862-4.994-5.105-5.193-5.248-5.281-5.306-5.324-5.335-5.339-5.336-5.326
40    -.576 -.569 -.545 -.417 -.251 -.099  .055  .259  .494  .742  .982 1.197
41    1.367 1.473 1.580 1.684 1.786 1.885 1.980 2.070 2.156 2.234 2.305 2.369
42    2.423 2.467 2.499 2.517 2.519 2.514 2.510 2.505 2.499 2.499 2.499 2.499
43    1.710 1.690 1.628 1.394 1.088  .789  .472  .077 -.368 -.839-1.309-1.751
44   -2.139-2.447-2.752-3.045-3.327-3.596-3.853-4.096-4.326-4.536-4.731-4.910
45   -5.071-5.213-5.337-5.439-5.505-5.547-5.585-5.617-5.644-5.666-5.683-5.695
46    -.576 -.569 -.546 -.419 -.256 -.106  .046  .251  .489  .741  .987 1.207
47    1.383 1.494 1.612 1.726 1.836 1.941 2.042 2.138 2.228 2.310 2.386 2.455
48    2.515 2.567 2.608 2.639 2.649 2.649 2.652 2.655 2.658 2.658 2.658 2.658
49    1.710 1.690 1.628 1.395 1.088  .789  .471  .073 -.378 -.856-1.333-1.783
50   -2.180-2.496-2.812-3.117-3.408-3.687-3.951-4.202-4.438-4.658-4.861-5.049
51   -5.219-5.372-5.507-5.622-5.699-5.750-5.800-5.846-5.888-5.926-5.960-5.990
52    -.576 -.569 -.547 -.422 -.260 -.112  .039  .244  .484  .738  .987 1.212
53    1.392 1.508 1.632 1.752 1.868 1.978 2.082 2.182 2.275 2.361 2.441 2.514
54    2.580 2.638 2.689 2.730 2.748 2.753 2.762 2.772 2.784 2.784 2.784 2.784
55    1.710 1.690 1.628 1.395 1.089  .790  .472  .073 -.381 -.861-1.341-1.795
56   -2.194-2.512-2.832-3.140-3.435-3.716-3.984-4.236-4.474-4.697-4.903-5.094
57   -5.267-5.423-5.562-5.682-5.762-5.816-5.870-5.921-5.968-6.011-6.050-6.085
58    -.576 -.569 -.548 -.423 -.262 -.115  .035  .240  .481  .736  .987 1.213
59    1.395 1.512 1.639 1.761 1.878 1.989 2.095 2.196 2.290 2.378 2.459 2.534
60    2.601 2.662 2.715 2.760 2.781 2.787 2.798 2.811 2.826 2.826 2.826 2.826
61    1.710 1.690 1.628 1.395 1.088  .789  .471  .073 -.379 -.857-1.335-1.785
62   -2.182-2.498-2.815-3.120-3.413-3.692-3.958-4.209-4.446-4.667-4.873-5.062
63   -5.234-5.389-5.526-5.644-5.722-5.776-5.828-5.877-5.922-5.963-6.000-6.033
```


Table 7-1. SASS1 G-H Table (contd)

```
64    -.576 -.569 -.547 -.422 -.259 -.112  .039  .244  .484  .739  .988 1.213
65    1.393 1.509 1.634 1.754 1.870 1.980 2.085 2.185 2.278 2.366 2.446 2.520
66    2.587 2.646 2.697 2.741 2.760 2.766 2.776 2.788 2.801 2.801 2.801 2.801
67    1.710 1.690 1.628 1.394 1.088  .788  .471  .076 -.371 -.844-1.316-1.760
68   -2.150-2.460-2.771-3.070-3.358-3.634-3.897-4.146-4.381-4.603-4.808-4.997
69   -5.169-5.323-5.459-5.575-5.654-5.708-5.760-5.809-5.852-5.889-5.920-5.945
70    -.576 -.569 -.546 -.420 -.256 -.106  .046  .251  .489  .742  .988 1.210
71    1.387 1.500 1.620 1.737 1.850 1.958 2.061 2.160 2.252 2.339 2.419 2.493
72    2.558 2.616 2.665 2.705 2.724 2.731 2.740 2.752 2.764 2.764 2.764 2.764
73    1.710 1.690 1.628 1.394 1.087  .788  .471  .079 -.362 -.827-1.289-1.724
74   -2.106-2.409-2.712-3.005-3.289-3.561-3.822-4.071-4.306-4.528-4.736-4.927
75   -5.100-5.256-5.392-5.509-5.590-5.649-5.704-5.755-5.800-5.839-5.872-5.899
76    -.576 -.569 -.545 -.417 -.251 -.100  .055  .261  .498  .748  .991 1.209
77    1.381 1.489 1.604 1.716 1.825 1.931 2.033 2.131 2.223 2.310 2.390 2.463
78    2.528 2.585 2.632 2.671 2.689 2.698 2.709 2.722 2.734 2.734 2.734 2.734
79    1.710 1.690 1.628 1.393 1.087  .789  .473  .085 -.349 -.806-1.259-1.684
80   -2.057-2.352-2.647-2.935-3.215-3.486-3.746-3.994-4.230-4.453-4.660-4.852
81   -5.026-5.181-5.317-5.432-5.515-5.577-5.634-5.685-5.730-5.769-5.802-5.829
82    -.576 -.568 -.544 -.413 -.245 -.092  .065  .271  .508  .756  .996 1.209
83    1.376 1.478 1.587 1.695 1.801 1.905 2.006 2.102 2.194 2.280 2.360 2.432
84    2.495 2.550 2.595 2.629 2.647 2.658 2.669 2.682 2.694 2.694 2.694 2.694
85    1.710 1.690 1.628 1.392 1.085  .787  .471  .088 -.339 -.786-1.229-1.645
86   -2.009-2.298-2.585-2.867-3.143-3.411-3.670-3.918-4.153-4.373-4.578-4.766
87   -4.936-5.088-5.219-5.329-5.409-5.471-5.525-5.573-5.613-5.645-5.669-5.685
88    -.576 -.568 -.542 -.408 -.237 -.079  .082  .289  .524  .768 1.003 1.211
89    1.372 1.469 1.571 1.675 1.778 1.880 1.979 2.075 2.165 2.250 2.327 2.396
90    2.456 2.507 2.546 2.574 2.588 2.599 2.609 2.619 2.627 2.627 2.627 2.627
91    1.710 1.690 1.627 1.391 1.082  .781  .463  .083 -.338 -.776-1.208-1.613
92   -1.968-2.250-2.530-2.806-3.077-3.342-3.597-3.843-4.076-4.291-4.491-4.675
93   -4.840-4.986-5.112-5.214-5.291-5.350-5.401-5.442-5.475-5.500-5.517-5.526
94    -.576 -.567 -.539 -.403 -.226 -.063  .104  .313  .546  .785 1.014 1.215
95    1.370 1.462 1.559 1.658 1.758 1.857 1.954 2.048 2.137 2.218 2.292 2.358
96    2.414 2.459 2.492 2.512 2.522 2.532 2.540 2.546 2.550 2.550 2.550 2.550
97    1.710 1.689 1.626 1.389 1.076  .773  .451  .072 -.343 -.773-1.196-1.591
98   -1.937-2.213-2.486-2.756-3.022-3.282-3.533-3.774-4.004-4.217-4.414-4.595
99   -4.758-4.901-5.022-5.120-5.195-5.255-5.303-5.341-5.370-5.390-5.401-5.403
100   -.576 -.566 -.536 -.396 -.213 -.044  .131  .342  .572  .806 1.027 1.220
101   1.369 1.457 1.549 1.644 1.741 1.837 1.932 2.023 2.110 2.190 2.261 2.325
102   2.378 2.419 2.448 2.462 2.469 2.479 2.486 2.490 2.490 2.490 2.490 2.490
103   1.710 1.689 1.626 1.386 1.071  .764  .440  .062 -.349 -.773-1.190-1.578
104  -1.918-2.189-2.458-2.723-2.985-3.240-3.488-3.726-3.952-4.164-4.361-4.542
105  -4.705-4.847-4.968-5.066-5.141-5.202-5.251-5.290-5.318-5.335-5.341-5.336
106   -.576 -.566 -.534 -.390 -.203 -.027  .154  .366  .594  .823 1.039 1.226
107   1.369 1.454 1.543 1.636 1.730 1.824 1.916 2.006 2.091 2.169 2.240 2.303
108   2.354 2.394 2.421 2.432 2.439 2.450 2.457 2.460 2.460 2.460 2.460 2.460
109   1.710 1.689 1.625 1.385 1.069  .761  .434  .056 -.354 -.775-1.188-1.574
110  -1.911-2.181-2.448-2.712-2.971-3.225-3.471-3.708-3.933-4.145-4.343-4.524
111  -4.687-4.830-4.951-5.049-5.125-5.187-5.237-5.276-5.305-5.324-5.333-5.332
112   -.576 -.565 -.533 -.388 -.199 -.020  .163  .375  .602  .830 1.043 1.227
113   1.369 1.453 1.541 1.633 1.725 1.819 1.910 1.999 2.084 2.162 2.233 2.295
114   2.347 2.386 2.412 2.423 2.430 2.441 2.448 2.452 2.452 2.452 2.452 2.452
115   1.710 1.688 1.619 1.365 1.036  .731  .429  .083 -.291 -.674-1.049-1.399
116  -1.707-1.955-2.172-2.367-2.541-2.696-2.833-2.953-3.057-3.145-3.220-3.283
117  -3.341-3.392-3.439-3.460-3.509-3.526-3.539-3.549-3.560-3.572-3.585-3.599
118   -.576 -.565 -.528 -.373 -.174  .004  .173  .368  .576  .786  .985 1.161
119   1.303 1.398 1.473 1.536 1.589 1.632 1.665 1.690 1.708 1.719 1.723 1.724
120   1.724 1.724 1.724 1.724 1.724 1.724 1.724 1.724 1.724 1.724 1.724 1.724
121   1.710 1.688 1.620 1.369 1.042  .740  .440  .092 -.285 -.673-1.054-1.409
122  -1.721-1.971-2.189-2.385-2.560-2.716-2.852-2.972-3.075-3.163-3.237-3.300
123  -3.357-3.408-3.454-3.494-3.524-3.540-3.552-3.563-3.573-3.582-3.590-3.597
124   -.576 -.565 -.530 -.378 -.182 -.009  .156  .351  .562  .776  .981 1.163
125   1.308 1.404 1.480 1.545 1.598 1.642 1.676 1.702 1.719 1.730 1.735 1.735
126   1.735 1.735 1.735 1.735 1.734 1.734 1.734 1.734 1.733 1.733 1.733 1.733
127   1.710 1.688 1.623 1.375 1.056  .760  .463  .111 -.276 -.678-1.073-1.442
128  -1.764-2.019-2.241-2.440-2.617-2.774-2.911-3.031-3.133-3.220-3.292-3.353
```

H-POLARIZATION

V-POLARIZATION

Table 7-1. SASS1 G-H Table (contd)

129	-3.409	-3.459	-3.503	-3.541	-3.569	-3.583	-3.593	-3.601	-3.610	-3.620	-3.631	-3.643	
130	-.576	-.565	-.534	-.388	-.201	-.037	.121	.316	.534	.758	.974	1.167	
131	1.321	1.421	1.502	1.570	1.627	1.673	1.709	1.736	1.755	1.766	1.770	1.771	
132	1.771	1.770	1.769	1.768	1.767	1.765	1.764	1.763	1.761	1.761	1.761	1.761	
133	1.710	1.689	1.625	1.382	1.068	.777	.483	.125	-.275	-.694	-1.108	-1.495	
134	-1.831	-2.094	-2.325	-2.530	-2.713	-2.874	-3.014	-3.136	-3.239	-3.325	-3.396	-3.456	
135	-3.509	-3.556	-3.595	-3.629	-3.652	-3.662	-3.667	-3.671	-3.675	-3.679	-3.683	-3.687	
136	-.576	-.567	-.539	-.399	-.221	-.066	.083	.279	.504	.741	.971	1.177	
137	1.342	1.447	1.536	1.611	1.673	1.724	1.765	1.795	1.816	1.829	1.835	1.835	
138	1.835	1.833	1.831	1.827	1.824	1.820	1.816	1.812	1.809	1.809	1.809	1.809	
139	1.710	1.689	1.625	1.385	1.074	.785	.490	.124	-.289	-.724	-1.156	-1.561	
140	-1.914	-2.190	-2.435	-2.652	-2.846	-3.015	-3.163	-3.290	-3.398	-3.488	-3.561	-3.620	
141	-3.671	-3.713	-3.747	-3.774	-3.790	-3.793	-3.792	-3.790	-3.788	-3.786	-3.784	-3.782	
142	-.576	-.568	-.541	-.407	-.235	-.086	.059	.257	.488	.734	.975	1.192	
143	1.367	1.480	1.579	1.664	1.736	1.794	1.842	1.878	1.904	1.922	1.931	1.934	
144	1.934	1.931	1.926	1.920	1.913	1.906	1.899	1.891	1.884	1.884	1.884	1.884	
145	1.710	1.689	1.626	1.385	1.074	.783	.484	.109	-.316	-.766	-1.215	-1.637	
146	-2.006	-2.297	-2.560	-2.796	-3.005	-3.190	-3.351	-3.490	-3.609	-3.708	-3.788	-3.852	
147	-3.903	-3.942	-3.972	-3.994	-4.004	-4.002	-3.996	-3.989	-3.981	-3.972	-3.962	-3.951	
148	-.576	-.568	-.543	-.410	-.240	-.092	.052	.251	.485	.736	.984	1.209	
149	1.393	1.516	1.628	1.725	1.808	1.878	1.935	1.981	2.016	2.042	2.058	2.066	
150	2.068	2.066	2.061	2.054	2.045	2.034	2.024	2.014	2.004	2.004	2.004	2.004	
151	1.710	1.689	1.625	1.384	1.071	.777	.471	.087	-.348	-.810	-1.272	-1.709	
152	-2.094	-2.402	-2.687	-2.943	-3.173	-3.377	-3.556	-3.713	-3.848	-3.963	-4.058	-4.132	
153	-4.190	-4.235	-4.268	-4.291	-4.300	-4.297	-4.290	-4.282	-4.273	-4.263	-4.252	-4.240	
154	-.576	-.568	-.543	-.411	-.241	-.092	.055	.256	.493	.746	.997	1.227	
155	1.417	1.549	1.675	1.785	1.881	1.964	2.034	2.092	2.139	2.176	2.203	2.220	
156	2.230	2.233	2.232	2.228	2.219	2.209	2.198	2.188	2.178	2.178	2.178	2.178	
157	1.710	1.689	1.625	1.384	1.069	.772	.461	.071	-.374	-.845	-1.319	-1.768	
158	-2.167	-2.490	-2.794	-3.071	-3.321	-3.545	-3.744	-3.921	-4.075	-4.207	-4.320	-4.412	
159	-4.485	-4.543	-4.587	-4.619	-4.634	-4.637	-4.636	-4.633	-4.630	-4.627	-4.624	-4.621	
160	-.576	-.568	-.544	-.412	-.242	-.092	.057	.260	.497	.752	1.006	1.240	
161	1.436	1.576	1.713	1.835	1.943	2.038	2.121	2.192	2.252	2.301	2.341	2.371	
162	2.391	2.405	2.413	2.415	2.412	2.404	2.397	2.390	2.383	2.383	2.383	2.383	
163	1.710	1.689	1.625	1.384	1.069	.770	.457	.063	-.387	-.866	-1.348	-1.806	
164	-2.215	-2.548	-2.866	-3.157	-3.421	-3.660	-3.874	-4.065	-4.234	-4.382	-4.510	-4.617	
165	-4.707	-4.780	-4.837	-4.881	-4.905	-4.916	-4.924	-4.930	-4.935	-4.939	-4.942	-4.944	
166	-.576	-.566	-.545	-.414	-.245	-.096	.053	.256	.496	.753	1.010	1.247	
167	1.446	1.593	1.737	1.867	1.984	2.088	2.180	2.260	2.329	2.389	2.438	2.479	
168	2.510	2.534	2.552	2.563	2.565	2.563	2.561	2.558	2.556	2.556	2.556	2.556	
169	1.710	1.689	1.625	1.384	1.069	.770	.456	.060	-.392	-.874	-1.359	-1.820	
170	-2.232	-2.568	-2.891	-3.186	-3.455	-3.699	-3.919	-4.115	-4.290	-4.443	-4.576	-4.690	
171	-4.786	-4.865	-4.929	-4.977	-5.005	-5.021	-5.033	-5.042	-5.051	-5.060	-5.069	-5.078	
172	-.576	-.569	-.545	-.415	-.247	-.099	.050	.254	.494	.752	1.010	1.250	
173	1.452	1.599	1.745	1.878	1.997	2.104	2.199	2.283	2.356	2.418	2.472	2.516	
174	2.552	2.580	2.602	2.616	2.622	2.622	2.622	2.622	2.622	2.622	2.622	2.622	
175	1.710	1.689	1.625	1.384	1.069	.769	.456	.061	-.389	-.868	-1.350	-1.808	
176	-2.216	-2.548	-2.867	-3.159	-3.424	-3.664	-3.879	-4.071	-4.241	-4.390	-4.518	-4.627	
177	-4.718	-4.792	-4.851	-4.895	-4.920	-4.932	-4.941	-4.948	-4.953	-4.956	-4.957	-4.956	
178	-.576	-.569	-.545	-.414	-.246	-.096	.052	.255	.495	.752	1.010	1.248	
179	1.449	1.594	1.738	1.869	1.986	2.090	2.183	2.264	2.334	2.394	2.444	2.485	
180	2.517	2.542	2.560	2.572	2.575	2.573	2.571	2.569	2.568	2.568	2.568	2.568	
181	1.710	1.689	1.625	1.383	1.068	.770	.458	.067	-.377	-.849	-1.322	-1.771	
182	-2.171	-2.495	-2.805	-3.087	-3.342	-3.572	-3.778	-3.961	-4.122	-4.261	-4.380	-4.479	
183	-4.560	-4.624	-4.673	-4.710	-4.730	-4.737	-4.740	-4.742	-4.743	-4.743	-4.742	-4.740	
184	-.576	-.568	-.544	-.411	-.241	-.091	.059	.262	.500	.755	1.009	1.243	
185	1.440	1.581	1.720	1.846	1.957	2.056	2.143	2.218	2.282	2.336	2.379	2.413	
186	2.439	2.456	2.467	2.474	2.472	2.468	2.463	2.458	2.453	2.453	2.453	2.453	
187	1.710	1.689	1.625	1.383	1.069	.772	.464	.080	-.355	-.816	-1.278	-1.716	
188	-2.104	-2.418	-2.716	-2.987	-3.233	-3.453	-3.650	-3.824	-3.976	-4.106	-4.217	-4.308	
189	-4.381	-4.437	-4.480	-4.512	-4.529	-4.534	-4.534	-4.533	-4.531	-4.528	-4.524	-4.519	
190	-.576	-.568	-.543	-.409	-.238	-.087	.062	.264	.500	.753	1.004	1.235	
191	1.428	1.564	1.697	1.816	1.922	2.015	2.096	2.165	2.223	2.270	2.308	2.335	
192	2.354	2.366	2.371	2.372	2.369	2.362	2.356	2.350	2.343	2.343	2.343	2.343	
193	1.710	1.689	1.625	1.384	1.070	.775	.470	.094	-.330	-.778	-1.226	-1.649	

Table 7-1. SASS1 G-H Table (contd)

194	-2.025	-2.329	-2.616	-2.879	-3.117	-3.331	-3.522	-3.690	-3.837	-3.964	-4.070	-4.157	
195	-4.227	-4.280	-4.320	-4.351	-4.368	-4.374	-4.374	-4.374	-4.373	-4.371	-4.368	-4.364	
196	-.576	-.568	-.542	-.408	-.235	-.084	.066	.268	.503	.754	1.002	1.229	
197	1.416	1.546	1.673	1.787	1.888	1.977	2.053	2.118	2.172	2.216	2.249	2.273	
198	2.288	2.296	2.297	2.296	2.292	2.285	2.279	2.273	2.267	2.267	2.267	2.267	
199	1.710	1.689	1.625	1.382	1.066	.771	.465	.095	-.316	-.747	-1.177	-1.583	
200	-1.944	-2.238	-2.518	-2.776	-3.009	-3.221	-3.410	-3.578	-3.725	-3.851	-3.957	-4.045	
201	-4.115	-4.168	-4.208	-4.241	-4.260	-4.268	-4.271	-4.272	-4.273	-4.274	-4.275	-4.276	
202	-.576	-.567	-.540	-.403	-.226	-.071	.083	.285	.516	.762	1.003	1.222	
203	1.404	1.530	1.652	1.762	1.860	1.946	2.021	2.085	2.137	2.180	2.212	2.234	
204	2.248	2.253	2.253	2.251	2.247	2.242	2.237	2.232	2.227	2.227	2.227	2.227	
205	1.710	1.689	1.623	1.376	1.055	.753	.443	.080	-.316	-.728	-1.136	-1.523	
206	-1.869	-2.156	-2.432	-2.687	-2.920	-3.132	-3.323	-3.493	-3.642	-3.772	-3.882	-3.972	
207	-4.045	-4.099	-4.141	-4.176	-4.198	-4.209	-4.214	-4.219	-4.223	-4.226	-4.228	-4.229	
208	-.576	-.567	-.536	-.392	-.207	-.041	.122	.324	.550	.784	1.013	1.221	
209	1.394	1.516	1.635	1.743	1.840	1.926	2.001	2.065	2.118	2.161	2.194	2.217	
210	2.231	2.236	2.235	2.233	2.230	2.226	2.223	2.219	2.215	2.215	2.215	2.215	
211	1.710	1.688	1.620	1.366	1.036	.725	.405	.046	-.336	-.728	-1.114	-1.479	
212	-1.810	-2.091	-2.366	-2.620	-2.854	-3.067	-3.261	-3.434	-3.588	-3.722	-3.836	-3.931	
213	-4.007	-4.064	-4.107	-4.145	-4.171	-4.184	-4.193	-4.200	-4.208	-4.217	-4.227	-4.238	
214	-.576	-.565	-.530	-.377	-.179	.000	.178	.382	.600	.820	1.033	1.225	
215	1.387	1.506	1.624	1.731	1.827	1.913	1.989	2.055	2.110	2.155	2.189	2.214	
216	2.229	2.234	2.234	2.232	2.231	2.229	2.227	2.225	2.223	2.223	2.223	2.223	
217	1.710	1.687	1.617	1.356	1.017	.695	.368	.013	-.358	-.733	-1.102	-1.452	
218	-1.772	-2.050	-2.324	-2.578	-2.813	-3.028	-3.224	-3.401	-3.558	-3.695	-3.813	-3.911	
219	-3.990	-4.050	-4.095	-4.135	-4.164	-4.180	-4.191	-4.201	-4.211	-4.221	-4.231	-4.241	
220	-.576	-.563	-.525	-.363	-.155	.037	.227	.432	.643	.852	1.051	1.230	
221	1.383	1.500	1.617	1.723	1.820	1.907	1.984	2.051	2.108	2.154	2.191	2.217	
222	2.233	2.239	2.239	2.238	2.238	2.237	2.237	2.236	2.235	2.235	2.235	2.235	
223	1.710	1.687	1.615	1.351	1.008	.682	.352	-.001	-.368	-.738	-1.099	-1.443	
224	-1.759	-2.036	-2.309	-2.564	-2.799	-3.016	-3.212	-3.390	-3.548	-3.687	-3.806	-3.906	
225	-3.986	-4.046	-4.092	-4.133	-4.163	-4.180	-4.192	-4.203	-4.214	-4.225	-4.236	-4.247	
226	-.576	-.563	-.522	-.357	-.144	.053	.247	.452	.660	.865	1.058	1.233	
227	1.382	1.498	1.614	1.721	1.818	1.905	1.983	2.050	2.108	2.155	2.192	2.219	
228	2.235	2.241	2.241	2.241	2.241	2.241	2.241	2.241	2.241	2.241	2.241	2.241	

Operationally, the G and H functions are evaluated at given non-tabular values of θ_I and χ with an interpolation on the appropriate table entries. A first-order interpolation is sufficient in the θ_I dimension due to the near-linearity of the functions over a 2° step in θ_I. However, a second-order interpolation is needed in χ because the variation of the functions with azimuth is roughly cos 2χ. A six-point interpolation is therefore performed using three adjacent χ table values for each of two adjacent θ_I table values and the form

$$G(\theta_I,\chi,\varepsilon) = \sum_i^2 \sum_j^3 a_i b_j G_{ij} \tag{7-5}$$

(and similarly for $H(\theta_I,\chi,\varepsilon)$, where G_{ij} are the six table entries and where a_i and b_j are functions of the location of the point (θ_I,χ) within the region formed by the six corresponding interpolation grid points. (See Section 3 in [36] for further details on the calculation of the coefficients a_i and b_j.)

Given a particular G-H table coefficient set together with the attendant interpolation on θ_I and χ as described, Eq. (7-2) represents a SASS model function; i.e., a particular empirical relationship used to describe the dependence of $\sigma°$ on the 19.5-m neutral stability wind vector. It is such a functional relationship that is "inverted" by the SASS wind vector extraction algorithm to obtain wind solutions from backscatter data. The inversion of Eq. (7-2) using the SASS1 table given in Table 7-1 for G and H produced the GDR winds.

7.4 MODEL FUNCTION INVERSION: LEAST-SQUARES ESTIMATION OF WIND VECTOR

7.4.1 Introduction

The wind retrieval component of the geophysical processor performs a nonlinear, maximum likelihood estimation of the sea-surface wind speed and direction. The estimation process produces one wind solution for each sensor data group prepared for processing by the grouping component of the geophysical algorithm (see Subsection 7.1.2). For GDR processing, the cell-pairing mode used for grouping data generates one wind solution for every qualified orthogonal pair of $\sigma°$ measurements (see Subsection 7.2). A nonlinear estimation technique is required because the dependence of the sea-surface $\sigma°$ on the wind direction γ is

approximately given by cos $2(\gamma-\phi)$, where ϕ is the SASS antenna azimuth look angle (see Subsection 7.3.2).

The cosine dependence results in multiple local probability maxima in wind-speed, wind-direction space. These multiple maxima give rise to the so-called wind direction aliases, the multiply-ambiguous solutions that normally result from the wind estimation process with SASS data. The typical wind solution resulting from processing a $\sigma°$ pair has a fourfold ambiguity: it consists of four speed/direction pairs of which one such pair is the desired or "correct" wind vector solution and the other three pairs are extraneous and "incorrect." The four alias directions are usually quite different from each other and, normally, neither they nor any other product of the inversion mechanism offer any intrinsic clue as to which of the four is correct. (At least, such is the case for wind solutions derived from pairs of $\sigma°$ measurements. The binning mode (see Subsection 7.1.2) for grouping measurement cells may yield some measure of alias-removal skill, however -- see Subsection 9.1.) On the other hand, since the four alias speeds typically fall within a few percent of each other, the speed component of the solution is relatively insensitive to the alias choice. This is why the ambiguity due to aliases refers essentially to wind direction and not to speed. Wind-solution ambiguities also occur in the three- and two-alias varieties, although not as frequently as the four-alias solutions. Solutions with two aliases have direction about 180° apart, and occur least often.

7.4.2 Maximum Likelihood and Sum-of-Squares Functions

The most general statistical description of the wind speed and direction in terms of backscatter measurements is by means of the conditional probability density $P(U,\gamma|\{\sigma°_n\})$ that the wind speed and direction have the values U and γ (see Subsection 7.3.2), given the set $\{\sigma°_n\}$ of n backscatter measurements. Using a Bayesian formalism (see [31] for details) and a set of assumptions (Subsection 7.4.3), this density can be written as

$$P(U,\gamma|\{\sigma°_n\}) = \frac{\prod_{i=1}^{n} \exp\left\{-\left[\sigma°_i - f_i\right]^2 / 2\delta_i^2\right\}}{\int dU \int d\gamma \prod_{i=1}^{n} \exp\left\{-\left[\sigma°_i - f_i\right]^2 / 2\delta_i^2\right\}} \tag{7-6}$$

where: (1) σ°_i is the measured (by the scatterometer) value of the backscatter coefficient (NRCS); (2) $f_i = f(\theta_{I_i}, \chi_i, \varepsilon_i, U)$ is the NRCS derived from the assumed model function as represented by Eq. (7-2) coupled with the SASS1 G-H table given in Table 7-1; and (3) δ_i is the standard deviation of the total random error on σ°_i for i=1,2,...,n. The f_i term is the NRCS model function evaluated for the incidence angle, wind relative azimuth angle, and polarization type corresponding to the ith measurement, and the wind speed:

$$f_i = f(\theta_{I_i}, \gamma, \phi_i, \varepsilon_i, U) = G(\theta_{I_i}, \gamma, \phi_i, \varepsilon_i) + H(\theta_{I_i}, \gamma, \phi_i, \varepsilon_i) \log_{10} U \tag{7-7}$$

for the relative azimuth $\chi_i = \gamma - \phi_i$ (see Subsection 7.3.2). The integration in Eq. (7-6) is over all U,γ space; and σ°_i, f_i, and δ_i are all in logarithmic coordinates.

Equation (7-6) can be written as

$$P(U,\gamma|\{\sigma^\circ_n\}) = \frac{\exp\left[-\frac{1}{2}Q(U,\gamma,\{\sigma^\circ_n\})\right]}{\int dU \int d\gamma \exp\left[-\frac{1}{2}Q(U,\gamma,\{\sigma^\circ_n\})\right]} \tag{7-8}$$

where

$$Q(U,\gamma,\{\sigma^\circ_n\}) = \sum_{i=1}^{n} \left[\sigma^\circ_i - f(\theta_{I_i}, \gamma, \phi_i, \varepsilon_i, U)\right]^2 / \delta_i^2 \tag{7-9}$$

$Q(U,\gamma,\{\sigma^\circ_n\})$ is the weighted sum-of-squares over the n observations in a data group. The model function $f(\theta_{I_i}, \gamma, \phi_i, \varepsilon_i, U)$ is given by Eq. (7-7). Each term in the sum is weighted inversely by the variance δ_i^2 of the error on σ°_i.

Considering the density (7-8) to be a likelihood function, the maximum likelihood principle can be applied to obtain a solution U,γ that maximizes $P(U,\gamma|\{\sigma^\circ_n\})$. This is equivalent to finding the solution U,γ that minimizes the weighted sum-of-squares given in Eq. (7-9). For every data group $\{\sigma^\circ_n\}$ and the given model function f, the SASS wind vector solution is therefore obtained by a least-squares estimation process that finds the speed U and direction γ that

minimizes the Q functional. Note that since n=2 for the cell-pairing mode, GDR (primary swath) wind solutions are derived from a Q with only two terms in the sum.

7.4.3 Assumptions for Least-Squares Estimator

The validity of Eq. (7-8) as a likelihood function for U and γ and therefore the validity of Q in Eq. (7-9) as the functional to minimize to obtain the correct wind speed and direction depends upon the following assumptions that have been made:

(1) No a priori information is available on either the wind speed or direction.

(2) The noise on any σ° measurement is uncorrelated with the noise on any other measurement.

(3) The total measurement noise on the NRCS has a normal distribution in logarithmic coordinates; i.e., the noise is log-normally distributed [31]. Thus, considered as a random variable, $\sigma^\circ_i - f(\theta_{I_i}, \gamma, \theta_i, \varepsilon_i, U)$ in Eq. (7-9) (which is in logarithmic units) is normally distributed with zero mean and variance δ_i^2.

(4) The actual sea-surface NRCS is given by the assumed model function (7-2) (together with the SASS1 G-H table), so that there is no non-random model error. A random error in the model is assumed and accounted for by adding a constant rms component (.7 dB) due to this error source to the nominal computed measurement standard deviation to produce a total root-sum-square measurement-plus-model error standard deviation δ_i (see Subsection 7.4.4) [38].

(5) All backscatter measurements in a data group $\{\sigma^\circ_n\}$ are of the same wind speed and direction.

The extent to which these hypotheses are true is, to varying degrees, conjectural. In fact, it seems evident that their "degree of validity" is not constant in all cases over the course of the mission data span. The validity of assumption (5), for example, is dependent upon local weather gradients and the measurement (orthogonal) cell separation distances, both of which change throughout an orbit. Disagreement exists about whether assumption (3) is even valid at all:

the measurement error is considered by some to be normally distributed in antilog form (cf., Appendix D, Section 1 in [11]). (It is agreed, however, that for conditions yielding a relatively small δ_i; i.e., for NSD_i (see next subsection) less than, say, .5 and wind speeds greater than 6-8 m/s, the normal and log-normal distributions are essentially equivalent for numerical purposes. It is only for the lower wind speeds and higher values of K_p (see Subsection 5.4.1.1) that the difference between the two distributions becomes significant. The log-normal distribution was assumed for the production of GDR winds primarily because it led to a less complicated computational algorithm.) Adding a constant "random" error to the formal computed error in the backscatter observation in an attempt to make the resulting variances δ_i^2 approximately reflect a data "noise" component due to model uncertainty (assumption (4)) could be considered to be an engineering artifice to more accurately describe the actual scatter in the data. These questions will not be pursued further here.

7.4.4 σ° Measurement Error and Sum-of-Squares Weighting Factors

The weighting factors δ_i used in the penalty function (7-9) are the expected standard deviations between the σ°_i measurements and the measurement values predicted by the model function, and are derived as the sum of a computed measurement error and a constant-level modeling error. The total σ° measurement random error is computed by the sensor algorithms (see Subsection 5.4) as the root-sum-square of three error sources: communication noise, attitude pointing uncertainty, and instrument processing errors (see [3] for more details). When expressed in ratio (non-logarithmic) units, this total measurement error relative to the measurement itself is called the total normalized standard deviation (NSD -- see Table 8-3, channels 330-344). Thus, the NSD for the ith measurement can be expressed in ratio units as

$$NSD_i = \delta(\sigma^\circ_i)/\sigma^\circ_i \tag{7-10}$$

where $\delta(\sigma^\circ_i)$ is the ratio-units standard deviation on the ith measurement, and σ°_i is the measurement also in ratio units. To convert to logarithmic (dB) units, we use the definition

$$\sigma^\circ = 10^{(\sigma^\circ_{dB}/10)} \tag{7-11}$$

and compute to first order

$$NSD = \frac{\left[\partial\left(10^{(\sigma^\circ_{dB}/10)}\right)\Big/\partial\sigma^\circ_{dB}\right]\delta(\sigma^\circ_{dB})}{10^{(\sigma^\circ_{dB}/10)}} = \frac{\ln 10}{10}\,\delta(\sigma^\circ_{dB}) \tag{7-12}$$

where $\delta(\sigma^\circ_{dB})$ is the desired measurement-error portion of the (dB-units) ith weighting factor in Eq. (7-9).* The final weighting variances δ_i^2 are then computed as

$$\delta_i^2 = \left(\frac{10}{\ln 10}\,NSD_i\right)^2 + \delta_m^2, \tag{7-13}$$

where δ_m = .7 dB is the assumed constant rms modeling error.

7.4.5 Wind Solution Ambiguity Alias Phenomenon -- Why

For incidence angles of about 20° and greater, the NRCS is anisotropic in the relative wind direction χ, with the dominant dependence of σ° given approximately by cos 2χ as seen in Figure 7-1 (see Subsections 7.1.1 and 7.3). Heuristically, the same wind speed will therefore produce the same σ° value for as many as four different radar-viewing directions for a given θ_I and polarization. This characteristic of the SASS signal inherently yields the multiply-ambiguous (up to fourfold ambiguity) "alias" solutions described in Subsection 7.4.1 in the σ°-to-wind inversion process.

Consider a constant σ° value resulting, say, from a single, noise-free NRCS measurement. The corresponding locus of points in wind speed-wind relative

*Another form for the relationship is

$$NSD = \frac{1}{2}\left[10^{\delta(\sigma^\circ_{dB})/10} - 10^{-\delta(\sigma^\circ_{dB})/10}\right]$$

This form, which agrees with Eq. (7-12) to first order in $\delta(\sigma^\circ_{dB})$, is used in the sensor algorithms (see Section 2 in [3]).

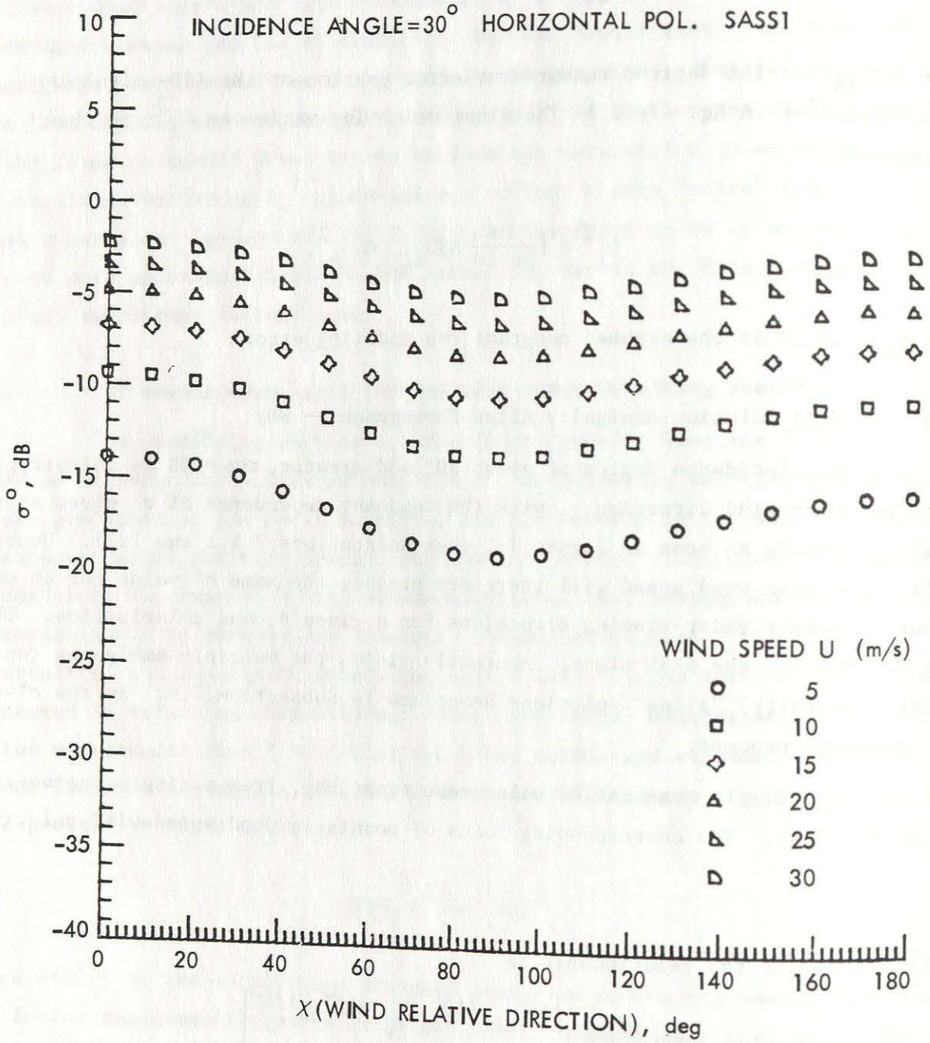

Figure 7-1. The Variation of $\sigma°$ With Wind Relative Azimuth (χ) for a Range of Wind Speeds at $\theta_I = 30°$ (Derived from the SASS1 G-H Model Table)

direction (U-χ) space describes a curve that is approximately sinusoidal [38], and, like the $\sigma°$-versus-χ dependence, has four extrema over the range $0° \leq \chi < 360°$. This can be partially deduced by noting that for the assumed model function (7-2): (1) for fixed θ_I, ε, and $\sigma°$, the U-χ dependence yields

$$\frac{\partial U}{\partial \chi} = - \frac{\frac{\partial G}{\partial \chi} + \log U \frac{\partial H}{\partial \chi}}{\log_e(H/U)} \tag{7-14}$$

for $H = H(\chi) \neq 0$, and (2) for fixed θ_I, ε, and U, the $\sigma°$-χ dependence yields

$$\frac{\partial \sigma°}{\partial \chi} = \frac{\partial G}{\partial \chi} + \log U \frac{\partial H}{\partial \chi} \tag{7-15}$$

Since the expressions in (7-14) and (7-15) vanish for the same value of χ, both the U-χ relationship and the $\sigma°$-χ relationship have extrema at the same points: $\chi = 0°$, 90°, 180°, and 270°.

For the case of two nearly orthogonal (GDR cell pairing mode) noise-free measurements of the same wind at a given site; i.e., $\chi_2 \cong \chi_1 + 90°$, where χ_1 is the wind direction relative to the forward (control) beam and χ_2 is for the aft beam, the wind "solution" can occur only at the intersections of the two curves in U-χ space corresponding to the individual measurements. As seen in Figure 7-2, this can result in various solution configurations depending on how the two curves intersect. The number of solution intersections ranges from one to four depending on the value of χ_1 and the measurement value $\sigma°_2$ relative to $\sigma°_1$. In the figure, the solid intersection dot corresponds to the "true" correct solution and the open circles denote the extraneous alias solutions. These multiple solutions yield nearly the same wind speed, but widely varying directions. The top example in Figure 7-2 depicts an "upwind" condition (i.e., control antenna pointing into the wind): the alias at $\chi = 0°$ is the correct solution, while the two extraneous aliases are a few degrees apart and located with approximate symmetry about $\chi = 180°$. The middle example indicates the configuration where the wind direction approximately splits the two orthogonal beam patterns: the correct solution and the three remaining aliases are (roughly) mutually perpendicular. Examples of these multi-solution wind vectors and a technique for selecting the correct alias are given in [40].

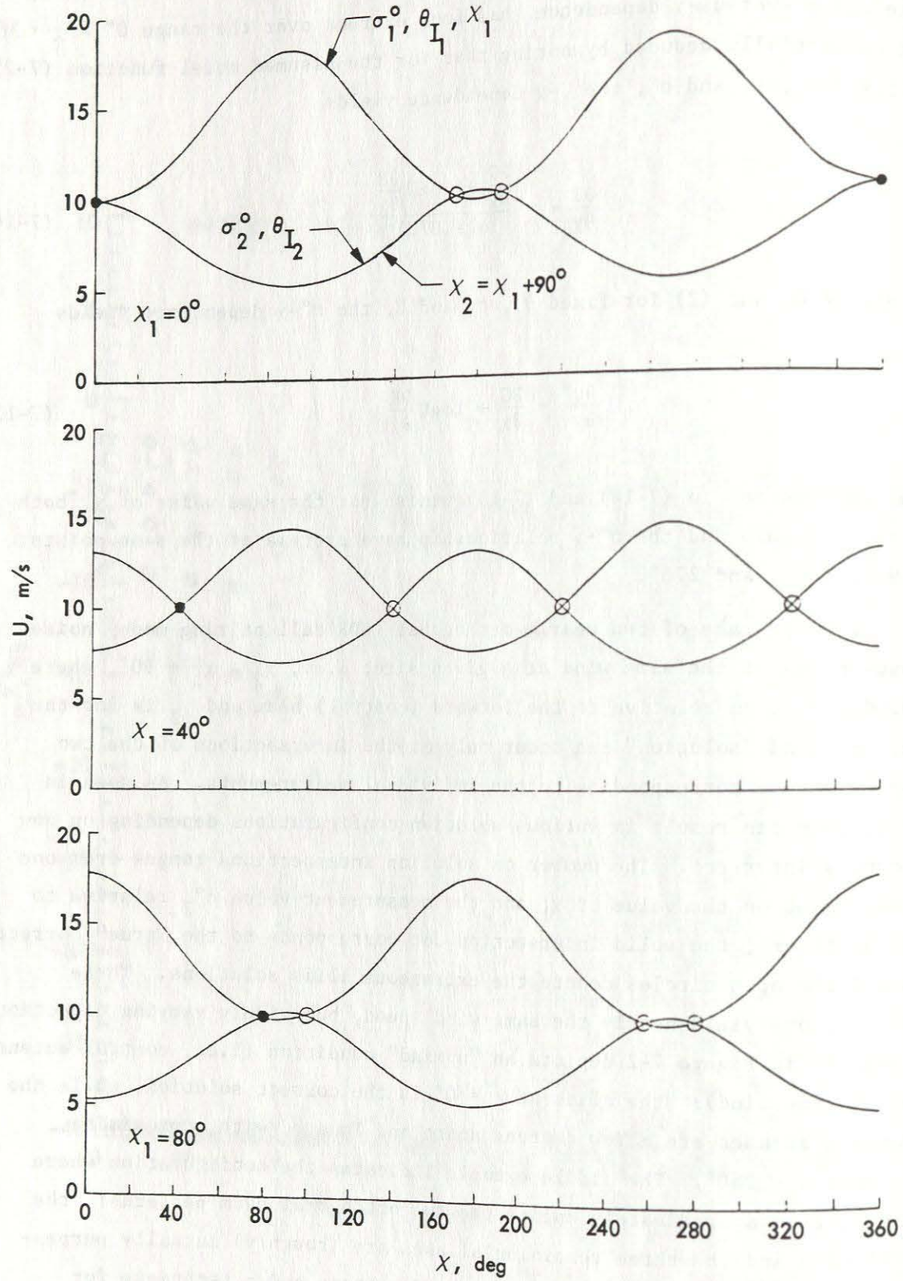

Figure 7-2. Examples of Noise-Free Solutions for Beam Patterns 90° Apart, Vertical Polarization, and a Wind Speed of 10 m/s for Wind Directions of χ_1 = 0°, 40°, and 80°

The situation becomes significantly more abstruse in the presence of realistic measurement noise. In this case, the possible solutions fall within regions that spread over neighboring areas of the intersections. Additionally, if there are more than two measurements in a data group (cell binning mode), the complications increase since many such areas become possible. Solutions yielding more than four aliases occurred rarely during GDR processing and were thrown out (i.e., not included in the output geophysical records) as unfit -- see following subsection.

7.4.6 Least-Squares Wind Estimation

Since the model function relationship is nonlinear in wind direction, the inversion algorithm finds the local maxima of $P(U,\gamma|\{\sigma^\circ_n\})$ (see Subsection 7.4.2) for a given data group $\{\sigma^\circ_n\}$ with a two-stage process. In the first stage the algorithm does a global coarse search in 5°-direction steps to isolate the (multiple) candidate solutions in U-γ space to within the search-step interval. This is followed by the second processing stage which refines the approximate solutions to yield the (up to four) alias solutions to within 1° in wind direction. A wind solution cannot be found in general with only a single-step least-squares search because the aliasing phenomenon implies that the Q functional (7-9) has more than one local minimum over the global range of γ.

In order to locate the approximate local minima of Q in U-γ space for a given group $\{\sigma^\circ_n\}$, the algorithm computes Q for each of the wind directions γ_k, k = 1,2,...,72, ranging from 0° to 355° in 5° steps. For the kth wind direction, a speed U_k is found that minimizes Q. Because the model function is linear in terms of σ°(dB) and log U, the wind speed U_k is given simply by

$$\log U_k = S_{1_k}/S_{2_k} \tag{7-16}$$

where

$$S_{1_k} = \sum_{i=1}^{n} H(\theta_{I_i},\chi_{ik},\varepsilon_i)\left[\sigma_i^\circ - G(\theta_{I_i},\chi_{ik},\varepsilon_i)\right]\Big/\delta_i^2 \tag{7-17}$$

$$S_{2_k} = \sum_{i=1}^{n} H^2(\theta_{I_i}, \chi_{ik}, \varepsilon_i) / \delta_i^{\,2} \tag{7-18}$$

with

$$\chi_{ik} \equiv \gamma_k - \phi_i \tag{7-19}$$

The minimum Q_k value is then found by substituting γ_k and $\log U_k$ into Eq. (7-9) for $k = 1,2,\ldots,72$.

Because of the model function $\cos 2\chi$ dependence, Q has several local minima for a given data set $\{\sigma^\circ_n\}$ -- even for $n = 2$. These minima are found to the nearest 5° coarse-direction step by comparing Q_k to Q_{k-1} and Q_{k+1}: if Q_k is less than either adjacent Q, then there is a local least-squares minimum nearby the point (U_k, γ_k). The number of these local minima varies from two to four, and in rare cases is greater than four. A data set $\{\sigma^\circ_n\}$ yielding more than four minima (aliases) is rejected from further processing -- and not entered into the GDR data records. This procedure of comparing adjacent Q_k's provides a set of approximate candidate solution wind vector aliases.

The location of each approximate minimum resulting from this coarse search process is then determined more precisely by a six-point fitting procedure using a second-order, two-dimensional polynomial approximation of the Q function in the neighborhood of the candidate minimum point. This interpolation polynomial also yields information about the shape of the Q function in the neighborhood of the minimum. In particular, along with each refined solution (minimum) (U,γ), formal standard deviations -- assuming the hypotheses listed in Subsection 7.4.3 -- on both U and γ are computed (see channels 1801-2200 and 2601-3000 in Table 8-1), as are the "relative probabilities" for the minimum (see [36] and channels 3001-3400), from the approximating polynomial.

For a given data group $\{\sigma^\circ_n\}$ and for a given approximate solution (U_a, γ_a) resulting from a first-stage coarse search, an interpolation polynomial is generated that passes through the set of six points $\{(U_\beta, \gamma_\beta)\}$, $\beta = 1,2,\ldots,6$, where

$$\left\{(U_\beta, \gamma_\beta)\right\} = \left\{\begin{array}{l} (U_a, \gamma_a) \\ (U_a, \gamma_a \pm \Delta\gamma) \\ (U_a \pm \Delta U, \gamma_a) \\ (U_a + \Delta U, \gamma_a + \Delta\gamma) \end{array}\right\} \tag{7-20}$$

for small given increments ΔU and $\Delta\gamma$ in U and γ. There results a polynomial Q_p of the form

$$Q_p(U, \gamma, \{\sigma^\circ_n\}) = a_1 u^2 + a_2 u + a_3 v^2 + a_4 v + a_5 uv + a_6 \tag{7-21}$$

where

$$\left.\begin{array}{l} u = (U - U_a)/\Delta U \\ v = (\gamma - \gamma_a)/\Delta\gamma \end{array}\right\} \tag{7-22}$$

and where the coefficients a_i are computed as functions of $Q_\beta = Q(U_\beta, \gamma_\beta, \{\sigma^\circ_n\})$, $\beta = 1,2,\ldots,6$ [36]. The values Q_β are computed using Eqs. (7-7) and (7-9).

The various minima of $Q(U,\gamma,\{\sigma^\circ_n\})$ for a given data group $\{\sigma^\circ_n\}$ are assumed to be isolated from each other. Thus, a region R about each approximate minimum solution point (U_a, γ_a) is assumed to exist such that within R, the fit $Q_p(U,\gamma,\{\sigma^\circ_n\})$ is a good approximation to the function $Q(U,\gamma,\{\sigma^\circ_n\})$, and furthermore that Q_p evaluated on the boundary of R is much greater than its minimum value located near the center of R. Using these assumptions, Wentz [36] defines the minimum solution (U,γ) in terms of a mean $\bar{U}$ and $\bar{\gamma}$ computed by an integration of the approximating probability density function over R (cf., Eq. 7-8):

$$\overline{U} = \frac{\iint_R dU\, d\gamma\, U \exp\left[-\frac{1}{2} Q_p(U,\gamma,\{\sigma^\circ{}_n\})\right]}{\iint_R dU\, d\gamma \exp\left[-\frac{1}{2} Q_p(U,\gamma,\{\sigma^\circ{}_n\})\right]} \tag{7-23}$$

and similarly for $\overline{\gamma}$. With a similar integration, Wentz computes the expected variances on these wind speed and direction solutions (see Subsection 9.11).

With the assumption that $Q_p(U,\gamma,\{\sigma^\circ{}_n\})$ is much greater outside the region R than at its minimum value, Wentz increases the region R of integration to extend over all of the U-γ space without introducing significant error in the integrals. The integrals yielding the refined solution (U,γ) that minimizes $Q(U,\gamma,\{\sigma^\circ{}_n\})$, as well as the formal standard deviation on U and γ, can then be solved explicitly -- and easily -- as simple algebraic expressions involving only U_a, γ_a, ΔU, $\Delta\gamma$, and the known coefficients a_i in Eq. (7-21). See [36] for further details on this scheme, its derivation, and on the resulting processing.

Each member of the set of (four or fewer) approximate alias solutions $\{(U_a,\gamma_a)\}$ generated during the first-stage coarse-search procedure for a given orthogonal data pair $\{\sigma^\circ{}_1,\sigma^\circ{}_2\}$ is further refined with this polynomial fit/integration scheme. The result is the final set of four or fewer alias solutions $\{(U,\gamma)\}$ that constitutes the GDR multiple wind vector solution corresponding to the primary swath observation pair $\{\sigma^\circ{}_1,\sigma^\circ{}_2\}$.

As discussed in Subsection 7.1.1, the model function does not depend on wind direction for nadir-swath measurements. In this case, a single wind speed and no wind direction is calculated. The nadir wind speed is calculated simply from Eqs. (7-16) - (7-19) using an arbitrary wind direction $\gamma = \gamma_k$ of 0°. n for GDR nadir solutions can be 1,2, or more (see Subsection 7.1.2.4).

A functional flow diagram of this least-squares wind inversion component of the SASS geophysical processor is given in Figure 7-3.

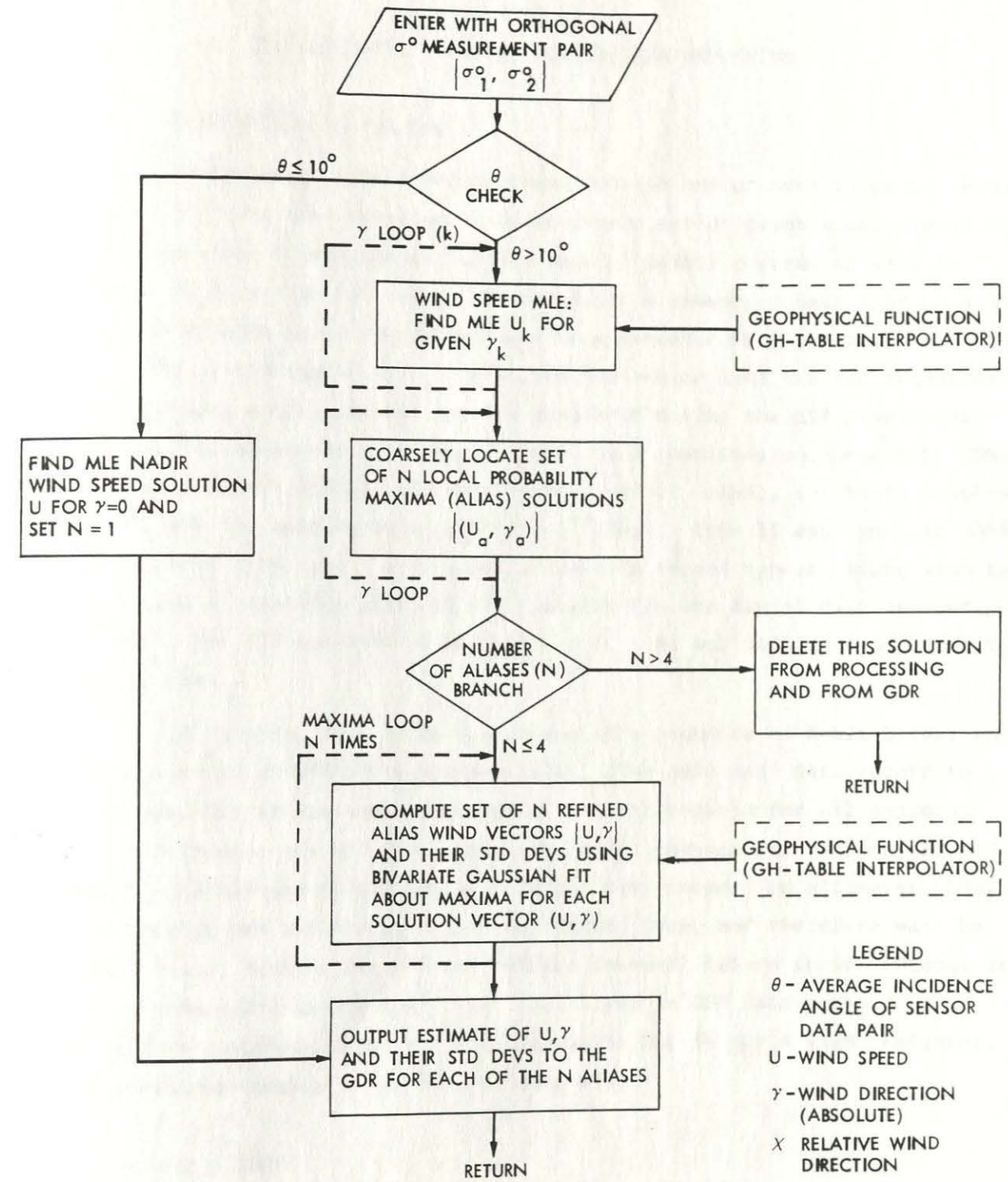

Figure 7-3. SASS Geophysical Algorithm Least-Squares Wind Vector Estimation Module

SECTION 8

GDR CONTENTS, FORMATS, READING AND UNPACKING

8.1 INTRODUCTION TO THE GDR

The Geophysical Data Record tapes contain one or more files of Seasat sensor data that has been processed through sensor and/or geophysical algorithms. A GDR tape consists of geophysical and (possibly) sensor records as well as descriptive text records for one of the satellite's sensors. Each file on a GDR contains one or more text records followed by a sequence of integer-valued data records. The scatterometer type I GDRs (see Subsection 1.6) are the fundamental single-file tapes containing all records generated during the ADF processing of a quarter-day of SASS data. The data record types contained on these SASS GDRs are (1) basic sensor (SASB), (2) supplemental sensor (SASS), (3) basic geophysical (SAGB), and (4) supplemental geophysical (SAGS). Type II and type III SASS GDRs are derived from type I's by deleting certain record types: along with text records a type II contains SAGB and SAGS records for one day of data in four files, and a type III consists of eight files of text and SAGB records covering two days of data.

GDR records, text or data, consist of a sequence of 8-bit bytes, and are constrained to an 8064-byte maximum size. (The only SASS data record to approach this size is the basic geophysical.) Text records for all sensors except the altimeter are written solely with ASCII characters. (Either EBCDIC characters or ASCII characters may be used for text records on altimeter GDRs.) The data records are written in a "packed" binary form, and therefore must be "unpacked" (i.e., scaling factors and offsets removed) before their contents can be used as meaningful geophysical data. All items in GDR data records are represented as <u>unsigned</u> integers: the high-order bit is <u>not</u> a sign indicator, and therefore may contain a significant data bit.

8.2 GDR RECORDS

8.2.1 Text Records

GDR text records appear in five basic types, with each type containing certain minimum information (see Figure 8-1 for the typical SASS GDR text record ordering scheme):

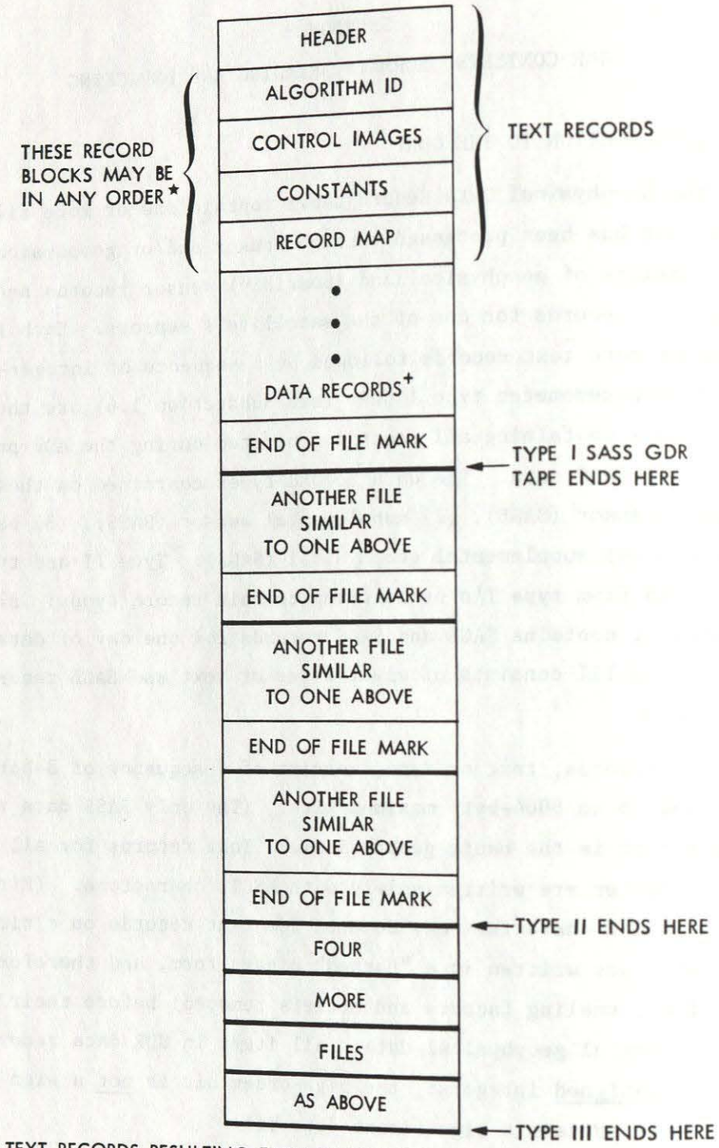

* MULTIPLE TEXT RECORDS RESULTING FROM THREE SASS ADF PROCESSING STAGES MAY BE INTERLEAVED TO A DEGREE. HOWEVER, MULTIPLE RECORDS OF THE SAME TYPE (e.g., CONSTANTS) RESULTING FROM A SINGLE PROCESSING STAGE WILL BE CONTIGUOUS ON THE TAPE.

+ DATA RECORDS CONSIST OF INTERLEAVED SENSOR AND GEOPHYSICAL RECORDS IF SASS GDR IS TYPE I. FOR TYPES II AND III THESE RECORDS ARE GEOPHYSICAL ONLY.

Figure 8-1. SASS GDR File(s) Text/Data Record Structure

(1) Header Record. Contains overall GDR software-version identification information as well as the time and date that the file (containing this record) was produced. There is only one header record on a GDR file, and it is the first record on the file.

(2) Algorithm ID Record. Contains software pedigree information that identifies the version of all algorithms/subroutines used in producing the sensor and geophysical records on the file. At least two ID records are generated by each stage of a sensor's ADF processing. A scatterometer GDR file contains 10 such records that include not only those emanating from the SASS sensor, attenuation/TOIL, and geophysical stages, but also those resulting from upstream SMMR processing that generates the T_B GDR files that are input to the SASS second stage (see Figure 4-4). (For the ALT geophysical file, the ID records also identify the reference orbit used, the geoid model, and the subroutine identifications for SMMR software used to calculate altimeter atmospheric corrections.)

(3) Control Images Record. Contains all processor control card (option settings, etc.) images used to produce the file. A SASS GDR file usually accumulates six of these records as a result of the multiple-stage processing.

(4) Constants Record. Contains text (i.e., character, not computer number, form) values of all constants and tables used in the processing to generate the file. The total set of constants used in each processing stage is grouped together in one such record, or in several consecutive records (due to the maximum record size constraint) if there are a large number of constants. The constants for SASS sensor processing, which requires numerous large tables of numbers such as relative antenna gains and various parameter sensitivity partial derivatives, are contained in 55 contiguous constants records. SASS geophysical constants, including the 2736-entry G-H table wind-to-σ° model function, are contained in 28 records. Each SASS file also

contains 6 SMMR constants records derived from upstream T_B processing. The general format description of these constants records is given in Subsection 8.3.6.2.

(5) Record Map Record. Contains the definitive descriptions of the format and contents of the GDR sensor and geophysical records. These records describe the offsets and scaling factors that are necessary for unpacking the data and give a brief definition of each item that appears in the GDR data records. One of these descriptive records exists for each type of sensor/geophysical data record: there are thus four such records on a SASS file describing respectively the SASB, SASS, SAGB, and SAGS records. These SASS record map contents are reproduced almost exactly in Tables 8-1, 8-2, 8-3, and 8-4. The general format description of these record map records appears in Subsection 8.3.6.3.

This information represents the minimum that is always present on these text records; they may contain additional descriptive information not listed here. As noted, records pertaining to upstream SMMR processing are also included in the SASS GDR files. The typical text/data record structure of SASS type I, II, and III GDRs is given in Figure 8-1.

8.2.2 SASS Data Records

8.2.2.1 Sensor Records. A SASS GDR basic sensor record contains the results of processing one frame of scatterometer telemetry data with the $\sigma°$ sensor algorithms (see Subsection 5.6.1.2.1). As such, this record contains the final computed -- and atmosphere attenuation corrected -- backscatter coefficients and all significant supporting parameters for the 15 Doppler channel measurements. The byte-by-byte contents of the SASS basic sensor record are given in Table 8-3.

A SASS GDR supplemental sensor record contains the results of processing a four-frame scatterometer calibration data sequence (see Subsections 4.5.1 and 5.6.1.2.2) by the sensor calibration algorithms (see Subsection 5.6.2). This record contains the gain calibration and ancillary parameters used to compute antenna gains for the 124-frame block of SASS $\sigma°$ data following the calibration sequence; its byte-level contents are given in Table 8-4.

8.2.2.2 Basic Geophysical Record. A SASS GDR basic geophysical record contains the end product ocean-surface wind vector solutions derived from processing $\sigma°$ data with the geophysical algorithms. Each record contains 100 wind solutions -- the four alias directions and associated speeds arising from the wind extraction process is considered to be one solution -- and supporting parameters. For most users of scatterometer GDRs, this record will probably be the only one read and unpacked; its contents are given in Table 8-1.

Since the pairing mode for grouping $\sigma°$ data was used by the geophysical algorithms in the wind retrieval process (see Subsection 7.1.2.1), each solution results from processing an orthogonal pair (i.e., one from a forward beam and one from an aft beam) of $\sigma°$ measurements. The wind solutions are ordered within a record, as well as between records, as they are generated by the geophysical algorithms; this order in turn is due to the $\sigma°$-pair order established by the cell pairing mechanism described in Subsection 7.2. This "moving window" cell pairing method delineates candidate measurement pairs and further prepares them for wind-extraction processing in an order that is somewhat random in space and time locally within the boundaries of the window. As this pairing window "moves" along the SASS swath in the direction of spacecraft motion, the time-tags and locations of the resulting paired $\sigma°$ measurements move globally along with the window in an average sense, paralleling the window center to within a few minutes and degrees (location). The result is that time-tags and locations of successive wind solutions within a geophysical record, as well as those crossing record boundaries, tend to jump around erratically within the time/space domain of the pairing window. However, the gradual record-by-record trend is solution time-tags that increase chronologically and locations that follow the SASS swath.

8.2.2.3 Supplemental Geophysical Record. As already noted, SASS $\sigma°$ data is organized in a time/space domain on GDR basic sensor records in a manner quite different from that required for geophysical processing. The former is structured as the data is received from the spacecraft (i.e., a record contains 15 $\sigma°$ measurements derived from, and distributed along, one antenna illumination pattern extending hundreds of kilometers over the Earth's surface), and the latter requires a pair of nearly-coincident $\sigma°$ measurements taken from two antennas at two different times. The mapping between these two sensor data grouping schemes is provided by the cell pairing front-end stage of geophysical processing. If a SASS

GDR tape contained only the record types described above, the restructured file that results from cell pairing -- the most complex component of the sensor data manipulations that precede wind retrieval computations -- would be unavailable for use beyond GDR processing. Therefore this file is present on SASS GDRs in the form of supplemental geophysical records that provide the paired sensor data in parallel with the corresponding wind solutions contained in the basic geophysical records.

A supplemental geophysical record contains sensor data parameter pairs from the forward and aft beam for each of the 100 solutions in the corresponding SAGB record. The SAGS record contains all paired sensor data used in the wind inversion process (i.e., $\sigma°$, incidence and azimuth angles of the measurement cells, and polarization types), as well as several other parameters (location, time-tag, etc.) associated with each of the paired backscatter measurements. Sensor and geophysical data for particular wind solutions may be easily extracted from the two matched records as the data contained within them is ordered in a straightforward one-to-one correspondence. The mated SAGB and SAGS records occur back-to-back on (type I and type II) SASS GDR files, with the SAGS always following the SAGB.

The envisioned users of the SAGS record contents fall into two main categories. (1) $\sigma°$-to-wind model function investigators can perform further data inversion studies with the SASS data (in the pairing mode) without having to first develop complicated cell grouping software. (2) Particular wind solutions that appear to be "outliers," pathological, or otherwise in need of further scrutiny, can easily be traced back to their two $\sigma°$ measurement progenitors for a more detailed sensor-level investigation. Both of these processes would be intractable on any significant scale without the SAGS record.

8.2.2.4 Data Record Ordering. Sensor data records on a type I SASS GDR file are ordered chronologically according to data frame time-tags as they appear in the telemetry stream; time-tags for consecutive SASB records increase by 1.891 s for nominal frame sequences (see Subsection 4.5). One supplemental sensor calibration record occurs nominally after every group of 124 SASB records: calibration records therefore occupy only a small part of a GDR's sensor data volume. The paired basic and supplemental SASS geophysical records are interspersed among the sensor records on a given GDR tape in a somewhat random, yet approximately

chronological, order with the time-tags of the 100 wind solutions contained in a geophysical record roughly paralleling (within a few minutes) the time-tags of neighboring -- strictly chronologically ordered -- sensor records.* No sensor records can occur between a SAGB/SAGS record pair on a type I GDR.

A typical type I SASS GDR contains roughly 25 sensor records for every geophysical record pair (see Subsection 1.7 for data volumes). The geophysical data records remaining on the type II (geophysical pairs) and type III (SAGB only) SASS GDR files occur in the same order as they do (ignoring sensor records) on the original type I GDRs.

8.3 READING AND UNPACKING A SASS GDR

8.3.1 Record Sizes

General format descriptions of GDR records are given in Subsections 8.3.2 (text) and 8.3.3 (data). The four SASS data record types have the following (fixed) lengths in terms of numbers of 8-bit bytes: (1) Basic Geophysical = 8028 bytes, (2) Supplemental Geophysical = 3834 bytes, (3) Basic Sensor = 1656 bytes, and (4) Supplemental Sensor = 936 bytes. These record sizes include 4, 10, 5, and 12 zero-filled pad bytes, respectively, at the end of each record type. These pad bytes yield record sizes that are multiples of 18 bytes, an ADF requirement that is an attempt to minimize GDR tape-read problems due to computer word length variations at different installations.

---

* A SAGB/SAGS record pair is written out onto an output SASS type I GDR by the geophysical algorithms whenever their internal buffers of dimension 100 are filled. This is preceded on the GDR tape file by the sensor records containing the $\sigma°$ data frames processed up to that point.

8.3.2 GDR Text Record Format

EIGHT TYPES OF GDR TEXT RECORDS ARE DEFINED, ALL OF WHICH SHARE THE SAME BASIC FORMAT:

BYTE	CONTENTS
1	RECORD TYPE 0 = HEADER (HD) 1 = ALGORITHM ID (ID) 2 = CONTROL IMAGES (CI) 3 = USER CONSTANTS (UC) 4 = BASIC SENSOR RECORD MAP (SBRM) 5 = SUPPL. SENSOR RECORD MAP (SSRM) 6 = BASIC GEOPHYSICAL RECORD MAP (GBRM) 7 = SUPPL. GEOPHYSICAL RECORD MAP (GSRM)
2	DATA TYPE 1 = ALT, OR RECORD TYPE IS 0, 1, OR 2 2 = SASS 3 = SMMR 4 = VIRR
3-4	RECORD SEQUENCE NUMBER
5-6	NUMBER OF TEXT IMAGES TO FOLLOW IN THIS RECORD (MAXIMUM 111)
7-8	CHARACTER SET (0=ASCII, 1=EBCDIC)
9-72	SPARE (ZEROES) (BYTES 1-72 ARE BINARY)
73-N	72-CHARACTER ASCII (EBCDIC) TEXT IMAGES HEADER RECORD: TAPE ID, PROJECT AND SPACECRAFT ID, SYSTEM SOFTWARE VERSION DATE/TIME, DATE/TIME OF TAPE PRODUCTION ALGORITHM ID RECORD: LIST OF ELEMENT NAME, DATE, TIME FOR EACH ELEMENT USED TO CREATE SOFTWARE WHICH PRODUCED THIS TAPE. CONTROL IMAGE RECORD: IMAGES OF CONTROL STATEMENTS USED TO CREATE THIS TAPE, INCLUDING SENSORS REQUESTED, TIME INTERVALS REQUESTED, AND RECORD TYPES REQUESTED. USER CONSTANTS RECORD: COPY OF IMAGES FROM FILE(S) USED TO INITIALIZE USER PROCESSING CONSTANTS, TABLES, ETC. RECORD MAPS: TEXT DESCRIPTION OF CORRESPONDING DATA RECORD, INCLUDING DEFINITION AND UNITS OF EACH DATA CHANNEL.

IN GENERAL, A GDR-FORMATTED TAPE WILL CONTAIN ONE HEADER RECORD AT THE BEGINNING, FOLLOWED BY ONE OR MORE OF EACH OF THE OTHER TYPES OF TEXT RECORDS. EXCEPT FOR THE HEADER RECORD, THE ORDER OF THE OTHER RECORDS IS UNDEFINED.

A PHYSICAL (TEXT) RECORD IS COMPOSED OF 2 TO 112 "LOGICAL RECORDS" OF 72 BYTES EACH AS FOLLOWS:

FIRST LOGICAL RECORD: BINARY CONTROL INFORMATION. THIS IS REFERRED TO AS THE RECORD HEADER (NOT TO BE CONFUSED WITH HEADER RECORD). BYTES 1-8 ARE AS DESCRIBED ABOVE; BYTES 9-72 ARE FILL. INCLUDES IMAGE COUNT (BYTES 5-6) SPECIFYING HOW MANY LOGICAL RECORDS FOLLOW THIS ONE IN THIS PHYSICAL RECORD.

LOGICAL RECORD 2 - IMAGE NUMBER 1 - 72 TEXT BYTES.
LOGICAL RECORD 3 - IMAGE NUMBER 2 - 72 TEXT BYTES.
.
.
.
LOGICAL RECORD N+1 - IMAGE NUMBER N - 72 TEXT BYTES,
N = IMAGE COUNT AS IN RECORD HEADER.

8.3.3 GDR Data Record Format

FOUR TYPES OF GDR DATA RECORDS ARE DEFINED, ALL OF WHICH SHARE THE SAME BASIC FORMAT:

```
 BYTE  CONTENTS
 ----  --------
    1  RECORD TYPE
          8 = BASIC SENSOR        (SB)
          9 = SUPPL. SENSOR       (SS)
         10 = BASIC GEOPHYSICAL   (GB)
         11 = SUPPL. GEOPHYSICAL  (GS)
    2  DATA TYPE
          1 = ALT
          2 = SASS
          3 = SMMR
          4 = VIRR
  3-4  RECORD SEQUENCE NUMBER
  5-8  TIME TAG 1, SECONDS (NOTE 1)
 9-12  TIME TAG 2 (NOTE 1)
13-14  NUMBER OF FOUR-BYTE LOCATION DATA CHANNELS (N1)
15-16  NUMBER OF FOUR-BYTE SCIENCE DATA CHANNELS  (N2)
17-18  NUMBER OF TWO-BYTE LOCATION DATA CHANNELS  (N3)
19-20  NUMBER OF TWO-BYTE SCIENCE DATA CHANNELS   (N4)
21-22  NUMBER OF ONE-BYTE CHANNELS                (N5)
23-24  SPECIAL (NOTE 2)
25---  N1 FOUR-BYTE LOCATION DATA CHANNELS
       N2 FOUR-BYTE SCIENCE DATA CHANNELS
       N3 TWO-BYTE LOCATION DATA CHANNELS
       N4 TWO-BYTE SCIENCE DATA CHANNELS
       N5 ONE-BYTE CHANNELS
       PAD (ZEROES) TO MULTIPLE OF 18 BYTES TOTAL.
```

ALL ENTRIES IN DATA RECORDS ARE UNSIGNED BINARY INTEGERS. RECORDS MAY BE INTERMIXED IN RANDOM ORDER, EXCEPT THAT RECORDS OF A GIVEN RECORD TYPE AND DATA TYPE WILL BE IN CHRONOLOGICAL ORDER. TOTAL LENGTH IS 24 + 4*(N1+N2) + 2*(N3+N4) + N5 + PAD. MAXIMUM LENGTH IS 8064 BYTES.

NOTE 1: FOR RECORDS CONTAINING A SINGLE TIME POINT WHERE HIGH RESOLUTION TIMING IS IMPORTANT, TIME TAG WORD 2 WILL CONTAIN THE FRACTIONAL SECONDS OF THE TIME TAG IN MICROSECONDS. OTHERWISE, TIME TAG 2 WILL CONTAIN THE LATEST TIME IN THE RECORD, IN SECONDS, AND TIME TAG 1, THE EARLIEST. INDIVIDUAL TIME TAGS MAY BE CONTAINED IN THE 4-BYTE LOCATION CHANNELS IN THIS CASE. TIME IS REFERENCED TO BEGINNING OF THE YEAR 1978.

NOTE 2: FOR SMMR BRIGHTNESS TEMPERATURE RECORDS (RECORD TYPE 8, DATA TYPE 3) BYTES 23-24 WILL CONTAIN ZERO FOR THE GRIDS 1-3 DATA, AND ONE FOR THE GRID 4 DATA. THIS FIELD WILL BE REFERRED TO AS THE RECORD SUB-TYPE (SMMR ONLY). A SUBTYPE-1 RECORD ALWAYS IMMEDIATELY FOLLOWS A SUBTYPE-0 RECORD. FOR THE ALTIMETER RECORDS (TYPES 8-11, DATA TYPE 1) AND SASS GEOPHYSICAL RECORDS (RECORD TYPES 10-11, DATA TYPE 2), BYTES 23-24 WILL CONTAIN A COUNT OF THE NUMBER OF DATA POINTS CONTAINED IN THE RECORD (MAX 100).

A PHYSICAL RECORD IS NOT DIVIDED INTO LOGICAL RECORDS, BUT DOES HAVE SEVERAL PARTS, AS FOLLOWS:

RECORD HEADER: BYTES 1-24 CONTAIN CONTROL INFORMATION AS DEFINED ABOVE.

FOUR-BYTE LOCATION DATA CHANNELS, BEGINNING AT BYTE 25. THERE ARE N1 OF THESE, OCCUPYING 4*N1 BYTES. N1 MAY BE 0.

FOUR-BYTE SCIENCE DATA CHANNELS. N2 CHANNELS OCCUPYING 4*N2 BYTES. N2 MAY BE ZERO.

TWO-BYTE LOCATION DATA CHANNELS. N3 CHANNELS OCCUPYING 2*N3 BYTES. N3 MAY BE ZERO.

TWO-BYTE SCIENCE DATA CHANNELS. N4 CHANNELS OCCUPYING 2*N4 BYTES. N4 MAY BE ZERO.

ONE-BYTE STATUS CHANNELS. N5 CHANNELS OCCUPYING N5 BYTES. N5 MAY BE ZERO.

PAD BYTES AS NECESSARY TO MAKE RECORD A MULTIPLE OF 18 BYTES TOTAL.

8.3.4 Data Organization on the Records

8.3.4.1 Basic Geophysical Record. Each SAGB record contains 100 Earth-located and time-tagged wind vector solutions derived from scatterometer data. Data is stored sequentially in parameter blocks; i.e., a record contains 100 time-tags followed by 100 latitude values (in the same order), followed by 100 longitude values, etc., for a total of 38 parameters. Four bytes are required for each time-tag; the other 37 parameters are two-byte channels. Solutions are not ordered within a record in any apparent pattern in either space or time (see Subsection 8.2.2.2). The last SAGB record on a GDR file will contain, in general, fewer than 100 solutions. In this case, unused portions of the record are filled with zeroes.

8.3.4.2 Supplemental Geophysical Record. Each SAGS record contains the paired sensor data ($\sigma°$s and supporting parameters) used to generate, and organized in the same manner as, the 100 wind solutions contained in the mated SAGB record. Thus, data is stored sequentially in paired 100-length parameter blocks; i.e., 100 fore-beam (sensor) measurement time-tags are followed by 100 aft-beam time-tags, which are followed in turn by 100 fore-beam measurement (Doppler cell center) latitudes, etc. Nine parameters are included for each of the orthogonal beams. The kth item ($1 \leq k \leq 100$) in each parameter block corresponds to the kth solution items found in the SAGB parameter blocks.

8.3.4.3 Sensor Records. Each SASB record contains scatterometer $\sigma°$ measurements and supporting parameters for the 15 Doppler channel resolution cells comprising an antenna illumination pattern (i.e., one minor frame of sensor data). Data is stored sequentially in parameter blocks, except for some spacecraft orbit and attitude parameters at the beginning of the record, and a few other single-channel quality flag and spacecraft status indicators. Within the block portion of the record 15 cell-center latitudes are followed by 15 longitudes, etc.: the Doppler channel designations given in Figure 3-5 for k = 1,2,...,15 are maintained here as the implied ordering within each block. Thus, the first 12 values in each ordered set correspond to the primary swath Doppler cells in the sequence k = 1(inner),2,...,12(outer), and the remaining three values are for the nadir-region cells ordered as k = 13,14,15(nadir).

Each SASS (supplemental) record contains data resulting from an instrument calibration sequence. Blocks of length four within the record contain the values of a given parameter in the order derived from the four consecutive calibration frames of the sequence.

8.3.5 Unpacking Data Channels

Data values are written on a GDR in a "packed" binary form. Associated with each data channel is an offset number and a scale factor that must be used to obtain the parameter's actual value. These offsets and scales were used to transform the data values into unsigned positive integers when the GDR records were generated. For example, if a GEOCENTRIC LATITUDE (see Table 8-1) had a real value of -12.34 deg, it was first multiplied by the scale factor 100 and then biased positive by adding 9000, resulting in the packed value of 7766 being written as an integer on the SAGB record. To retrieve the real value, this process must be reversed by first subtracting the offset 9000 from the tape value and then multiplying by the scale .01. All channels in a given parameter block (e.g., the blocks of length 100 in the SAGB record) have the same packing offsets and scales.

8.3.6 Record Contents -- General

All GDR text records have the same basic format as shown in Subsection 8.3.2. In fact, the first four bytes of both text and data records contain identically formatted information that allows the determination of (1) record type (out of 12 possible), (2) sensor type* (value = 2 indicates scatterometer records), and (3) record sequence number (starts at 1 at the beginning of each SASS GDR file).

8.3.6.1 Text Records. The first 72 eight-bit bytes (i.e., one "logical record") of any text record are integer values. Subsequent 72-byte logical records (representing 72 characters) contain the appropriate text images as

*Early GDR designs were to have data from more than one sensor (perhaps all four) on a given GDR tape: such a format required a sensor discrimination key.

described in Subsection 8.2.1; a maximum of 112 logical records (corresponding to the maximum of 8064 bytes per record) is therefore contained in a given text record. Bytes 7 and 8 specify the character set type for the text records. For scatterometer GDRs, the specification is ASCII (0). The format descriptions of GDR-processing data initialization files, from which the constants text records are derived, and record map records (see Subsection 8.2.1) follow.

8.3.6.2 Data Initialization File (Contents of the Constants Records)

THIS FILE CONTAINS RECORDS IN FORTRAN-READABLE CARD IMAGE FORMAT. EACH RECORD CORRESPONDS TO A LINE OF TEXT AND CONTAINS A VALUE TO BE USED TO INITIALIZE ONE OR MORE ELEMENTS OF COMMON BLOCK /XXSAVE/, (WHERE XX IS THE SENSOR CODE), PLUS A REPEAT COUNT AND EXPLANATORY TEXT. THESE IMAGES ARE COPIED TO THE "USER CONSTANTS" TEXT RECORD (RECORD TYPE = 3) AT THE BEGINNING OF THE OUTPUT GDR.

DOUBLE PRECISION ITEMS COME FIRST, FOLLOWED BY A MARKER IMAGE, THEN INTEGER ITEMS, FOLLOWED BY A MARKER IMAGE, THEN REAL ITEMS AND ANOTHER MARKER IMAGE. CONSTANTS PRECEDE VARIABLES IN EACH CLASS. THE RECORD FORMAT IS:

CHAR*	CONTENTS
1-4	INDEX TO DOUBLE, REAL OR INTEGER ARRAY ITEM(S) TO BE INITIALIZED BY THIS VALUE
5	BLANK
6-7	REPEAT COUNT: -1 = COMMENT LINE, IGNORE VALUE 00 = END MARKER 01 = SINGLE ITEM NN = THIS VALUE INITIALIZES NEXT NN ELEMENTS
8	BLANK
9-20	VALUE TO BE USED TO INITIALIZE ITEM(S) FORMAT D12.0 FOR DOUBLE PRECISION ITEMS FORMAT I12 FOR INTEGERS FORMAT E12.0 OR F12.0 FOR REALS
21	BLANK
22-72	FREE TEXT, INCLUDING UNITS AND DEFINITION

INTEGER VALUES MUST BE RIGHT JUSTIFIED; REAL VALUES NEED NOT BE JUSTIFIED, BUT MUST HAVE AN EXPLICIT DECIMAL POINT.

*CHARACTER COLUMNS

8.3.6.3 GDR Record Map Record Format

A RECORD MAP RECORD (SEE SUBSECTION 8.2.1) CONTAINS A SEQUENCE OF 72-CHARACTER TEXT LINE IMAGES, EACH OF WHICH DESCRIBES A DATA CHANNEL OR DATA CHANNEL BLOCK IN A GDR DATA RECORD. EACH MAP RECORD DESCRIBES A SINGLE SENSOR RECORD TYPE AND DATA TYPE. THE FIRST TWO CHARACTERS OF THE MAP NAME ARE THE SENSOR CODE (AL, SA, SM, OR VI), AND THE SECOND TWO ARE THE RECORD TYPE (SB, SS, GB, OR GS), FOR THE RECORD BEING DESCRIBED. THUS, THE BASIC GEOPHYSICAL RECORD MAP FOR THE SCATTEROMETER IS LABELED SAGB. EACH LINE IMAGE HAS THE FOLLOWING FORMAT:

CHAR*	CONTENTS
1-4	SEQUENTIAL CHANNEL NUMBER (CHANNEL 0001 IS THE FIRST FOUR-BYTE LOCATION DATA CHANNEL, IF PRESENT; OTHERWISE, THE FIRST CHANNEL OF ANY LENGTH.)
5	BLANK
6	CHANNEL LENGTH (4, 2, OR 1)
7	BLANK
8-9	REPEAT COUNT INDICATING NUMBER OF SEQUENTIAL CHANNELS TO WHICH THIS LINE APPLIES. IF NEGATIVE (-1) THIS LINE IS A COMMENT.
10	BLANK
11-16	OFFSET TO BE SUBTRACTED FROM CHANNEL WHEN READING GDR. OFFSET IS EXPRESSED AS AN INTEGER IN I6 FORMAT. NOTE: NADIR LATITUDE, A FOUR-BYTE CHANNEL, ALWAYS HAS OFFSET 90000000 (90 DEGREES EXPRESSED AS MICRODEGREES), BUT THE OFFSET IS STATED HERE AS 000000.
17	BLANK
18-29	UNITS OF LEAST SIGNIFICANT BIT, AS FOLLOWS: 18-23 MULTIPLIER IN FORMAT F6.N OR E6.N 24 BLANK 25-29 UNITS FROM TABLE OF STANDARD ABBREVIATIONS BELOW
30	BLANK
31-72	A BRIEF DEFINITION OF THE CONTENT OF THE CHANNEL, IN FREE-FORM TEXT. ONLY CHARACTERS IN THE ANSI 1966 FORTRAN CHARACTER SET MAY BE USED. (THESE ARE LETTERS A-Z, DIGITS 0-9, AND SPECIAL CHARACTERS = + - * / ( ) , . $ AND BLANK.)

FOR DEFINITIONS OF UNITS, THE FOLLOWING STANDARD ABBREVIATIONS ARE USED:

DB	- DECIBELS
DBW	- DECIBELS RELATIVE TO ONE WATT
DEG	- DEGREES ANGULAR MEASURE
DN	- DATA NUMBER (RAW MEASUREMENT)
K	- DEGREES KELVIN
KM	- KILOMETERS
KM2	- SQUARE KILOMETERS
KM/S	- KILOMETERS PER SECOND
M	- METERS
M/S	- METERS PER SECOND
M/S2	- METERS PER SECOND PER SECOND
MB	- MILLIBARS
MG/CM2	- MILLIGRAMS PER SQUARE CENTIMETER
MM	- MILLIMETERS
MM/H	- MILLIMETERS PER HOUR
PCT	- PERCENT (.01 RATIO)
SEC	- SECONDS
UDEG	- MICRODEGREES ANGULAR MEASURE
USEC	- MICROSECONDS
V	- VOLTS
W	- WATTS
1	- UNITLESS INTEGER, OR DISCRETE STATUS BITS

*EACH CHARACTER (CHAR) COLUMN INTERVAL HERE CORRESPONDS TO A DIFFERENT HEADING ITEM IN TABLES 8-1, 8-2, 8-3, AND 8-4, FOR WHICH THIS FORMAT APPLIES.

EACH CHANNEL WILL BE EXPRESSED AS SOME POWER OF TEN TIMES ONE OF THE BASIC UNITS LISTED ABOVE, E.G.:

.01 DEG - ONE HUNDREDTH OF A DEGREE (ANGLE)
1.E-6 DEG - ONE MICRODEGREE (ANGLE)

EXAMPLES:

```
         1         2         3         4         5         6
123456789012345678901234567890123456789012345678901234567890123456
0001 4 01 000000  1.E-6 DEG    NADIR POINT LATITUDE
   2 4  1      0  1.E-6 DEG    NADIR POINT LONGITUDE
  .
  .
  .
  39 2  1      0    1.0 MM/H   RAIN RATE
```

THE INPUT AND OUTPUT ADF SCALING ROUTINES WILL APPLY THE OFFSETS AND MULTIPLIERS AS INDICATED, SO THAT THE CHANNEL VALUES WILL BE DELIVERED TO/RECEIVED FROM THE USER ROUTINES IN THE UNITS SPECIFIED IN COLUMNS 25-29. ALL VALUES WILL BE AVAILABLE INTERNALLY TO ADF PROCESSING ALGORITHMS AS PROPERLY SIGNED, FLOATING-POINT (REAL) VARIABLES, EXCEPT CHANNELS WITH UNITS "1" (STATUS BITS) WILL BE AVAILABLE AS INTEGERS.

8.3.6.4 Data Records. For data records, the first 24 eight-bit bytes contain identifying and specification information. Bytes 5 through 8 contain the start time of the current record truncated to the nearest whole second past the beginning of year 1978. Bytes 9 through 12 contain the record end time truncated to the nearest whole second. For scatterometer geophysical records, the first time is the time-tag of the earliest of the 100 solutions appearing in the record, and the second is the latest time-tag appearing in the record. Bytes 13 through 22 contain the number of data channels within the record which have lengths of 4, 2, or 1 byte (the only possibilities). Bytes 23-24 contain the number of data points in the current record. For SASS geophysical records, this number will be 100 except for the last record (both SAGB and SAGS) on a GDR file, which will contain some number $N \leq 100$.

Bytes 25 and on contain the actual data values, excluding the end-record pad bytes described in Subsection 8.3.1. Multi-byte quantities are written with the high-order byte first on the tape, low-order byte last. Some manufacturers' equipment (e.g., DEC PDP-11) uses a different convention, requiring, for example, that the order of bytes be reversed by pairs.

8.3.7 Basic Geophysical Record (SAGB) Contents

The SASS basic geophysical record content description (map) is given in Table 8-1. Some additional aspects of the wind solutions and their supporting parameters as they are contained in these records should be noted before the data is put to use.

(1) The derived wind speeds contained in the record are defined to be neutral-stability wind magnitudes at a 19.5-m reference height, and are denoted by U(19) in the parameter descriptions (see Table 8-1, parameter channels 1001-1400). The neutral stability wind is defined as the wind speed that would result from a given friction velocity u^* if the atmosphere were neutrally stratified with an adiabatic lapse rate. The magnitude of the friction velocity, which is related to the ocean-surface wind stress τ by $u^* = \sqrt{\tau/\rho}$, where ρ is the air density, is also derived and included in the record (U*, channels 601-1000). The model used to compute u^* from $U_{19.5}$ is given in Subsection 9.4.

(2) Due to the direction ambiguity effect that is inherent in the scatterometer data, each derived primary swath (non-nadir) wind solution typically consists of four multiply-defined "alias" wind directions and four corresponding wind speeds. Since these multiple solution directions tend to be distributed around the four quadrants and are each, on the average, equally likely to be the "correct" solution, there is generally no immediate criterion available for choosing one alias over another (i.e., "de-aliasing") using only the information provided by a SASS GDR. If an unambiguous wind vector solution is nonetheless required, the user must provide the means for performing the direction ambiguity removal for the current form of the GDR data.

Each of the alias directions has a specific speed associated with it, and while the four speeds are usually within .5 m/s of each other, they sometimes differ by more than 1 m/s. The four $U_{19.5}$ speeds are found in the record in the four groups U(19) FIRST SOLUTIONS FOR POINTS 1-100 (channels 1001-1100), U(19) SECOND SOLUTIONS FOR POINTS 1-100, etc. (Note that the FIRST, SECOND, THIRD, and FOURTH SOLUTIONS in the record parameter descriptions refer to the different possible alias multiples of a given wind solution and not to four different wind solutions.) These $U_{19.5}$ arrays are ordered to correspond to the four alias directions found in the channel arrays WIND DIR 1ST SOLNS FOR POINTS 1-100, WIND DIR 2ND ... (2201-2600); i.e., the FIRST SOLUTIONS speeds go with the 1ST SOLN directions, etc. Four friction velocity magnitude measurements u^* are also associated with the alias directions, and are similarly ordered in channels 601-1000.

Some primary swath solutions (less than 10 percent) have only three or even two alias directions.† Three-alias solutions in the record are characterized by having their last channel

†A rumor abounds that there exists a single-alias (no direction ambiguities) solution somewhere in the 15.9 million total.

(FOURTH SOLUTIONS) in the various four-solution groups (speeds, directions, etc.) set to zero, and two-alias solutions have their THIRD and FOURTH alias components both set to zero.

(3) Nadir and non-nadir region solutions are intermingled within a record more or less randomly. Direction information cannot be determined for nadir region wind solutions which, therefore, do not require that $\sigma°$ measurements be taken from orthogonal beams. A nadir solution is thus derived from the one, two, or more $\sigma°$ measurements from Doppler cells 14 and 15 (see Figure 3-5), and taken from one or more beams, that fall within a 1/2 deg square bin (see Subsection 7.1.2.4). (Doppler cell 13, which views the Earth with an incidence angle of about 8 deg and is used to monitor instrument stability, contains little wind sensitivity in its signal and therefore is not used in computing wind solutions.) Nadir speeds appear in the U(19) FIRST SOLUTIONS array (and surface stress in U* FIRST SOLUTIONS); the other three alias speed channels and all four alias direction channels are zero-filled as an unambiguous absence-of-direction-information flag. (Of course, nadir solutions are also characterized by incidence angles smaller than 15 deg.)

(4) The primary-swath solution time-tags, Earth locations (latitudes and longitudes), and incidence angles are somewhat arbitrarily defined as the midpoints of the times, locations, and incidence angles of the sensor data ($\sigma°$) measurements pair that generated the wind solution. This means that a solution time-tag can be as little as a few seconds to as much as nearly two minutes removed from the actual times that the two $\sigma°$ measurements were taken, depending on the cross-track distance of the measurements from the subtrack. A solution location bisects the line joining the centers of the Doppler measurement cell pair, which can range from being coincident to being separated by up to 37 or 50 km (see Subsection 7.1.2.1), depending on whether the data results from a one- or two-sided scatterometer mode. The maximum solution displacement from a $\sigma°$ measurement region center is

therefore on the order of an integrated cell width. (Note that even if the two participating Doppler cells are coincident, they will cover somewhat different regions of the ocean since their orientations are roughly orthogonal.)

Since a nadir region solution is derived from the (one or more) $\sigma°$ measurements that fall within an Earth-fixed bin, its location is defined as the geometric mean of the binned measurements. Similarly, nadir solution time-tags and incidence angles are derived by averaging over the sensor measurements in the bin.

(5) Wind directions are measured in degrees clockwise over the range 0-360 deg in the meteorological "out-of" sense. Thus, 0 or 360 means that the wind is out of the North and 90 means that the wind is out of the East.

(6) There is no preferential ordering implied by the four alias wind direction channels contained within a record: the WIND DIR 1ST SOLNS are, on the average, just as likely to be closest to the "true" wind direction as are any of the other aliases. (They are also just as likely to be farthest from the true direction.) In fact, aliases are usually ordered among the four channels according to increasing angular direction magnitudes.

(7) The PAIR SEPARATION DISTANCE is the distance between Doppler cell centers for the two sensor measurements generating a wind solution. This parameter is undefined (zero-filled) for nadir solutions.

(8) The NUMBER OF BACKSCATTER MEASUREMENTS involved in generating a solution (channels 501-600) would contain more useful information had the binning mode been chosen for grouping all SASS sensor data for GDR production. Due to the cell pairing mode used, these channels are redundantly set to 2 for primary swath solutions, but do give the $\sigma°$ count for the nadir solution bins.

(9) The GEOCENTRIC LATITUDE (101-200) ϕ' and the geodetic latitude ϕ of the solution locations are shown in Figure 8-2. The geodetic latitude ϕ of a point P is the angle that the normal to the

Earth reference ellipsoid forms with the equatorial plane. Normally, map coordinates are expressed in the geodetic system. Thus, if high-resolution wind solution locations are desired, these geocentric latitudes on the record must be converted to geodetic. A good approximate conversion is given by

$$\phi = \phi' + .192429 \sin(2\phi') + .0003219 \sin(4\phi') \qquad (8\text{-}1)$$

where ϕ and ϕ' are in degrees. The conversion (8-1) is accurate to at least .01 deg throughout the range of ϕ (-90°, 90°) and the maximum difference between the two angles (at $\phi' = \pm 45°$) is .19 deg.

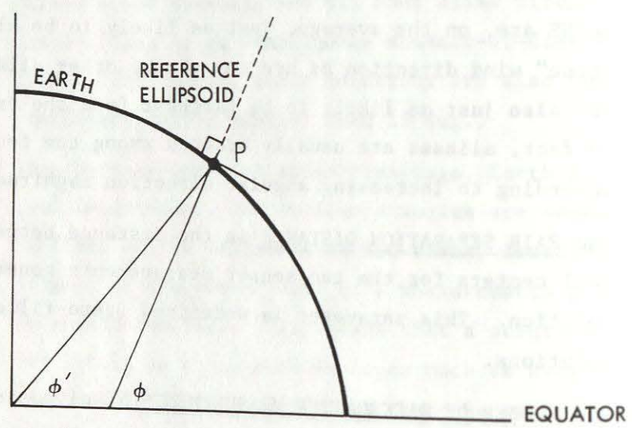

Figure 8-2. Geodetic and Geocentric Latitudes

(10) Solution location LONGITUDES are measured East over the range 0-360 deg.

(11) Wind solutions located several thousand kilometers apart will sometimes be found within the same record due to the appearance of a land mass in the SASS data swath. As a result, intermixing of solutions taken from different oceans can occur within a given record as well as over a number of consecutive records on a GDR.

(12) SIGMA(U*), SIGMA(U19), and SIGMA(DIR) are the formally computed 1-sigma standard deviations on the wind solution components. These solution error levels are derived on the basis of several assumptions (see Subsection 9.11), and are realistic only to the extent that these assumptions are true. A prudent user of the data would probably employ these solution error measures primarily to discriminate relative, rather than to determine absolute, quality.

(13) The RELATIVE PROBABILITY OF SOLN 1, etc. (3001-3400, should, for all practical purposes, be ignored. They are essentially useless as an aid in making the correct choice among the multiple-alias GDR solutions -- see Subsection 10.4.

(14) FORE and AFT BEAM MEASUREMENT ATTENUATION are the (two-way) atmospheric attenuation corrections to the $\sigma°$ pairs computed by the SASS attenuation algorithms (see Section 6). These corrections, which account for that part of the total atmospheric attenuation of the radar signal that exceeds the "clear-air" attenuation, are added to the SASS $\sigma°$ measurements before the sensor data is inverted to obtain the wind solutions. Although total $\sigma°$ attenuation corrections must be nonnegative, the signal loss beyond that due to clear air can have values computed by the attenuation algorithms as small as zero (see Subsection 6.3.5.2).

Since the attenuation computations require SMMR T_B data and the SMMR was a right-side-only viewing instrument, such corrections can only be computed for the SASS measurements taken on the

right side of the subtrack.* Right-side SASS sensor data is, in fact, not always attenuated either: right-side wind solutions derived from wholly unattenuated data or even from $\sigma°$ pairs that are half-corrected and half-uncorrected can result (see Subsection 9.5). To enable a user of the data to determine unambiguously what has been done or not done with regard to atmospheric corrections, a number-magnitude flag scheme has been incorporated into the attenuation channels (3401-3600) for discriminating between the following situations (see Subsection 6.3.6): (a) attenuation corrections that are zero by default because they could not be computed due to an absence of SMMR data (left or right side), and (b) corrections that are computed as zero because of low-attenuation conditions reported by the SMMR. A floor value of .01 dB is the minimum computed attenuation that will be found in the attenuation channels. An identically zero value contained in an attenuation channel is a signal that no attenuation computation could be performed for the corresponding $\sigma°$ measurement.

In addition, an upper-end flag value 99.99 dB is entered into these channels whenever the attenuation value computed by the attenuation processor gets too large. This occurs when the computed attenuation exceeds a certain threshold level beyond which the attenuation algorithms used are thought to break down and to begin yielding increasingly unreliable correction values. Details concerning the conditions under which this upper threshold is reached are given in Subsections 6.3.6 and 9.5.

For nadir region solutions, these channels contain the corrections for the first two (if there is more than one) $\sigma°$ measurements involved in the nadir binning process. The measurement(s) reported may or may not be fore or aft beam data.

*The SMMR swath actually extended slightly to the left of nadir.

(15) FORE and AFT MSMT DATA QUALITY (NSD) contain the normalized standard deviations of the $\sigma°$ measurement pairs corresponding to each wind solution. These NSDs are the RSS total 1-σ errors on the sensor data due to the three primary sources of random error that are intrinsic to the scatterometer measuring process (see Subsection 5.4.1). These basic $\sigma°$ measurement quality factors are computed by the sensor algorithms in the $\delta\sigma°/\sigma°$ sense (see Subsection 7.4.4) and are in percent units over the range 0-100 on the record. Even though $\sigma°$s occur in the SASB sensor records with computed NSDs greater than 100 percent, such values will not be found in these wind record channels because wind solutions are not generated from backscatter measurements having errors exceeding this cut-off value (see Subsection 9.8).

These channels contain the NSDs for the first two $\sigma°$ measurements involved in the binning process for nadir region solutions.

Table 8-1. Scatterometer Basic Geophysical (SAGB) Record Contents Map[a]

Sequential Parameter Channel Position	Channel Byte-Length	No. Repetitions Per Channel Group	Bias-Packing Offset[b]	Scaling Factor[c]	Units	Parameter Description
		-1				SASS BASIC GEOPHYSICAL RECORD MAP CONTROL
		-1				NOTE: ITEM 1 PRECEDED BY 24 BYTES CONTROL INFO[d]
		-1				NOTE:
		-1				EACH RECORD CONTAINS 100 DATA POINTS (WIND SOLUTIONS).
		-1				EACH POINT IS TAGGED WITH THE AVERAGE
		-1				TIME TAG, LATITUDE, LONGITUDE AND
		-1				INCIDENCE ANGLE OF THE BACKSCATTER
		-1				MEASUREMENTS FROM WHICH IT WAS DERIVED.
		-1				IN ADDITION, EACH POINT CONTAINS FOUR ALIAS
		-1				SOLUTIONS FOR WINDS (BOTH U* AND U19).
		-1				BYTES 23-24 (ITEM 11 OF THE CONTROL INFO
		-1				IN THE RECORD HEADER) CONTAIN A COUNT OF
		-1				THE NUMBER OF POINTS ACTUALLY PRESENT IN
		-1				THE RECORD (NOMINALLY 100).
		-1				IF THIS IS LESS THAN 100, UNUSED POINTS
		-1				WILL CONTAIN ZEROES. IF FEWER THAN FOUR ALIAS
		-1				SOLUTIONS ARE DERIVED FOR A POINT,
		-1				UNUSED SOLUTION CHANNELS WILL CONTAIN ZEROES.
1[e]	4	100	0	1.0	SEC	TIME TAGS FOR POINTS 1-100[f]
101	2	100	9000	.01	DEG	GEOCENTRIC LATITUDES FOR POINTS 1-100
201	2	100	0	.01	DEG	LONGITUDES FOR POINTS 1-100
301	2	100	0	.01	DEG	INCIDENCE ANGLES FOR POINTS 1-100
401	2	100	0	1.0	KM	PAIR SEPARATION DISTANCE (KM) POINTS 1-100
0	0	-1				(ZERO FOR NADIR MEASUREMENTS)
501	2	100	0	1.0	1	NUMBER OF BACKSCATTER MEASUREMENTS
0	0	-1				INCLUDED IN DATA POINTS 1-100
601	2	100	0	.0001	M/S	U* FIRST SOLUTIONS FOR POINTS 1-100
701	2	100	0	.0001	M/S	U* SECOND SOLUTIONS FOR POINTS 1-100
801	2	100	0	.0001	M/S	U* THIRD SOLUTIONS FOR POINTS 1-100
901	2	100	0	.0001	M/S	U* FOURTH SOLUTIONS FOR POINTS 1-100
1001	2	100	0	.01	M/S	U(19) FIRST SOLUTIONS FOR POINTS 1-100
1101	2	100	0	.01	M/S	U(19) SECOND SOLUTIONS FOR POINTS 1-100
1201	2	100	0	.01	M/S	U(19) THIRD SOLUTIONS FOR POINTS 1-100
1301	2	100	0	.01	M/S	U(19) FOURTH SOLUTIONS FOR POINTS 1-100
1401	2	100	0	.0001	M/S	SIGMA (U*) 1ST SOLNS FOR POINTS 1-100
1501	2	100	0	.0001	M/S	SIGMA (U*) 2ND SOLNS FOR POINTS 1-100
1601	2	100	0	.0001	M/S	SIGMA (U*) 3RD SOLNS FOR POINTS 1-100
1701	2	100	0	.0001	M/S	SIGMA (U*) 4TH SOLNS FOR POINTS 1-100
1801	2	100	0	.01	M/S	SIGMA (U19) 1ST SOLNS FOR POINTS 1-100
1901	2	100	0	.01	M/S	SIGMA (U19) 2ND SOLNS FOR POINTS 1-100
2001	2	100	0	.01	M/S	SIGMA (U19) 3RD SOLNS FOR POINTS 1-100
2101	2	100	0	.01	M/S	SIGMA (U19) 4TH SOLNS FOR POINTS 1-100
2201	2	100	0	.01	DEG	WIND DIR 1ST SOLNS FOR POINTS 1-100
2301	2	100	0	.01	DEG	WIND DIR 2ND SOLNS FOR POINTS 1-100
2401	2	100	0	.01	DEG	WIND DIR 3RD SOLNS FOR POINTS 1-100
2501	2	100	0	.01	DEG	WIND DIR 4TH SOLNS FOR POINTS 1-100
2601	2	100	0	.01	DEG	SIGMA (DIR) 1ST SOLNS FOR POINTS 1-100
2701	2	100	0	.01	DEG	SIGMA (DIR) 2ND SOLNS FOR POINTS 1-100
2801	2	100	0	.01	DEG	SIGMA (DIR) 3RD SOLNS FOR POINTS 1-100
2901	2	100	0	.01	DEG	SIGMA (DIR) 4TH SOLNS FOR POINTS 1-100
3001	2	100	0	.0001	1	RELATIVE PROBABILITY OF SOLN 1 FOR POINTS 1-100
3101	2	100	0	.0001	1	RELATIVE PROB OF SOLN 2 FOR POINTS 1-100
3201	2	100	0	.0001	1	RELATIVE PROB OF SOLN 3 FOR POINTS 1-100
3301	2	100	0	.0001	1	RELATIVE PROB OF SOLN 4 FOR POINTS 1-100
3401	2	100	0	0.01	DB	FORE BEAM MEASUREMENT ATTENUATION FOR POINTS 1-100
3501	2	100	0	0.01	DB	AFT BEAM MEASUREMENT ATTENUATION FOR POINTS 1-100
0	0	-1				(CELL PAIRING MODE ONLY)
3601	2	100	0	0.1	PCT	FORE MSMT DATA QUALITY (NSD) FOR POINTS 1-100
3701	2	100	0	0.1	PCT	AFT MSMT DATA QUALITY (NSD) FOR POINTS 1-100
3801	2	100	0	1.0		SPARES (100)
						END OF SAGB RECORD MAP[g]

Table 8-1. Scatterometer Basic Geophysical (SAGB) Record Contents Map[a] (contd)

[a]See the GDR record map description in Subsection 8.3.6.3. Each character (CHAR) column interval there corresponds to a different heading item in this table.

[b]When unpacking a data record, first subtract this bias from the channel value found on the GDR.

[c]After subtracting the bias, multiply the result by this scale factor to obtain actual parameter value having units shown in Units column.

[d]The 24 bytes of control data at the beginning of each scatterometer SAGB record contains the following integer information (see data record format, Subsection 8.3.3):

Byte 1 = 10; Byte 2 = 2; Bytes 3-4 = record sequence number.

Bytes 5-8 = earliest solution time contained in record, seconds past beginning of year.

Bytes 9-12 = latest solution time contained in record, seconds past beginning of year.

Bytes 13-14 = 100; Bytes 15-16 = 0; Bytes 17-18 = 400; Bytes 19-20 = 3400; Bytes 21-22 = 0.

Bytes 23-24 = number count of wind solutions contained within record -- nominally 100, except for last record on a GDR file (which will contain ≤ 100 solutions).

[e]This column is the running data channel count, and <u>not</u> the running byte count, within the record. Data channel No. 1, which immediately follows the 24 control bytes, is the first of 100 four-byte time-tags.

[f]Units are seconds past beginning of year 1978.

[g]There is a 4-byte pad (zeroes) at the end of this 8028-byte record.

8.3.8 Supplemental Geophysical Record (SAGS) Contents

The SASS supplemental geophysical record content map is given in Table 8-2. A few aspects of the data contained in the SAGS record, the fore and aft beam sensor measurement pairs that correspond one-to-one to the wind solutions contained in the companion SAGB record (see Subsections 8.2.2.3 and 8.3.4.2), are noted:

(1) The record content is mostly of value for primary swath wind solutions since the nadir binning procedure can involve varying numbers of σ° measurements per solution. For nadir solutions, the fore/aft channels contain the sensor data for the first two σ° measurements involved in the binning process, in no particular order.

(2) Measurement latitudes (channels 201-400) are in the geocentric system. If geodetic latitudes are desired, the conversion given in item (9) of Subsection 8.3.7 applies. Longitudes are again measured East over the range 0-360 deg.

(3) σ°s that are both corrected (1001-1200) and uncorrected (1201-1400) for attenuation are included, with wind solutions being derived from the former.

(4) The NSDs are the same as those included in the SAGB record.

(5) The polarization type -- 0 for horizontal (H) and 1 for vertical (V) -- is given for the measurement pair. Fore/aft polarization pairs occur in one of the four forms: (H,H), (V,V), (V,H), or (H,V).

Table 8-2. Scatterometer Supplemental Geophysical (SAGS) Record Contents Map

Sequential Parameter Channel Position Number	Channel Byte-Length	No. Repetitions Per Channel Group	Bias-Packing Offset	Scaling Factor	Units	Parameter Description
		-1				SASS SUPPLEMENTAL GEOPHYSICAL RECORD MAP
		-1				NOTE ITEM 1 PRECEDED BY 24 BYTES CONTROL INFO[a]
		-1				EACH RECORD CONTAINS 100 DATA POINTS OF SENSOR
		-1				DATA PAIRS. EACH POINT IS TAGGED WITH TIME
		-1				TAG, LATITUDE, AND LONGITUDE. EACH POINT COR-
		-1				RESPONDS TO THE POINT WITH THE SAME INDEX IN
		-1				THE ACCOMPANYING BASIC GEOPHYSICAL RECORD.
		-1				BYTES 23-24 (ITEM 11 OF THE CONTROL INFO
		-1				IN THE RECORD HEADER) CONTAIN A COUNT OF
		-1				THE NUMBER OF POINTS ACTUALLY PRESENT IN
		-1				THE RECORD (NOMINALLY 100). IF LESS THAN
		-1				100, UNUSED POINTS WILL CONTAIN ZEROES.
		-1				FOR NADIR, THE FIRST 2 MSMTS ARE REPORTED,
		-1				THEY MAY OR MAY NOT BE FORE/AFT.
1	4	100	0	1.0	SEC	FORE MEASUREMENT TIME TAG FOR POINTS 1-100
101	4	100	0	1.0	SEC	AFT MEASUREMENT TIME TAG FOR POINTS 1-100
201	2	100	9000	.01	DEG	FORE MSMT GEOCENTRIC LATITUDE FOR POINTS 1-100
301	2	100	9000	.01	DEG	AFT MSMT GEOCENTRIC LATITUDE FOR POINTS 1-100
401	2	100	0	.01	DEG	FORE MSMT LONGITUDE FOR POINTS 1-100
501	2	100	0	.01	DEG	AFT MSMT LONGITUDE FOR POINTS 1-100
601	2	100	0	.01	DEG	FORE MSMT INCIDENCE ANGLE FOR POINTS 1-100
701	2	100	0	.01	DEG	AFT MSMT INCIDENCE ANGLE FOR POINTS 1-100
801	2	100	0	.01	DEG	FORE MSMT AZIMUTH ANGLE FOR POINTS 1-100
901	2	100	0	.01	DEG	AFT MSMT AZIMUTH ANGLE FOR POINTS 1-100
0	0	-1				(CORRECTED FOR ATTENUATION--)
1001	2	100	30000	.01	DB	FORE MSMT BACKSCATTER FOR POINTS 1-100
1101	2	100	30000	.01	DB	AFT MSMT BACKSCATTER FOR POINTS 1-100
0	0	-1				(UNCORRECTED FOR ATTENUATION--)
1201	2	100	30000	.01	DB	FORE MSMT BACKSCATTER FOR POINTS 1-100
1301	2	100	30000	.01	DB	AFT MSMT BACKSCATTER FOR POINTS 1-100
1401	2	100	0	0.1	PCT	FORE MSMT NORMALIZED STD DEV FOR POINTS 1-100
1501	2	100	0	0.1	PCT	AFT MSMT NORM STD DEV FOR POINTS 1-100
1601	1	100	0	1.0	1	FORE MSMT POLARIZATION FOR POINTS 1-100
1701	1	100	0	1.0	1	AFT MSMT POLARIZATION FOR POINTS 1-100
						(0=H, 1=V)
						END OF SAGS RECORD MAP[b]

[a]The 24 bytes of control data at the beginning of each SAGS record contains the following integer information (see data record format, Subsection 8.3.3):

Byte 1 = 11; Byte 2 = 2; Bytes 3-4 = record sequence number.

Bytes 5-8 = earliest wind solution time corresponding to sensor data contained in record, seconds past beginning of year.

Bytes 9-12 = latest wind solution time represented in record.

Bytes 13-14 = 200; Bytes 15-16 = 0; Bytes 17-18 = 800; Bytes 19-20 = 600; Bytes 21-22 = 200.

Bytes 23-24 = same solution count number as in Bytes 23-24 of SAGB record mate.

[b]There is a 10-byte pad (zeroes) at the end of this 3834-byte record.

8.3.9 Basic and Supplemental Sensor Record (SASB and SASS) Contents

The SASS basic and supplemental sensor record content maps are given in Tables 8-3 and 8-4, respectively. A detailed description of the sensor parameters contained in these records -- what they are and how they were computed -- is given in the scatterometer sensor algorithm specifications [3]. Included there is a delineation of all sensor status and data quality flags that were maintained during sensor file processing (see Table 8-3, channels 765-823, and Table 8-4, channels 404-411) to allow the status and health of the scatterometer and the quality of its measurements to be continuously monitored over the mission data set. A subset of these flags that allows the geophysical algorithms to screen out from the inversion process certain σ° measurements that would otherwise lead to wind solutions of impugnable quality is described in Subsection 9.8.

Table 8-3. Scatterometer σ° Basic Sensor (SASB) Record Contents Map

Sequential Parameter Channel Position Number	Channel Byte-Length	No. Repetitions Per Channel Group	Bias-Packing Offset	Scaling Factor	Units	Parameter Description
						SASS BASIC SENSOR RECORD MAP
						NOTE: 24 BYTES CONTROL INFO PRECEDE ITEM 1[a]
1	4	1	000000	1.E-6	DEG	S/C NADIR POINT GEODETIC LATITUDE
2	4	1	0	1.E-6	DEG	S/C NADIR POINT LONGITUDE
3	4	1	0	1.E-6	KM	S/C GEODETIC ALTITUDE
4	4	1	0	1.0		SPARE
5	4	1	0	1.0		SPARE
6	2	1	9000	.01	DEG	ROLL
7	2	1	9000	.01	DEG	PITCH
8	2	1	9000	.01	DEG	YAW
9	2	1	0	.001	KM/S	S/C ALONG TRACK VELOCITY
10	2	1	0	.01	DEG	S/C VELOCITY AZIMUTH ANGLE FROM NORTH
11	2	1	0	.01	DEG	SQUINT ANGLE
12	2	3	0	1.0		SPARES
15	2	15	9000	.01	DEG	CELL LATITUDES (GEOCENTRIC)[b]
30	2	15	0	.01	DEG	CELL LONGITUDES
45	2	15	0	.1	KM	STD DEV OF CELL LOCATIONS
60	2	15	0	.01	DEG	DOPPLER LINE AZIMUTH ORIENTATIONS
75	2	15	0	.01	DEG	INCIDENCE ANGLES (THETA SUB 1)
90	2	15	0	.01	DEG	STD DEV OF INCIDENCE ANGLES
105	2	15	0	.1	KM	SLANT RANGE TO CELLS
120	2	15	9000	.01	DEG	CELL CORNER LATITUDES - LAT1 (GEOCENTRIC)
135	2	15	9000	.01	DEG	CELL CORNER LATITUDES - LAT2 (GEOCENTRIC)
150	2	15	0	.01	DEG	CELL CORNER LONGITUDES - LONG1
165	2	15	0	.01	DEG	CELL CORNER LONGITUDES - LONG2
180	2	15	0	.01	KM	EQUIVALENT CELL BASE LENGTHS
195	2	15	0	.01	KM	EQUIVALENT CELL WIDTHS
210	2	15	0	.01	KM	INSTANTANEOUS CELL BASE LENGTHS
225	2	15	0	.1	KM2	INSTANTANEOUS CELL AREAS
240	2	15	0	.1	KM2	INTEGRATED CELL AREAS
255	2	15	0	1.0		SPARES
270	2	15	0	1.0		SPARES
285	2	15	30000	.01	DB	ANT. PATTERN CORRECTED BACKSCATTER COEFF[c]
300	2	15	30000	.01	DB	INSTRUMENT CORRECTED BACKSCATTER COEFF[d]
315	2	15	30000	.01	DB	FINAL INSTR+ATMOS CORR BACKSCATTER COEFF[e]
330	2	15	0	0.1	PCT	TOTAL NORMALIZED STD DEV OF SIGMA NOUGHT
345	2	15	10000	.01	DB	SIGMA NOUGHT CORRECTION DUE TO ANT. PATT.
360	2	15	0	.01	DB	STD DEV SIGMA-O DUE TO ATTITUDE UNCERT
375	2	15	0	1.0	PCT	NORM STD DEV SIGMA-O DUE COMMUNICATION NOISE
390	2	15	10000	.01	DB	SIGMA NOUGHT ATTENUATION CORRECTIONS
405	2	15	0	1.0		SPARES
420	2	15	30000	.01	DBW	RECEIVED POWER
435	2	15	30000	.01	DBW	ABSOLUTE VALUE OF NEGATIVE RECEIVED POWER
450	2	15	30000	.01	DBW	MEAN NOISE POWER
465	2	15	30000	.01	DBW	CURRENT NOISE POWER
480	2	15	30000	.01	DB	SIGNAL TO NOISE RATIO
495	2	15	0	.001	V	SIGNAL PLUS NOISE
510	2	15	0	.001	V	NOISE
525	2	15	0	.01	DB	INSTRUMENT GAINS FOR SIGNAL PLUS NOISE
540	2	15	0	.01	DB	INSTRUMENT GAINS FOR NOISE ONLY
555	2	15	0	.01	DB	ANTENNA GAIN AT CELLS
570	2	15	30000	.01	DB	SIGMA NOUGHT ANTENNA BIAS CORRECTIONS
585	2	15	0	1.0		SPARES
600	2	15	9000	.01	DEG	ANTENNA ANGLES
615	2	15	0	.01	DEG	AZIMUTH CLOCK ANGLE OF CELLS
630	2	15	0	1.0		SPARES
645	2	15	0	0.1	K	PORT TOTAL SYSTEM TEMPERATURES
660	2	15	0	.01	K	ANTENNA TEMPERATURES

Table 8-3. Scatterometer σ° Basic Sensor (SASB) Record Contents Map (contd)

Sequential Parameter Channel Position Number	Channel Byte-Length	No. Repetitions Per Channel Group	Bias-Packing Offset	Scaling Factor	Units	Parameter Description
675	2	15	0	1.0		SPARES
690	2	1	0	.1	W	TRANSMITTER POWER
691	2	2	10000	.001	DB	ANT SWITCHING ASSY GAINS RECEPTN, TRANSMSN
693	2	1	0	1.0	1	RUNNING FRAME NUMBER COUNTER
694	2	1	0	1.0	1	ORBIT REVOLUTION NUMBER[f]
695	2	1	0	1.0		SPARE
696	2	9	0	1.0		SPARES
705	2	15	0	1.0		SPARES
720	2	15	0	1.0		SPARES
735	2	15	0	1.0		SPARES
750	2	15	0	1.0	1	TOIL FLAGS FOR EXTENDED FOOTPRINTS[g]
765	2	15	0	1.0	1	DATA QUALITY FLAGS[h]
780	1	30	0	1.0		SPARES
810	1	2	0	1.0	1	STATUS FLAGS
812	1	2	0	1.0		SPARES
814	1	6	0	1.0	1	ENGINEERING DATA QUALITY FLAGS[h]
820	1	1	0	1.0	1	DATA QUAL SUMMARY FLAG
821	1	1	0	1.0	1	OPERATING MODE (0-10)
822	1	1	0	1.0	1	ANTENNA BEAM NUMBER (1-4)
823	1	1	0	1.0	1	POLARIZATION (H=0, V=1)
824	1	15	0	1.0	1	TOIL FLAGS (0=OCEAN, 1=LAND, 2=MIXED/UNK)
						END OF RECORD MAP[i]

[a]The 24 bytes of control data at the beginning of each scatterometer basic sensor record contains the following integer information:

Byte 1 = 8; Byte 2 = 2; Bytes 3-4 = record sequence number.

Bytes 5-8 contain the seconds (past the beginning of year 1978) component of the time-tag associated with the frame of data in the record.

Bytes 9-12 contain the fractional seconds component of the time-tag in units of microseconds. Thus, to obtain a high-resolution time-tag, multiply this number by 10^{-6} and add to previous number.

Bytes 13-14 = 5; Bytes 15-16 = 0; Bytes 17-18 = 114; Bytes 19-20 = 660; Bytes 21-22 = 59; Bytes 23-24 = 0 -- not used.

[b]This 15-vector set of measurement values (and all of those following) corresponds to the 15 Doppler-channel components of the given antenna frame. The Doppler channel designations given in Figure 3-5 for k = 1,2,...,15 are maintained here as the implied ordering within the record. Thus, the first 12 values in the ordered set are for the primary swath Doppler cells in the sequence k = 1,2,...,12, and the remaining three values are for the nadir-region cells ordered as k = 13,14,15(nadir cell).

[c]These σ°s are directly out of the radar equation, but corrected for the antenna pattern approximations -- see Subsection 5.3.

[d]These σ°s are formed by adding the antenna biases -- see Subsection 5.4.2 -- to the previous σ°s.

[e]These σ°s are formed by adding the atmospheric attenuation corrections to the previous σ°s. These corrections for atmospheric attenuation are computed and appended to the SASS GDR by the attenuation processor whenever possible -- see Section 6. These σ°s are the final backscatter measurements entered into the geophysical algorithms for wind retrieval computations.

[f]Due to approximation used, the orbit revolution number may be in error by several minutes at some orbit number boundaries.

[g]0 = ocean; 1 = land; 2 = mixed or unknown.

[h]See Section 9.

[i]There is a 5-byte pad (zeroes) at the end of this 1656-byte record.

Table 8-4. Scatterometer Supplemental Sensor (SASS) Record Contents Map

Sequential Parameter Channel Position Number	Channel Byte-Length	No. Repetitions Per Channel Group	Bias-Packing Offset	Scaling Factor	Units	Parameter Description
						SASS SUPPLEMENTAL SENSOR RECORD
						NOTE: 24 BYTES OF CONTROL INFO PRECEDE ITEM 1[a]
1	4	4	000000	1.E-6	DEG	S/C NADIR POINT GEODETIC LATITUDES (4)[b]
5	4	4	0	1.E-6	DEG	S/C NADIR POINT LONGITUDES (4)[b]
9	4	4	0	1.E-6	KM	S/C NADIR POINT ALTITUDES (4)[b]
13	4	4	0	.01	K	HIGH CALIBRATION NOISE TEMPS (4)[b]
17	4	4	0	.01	K	LOW CALIBRATION NOISE TEMPS (4)[b]
21	4	1	0	.01	K	RECEIVER NOISE TEMP
22	4	3				SPARES
25	2	4	9000	.01	DEG	S/C ATTITUDES (4) ROLL[b]
29	2	4	9000	.01	DEG	S/C ATTITUDES (4) PITCH[b]
33	2	4	9000	.01	DEG	S/C ATTITUDES (4) YAW[b]
37	2	4	0	.001	KM/S	S/C ALONG TRACK VELOCITIES (4)[b]
41	2	4	0	.01	DEG	S/C VELOCITY AZIMUTH ANGLES (4)[b]
42	2	15				SPARES
60	2	56	0	.01	DB	INSTR GAIN CURVE INTERCEPTS (1-2,1-4,1-7)
116	2	64	0	.01	DB	INSTR GAIN CURVE INTERCEPTS (1-2,1-4,8-15)
180	2	60				SPARES
240	2	60	0	.001	V	AVG VOLT MEASUREMENTS FROM CAL FRAMES
300	2	30	0	.01	DB	NOISE FIGURE FOR EACH CHANNEL
330	2	1	0	.01	DB	MEAN RECEIVER NOISE FIGURE
331	2	1	0	.001	PCT	ANTENNA SWITCHING ASSY GAIN FOR CALIBRATION
332	2	8				SPARES
340	1	60	0	1.0	1	GAIN CURVE USED FOR EACH GAIN CALIB CALC
400	1	4	0	1.0	1	ANTENNA PORTS
404	1	8	0	1.0	1	STATUS FLAGS (SF1, SF2, FOR FOUR FRAMES)
412	1	2	0	1.0	1	SPARES FOR FLAGS
414	1	50				SPARES
464	1	50				SPARES
						END OF RECORD MAP[c]

[a]The 24 bytes of control data at the beginning of each scatterometer supplemental sensor record contains the following integer information:

Byte 1 = 9; Byte 2 = 2; Bytes 3-4 = record sequence number.

Bytes 5-8 = time-tag in seconds of first frame of the four-frame calibration sequence.

Bytes 9-12 = time-tag in seconds of last frame of the four-frame calibration sequence.

Bytes 13-14 = 12; Bytes 15-16 = 12; Bytes 17-18 = 20; Bytes 19-20 = 295; Bytes 21-22 = 174; Bytes 23-24 = 0 -- not used.

[b]Four values derived from four consecutive calibration frames.

[c]There is a 12-byte pad (zeroes) at the end of this 936-byte record.

SECTION 9

SASS GDR WINDS: CAVEATS AND DISCUSSION

9.1 INTRODUCTION: GENERAL SPEED AND DIRECTION CAVEATS

A prudent user of the scatterometer-derived wind data contained in the SASS GDR tapes would exercise a certain degree of caution. Even a casual reading of the previous sections and some of the cited references -- as well as any familiarity with remotely sensed geophysical data -- will reveal a spectrum of reasons why the instrument's measurements and the sequence of algorithms that constitute the complete processing transfer function could yield some uncertainty in the interpretation and assessment of the end-product wind solutions. In addition, inferences made about the overall statistical quality of the global data set (e.g., estimates of error scatter and bias in the derived wind speeds) based on the results of examining a limited number of selected spot samples could be tenuous -- as could inferences drawn in the reverse direction. The quality of the derived winds could vary throughout the data set in an unpredictable manner due to a number of factors to be delineated below as well as to: (1) possible time variations in instrument communication noise; (2) time-varying instrument health: imperfect instrument status evaluation, undetected telemetry (bit stream) errors; (3) possible undetected land or ice contamination of signal; (4) variations in spacecraft attitude control and pointing error, and attitude anomalies; and (5) effects of possible inappropriate weighting in the least-squares wind estimator combined with variations in the weighting factors (measurement normalized standard deviations).

In spite of all this, Table 1 of [32] summarizes evaluations of data performed to date and shows that, under the best of controlled circumstances (i.e., JASIN [13]) where data sets have been carefully selected to include the best-behaved SASS and surface truth comparison data, results generally fall well within the accuracy specifications imposed prior to the development of the satellite (see Subsection 2.2.1). Nonetheless, even though the GDR data has been screened for detectable anomalies and corrected for known errors to the extent possible within mission constraints, it remains impossible to offer an unqualified and sweeping endorsement. Only a minimal set of data has been subject to close scrutiny during the evaluation workshops [11,12,13,14], and numerous

aspects of the entire process remain unassessed. For example, analyses performed to date have evaluated only mid-latitude, northern hemisphere data*, and the attenuation-correction algorithm assessment has been severely impeded by the lack of accurate surface truth. It is hoped that the entire global SASS wind data set will continue to be evaluated and will yield corroboration of the high-quality assessment offered by the JASIN Workshop effort.

As discussed in Subsection 7.4, the wind vector estimator produces up to four ambiguous "solutions" (aliases) for each off-nadir swath (incidence angle $\theta_I > 20°$) solution attempt. These primary-swath solutions consist of four (or sometimes fewer) speed/direction pairs of which one pair is the desired or "correct" wind vector solution for that data group ($\sigma°$ pair) and the other three pairs are extraneous and "incorrect." The four wind speeds are approximately equal for the set of aliases, but the four alias directions vary greatly. Thus the ambiguity due to aliases refers primarily to direction rather than speed. In general, there is no intrinsic preferred direction implied by the order of the aliases within a solution group (or by any other product of the inversion mechanism): the least-squares estimator yields essentially equal-probability aliases when inverting pairs of $\sigma°$ measurements (see Subsection 7.1.2) to obtain GDR solutions.

There is a school of thought, however, that if the SASS $\sigma°$ data were reprocessed to wind vector using the binning mode (groups of more than two measurements in a solution group -- see Subsection 7.1.2) instead of the pairing mode, then the resulting alias solutions would demonstrate some skill in selecting a preferred wind direction streamline. Such a demonstration has not yet been made. On the other hand, there is information contained in the number of aliases present. Two-alias solutions, which align their directions about 180° apart -- and which occur infrequently compared to four-alias solutions -- usually align their resulting "streamline" direction with surface truth wind direction. This situation generally corresponds to a SASS antenna looking either upwind or downwind. Some weather features can also be extracted directly from fields of alias solutions: the location of high- or low-pressure centers is

*Significant amounts of data from all latitudes and hemispheres have more recently been examined -- with positive results -- by P. Woiceshyn's group, which is attempting to de-alias a global set of SASS-derived winds.

very evident on alias-solution wind vector ("sea-chicken") plots. Such observations were used successfully in a demonstration of manual alias removal (selecting the correct alias solutions in a field of SASS wind vectors) of scatterometer data [40].

It should be noted that statistics cited for any SASS wind direction evaluation, such as in Table 1 of [32], could be misleading. Such evaluations begin by first picking the alias direction that is closest to the ground truth direction for each SASS solution. Throughout these qualitative assessments, SASS is in every case given the benefit of the doubt: the SASS direction closest to the truth wind direction is assumed to be the one that SASS would have reported had the instrument been capable of producing a unique direction. In this sense, the more aliases generated by the instrument signal, the better its chances are. Conceivably, SASS could be wrong by 45°, and the fact could be obscured by a convenient alias. On the other hand, those 45° could represent an error in the "truth" wind direction, in which case the instrument would lose credit for resolving a small-scale feature in an erroneous comparison truth field. Clearly, then, there is difficulty in determining exactly the level of direction skill being exhibited by SASS from such statistical figures of merit. Evidence is given in [38] that this procedure for evaluating the wind direction accuracy is nonetheless justified. It is concluded there that choosing the closest alias direction is the best means for assessing the direction measurement accuracy until an objective selection scheme is implemented.

The principal components of the mechanism used to derive winds from SASS NRCS measurements are a wind vector-to-$\sigma°$ model function (see Subsection 7.3) and a least-squares estimator (see Subsection 7.4) for inverting the data. Since there are uncertainties in both stages of this processing, some caution should be exercised whenever wind results that lie outside the parametric range within which good results have been experienced are used. Possible shortcomings in the inversion process include (see Subsection 7.4.3 for more details): (1) the assumption that uncorrelated Gaussian statistics apply to the distribution of wind-speed error; and (2) the assumption that the general relationship between $\sigma°$(dB) and $\log_{10}$(wind speed) is linear, when, in fact, a more complex relationship probably exists [32]. The model function itself (see SASS1 G-H table, Table 7-1) is based in large part on aircraft data (about 20 aircraft

scatterometer flights) plus some SASS measurements over a limited set of parametric conditions, i.e.:

(1) The wind speed range is about 4 to 28 m/s.

(2) The incidence angle range ($20° \lesssim \theta_I \lesssim 70°$) is divided into only three or four discrete intervals (bins).

(3) The number of data samples for each set of parameter (bin) values is usually 10 to 20.

(4) The measurement Doppler resolution cell sizes differ from SASS to aircraft.

(5) The theories are incomplete (unknown effects exist due to parameters partially or totally unaccounted for).

Such shortcomings establish limits on the range of data that can be used with reasonable confidence. The data base from which the SASS1 model has been derived (i.e., aircraft scatterometer flights, portions of 12 GOASEX [11,12] and North Atlantic SASS overflights, and, finally, the SASS JASIN triangle data set) is very small. This data base has been stretched very far for the purpose of specifying the NRCS signature for both polarizations (V and H), incidence angles from 20° to greater than 60°, all look azimuths, and the full range of wind speeds that need to be included. For this reason, the SASS model function can be considered an NRCS signature only in those parametric areas where large numbers of comparisons have verified the correlation. Much needs to be done to validate -- and possibly improve -- the scatterometer model function, especially at incidence angles below about 25° and above about 50° and at wind speeds above 20 m/s, where high-quality comparison data has been scarce to date. An extensive discussion of the historical development of scatterometry, the synthesis of the SASS1 model function, and an assessment of the derived GDR winds is contained in [32,37,38,39].

The following summarizes those parameter ranges and conditions within which the GDR off-nadir winds should be more carefully scrutinized before in toto acceptance.

(1) Low wind speeds (<5 m/s), especially when combined with higher incidence angles where the signal-to-noise ratio is low. The SASS1-derived NRCS signature is more sensitive to wind speed changes at low incidence angles and less sensitive at high incidence angles than earlier model functions, when weighted aircraft measurements more heavily.

(2) High wind speeds (>25 m/s) -- due to lack of comparison data for model function development.

(3) Incidence angles below about 22° and above 55° -- also where limited data exists for model development. The model H-polarization NRCS-incidence angle dependence for $\theta_I > 50°$ does not conform to previous aircraft measurements or theory. This is believed to be due to the empirical fitting procedure used and the lack of data. However, for the SASS data set, the model is adequate for $\theta_I > 55°$ because very few winds are measured there.

(4) High local wind gradient conditions, where the SASS measurement (Doppler) cell resolution is apt to average out either peak or null wind conditions.

(5) $\sigma°$ measurements not corrected for attenuation, which can result in a significant underestimation of the wind speed in heavy rain conditions -- see Subsection 9.5.

Within the limitations discussed above, the SASS winds have been demonstrated to be within the following limits during the JASIN experiment:

	Mean	Std Dev
Wind speed, m/s	<.1	1.3
Wind direction, deg	<1.7	16.3

These comparisons are well within the tolerances stated as desirable by user groups prior to Seasat launch. The standard deviations here are commensurate with those expected due to the summed effect of measurement noise, absolute NRCS biases, SASS versus truth sampling area differences, mesoscale turbulence, anemometer errors, etc. The SASS has apparently yielded a very successful demonstration of remote sensing anemometry. However, when viewing the rather impressive statistics above, it would be imprudent to ignore the fact that the

SASS1 model function was quite closely "tuned" (by a fitting procedure which essentially minimized the biases observed between the SASS and surface truth winds) to a selected set of the very JASIN data that these statistics are based on.

The remainder of this section is a compilation of more specific caveats, exhortations, and just plain useful information that will hopefully aid in the use, interpretation, and understanding of the SASS data contained on the GDR tapes.

9.2 WIND SOLUTION COMPUTATION USING INCORRECT AZIMUTH ANGLE: CAUSE, EFFECT, AND CORRECTION

The σ° measurement azimuth clock angles provided by the IDPS to the SASS geophysical algorithms via the SDR (see Subsection 4.4.2.7, item 7) were computed relative to the longitude line passing through the satellite nadir point. On the other hand, the σ° azimuth angles ϕ required in the argument χ of the wind-to-σ° model function G-H table (see Subsection 7.3.2) are defined relative to the longitude line located at each σ° measurement footprint (Doppler cell) location. Due to an oversight, the nadir-relative azimuths were erroneously used as arguments to the model function during the geophysical processing that generated the scatterometer GDR wind solution data set. Since the pairing mode for grouping sensor data was used by the wind retrieval algorithms (see Subsections 7.1.2 and 7.2), every primary (off-nadir) swath solution was computed using one forward and one aft antenna σ° measurement that were both azimuthally mislocated. Nadir swath solutions are independent of the error since they consist only of speed and do not depend on azimuth angle.

The effect of using the incorrect azimuth angles on the resulting wind speed and direction solutions contained in the GDRs has been analyzed by Wentz [41]. The total error induced in these solutions by the incorrect azimuth angles can be decomposed into two parts: (1) a bias or absolute offset error on the derived wind direction, and (2) a small residual rms error on both the retrieved wind speed and wind direction. If we let $\hat{\phi}_f$, $\hat{\phi}_a$ be the incorrect forward and aft

antenna azimuth angles, and ϕ_f, ϕ_a be the correct azimuth angles, Wentz shows that if

$$\left.\begin{aligned} \hat{\phi}_f &= \phi_f + B + \gamma \frac{\varepsilon}{2} \\ \hat{\phi}_a &= \phi_a + B - \gamma \frac{\varepsilon}{2} \end{aligned}\right\} \qquad (9\text{-}1)$$

where γ is the sign choice +1 for spacecraft left-side antenna beams (3 and 4 -- see Figure 3-3) and -1 for right-side beams (1 and 2), then:

(1) The direction bias error is deterministic and correctable and, in fact, is equal to B in the incorrect-minus-correct sense: subtracting this bias B from the wind alias directions contained in the GDR SAGB records will result in unbiased solutions. Unbiased here means that when the difference between the corrected direction and the true direction is averaged over the ensemble of possible true wind directions, the resulting mean will be zero.

(2) No such bias occurs in the wind speeds that are retrieved using the incorrect azimuth angles.

(3) A nonzero ε induces residual errors in both retrieved speed and direction which, for a given ε, have zero mean and nonzero rms over the wind direction ensemble. These residual rms errors increase with increasing ε magnitude, but an explicit functional relationship between the errors and ε is not available.

(4) Both the direction bias error B and ε -- and therefore the residual rms speed and direction errors -- increase with increasing latitude magnitude and solution incidence angle. For the lower latitudes both error components are small. The removable bias error is bounded by $-5.8^\circ \le B \le 5.2^\circ$ for $|\text{latitude}| \le 40^\circ$, and by $-15.^\circ \le B \le 7.2^\circ$ over the entire useful mission data set. The residual rms errors in speed and direction

are essentially negligible for |latitude| $\leq 45°$, and are bounded by .7 m/s and 4.5° over the mission data set that omits extreme latitudes and incidence angles. Thus, the wind solution error resulting from the use of incorrect azimuths is seen to be relatively small for much of the data, and is probably ignorable for most purposes after the bias has been removed.

From Eq. (9-1) we see that

$$B = \left[(\hat{\phi}_f + \hat{\phi}_a) - (\phi_f + \phi_a)\right]/2 \tag{9-2}$$

and ε, the relative azimuth separation error, is given by

$$\varepsilon = \gamma(\Delta Az_f - \Delta Az_a) \tag{9-3}$$

where

$$\left.\begin{aligned} \Delta Az_f &= \hat{\phi}_f - \phi_f \\ \Delta Az_a &= \hat{\phi}_a - \phi_a \end{aligned}\right\} \tag{9-4}$$

are the forward and aft beam azimuth angle errors. B can therefore be computed as

$$B = (\Delta Az_f + \Delta Az_a)/2 \tag{9-5}$$

Using the sign convention γ, the azimuth separation error can also be written as

$$\varepsilon = \left|\hat{\phi}_f - \hat{\phi}_a\right| - \left|\phi_f - \phi_a\right| \tag{9-6}$$

which is valid for both port and starboard sides of the groundtrack.

Both the incorrect and correct azimuth angles must be known in order to determine the bias correction factor B and the azimuth separation error ε from Eqs. (9-3, -4, -5). Neither of these angles is available in the GDR basic

geophysical (SAGB) data record, and only the incorrect azimuth angle is available in the supplemental geophysical (SAGS) record -- see Tables 8-1 and 8-2. The azimuth angles for each Doppler cell are essentially fixed for each antenna beam as a function of incidence angle θ_I and cell latitude. (Small insignificant variations occur due to small spacecraft attitude angle oscillations.) Using data from $\sigma°$ basic sensor (SASB -- Table 8-3) records and a set of equations given below, the correct azimuth angle was determined for each beam, θ_I, and latitude. Tables 9-1 and 9-2, which give ΔAz_f, ΔAz_a, B, and ε as a function of latitude, incidence angle, and spacecraft direction (northbound or southbound), were then compiled using Eqs. (9-3, -4, -5).

To use Tables 9-1 and 9-2 the spacecraft direction and wind measurement side (left or right of subtrack) must be known. If the measurement side (or antenna beam numbers) and orbit direction corresponding to the wind solution are not known <u>a priori</u> -- they are not included in the GDR records -- they can be determined by using the incorrect fore and aft beam azimuth angles found in the supplemental geophysical GDR records and Table 9-3. Using the side and direction determined from the fore/aft measurement pair azimuth quadrants and Table 9-3, the wind measurement latitude and incidence angle (contained in the SAGB record) can then be used in Table 9-1 or 9-2 to determine the bias correction factor B and the azimuth separation error ε. Linear interpolation can be used for values of θ_I and latitude not given in the tables.

Table 9-1 is for right-side northern hemisphere and left-side southern hemisphere for both northbound and southbound satellites; Table 9-2 is for left-side northern hemisphere and right-side southern hemisphere. The actual table entries are for the northbound case: southbound entries are obtained by changing the signs and switching the positions of all forward and aft values ΔAz_f and ΔAz_a. For southbound, B retains the same magnitude but changes sign, whereas ε remains unchanged. The top column headings for ΔAz_f and ΔAz_a apply to northern-hemisphere (right-side solutions for Table 9-1 and left-side solutions for Table 9-2) entries, and the lower switched and parenthetically enclosed headings apply to negative latitude (left side for Table 9-1 and right side for Table 9-2) entries. B and ε are independent of latitude sign.

The angle information contained in the tables is accurate to within less than .5°. Note that for the lower latitudes (less than 40°) the bias

Table 9-1. Azimuth Error Bias Corrections and Separation Errors: Right-Side Northern Hemisphere and Left-Side Southern Hemisphere*

Incidence Angle θ_I	Measurement Latitude	ΔAz_f - Beam 1 (ΔAz_a - Beam 3)	ΔAz_a - Beam 2 (ΔAz_f - Beam 4)	Bias Correction Factor B	Azimuth Separation Error ε
20	10(-10)	-.13	-.45	-.3	-.3
25		-.15	-.55	-.4	-.4
30		-.20	-.65	-.4	-.5
35		-.24	-.78	-.5	-.5
40		-.30	-.93	-.6	-.6
45		-.36	-1.12	-.7	-.8
50		-.44	-1.33	-.9	-.9
55		-.55	-1.60	-1.1	-1.1
60		-.68	-1.92	-1.3	-1.2
20	20(-20)	-.27	-.90	-.6	-.6
25		-.34	-1.08	-.7	-.7
30		-.46	-1.28	-.9	-.8
35		-.52	-1.52	-1.0	-1.0
40		-.67	-1.81	-1.2	-1.1
45		-.78	-2.16	-1.5	-1.4
50		-1.10	-2.57	-1.8	-1.5
55		-1.18	-3.06	-2.1	-1.9
60		-1.57	-3.65	-2.6	-2.1
20	30(-30)	-.46	-1.41	-.9	-1.0
25		-.56	-1.68	-1.1	-1.1
30		-.71	-2.00	-1.4	-1.3
35		-.83	-2.37	-1.6	-1.5
40		-1.06	-2.82	-1.9	-1.8
45		-1.23	-3.35	-2.3	-2.1
50		-1.57	-3.99	-2.8	-2.4
55		-1.83	-4.74	-3.3	-2.9
60		-2.38	-5.64	-4.0	-3.3

Table 9-1. Azimuth Error Bias Corrections and Separation Errors: Right-Side Northern Hemisphere and Left-Side Southern Hemisphere* (contd)

Incidence Angle θ_I	Measurement Latitude	ΔAz_f - Beam 1 (ΔAz_a - Beam 3)	ΔAz_a - Beam 2 (ΔAz_f - Beam 4)	Bias Correction Factor B	Azimuth Separation Error ε
20	40(-40)	-.65	-2.03	-1.3	-1.4
25		-.80	-2.42	-1.6	-1.6
30		-.97	-2.89	-1.9	-1.9
35		-1.18	-3.45	-2.3	-2.3
40		-1.45	-4.12	-2.8	-2.7
45		-1.77	-4.92	-3.3	-3.2
50		-2.15	-5.88	-4.0	-3.7
55		-2.63	-7.01	-4.8	-4.4
60		-3.21	-8.38	-5.8	-5.2
20	50(-50)	-.80	-2.99	-1.9	-2.2
25		-.98	-3.56	-2.3	-2.6
30		-1.20	-4.23	-2.7	-3.0
35		-1.48	-5.03	-3.3	-3.6
40		-1.81	-5.98	-3.9	-4.2
45		-2.21	-7.11	-4.7	-4.9
50		-2.72	-8.45	-5.6	-5.7
55		-3.33	-10.04	-6.7	-6.7
60		-4.08	-11.93	-8.0	-7.9
20	55(-55)	-.79	-3.54	-2.2	-2.8
25		-.97	-4.23	-2.6	-3.3
30		-1.25	-5.05	-3.2	-3.8
35		-1.55	-6.03	-3.8	-4.5
40		-1.91	-7.19	-4.6	-5.3
45		-2.33	-8.59	-5.5	-6.3
50		-2.84	-10.26	-6.6	-7.4
55		-3.46	-12.25	-6.9	-8.8
60		-4.21	-14.62	-9.4	-10.4

Table 9-1. Azimuth Error Bias Corrections and Separation Errors: Right-Side Northern Hemisphere and Left-Side Southern Hemisphere* (contd)

Incidence Angle θ_I	Measurement Latitude	ΔAz_f - Beam 1 (ΔAz_a - Beam 3)	ΔAz_a - Beam 2 (ΔAz_f - Beam 4)	Bias Correction Factor B	Azimuth Separation Error ε
20	60(-60)	-.66	-4.25	-2.5	-3.6
25		-.84	-5.24	-3.0	-4.4
30		-1.07	-6.00	-3.5	-4.9
35		-1.38	-7.42	-4.4	-6.0
40		-1.76	-8.45	-5.1	-6.7
45		-2.25	-10.51	-6.4	-8.3
50		-2.87	-11.82	-7.3	-9.0
55		-3.77	-14.88	-9.3	-11.1
60		-4.69	-17.71	-11.2	-13.0
20	65(-65)	-.06	-5.36	-2.7	-5.3
25		-.31	-6.39	-3.4	-6.1
30		-.57	-7.63	-4.1	-7.1
35		-.89	-9.11	-5.0	-8.2
40		-1.30	-10.87	-6.1	-9.6
45		-1.82	-12.98	-7.4	-11.2
50		-2.44	-15.49	-9.0	-13.1
55		-3.22	-18.50	-10.9	-15.3
60		-4.21	-22.08	-13.1	-17.9

Table 9-1. Azimuth Error Bias Corrections and Separation Errors: Right-Side Northern Hemisphere and Left-Side Southern Hemisphere* (contd)

Incidence Angle θ_I	Measurement Latitude	ΔAz_f - Beam 1 (ΔAz_a - Beam 3)	ΔAz_a - Beam 1 (ΔAz_f - Beam 4)	Bias Correction Factor B	Azimuth Separation Error ε
20	70	.95	-6.74	-2.9	-7.7
25		.84	-8.02	-3.6	-8.9
30		.68	-9.54	-4.4	-10.2
35		.35	-11.35	-5.5	-11.7
40		.07	-13.50	-6.7	-13.6
45		-.16	-16.06	-8.1	-15.9
50		-.77	-19.11	-9.9	-18.3
55		-1.75	-22.73	-12.2	-21.0
60		-2.95	-27.04	-15.0	-24.1

*All table entries are in degrees. Table is for northbound satellite: for the southbound case, interchange the forward and aft values ΔAz_f and ΔAz_a and also change their signs. Use the same magnitude for B but with opposite sign for southbound. ε is independent of satellite direction. The top column headings ΔAz_f - Beam 1 and ΔAz_a - Beam 2 apply to right-side wind solutions in the northern hemisphere; the lower headings in parentheses apply to left-side southern-hemisphere solutions. For the southbound southern-hemisphere case, the sign change and both interchanges of headings and entries are necessary.

Table 9-2. Azimuth Error Bias Corrections and Separation Errors: Left-Side Northern Hemisphere and Right-Side Southern Hemisphere*

Incidence Angle θ_I	Measurement Latitude	ΔAz_f - Beam 4 (ΔAz_a - Beam 2)	ΔAz_a - Beam 3 (ΔAz_f - Beam 1)	Bias Correction Factor B	Azimuth Separation Error ε
20	10(-10)	.36	.19	.3	.2
25		.42	.26	.3	.2
30		.49	.33	.4	.2
35		.57	.41	.5	.2
40		.67	.49	.6	.2
45		.78	.60	.7	.2
50		.91	.73	.8	.2
55		1.07	.90	1.0	.2
60		1.25	1.07	1.2	.2
20	20(-20)	.65	.35	.5	.3
25		.92	.48	.7	.4
30		1.05	.61	.8	.4
35		1.28	.74	1.0	.5
40		1.52	.88	1.2	.6
45		1.79	1.06	1.4	.7
50		2.12	1.29	1.7	.8
55		2.51	1.47	2.0	1.0
60		2.90	1.77	2.3	1.1
20	30(-30)	1.19	.53	.9	.7
25		1.52	.71	1.1	.8
30		1.79	.88	1.3	.9
35		2.12	1.06	1.6	1.1
40		2.51	1.25	1.9	1.3
45		2.96	1.49	2.2	1.5
50		3.51	1.73	2.6	1.8
55		4.14	2.00	3.1	2.1
60		4.90	2.36	3.6	2.5

Table 9-2. Azimuth Error Bias Corrections and Separation Errors: Left-Side Northern Hemisphere and Right-Side Southern Hemisphere* (contd)

Incidence Angle θ_I	Measurement Latitude	ΔAz_f - Beam 4 (ΔAz_a - Beam 2)	ΔAz_a - Beam 3 (ΔAz_f - Beam 1)	Bias Correction Factor B	Azimuth Separation Error ε
20	40(-40)	1.89	.66	1.3	1.2
25		2.25	.88	1.6	1.4
30		2.67	1.10	1.9	1.6
35		3.17	1.32	2.2	1.9
40		3.89	1.54	2.7	2.4
45		4.48	1.77	3.1	2.7
50		5.32	2.03	3.7	3.3
55		6.33	2.35	4.3	4.0
60		7.52	2.65	5.1	4.9
20	50(-50)	2.89	.75	1.8	2.1
25		3.42	.91	2.2	2.5
30		4.05	1.09	2.6	3.0
35		4.80	1.25	3.0	3.6
40		5.68	1.42	3.6	4.3
45		6.72	1.55	4.1	5.2
50		7.96	1.66	4.8	6.3
55		9.42	1.75	5.6	7.7
60		11.15	1.64	6.4	9.5
20	55(-55)	3.45	.65	2.1	2.8
25		4.11	.74	2.4	3.4
30		4.89	.83	2.9	4.1
35		5.83	.91	3.4	4.9
40		6.95	.92	3.9	6.0
45		8.29	.82	4.6	7.5
50		9.88	.68	5.3	9.2
55		11.77	.34	6.1	11.4
60		14.03	.37	7.2	13.7

Table 9-2. Azimuth Error Bias Corrections and Separation Errors: Left-Side Northern Hemisphere and Right-Side Southern Hemisphere* (contd)

Incidence Angle θ_I	Measurement Latitude	ΔAz_f - Beam 4 (ΔAz_a - Beam 2)	ΔAz_a - Beam 3 (ΔAz_f - Beam 1)	Bias Correction Factor B	Azimuth Separation Error ε
20	60(-60)	4.38	.30	2.3	4.1
25		5.20	.21	2.7	5.0
30		6.18	.12	3.2	6.1
35		7.35	-.08	3.6	7.4
40		8.56	-.40	4.1	9.0
45		10.39	-.93	4.7	11.3
50		12.12	-1.75	5.2	13.9
55		14.69	-3.12	5.8	17.8
60		17.46	-4.97	6.2	22.4
20	65(-65)	5.43	-.62	2.4	6.1
25		6.47	-1.18	2.6	7.7
30		7.72	-1.80	3.0	9.5
35		9.21	-2.67	3.3	11.9
40		10.98	-3.90	3.5	14.9
45		13.09	-5.81	3.6	18.9
50		15.68	-8.27	3.7	24.0
55		18.61	-11.14	3.7	29.8
60		22.19	-14.01	4.1	36.2

Table 9-2. Azimuth Error Bias Corrections and Separation Errors: Left-Side Northern Hemisphere and Right-Side Southern Hemisphere* (contd)

Incidence Angle θ_I	Measurement Latitude	ΔAz_f - Beam 4 (ΔAz_a - Beam 2)	ΔAz_a - Beam 3 (ΔAz_f - Beam 1)	Bias Correction Factor B	Azimuth Separation Error ε
20	70		DOES NOT GO TO THIS LAT.		
25					
30					
35					
40					
45					
50					
55					
60					

*All table entries are in degrees. Table is for northbound satellite: for the southbound case, interchange the forward and aft values ΔAz_f and ΔAz_a and also change their signs. Use the same magnitude for B but with opposite sign for southbound. ε is independent of satellite direction. The top column headings ΔAz_f - Beam 4 and ΔAz_a - Beam 3 apply to left-side wind solutions in the northern hemisphere; the lower headings in parentheses apply to right-side southern-hemisphere solutions. For the southbound southern-hemisphere case, the sign change and both interchanges of headings and entries are necessary.

Table 9-3. Spacecraft Measurement Side and Orbit Direction

S/C Side	Beams F*/A*	Azimuth Angle Quadrant† F*	Azimuth Angle Quadrant† A*	Azimuth of Forward Antenna	Orbit Direction
Right	1/2	1	2	-	Northbound
Right	1/2	3	4	-	Southbound
Right	1/2	4	1	AZ > 315°	Northbound
Right	1/2	4	1	AZ < 315°	Southbound
Left	4/3	4	3	-	Northbound
Left	4/3	2	1	-	Southbound
Left	4/3	3	2	AZ > 225°	Northbound
Left	4/3	3	2	AZ < 225°	Southbound

*F = forward antenna; A = aft antenna.

†The azimuth angle AZ is in the kth quadrant if $(k-1)\cdot 90° \leq AZ < k\cdot 90°$ for $k = 1,2,3,4$. AZ is the incorrect azimuth angle taken from the GDR SAGS record.

corrections and azimuth separation errors are small. Data is not provided for latitudes beyond 70° or -65° since these higher latitudes contain either ice or land. If azimuth difference angles ΔAz_f, ΔAz_a are desired at the higher latitudes, or more accurate values than given in the tables are required, the equations given below and σ° SASB record data can be used to make the necessary calculations. Figures 9-1 and 9-2 summarize the table bias correction data: B is given as a function of latitude in 10° incidence angle steps for $20° \leq \theta_I \leq 60°$.

Table 9-4 shows how the actual wind speed and direction errors due to the relative azimuth separation error ε vary as a function of that parameter and the actual wind direction. The table is for vertical polarization, $\theta_I = 40°$, and a wind speed of 8 m/s; the wind speed and direction errors are given in units of .1 m/s and degrees. The errors are seen to be greater for the larger azimuth

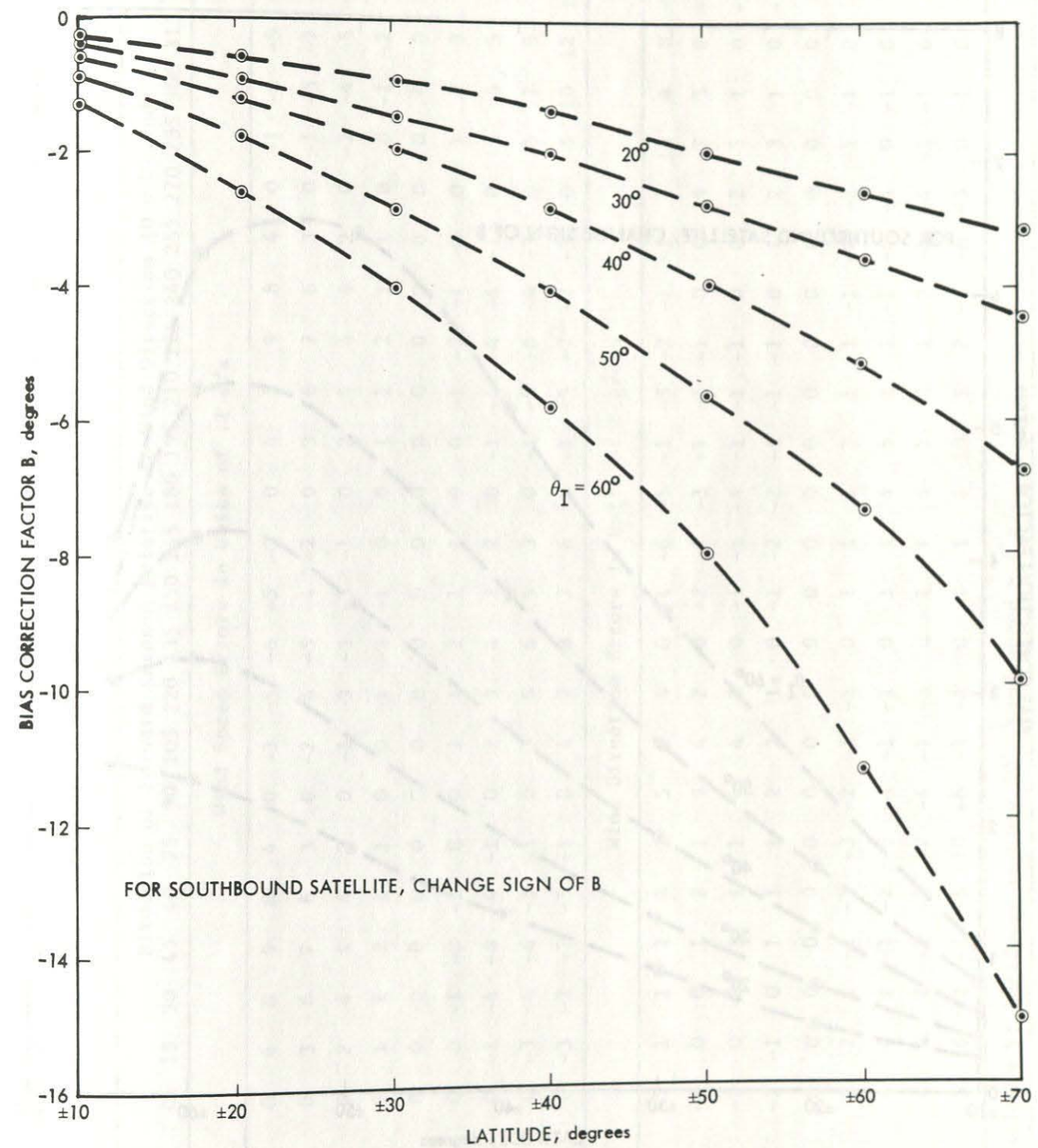

Figure 9-1. Azimuth Error Bias Corrections: Right Side, Northern Hemisphere and Left Side, Southern Hemisphere, Northbound Satellite

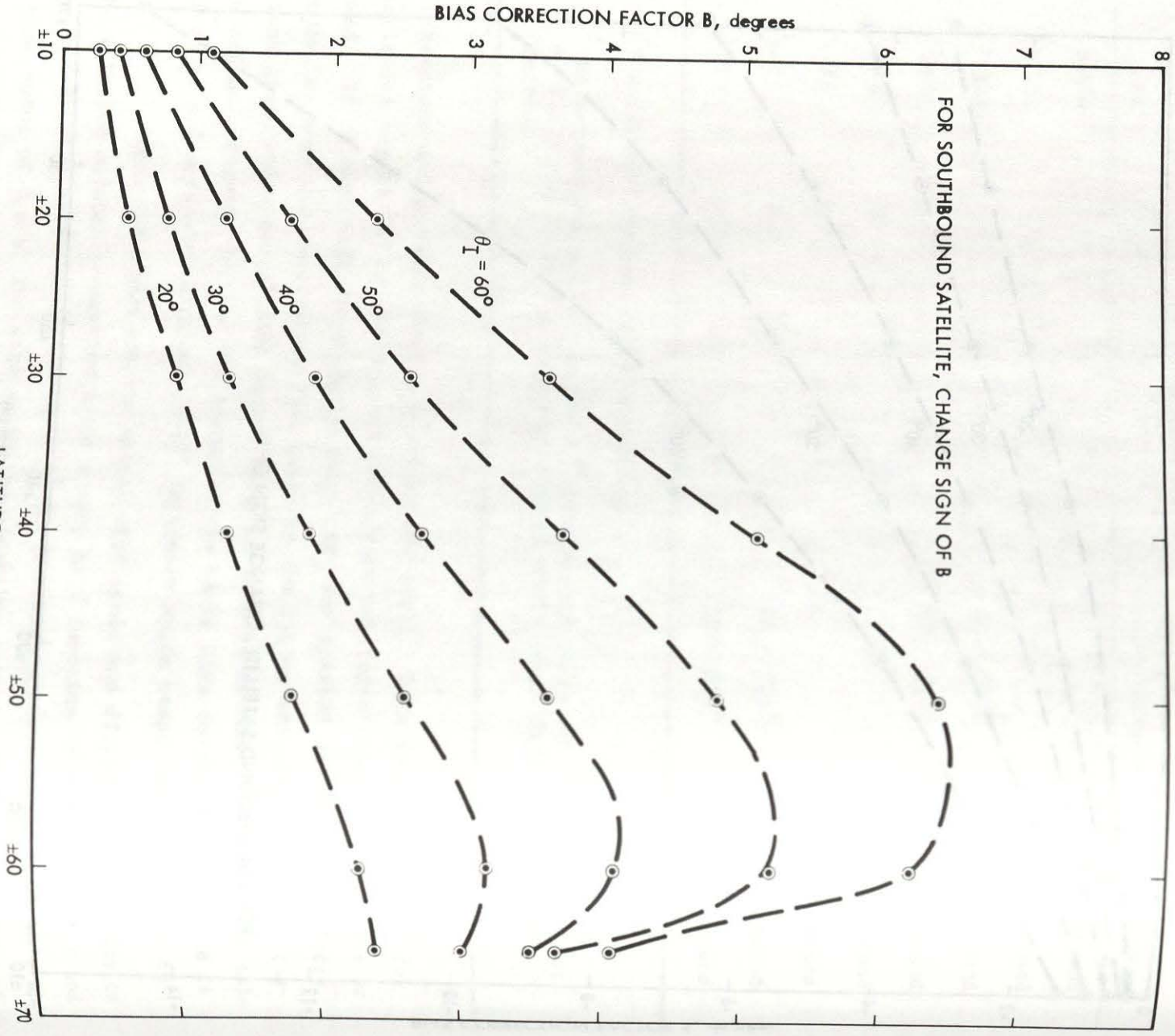

Figure 9-2. Azimuth Error Bias Corrections: Left Side, Northern Hemisphere and Right Side, Southern Hemisphere, Northbound Satellite

Table 9-4. Wind Speed and Direction Errors Versus Relative Azimuth Separation Error ε and True Wind Direction

Relative Error ε	Direction of Forward Antenna Relative to Wind Direction (0 = Upwind)																							
	0	15	30	45	60	75	90	105	120	135	150	165	180	195	210	225	240	255	270	285	300	315	330	345
	Wind Speed Errors in Units of .1 m/s																							
-20	0	4	8	9	8	4	0	-3	-5	-6	-5	-3	0	4	8	9	8	4	0	-1	-6	-9	-6	-1
-15	0	3	6	7	6	3	0	-2	-4	-5	-4	-2	0	3	6	7	6	3	0	-1	-5	-7	-5	-1
-10	0	2	4	4	4	2	0	-1	-3	-3	-3	-1	0	2	4	4	4	2	0	-1	-4	-5	-4	-1
-5	0	1	1	2	1	1	0	0	-1	-2	-1	0	0	1	1	2	1	1	0	0	-1	-2	-1	0
0	0	0	0	0	0	0	0	0	0	0	0	0	0	0	0	0	0	0	0	0	0	0	0	0
5	0	0	-1	-2	-1	0	0	1	1	2	1	1	0	0	-1	-2	-1	0	0	1	2	3	2	1
10	0	-1	-4	-4	-4	-1	0	2	3	4	3	2	0	-1	-4	-4	-4	-1	0	3	5	5	5	3
15	0	-3	-4	-6	-5	-1	0	3	5	6	5	3	0	-1	-5	-6	-4	-3	0	3	7	9	7	3
20	0	-3	-7	-7	-5	-1	0	4	7	8	7	4	0	-1	-5	-7	-7	-3	0	5	10	12	10	5
	Wind Direction Errors in Units of Degrees																							
-20	-5	1	1	2	3	1	5	6	4	0	-4	-6	-5	-1	-3	-2	-1	-1	5	10	4	0	-4	-10
-15	-4	0	0	1	2	1	3	4	2	0	-2	-4	-3	-1	-2	-1	0	0	4	7	3	0	-3	-7
-10	-2	0	0	1	1	1	4	4	1	0	-1	-4	-4	-1	-1	-1	0	0	2	5	1	0	-1	-5
-5	-2	-1	0	1	1	1	2	2	1	0	-1	-2	-2	-1	-1	-1	0	1	2	3	1	0	-1	-3
0	0	0	0	0	0	0	0	0	0	0	0	0	0	0	0	0	0	0	0	0	0	0	0	0
5	2	2	1	-1	-1	-3	-2	-1	-1	0	1	1	2	3	1	1	-1	-2	-2	-1	-1	0	1	1
10	4	4	1	-1	-2	-5	-4	-1	-1	0	1	1	4	5	2	1	-1	-4	-4	0	-1	0	1	0
15	4	4	2	-1	-3	-7	-4	-1	-1	0	1	1	4	7	3	1	-2	-4	-4	-1	-1	0	1	1
20	5	6	2	-2	-5	-10	-6	-1	-1	0	1	1	6	10	5	2	-2	-6	-5	0	-1	0	1	0

Polarization = V; incidence angle = 40°; wind speed = 8 m/s.

separation errors. A complete set of performance tables of the type shown in Table 9-4 has been parametrically generated for all combinations of the following wind states and instrument parameters:

(1) Wind speeds: 4, 6, 8, 12, and 24 m/s

(2) Wind directions: 0° to 345° in 15° steps

(3) Incidence angles: 20°, 30°, 40°, 50°, and 60°

(4) Polarizations: horizontal and vertical

(5) Relative azimuth separation errors (ε): ±20°, ±15°, ±10°, and ±5°

The resulting tables are too voluminous to reproduce here, but they are in the possession of NASA Langley's E.M. Bracalente. A summary of these tables is given in Table 9-5 in the form of wind speed and direction error statistics as a function of ε. The values in Table 9-5 represent the mean, rms, maximum, and minimum errors over all wind speeds and directions, all incidence angles, and both polarizations. No appreciable mean error occurs for either wind speed or direction: the zero mean speed error indicates that the use of the incorrect azimuth angle does not bias the wind speed retrieval. The zero mean direction error is a direct result of the wind direction bias B having already been removed as described above. The rms errors are seen to range from .2 m/s to .7 m/s and from 1.4° to 4.5°, depending on ε; the maximum absolute errors range from .6 m/s to 2.9 m/s and from 3° to 11°.

Using the spherical triangle figure and the equations below, the correct $\sigma°$ measurement azimuth angle for any footprint location can be computed from the incorrect azimuth angle and a few other location parameters found in the basic sensor (SASB) record. The following parameter definitions are needed:

NP = north pole

S/C = spacecraft location

F/P = $\sigma°$ footprint (cell) location

ϕ_{DS} = spacecraft geodetic latitude

f_ℓ = Earth flattening coefficient = 298.257

Table 9-5. Statistics on Wind Speed and Direction Errors Due to Azimuth Separation Error

Relative Azimuth Separation Error ε	Wind Speed Error, m/s				Wind Direction Error, deg			
	mean	rms	max	min	mean	rms	max	min
-20°	0	.7	2.7	-2.8	0	4.5	11.	-11.
-15°	0	.6	1.9	-2.1	0	3.3	8.	-8.
-10°	0	.4	1.3	-1.4	0	2.3	6.	-6.
-5°	0	.2	.6	-.7	0	1.4	3.	-3.
+5°	0	.2	.7	-.7	0	1.4	3.	-3.
+10°	0	.4	1.4	-1.4	0	2.4	6.	-6.
+15°	0	.6	2.1	-1.9	0	3.3	8.	-8.
+20°	.1	.7	2.9	-2.6	0	4.4	11.	-11.

ϕ_S = spacecraft geocentric latitude (not on GDR)

ϕ_F = footprint geocentric latitude

Ω_S, Ω_F = spacecraft and footprint east longitudes

E = spherical triangle excess

Az_I = incorrect footprint azimuth angle

Az_C = correct footprint azimuth angle

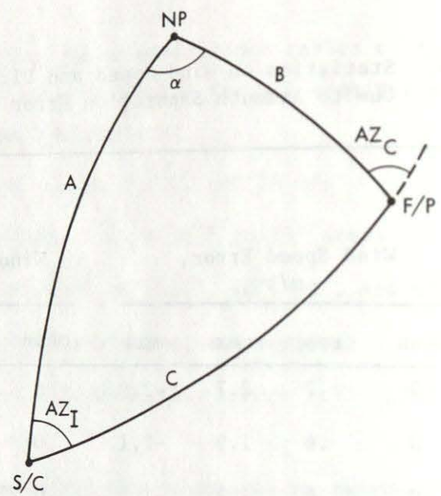

$$\phi_S = \tan^{-1}\left[\tan\phi_{DS}(1 - 1/f_\ell)^2\right]$$

$$A = 90° - \phi_S$$

$$B = 90° - \phi_F$$

$$C = \cos^{-1}\left[\cos\phi_S \cos\phi_F \cos(\Omega_F - \Omega_S) + \sin\phi_S \sin\phi_F\right]$$

$$\alpha = |\Omega_F - \Omega_S| \quad , \quad \text{set } \alpha = 360° - \alpha \text{ if } \alpha > 180°$$

$$S = \frac{1}{2}(A + B + C)$$

$$E = 4\tan^{-1}\left[\left\{\tan\left(\frac{S}{2}\right)\tan\left(\frac{S-A}{2}\right)\tan\left(\frac{S-B}{2}\right)\tan\left(\frac{S-C}{2}\right)\right\}^{1/2}\right]$$

$$\beta = 1, \text{ if } 0° < \Omega_F - \Omega_S \leq 180°; \text{ otherwise } \beta = -1$$

$$Az_C = Az_I + \beta(\alpha - E) \pmod{360°}$$

9.3 NADIR WIND SOLUTION ANOMALIES

Caution must be exercised in the use of SASS nadir wind speed data (see Subsection 3.4.3.5, Section 7, and Subsection 8.3.7). Although the model function for nadir measurements ($\theta_I \lesssim 4°$) is known reasonably well [32], relatively large errors in derived wind speed can result for small errors in the $\sigma°$ measurement value due to the small slope (small H-table coefficient values -- see Subsection 7.3) in the function $\sigma° = \sigma°(U)$ for wind speeds U at low incidence angles. Higher GDR nadir wind speeds (above ~20 m/s) should therefore be carefully scrutinized. Sometimes a few isolated high-magnitude nadir winds (>30 m/s, say) will be found embedded within a group of other relatively low nadir- and primary-swath wind speeds. If such a region of data is not known to be associated with a hurricane or tropical storm, then the isolated high wind speeds are most likely erroneous to some extent and probably should be discarded.

The errors in these high wind speeds can be due to either (1) the presence of rain which was not accounted for -- or which was insufficiently corrected for -- by the SASS atmospheric attenuation algorithm (see Section 6) as discussed in Subsection 9.5 and summarized in Table 9-6; or (2) $\sigma°$ measurements that are afflicted with a large normalized standard deviation (NSD -- see Subsection 7.4.4), i.e., a big measurement uncertainty, due to a low signal-to-noise ratio (SNR). NSDs computed for nadir measurements over water for low-to-medium wind speeds normally range from about 4 to 8%. However, for beams 2 and 3, vertical polarization, the antenna side-lobes, through which the nadir measurements are made, have relatively low antenna gains and therefore yield a lower SNR. The NSD for these beams can run much higher (30-80%) for medium wind speeds, especially if associated with a rain attenuation environment.

Since a .5°×.5° latitude/longitude bin was used for grouping nadir measurements in the wind algorithm (see Subsection 7.1.2.4), the effect of the poorer $\sigma°$ measurements taken by beams 2 and 3, V-Pol, will be essentially weighted out of the solution process in most cases by the superior measurements afforded by the other beam/polarization combinations that happen to fall within the solution group (see wind estimator data weighting -- Subsection 7.4.4). However, in some cases, when only a few (or even one) $\sigma°$ measurement(s) fall in a nadir solution data group, the measurements from the inferior beams may dominate.

Errors in σ° generally are negatively biased (particularly if due to uncorrected rain attenuation), which in turn yields an estimate of nadir wind speed that is too high (see [32], Fig. 9). (An under-estimate of winds will occur with lower σ° values in the primary swath, $\theta_I > 15°$.) By scanning the relevant portion of a σ° GDR sensor file (see Basic Geophysical Record, Table 8-1) to determine (1) if attenuation corrections were generated, and (2) NSD levels, a qualitative case can usually be made for discarding, retaining as is, or possibly reducing in value the nadir wind speed solutions in a given data set that appear to be pathologically large.

9.4 SASS NEUTRAL-STABILITY WINDS, u^*, AND BOUNDARY LAYER CONSIDERATIONS

A question that has not been completely answered is "What aspect of a wind field is it that the scatterometer actually measures?" This relates to what perhaps may be a significant component of the total error in the σ°-to-wind process: the uncertainty in the derived winds due to effects of unmodeled atmospheric stratification and additionally to the uncertain knowledge of the actual atmospheric conditions present when the sensor measurements were taken. Following scatterometer tradition, the model function has been constructed in terms of the neutral-stability 19.5-m wind. However, since the instrument effectively measures the amplitude of capillary and short gravity waves at the Bragg-resonant wavelength (see Subsection 7.1.1), it essentially measures the effect of wind stress on the sea surface. It may thus be more correctly described as a u^*- or τ-measuring device rather than a $U_{19.5}$-measuring device, where the friction velocity u^* and the wind stress τ are related by $\tau = \rho u^{*2}$, with ρ = atmospheric density. u^* (or τ) is the quantity of most interest to oceanographers and meteorologists since it quantifies the momentum exchange between the atmosphere and ocean. u^* is a practical parameter that finds frequent use in oceanographic applications (even though it is not routinely measured); in particular, τ is used to drive ocean wave and circulation models.

The SASS model function can be considered to be an empirical relation established between σ° and the effective neutral wind at 19.5 m. In effect, the model realizes a 19.5-m neutral wind by transforming what is essentially a u^* measurement "up" to the 19.5-m level with a relationship that is valid for a neutrally stable atmosphere. This transformation is intrinsic to the σ°-to-wind

inversion process described in Subsection 7.4 since it has been incorporated directly into the G-H model table values (see Subsection 7.3.3) as part of the overall wind-to-σ° transfer function. The fundamental question that arises is "To what extent do the resulting SASS-derived neutral winds depart from actual winds observed at 19.5 m for environmental departures from conditions of neutral stability at the measurement site?" Whatever the answer, the problem was unavoidable: the existence of a wide range of empirical relationships between wind speed and u^*, the complications of stability considerations, and the relative unavailability of stress measurements forced the scatterometer interpretation to be developed in terms of neutral stability winds. (The rather arbitrary and awkward level of 19.5 m is used because Cardone and Pierson determined that many of the weather ships measured winds with anemometers mounted at that mean height. Rather than extrapolate such measurements to a more reasonable height, 19.5 m became the convention and is still used today as a reference level. Ten meters is the more common reference level used in meteorological calculations.)

Since the scatterometer effectively measures surface roughness, σ° is somehow related to wind effects at the sea surface. The relationship between winds at the surface and winds measured at some height above the surface is dependent on the buoyancy effects of atmospheric stability (the air-sea temperature difference). For a stable atmosphere with a buoyancy flux downward, the momentum from a given wind speed at some height above the sea surface is more effectively transmitted to the water than for unstable conditions. The wind stress τ (and hence u^*) is thus correspondingly higher under stable conditions. When the air temperature is significantly less than the sea temperature, the resulting turbulence in the atmospheric boundary layer upsets the rather simple relationship that applies to a neutrally stable atmosphere; the scatterometer still measures u^*, but the neutral-stability ratio between u^* and $U_{19.5}$ no longer holds. Fortunately, severe variations in the relationship do not occur over major portions of the sea surface, but they are present at some interesting times, such as behind a cold front.

To account for the variation of surface wind profiles due to changes in atmospheric boundary layer stratification, empirical corrections can be obtained by means of the well-established Monin-Obhukov profiles:

$$U(z) = u^* k^{-1}\left[\ln(z/z_o) + \Psi(z/L)\right] \tag{9-7}$$

where

$U(z)$ = wind speed at a specific height z above surface

u^* = surface friction velocity = $\sqrt{\tau/\rho}$

k = von Karman constant $\cong .4$

z_o = surface roughness parameter

Ψ = stability function for momentum which adjusts the simple logarithmic (neutral stability) wind speed profile for atmospheric stability effects

L = Monin-Obhukov length

L is a function of instabilities induced by wind shear and buoyancy flux. For conditions of neutral stability, the buoyancy flux is zero, the Monin-Obhukov length is infinite, and Ψ vanishes; in this case U is called the neutral wind.

Over land, the roughness parameter z_o is generally assumed constant, dependent only on surface features. However, due to the effects of wind on a fluid surface, z_o is dependent on the wind speed over the ocean. While Eq. (9-7) can be derived from turbulence theory, the relationship between z_o and surface wind (as well as the shape of the function Ψ) has not yet been derived theoretically. Various empirical models have been proposed that assume that z_o is dependent only on u^* and increases roughly as u^{*2}; they are summarized in [42]. A form for this dependency is given in [43]:

$$z_o(u^*) = a_1 u^{*-1} + a_2 u^{*2} + a_3 \tag{9-8}$$

where the coefficients a_1, a_2, a_3 take on different values (including zero) from model to model.

For each $U_{19.5}$ wind solution computed for the GDR file, the geophysical processor also computes a corresponding u^* (see Table 8-1, parameter channels 601-1000). u^* is computed by solving the neutral-stability form ($\Psi = 0$) of Eq. (9-7), where $z_o(u^*)$ is given by the form (9-8) and particular coefficient values. Thus, after first computing a neutral wind solution $U_{19.5}$ directly by inverting the model function as described in Subsection 7.4, the corresponding friction velocity is derived by inverting Eq. (9-7) (with z set to 19.5 m) to obtain $u^* = u^*(U_{19.5})$.

The form (9-8) is used in the processing to obtain u^* from $U_{19.5}$, although a curious circumstance dictated a choice of values for the coefficients a_1, a_2, a_3 that do not correspond exactly to any previously espoused model. Kondo's surface layer model [44,45] was the basis for the planetary boundary layer model [46] which was used to generate portions of the "intercomparison data set" used in the JASIN Workshop effort [13]. For consistency, the Kondo model -- which does not reduce to the form (9-8) -- was therefore chosen as the basis for the GDR production for converting $U_{19.5}$ to u^*. However, the decision was made at such a late date that form (9-8), which had already been implemented into the GDR production software, could not be modified except to change coefficient values. It was therefore necessary to find with a fitting procedure the values of a_1, a_2, and a_3 that yielded the resulting function (9-8) that best approximated (in a least-squares sense) the Kondo relationship. The resulting correspondence between $U_{19.5}$ and u^* used to generate the GDR friction velocities is shown in Figure 9-3.

Computationally, several iterations of a Newton-Raphson scheme are used to find u^* for a given $U_{19.5}$: from Eqs. (9-7) and (9-8) with $\Psi = 0$, the $n+1^{\underline{th}}$ iterate value of u^* in terms of the $n^{\underline{th}}$ iterate is found as

$$\left.\begin{aligned} u^*_{n+1} &= \left(p_n + z_{o_n}\ln\left(z/z_{o_n}\right)\right)^{-1}\left(u^*_n p_n + U_{19.5} z_{o_n}/b\right) \\ z_{o_n} &= a_1 u_n^{*-1} + a_2 u_n^{*2} + a_3 \\ p_n &= a_1 u_n^{*-1} - 2a_2 u_n^{*2} \end{aligned}\right\} \tag{9-9}$$

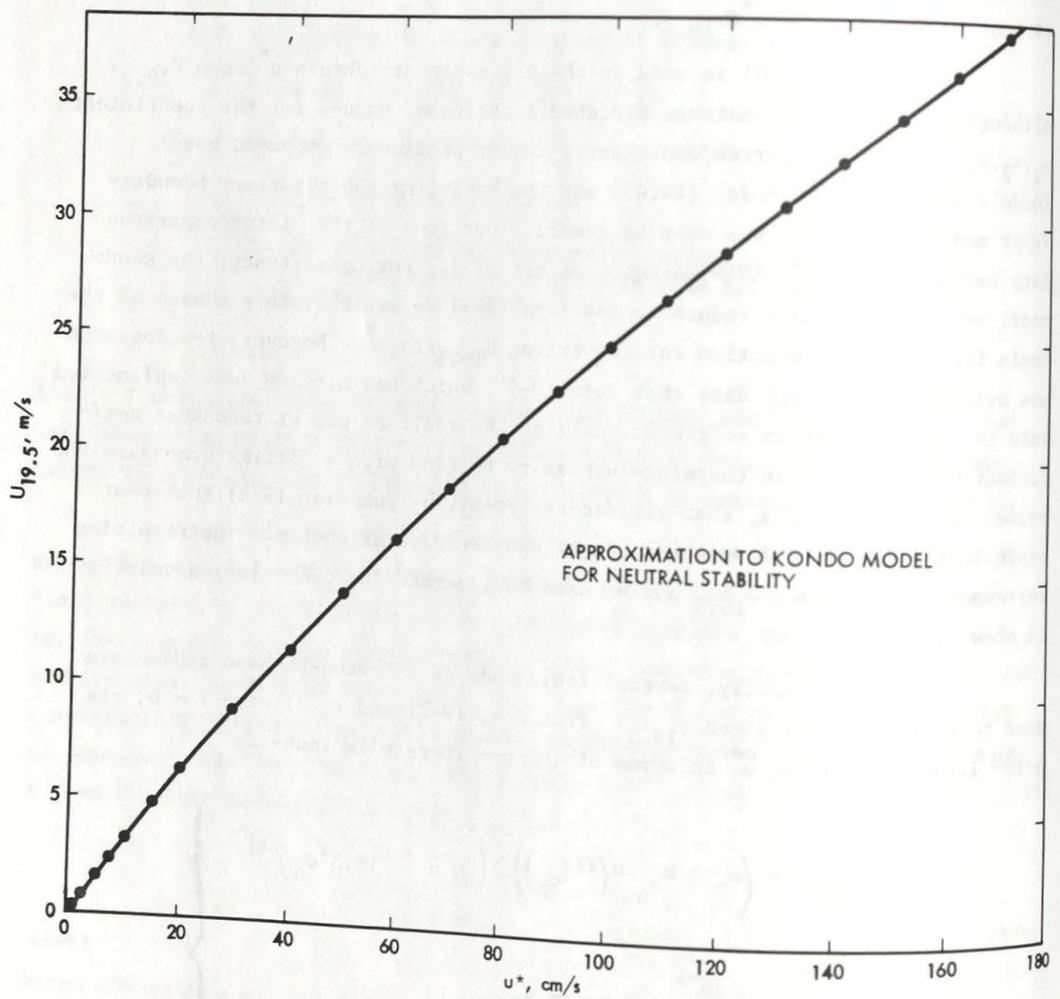

Figure 9-3. $U_{19.5}$ Versus u^* Relationship Used to Obtain SASS Wind Stress

where

u_n^* = wind stress (cm/s)

$U_{19.5}$ = input 19.5-m neutral wind speed (m/s)

z = reference height = 1950 cm

b = .025 (= .01/k)

a_1 = .3905

a_2 = 1.604×10^{-5}

a_3 = -.017465

n = 0,1,2,...

Iterative forms similar to Eqs. (9-9) are used to compute the formal 1-sigma standard deviations σ_{u^*} (see Table 8-1, parameter channels 1401-1800) on u^* as a function of $\sigma_{U_{19.5}}$, the 1-sigma standard deviations on $U_{19.5}$ (see channels 1801-2200). They are readily derived using

$$\sigma_{u^*} = \left(\frac{\partial U_{19.5}}{\partial u^*}\right)^{-1} \sigma_{U_{19.5}} \tag{9-10}$$

and Eqs. (9-7) and (9-8).

No correction is made to the SASS-derived wind directions to account for possible turning of the wind as a function of vertical location through the surface layer. Such turning of the wind through the surface layer could be a small source of error when comparing SASS winds against observations at various heights. It is assumed that the turning angle of the wind in the surface layer is generally less than 10° [42].

Halberstam [42,47] has studied the structure of the errors that can be expected when stability or height factors are ignored in comparing SASS-derived winds or wind stress. He shows that deriving neutral winds at a standard height mitigates errors. The neutrality assumption involves only minor errors ($\lesssim$6%) for unstable conditions but substantially larger errors for stable conditions. Height adjustments become significant for observation levels close to

the surface (<5 m) where the logarithmic profile becomes more pronounced. Although differences between various formulations of u^* can account for up to ∿15% of the stress value, he finds little statistical difference in comparisons between SASS and conventional observations as a function of variations in the u^* formulations. This is probably because the degree of refinement is within the combined noise level of the SASS data and the other observations.

9.5 σ° CORRECTION FOR ATMOSPHERIC ATTENUATION

The algorithm for computing the correction for the SASS two-way atmospheric attenuation and the underlying theory is described in Section 6 and [22] and evaluated in the latter. These attenuation corrections, which account for that part of the total atmospheric attenuation of the radar signal that exceeds the "clear-air" attenuation, are added to the σ° measurements before the sensor data is inverted to obtain the wind solutions. The clear-air attenuation component (i.e., the baseline signal loss incurred over the two-way paths through minimally attenuating clear air) is accounted for by different means: it is integrally incorporated into the σ°-to-wind model function used to invert the sensor data. Although σ° attenuation corrections must be nonnegative, the signal loss beyond that due to clear air can have values computed by the attenuation algorithms as small as zero. On the other hand, significant amounts of SASS data cannot be corrected for attenuation by the algorithm because of the lack of overlapping SMMR data (see below). To prevent potentially ambiguous zero values from appearing in the GDR records, a floor value of .01 dB is the minimum (two-way) attenuation that is entered into the attenuation channels (see Table 8-1, channels 3401-3600) -- and added to σ° -- when derived from SMMR data. A zero-dB value for a correction is a flag that means no attenuation computation could be performed for the corresponding σ° measurement (with no correction added) -- see Subsections 6.3.6 and 8.3.7.

Since the attenuation computations require SMMR T_B data and the SMMR was a right-side-only viewing instrument, such corrections are computed only for SASS measurements taken on the right side (beams 1 and 2) of the subtrack. (The SMMR swath actually extended slightly to the left of nadir, allowing a thin strip of left-side nadir (cell 15) data to be (sometimes) corrected for attenuation.) This means that right-side SASS wind solutions are derived from attenuated sensor

data (whenever possible) and left-side solutions result from unattenuated data. Right-side SASS σ° data is, in fact, not always attenuated either since, for various reasons (e.g., data outages, non-overlapping edges of SASS and SMMR swaths), SMMR data is not always available in coincidence with SASS data. Attenuation outages in SASS right-side sensor data can potentially yield wind solutions derived from σ° pairs that are half-corrected and half-uncorrected -- an undesirable circumstance if it occurs in a high-attenuation (high rain rate) region of data coverage.

Another problem sometimes occurs at the other end of the attenuation spectrum: when the computed attenuation exceeds a certain threshold level beyond which the algorithm used is thought to break down (saturate) and to begin yielding increasingly unreliable correction values, an upper-end flag value of 99.99 dB is entered into the attenuation channels (see Subsection 6.3.5). σ° measurements for which such corrections have been "calculated" are omitted from the wind inversion process; no wind solutions will therefore be found on the GDRs that would have been derived from such upper-limit (as perceived by the correction algorithm) attenuation environments. Of course, the occurrence of these out-of-range conditions can be observed by inspection of the GDR Basic Sensor Record (see Table 8-3, channels 390-404). Such a flag could yield useful information about high attenuation activity regions. It should be noted that many SMMR measurements of ice or partial-ice regions used by the SASS attenuation algorithm yield these upper-limit correction flag values, and they will therefore be frequently found at the more extreme latitudes where the TOILing process (see Subsections 6.1-2) has incorrectly flagged ice-contaminated measurements as "all-ocean" data (see Subsection 9.9).

The out-of-range flag is set under the following circumstance (see Subsection 6.3.6). Let α be the total one-way attenuation computed for the scatterometer frequency 14.6 GHz at the reference incidence angle $\theta_I = 49°$, and, furthermore, let α_1 and α_2 be those attenuations computed using SMMR channels 18 and 37 GHz, respectively. If both $\alpha_1 > 3.$ dB and $\alpha_2 > .4$ dB for the $k^{\underline{th}}$ Doppler cell, then the threshold is considered to be exceeded and 99.99 dB is entered into the $k^{\underline{th}}$ attenuation channel for the data frame being processed.

Since the right-side σ° measurement pairs where overlapping SMMR data was unavailable, as well as all left-side data, have no attenuation corrections applied, potentially large wind speed errors can result if high rain rates occurred in the Doppler cell field of view. σ° measurements with uncorrected attenuation yield wind speeds that are underestimated for primary off-nadir swath solutions ($\theta_I \geq 20°$), since such scatterometer-derived σ°s will be undervalued -- see [32]. For nadir-cell measurements the lower values of σ° result in an overestimate of wind speed, since backscatter decreases with increasing wind speed in this region.

Table 9-6 summarizes the percent wind speed error that is estimated to occur for various rain rates, incidence angles, and polarizations. The wind speed error entries have been calculated using the SASS1 model function G-H table (see Table 7-1) along with estimates of the attenuation that the SASS signal would suffer for a somewhat simplistic rain scenario. The table percentage error values were calculated for the upwind case ($\chi = 0°$), where the error is a maximum -- because H is a minimum. These errors are actually derived as the average of the results for the two look directions $\chi = 0°$ and $\chi = 90°$, which corresponds to a forward- and aft-beam view of the same wind. Figure 9-4 shows wind speed errors versus actual wind speed for vertical polarization at various rain rates and a nadir and off-nadir incidence angle. The attenuation values given in the table do not include attenuation due to cloud absorption (see Subsection 6.3.1.1), the effect of which is small (<.4 dB) and results in less than a 5% error in the table entries. The attenuation correction upper-limit threshold value discussed above occurs for a rain rate of approximately 8 mm/h.

Bracalente and Fedor (private communication) have recently obtained updated average values for the empirical constants K and p found in the rain absorption model equation (6-12) after examining data from several regions and several types of storms. Using their values (cf., Figure 6-5) and an assumed rain column of 3 km that is constant as a function of height, the two-way attenuation due to rain at an incidence angle θ_I can be expressed as follows using Eq. (6-12):

$$\alpha_{dB} = \frac{3}{\cos\theta_I} (.06R^{1.145}) \qquad (9\text{-}11)$$

Table 9-6. Estimate of Wind Speed Errors for Various Rain Rates, Incidence Angles, and Polarizations

Incidence Angle θ_I, deg	R = 4 mm/h			8 mm/h			12 mm/h			16 mm/h		
	Atten,[a] dB	Wind Speed Error,[b] % V-Pol	Wind Speed Error,[b] % H-Pol	Atten,[a] dB	Wind Speed Error,[b] % V-Pol	Wind Speed Error,[b] % H-Pol	Atten,[a] dB	Wind Speed Error,[b] % V-Pol	Wind Speed Error,[b] % H-Pol	Atten,[a] dB	Wind Speed Error,[b] % V-Pol	Wind Speed Error,[b] % H-Pol
20	1.01	-15	-16	2.15	-29	-30	3.42	-42	-44	4.75	-53	-66
40	1.2	-13	-12	2.54	-25	-24	4.	-36	-34	5.6	-47	-57
55	1.6	-16	-14	3.4	-30	-26	5.4	-44	-46	7.5	-55	-60
Nadir[c] 0°	.9	43	43	1.95	118	118	3.1	245	245	4.3	458	458

[a] α_{dB} = atten = two-way attenuation.

[b] Percent wind speed error = $100\left[1 - 10^{(-\alpha_{dB}/10H)}\right]$, where H = slope coefficient from G-H table.

[c] Nadir wind speed error is positive.

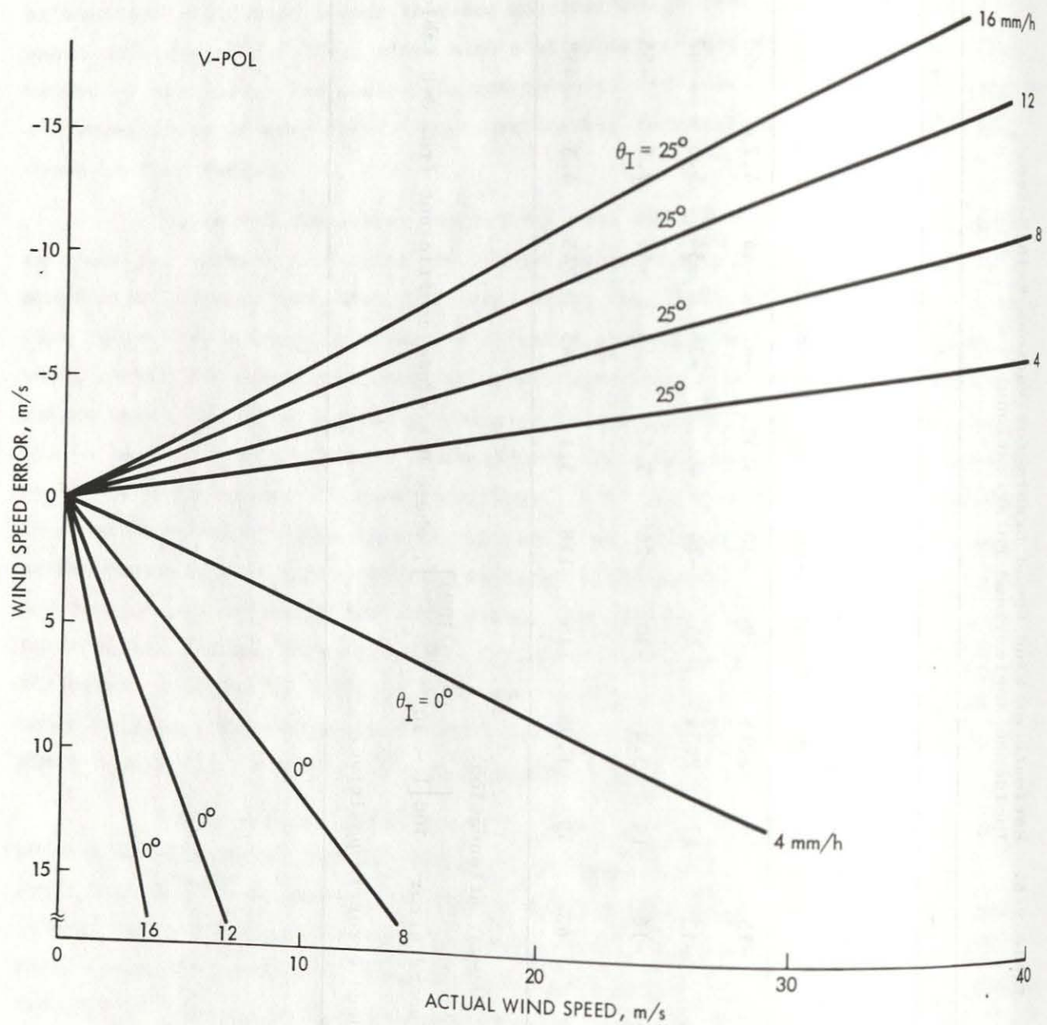

Figure 9-4. Estimate of Nadir and Off-Nadir Wind Speed Error for Various Rain Rates

where R is the rain rate in mm/h. The attenuation values given in Table 9-6 are derived from Eq. (9-11).

Using the model relationship given in Subsection 7.3.1 between $\sigma°$ and wind speed U, there results

$$U = 10^{H^{-1}(\sigma°/10 - G)} \tag{9-12}$$

where $\sigma°$ is now in dB units, U is in m/s, and G and H are values derived from the G-H table as functions of θ_I and the relative wind direction χ. If the measured backscatter value $\sigma°_m$ has suffered an attenuation, then the actual ocean-surface $\sigma°$ is given by $\sigma° = \sigma°_m + \alpha_{dB}$, where $\alpha_{dB} > 0$ is the two-way attenuation. Assuming that G and H remain constant for such a variation in $\sigma°$, the "correct" wind speed is given by Eq. (9-12), and the uncorrected speed is

$$U_m = 10^{H^{-1}(\sigma°_m/10 - G)} \tag{9-13}$$

so that

$$r \equiv U_m/U = 10^{H^{-1}(\sigma°_m - \sigma°)/10} = 10^{-\alpha_{dB}(10H)^{-1}} \tag{9-14}$$

The percent wind speed error $(\Delta U/U)\times 100$, where $\Delta U = U - U_m$, for Table 9-6 is then given by 100(1-r). If a SASS wind user has some knowledge of rain contamination in any left-side (or uncorrected right-side) data, Table 9-6 or the above expressions can provide a qualitative correction to the data.

As seen in Table 9-6 and Figure 9-4, nadir wind speed measurements are very sensitive to uncorrected attenuations -- see Subsection 9.3. If somewhat isolated values of high nadir wind speeds appear in the midst of relatively low winds, it is probably an indication that (1) rain was present in the solid angle subtended by one or more resolution cells in the region, and (2) at least some of this rain was not detected -- or was incompletely detected -- by the attenuation algorithm, and was therefore not properly accounted for.

9.6 σ° V-V, H-H, AND V-H POLARIZATION PAIRING COMBINATIONS: POTENTIAL RESULTING VARIABILITY IN WIND SOLUTION DIRECTIONS

Wind vector solutions derived from SASS data have not infrequently been observed to exhibit considerable variation in (alias) directions as a function of the polarization combination of the paired sensor data used to generate the solutions (see Subsection 7.1.2) for data taken in the dual-polarization instrument modes (3 and 4). Such direction variation is observed between off-nadir solutions contained within rather small regions -- sometimes even between neighboring solutions located just a few kilometers apart when there are no significant wind gradients in the area. As described in Subsection 7.1.2.3, solutions derived from mode 3 and 4 data frequently occur in tight spatially clustered groups of three, where the first member of the triple derives from the measurement-pair type (V,V), the last from type (H,H), and the middle from either (V,H) or (H,V) (see, for example, Figure 4-33 in [13]). Each of these wind vector solution groups results from two sets of adjacent fore- and aft-beam σ° pairs, where one of the V- or H-polarized σ°s is used (somewhat redundantly) in the generation of two of the triple's three solutions -- see Subsection 7.1.2.1. It is between individual members of such a solution triple that direction variability is most often observed: the (H,V) (or (V,H)) pair solution will show significant differences in each of the four (or fewer) alias directions when they are compared against the corresponding alias directions offered by the neighboring (V,V) or (H,H) solutions. At the same time, a comparison between the corresponding (V,V) and (H,H) alias directions will show complete agreement (to the accuracy level apparent on plots) for nearly all occurrences of such triples. A typical variability pattern for a three-alias solution triple is

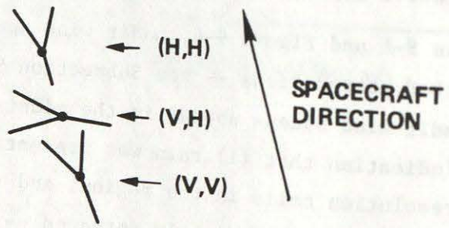

The cause of this erratic direction behavior in the cross-polarization data is not completely known, although the following observations yield a strong candidate. The vertical and horizontal polarization components of the SASS1 model function G-H table (see Subsection 7.3) were derived separately by the application of some fitting procedures on disjoint sets of V-pol and H-pol data. As a result, relative biases could certainly exist between the V and H model components due to polarization-dependent absolute NRCS errors or other inaccuracies in the data base used. Such relative biases could lead to unstable wind direction determination in those parametric regions of the Q-functional (Eq. 7-9) domain where Q, whose local minima yield the various wind vector alias solutions (see Subsection 7.4), is least sensitive to changes in its direction arguments. Thus, small discrepancies in the observational residuals (the right-hand-side terms in Eq. 7-9), coupled with low sensitivity of the sum-of-squares (Q) to direction, could generate wind vector solutions with the observed large direction variability. Perhaps fortunately, only a small fraction (<10%) of the SASS mission data set consists of this cross-polarization data because the instrument was in single-polarization modes most of the time.

Since the polarization type (V or H) of both σ°s in each fore-aft measurement pair that generates a GDR off-nadir wind solution is given separately in the SAGS record (see Table 8-2, channels 1601-1800), the user can easily omit all (or selected subsets of) cross-polarization solutions from any application of the data, if desired. Note that a type III GDR tape copy obtained from NOAA-EDIS (see Subsection 1.8) will not allow this selection process to be performed since these data files (extracted from the complete type I GDRs) do not contain the SAGS records -- see Subsection 1.6 and Section 8).

9.7 QUALITATIVE ERROR CONSEQUENCES OF FINITE-EXTENT, NON-COINCIDENT SASS MEASUREMENT CELLS, LOCAL WIND TURBULENCE, AND IMPERFECT SURFACE TRUTH OBSERVATIONS

The purpose of the Seasat Workshops has been in part to determine the ability of the SASS to measure the winds over the ocean. A significant portion of the workshop work has been expended on attempting to explain -- aside from any shortcomings in the model function relating σ° to winds -- why the SASS-derived winds do not agree exactly with the winds measured by an anemometer on a platform

located somewhere near the region where the SASS measurements were taken. Along with communication noise, attitude errors, and incorrect model function, the dominant causes of the scatter found when comparing SASS GDR winds and conventional winds are: (1) effects of mesoscale turbulence, (2) non-coincidence of fore and aft cells in SASS orthogonal measurement pair, (3) lack of exact space and time coincidence between SASS and conventional measurements, and (4) inaccurate conventional wind observations. The effect of communication noise and attitude errors on σ° is discussed in Subsection 5.4, and the manner in which these random measurement fluctuations propagate into random errors in the derived winds is discussed at length by Pierson in [48]. The effect of an imperfect model function is discussed previously in this section and in numerous other cited references.

The winds reported by SASS are not a measurement of a 50×50-km box on the surface of the Earth; rather, they are the wind derived by inverting a pair of orthogonal backscatter resolution cells separated in time by up to three minutes, with each extending over a region that is approximately 18×60 km, and oriented about ±45° relative to the spacecraft subtrack. These two cells have incidence angle differences of up to 2° and can be separated by cell center distances of up to 50 km (see Subsection 7.1.2). The differences in azimuth and incidence angle are accommodated by interpolation of the model function table (see Subsection 7.3), but meteorological considerations, examined rather extensively by Pierson [49] and others, are necessary to assess the variations in derived wind speed due to incomplete sampling of a measurement resolution cell, non-colocated cells, and time differences. It is well to recall here (Subsections 3.4.3.3 and 5.2) that a measurement cell "sample" is actually derived by an averaging process applied to a sequence of 61 overlapping IFOV samples of the surface distributed throughout a 1.89-s measurement period. In general, winds measured by SASS will in fact have variances due to incomplete area sampling as well as to the existence of time and distance gradients in the actual wind between the corresponding backscatter measurement samples used to derive the wind. The effects of these complex sources of "error" are typically not separable from the true synoptic wind, except perhaps on a statistical basis. Nonetheless, each SASS measurement is approximately equivalent to an anemometer measurement of a (constant) 10-m/s wind taken over a one-hour period: the number and density of

these equivalent "anemometer winds" available from SASS for use in wind modeling should therefore yield a significant addition to the existing data buoy-ship of opportunity system.

A related source of some potential scatter is the somewhat arbitrary definition of off-nadir SASS solution time-tags and Earth locations as the midpoints of the times and locations of the σ° measurement pair that generated each particular wind solution. Thus, for example, a solution time-tag can be as little as a few seconds to as much as nearly two minutes removed from the actual times that either of the two σ° measurements was taken, depending on the cross-track distance of the measurements from the subtrack (see Subsection 3.4.3). A solution "location" bisects the line joining the centers of the measurement cell pair, which can range from coincidence to a separation distance of up to 37 or 50 km (see Subsection 7.1.2.1), depending on whether the data results from a one- or two-sided instrument mode.

The complication that arises when the wind over the area sampled by the scatterometer is variable in space at the moment the sample is taken is obvious. When averaged over the area of a cell that is scanned, the average vector wind for that cell need not necessarily coincide with the average wind from a local anemometer, derived as the average over a time interval varying from perhaps 8 to 30 minutes, depending upon the platform. This effect of mesoscale variability is probably the least understood of all the sources of scatter in this problem, and work in this area is continuing [49]. An elementary inspection of an anemometer record obtained by a ship shows that the minute-by-minute variation of the wind over a given point on the ocean can be large. The mesoscale fluctuations in wind speed can be 10 to 20 percent of the wind speed averaged over a half hour or more. The fluctuations in direction can be 5 to 10 degrees on both sides of the average direction. In general, the anemometer record is a manifestation of a complicated three-dimensional variability in the winds over the ocean with a vertical scale that extends upward at least a kilometer and a lateral scale many times larger.

If the average wind over a cell scanned by the SASS is unequal to the anemometer average taken at a nearby point, then added significance is taken on by the fact that two different cells scanned by the SASS (corresponding to a

wind-generating $\sigma°$ pair) do not exactly coincide. The average of the winds over one of the cells is not necessarily equal to the average of the winds over the second cell. The difference between the two average winds can be much larger than the difference that would result from the gradient of the synoptic-scale wind over the distances involved. If the two cells have sampled disjoint regions of the ocean, as is often the case, an additional source of scatter is introduced when the wind derived from the SASS measurements is compared to a conventional wind measurement.

Conventional surface "truth" measurements of wind, either by anemometers or by wind field analyses derived from kinematic or boundary layer models, have identifiable, and at times removable, sources of bias and random error. Examples include (1) inadequacies in the techniques used to adjust for variations in anemometer height, (2) inappropriate anemometer averaging time in relation to the turbulent scatter of the wind field, (3) interference of the air flow being measured by the presence of the measuring platform, and, in the case of model winds, (4) inadequacies in the model used coupled with a paucity of data in some regions. In addition, wind measurements taken by non-scientific transient ships have an inherent accuracy that is highly variable because of lack of calibration and casual operating methods. Therefore, when comparing SASS winds with surface truth, the observed scatter must be partially attributed to each. There are no current means of separating the errors in conventional wind measurements from those inherent in the SASS measurements, except possibly on a statistical or spectral content basis (e.g., see [12], Subsection III-D). It is not presently known whether SASS or surface truth is a "better" measure of the synoptic wind field; this will probably be determined only from the application of SASS winds to dynamical studies in such disciplines as weather forecasting and upper-ocean response to variable winds.

Much of the surface truth data used for comparison against the SASS-derived winds for (1) evaluating the SASS's capabilities, and (2) developing the SASS1 model function G-H table is delineated and assessed in [50]. The surface data analyzed is in the form of spot observations and derived wind fields from the GOASEX and JASIN experiments and hurricanes FICO and Ella. Spot observations of various quality were considered, with the best data available being from meteorological buoys and scientific ships devoted to meteorological measurements.

Particular attention is given to the problem of establishing appropriate averages and extrapolations on the point wind measurements used in generating the comparison surface wind fields. Taylor's hypothesis (the assumption that a time average can be substituted for a space average) is invoked -- and its merit in the preparation of SASS comparison data is investigated -- with regard to the different surface measurement data groups.

9.8 "MISSING" SASS WINDS: WHY AND WHEN

The complete SASS data interval of 1820 GMT, July 6, 1978 to 0230 GMT, October 10, 1978 is overlaid with numerous sensor data outage gaps that accumulate to a total of over 13 days for which derived winds will not exist (see Table 1-1). After the initial instrument start-up period, these gaps range in size from just a single frame of data to several hours and are due to programmed and emergency on/off procedures, maneuvers, and minor communication problems (see Section 11) as well as to instrument operating characteristics. Figure 9-5 summarizes the major data outages (greater than one orbit) for each sensor; a complete compilation can be found in [5]. Note that no SASS winds will be corrected for attenuation during the SMMR gaps (see Subsection 9.5). In addition, GDR wind solutions are not derived from significant amounts of existing sensor data for a variety of reasons including, of course, the presence of any land (or ice) in individual $\sigma°$ resolution cell areas as indicated by the (imperfect) TOILing process (see Subsection 6.2). Beyond this, there remains a class of conditions pertaining primarily to perceived instrument ill health that causes candidate sensor measurements to be omitted from the wind inversion process.

A sizable portion of the SASS sensor data processing by the sensor algorithms involved the performance of data stream "housekeeping" and assessment functions. This background quality-control processing was responsible for inspecting the various status, science, and housekeeping telemetry channels for proper instrument operation, channel out-of-range (OR) conditions, and possible data stream bit errors. It provided a set of status and quality flags on the output sensor records for use in assessing the overall quality of the $\sigma°$ measurement. Whenever possible, the algorithms initiated "anomaly processing" to avoid the generation of erroneous data which would otherwise result because of key detectable bit errors and/or channel OR conditions. For example, it provided for

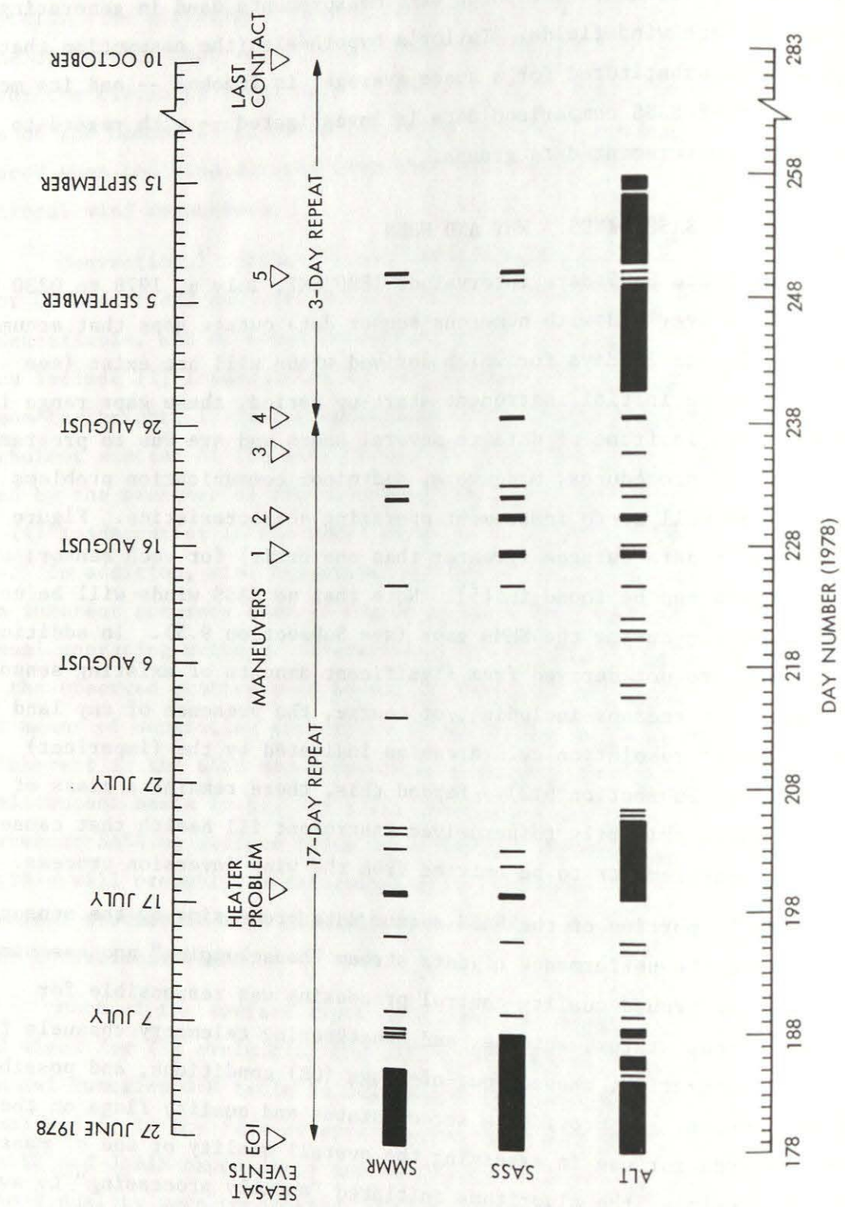

Figure 9-5. Data Outages of Duration Greater than One Orbit (100 min) for ALT, SASS, and SMMR

a continuance of sensor data processing when some -- or even all -- of the four calibration frames in a calibration sequence do not appear in the data stream. A complete description of the instrument/data status or quality attribute that is described by each flag contained in the sensor records (see Table 8-3, channels 750-838, and Table 8-4, channels 404-411), and the conditions under which the flag is set, or not set, is found in [3].

The SASS geophysical algorithms must screen out sensor σ° data that would yield obviously erroneous wind vector solutions. However, not all σ° data quality attribute categories monitored by the sensor algorithms (as given by the flag channels listed above) are such that an "on" flag condition is sufficient grounds to rule out the use of the associated σ° in computing a wind solution. For example, if σ°s were judged on the basis of the data quality summary flag -- an overall quality flag that is set according to the Boolean sum of all maintained science and calibration quality flags that <u>might</u> indicate a possible problem with one or more of the 15 Doppler channel measurements for that particular frame of data (see DQS flag description in [3], Sections 2 (algorithm S-00), 3, and 4) -- some potentially good wind solutions would have gone uncomputed as a result of data screening that is too stringent. GDR wind solutions are therefore computed, or not computed, on the basis of the following subset of the flags contained in the σ° sensor record. If any one or more of the six flags

EDQF1(B8)	(Transmitter Off)
EDQF2(B2)	(Receiver LO Lock)
EDQF2(B6)	(Transmitter Lock)
EDQF3(B1)	(Antenna Port Mismatch)
EDQF3(B4)	(Footprint Location Data Not Available)
EDQF3(B6)	(IFA/ISLO Mismatch)

is on (a negative condition), the entire frame of data (i.e., all 15 σ°s derived from the 15-Doppler cell set of data from one antenna illumination pattern -- see Subsection 4.5) is rejected from consideration for wind computation. In addition if any one or more of the three flags

DQF_k(B5)	($VSPN_k$ Out of Range -- Low)
DQF_k(B6)	($VSPN_k$ Out of Range -- High)
DQF_k(B10)	(Antenna Angle Out of Range)

is on for a given k, the $\sigma°$ measurement for the $k^{\underline{th}}$ Doppler channel is rejected on an individual basis from wind computation, for k = 1,2,...,15. With regard to sensor data quality, the implications of an "on" setting for only two of the above flags will be discussed here.

The antenna-port-mismatch flag on indicates a certain probable class of apparent data frame-sequence disorders due to frame synchronization errors, telemetry stream bit errors, etc. The implication is that there is an inconsistency between the expected antenna port number and that which is implied by antenna beam/polarization indicators. In such cases an adjustment is made so that the output sensor data is most likely valid. Even so, the infrequent occurrence of such a condition coupled with the risk of incorrectly "adjusting" such data dictated that it be excluded from processing beyond the $\sigma°$ level.

Due to frequency and duration of occurrence, a more significant abnormal condition is indicated in the data whenever the footprint-location-data-not-available flag is on. At various times in the mission data set, the IDPS (see Subsection 4.4) was unable to compute measurement cell location parameters. This typically happened over short bursts of data early in the mission because of attitude control problems (see Subsection 5.6.1.3). The number of such occurrences is currently unknown, but a complete account of the Seasat spacecraft attitude determination system and the attitude control knowledge and error histories over the mission time-span as they relate to the various sensors is given in [51]. The SASS sensor algorithms carried the processing of unlocated data to the point of received P_R (see Subsection 5.6.2) and no further -- corresponding output sensor data records therefore contain invalid $\sigma°$ values.

In addition to status flag rejection criteria, wind solutions are not generated for any σ_k° for which $\sigma_k^\circ < -50.$ dB, or $\sigma_k^\circ > 20.$ dB, for k = 1,2,...,15; the thinking here is to reject any measurements that fall outside of reasonable magnitude bounds. Note that this test will screen out all $\sigma°$ measurements that have received an out-of-range (high) attenuation correction (see Subsection 9.5). If the computed noise level of a backscatter coefficient gets too high, the measurement is also precluded from geophysical processing: wind solutions are derived only from σ_k° for which $NSD_k \leq 100.$, for the normalized standard deviation in the

percent units found on the GDR (see Subsections 5.4 and 7.4.4, and Table 8-3, channels 330-344). This rejection condition usually corresponds to a low-wind environment, particularly at higher incidence angles. In the region of a weather low, this will often result in the absence of any solutions with speeds less than, say, 3 or 4 m/s.

The final criterion for rejecting individual $\sigma°$ measurements from GDR wind consideration -- and perhaps a key one -- is the algebraic sign of the measured reflected signal power. The true value of a physically realizable quantity such as the returned signal power P_R (see Subsections 5.2 and 5.3) must, of course, be a non-negative number. Due to the averaging technique used to compute this measurement -- which allows a signal to be extracted from a low-SNR signal-plus-noise many times when it would be otherwise impossible -- the resulting P_{R_k} is a statistical quantity rather than a deterministic one. Therefore, in lower returned-power situations (typically associated with lower surface-wind conditions), the computed P_{R_k}'s can take on positive, zero, and negative values in a stochastic manner. The magnitude of negative P_{R_k}'s is thought by some to have useful information (see [48]) -- if in a statistical sense -- for wind extraction. Such magnitude information is therefore retained in the GDR $\sigma°$ sensor records (see Table 8-3, channels 435-449) and the negative-P_{R_k} situation is appropriately flagged ($DQF_k(B7) = 1$, $P_{R_k} = -300.$ dBw, and $\sigma_k^\circ < -100.$ dB) on a cell-by-cell basis. "Negative P_{R_k}" σ_k°'s found on the sensor file are thus easily distinguished, and should be of no value to most users: the current geophysical algorithm bypasses all such data in the generation of GDR wind solutions.

Instrument operating characteristics and algorithm design yield the final classification of what may appear to be "missing" wind solutions in a swath of data. If a particular off-nadir forward-beam $\sigma°$ measurement resolution cell does not have a matching orthogonal aft-beam $\sigma°$ cell (or vice versa) within a radius of 37 km for a single-sided instrument mode (50 km for a double-sided mode), it does not participate in the GDR inversion process (see Subsection 7.1.2). Among other things, this means that a significant number of unmatched cells in the outer non-overlapped portion of the wider forward or aft swath, as well as a smaller number of unmatched inner swath-edge cells, do not generate wind solutions (see Subsection 3.4.3). In addition, computer buffer-size limitations can

cause the pairing algorithm to occasionally delete orthogonal measurement pairs that would otherwise be solution candidates (i.e., within distance tolerances) -- see Subsection 7.2. Finally, a SASS calibration data cycle (four consecutive data frames extending over ∿9 s -- see Subsection 4.5) that occurs nominally about every four minutes (∿1600 km ground track) in the data stream will create a thin X-shaped gap (for a double-sided mode) centered about the nadir point in the wind-solution swath due to the resulting absence of σ° data in that region. A mode change (which also initiates a calibration cycle) from a left-side mode to a right-side mode, or vice versa, as well as a GDR-tape start-up will create a triangular-shaped gap (with vertex at nadir) of unpaired measurement cells and can also cause occasional solution losses due to algorithm buffering pathologies (see Subsection 7.2.6).

Conceivably, a user could investigate the cause of missing wind data in a σ°-covered region of high interest for the purpose of developing, say, a limited solution gap "fill-in" procedure. A curious aspect of such a process is that characteristics of candidate σ° orthogonal pairs are easily investigated only if they appear in the Supplemental Geophysical Record (see Subsections 8.2.2.3 and 8.3.8) -- a circumstance that only occurs if the pairs have already been processed to winds.

9.9 ICE "WIND" SOLUTIONS

Just as there are solutions "missing" from the GDR as discussed previously, there are a significant number of "winds" present that should not be there. These are the solutions derived from higher- and lower-latitude σ° data that is contaminated with ice. Measurement cell regions that contain any significant amount of ice will yield backscatter values whose dependence on local surface wind is, at best, unknown. The static TOIL ocean/land data base used to determine whether resolution cells are "all-ocean" is misnamed with regard to the ice ("I") component (see Subsection 6.1) since it contains no information relating to ice regions that are variable in time. In fact, essentially all ice regions away from continental boundaries are labeled as "ocean" in the data base. σ° measurements that have been corrected for attenuation using ice-contaminated SMMR data will often (but not always) receive the upper-end threshold-exceeded flag (see Subsection 9.5), and will therefore be correctly omitted from the

inversion process. However, since most ice-contaminated data that is uncorrected for attenuation (and some that has been corrected) will yield spurious winds, users of GDR data from the more extreme latitudes will have to carefully scrutinize the solutions and perhaps develop an editing procedure.

SASS wind solutions can be located at latitude extremities up to about ±78°. Certainly any solutions located at latitudes greater than 70°N (and less in some regions) in the northern hemisphere and lower than 62° - 65°S in the southern hemisphere should be viewed with suspicion. Of course, these are average limits since ice boundaries varied over the three-month duration of the Seasat mission.

A possible procedure for screening out contaminated data could be based on ice maps, such as those provided by Fleet Weather Central. Figure 9-6 is an example for the southern hemisphere (polar projection) for the week of July 27, 1978, the fourth week of the SASS data interval. Similar data is available for the northern hemisphere. Naturally, the resolution of the SASS measurements is considerably higher than the accuracy that can be expected with most ice truth data on a global scale. At any given time, there are inherent difficulties in establishing some ice/ocean boundaries because of the variable nature of ice edges. Complete error-free editing of ice-contaminated SASS data is thus a goal that probably cannot be reached for the entire data set.

A signature in the derived wind magnitudes as the SASS swath passes from ocean to ice (or vice versa) has been consistently observed in the data and could therefore yield an intrinsic method for discriminating sizable portions of the ice-contaminated data. Because of the backscatter response, the signature is more revealing for larger incidence angles; the ocean-ice transition evidence in the (wind speed) signal tends to disappear as the inner edge of the off-nadir primary swath is approached. It must be emphasized that the signature is not always observed, is sometimes contradictory, and can itself be contaminated by the presence of a high and variable wind environment in the region containing a suspected ocean/ice boundary.

Nonetheless, some typical observed effects are shown in Figure 9-7, where southern hemisphere SASS wind-solution swaths consisting of (northbound) segments from two consecutive orbits in September are plotted. The derived wind

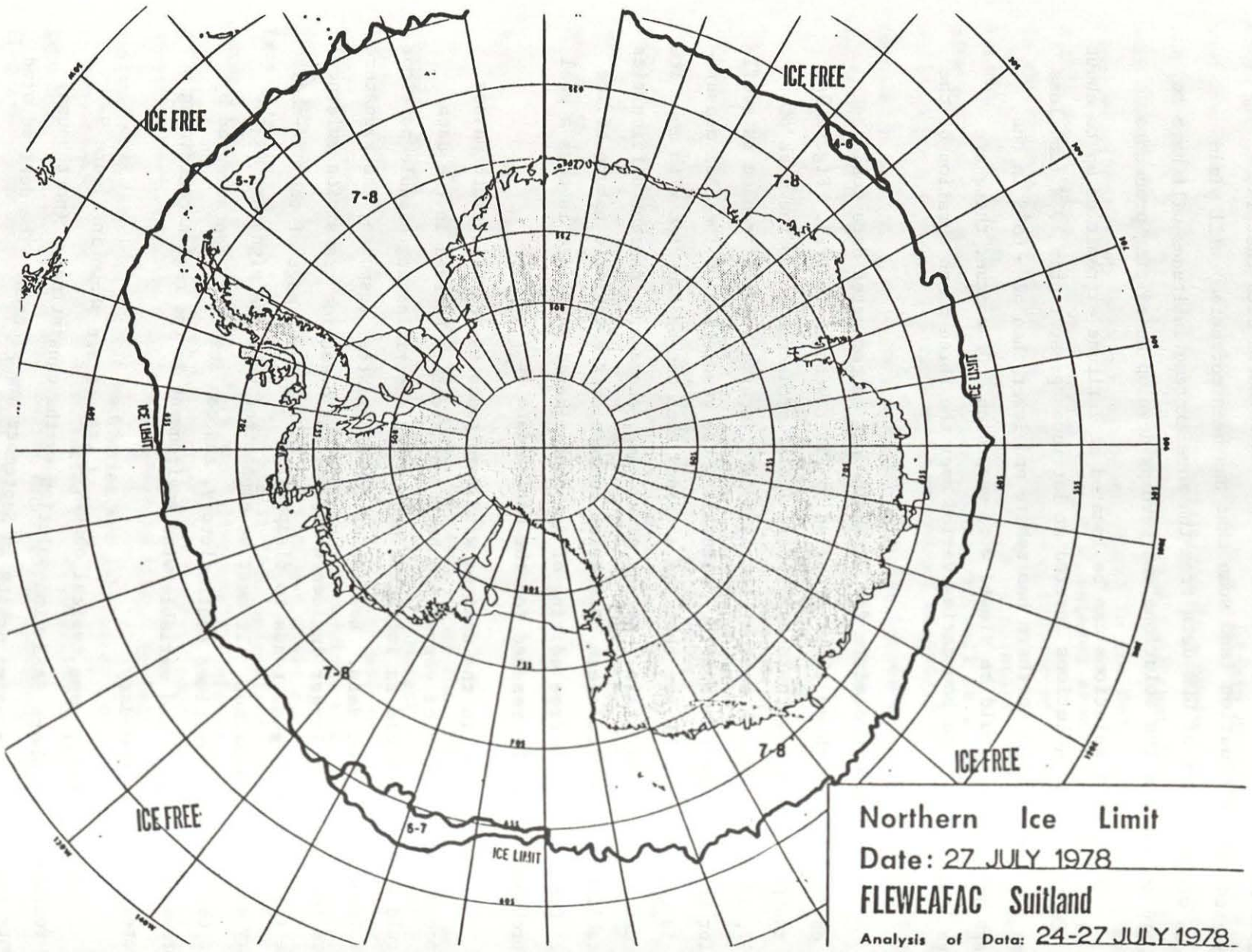

Figure 9-6. Southern Hemisphere Ice Map

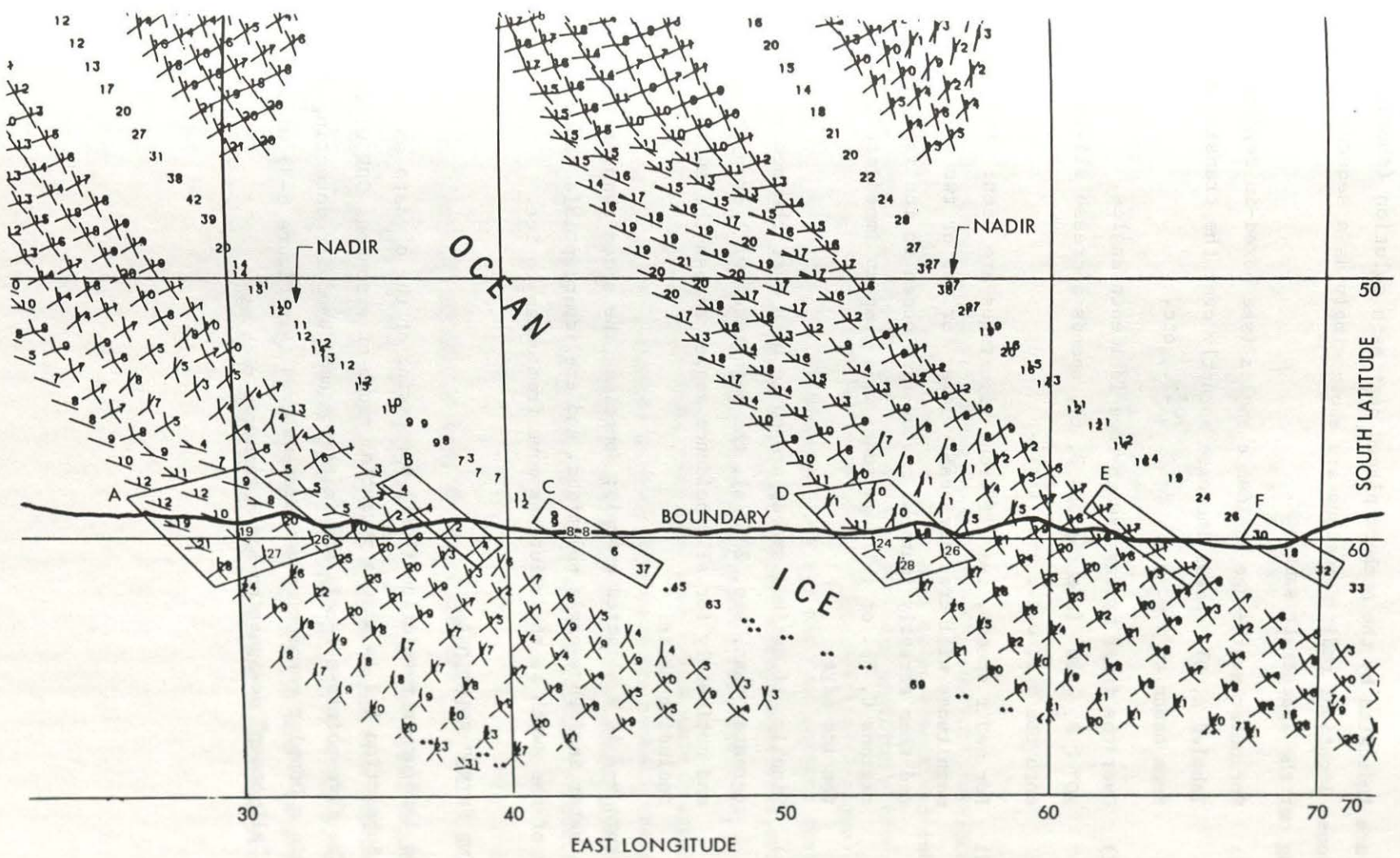

Figure 9-7. SASS Winds Indicating Ice Boundary

speeds (m/s) are indicated by the numbers placed near each solution (showing alias directions) location; nadir solutions are shown simply as a sequence of speeds tracing out the spacecraft subtrack.

(1) For outer swath-edge incidence angles (see boxed-in regions labeled A, D), speeds increase abruptly over the transition from ocean to ice; e.g., 8-20, 11-24, etc.

(2) Over the inner primary swath-edge incidence angles, $20° \lesssim \theta_I \lesssim 30°$ (see regions B, E), speeds decrease slightly onto the ice; e.g., 4-2, 17-11.

(3) For nadir speeds, two different signatures are seen: (a) the magnitudes will drop noticeably lower for one or two solutions and then abruptly increase moving from ocean to ice (see regions C, F), or (b) magnitudes will jump up immediately at the ice edge.

(4) Finally, if derived speeds are quite high over the ocean (greater than, say, 20 m/s), the magnitudes will drop abruptly and noticeably for all incidence angles across the swath, including nadir.

Figure 9-7 is a selected example; sometimes the speed changes are small for the outer incidence-angle solutions, and are imperceptible throughout the remainder of the swath as the solutions move from ocean to ice.

9.10 LAND "WIND" SOLUTIONS

The land/ocean resolution (TOIL) processing of the $\sigma°$ data as described in Subsection 6.2 is also a potential cause of erroneous GDR wind solutions. The five-points-per-cell examination scheme used for detecting land anywhere within a Doppler resolution measurement area (see Figure 6-3) will yield an incorrect "all-ocean" designation for a scenario such as

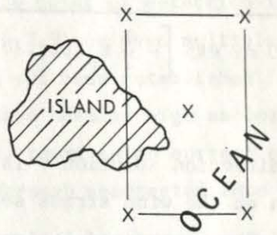

Related errors are also clearly possible because (1) the TOIL land/ocean data base used has a finite (5'x5') resolution as well as an advertised inherent absolute accuracy no better than 5-9 km, (2) attitude pointing errors (see Subsection 5.4.1.2) yield Doppler measurement cell location (1-sigma) uncertainties typically in the 3- to 10-km range, and (3) the four corners that are actually checked do not coincide with the Doppler measurement cell corners for cells that are rotated from a north-south alignment (see Figure 6-1).

SASS sensor measurements that have been erroneously flagged as "all-ocean" will yield "wind" solutions with error components probably ranging from imperceptible to completely evident. GDR wind solutions located near any land boundaries -- particularly small islands -- should be carefully scrutinized for such errors.

9.11 STANDARD DEVIATIONS ON WIND SOLUTION ERRORS

The 1-sigma standard deviation $\sigma_{U_{19.5}}$ on a wind speed solution $U_{19.5}$ is computed as part of the geophysical least-squares estimation process (see Subsection 7.4). For each refined alias solution $(U_{19.5}, \gamma) = (\overline{U}, \overline{\gamma})$, where $\overline{U}$ is given by an algebraic expression equivalent to Eq. (7-23) and $\overline{\gamma}$ is given by a similar relationship, the wind speed standard deviation is derived from the parallel form

$$\sigma^2_{U_{19.5}} = \frac{\iint_R dU\, d\gamma\, (U-\bar{U})^2 \exp\left[-\frac{1}{2} Q_p(U,\gamma,\{\sigma^\circ_n\})\right]}{\iint_R dU\, d\gamma \exp\left[-\frac{1}{2} Q_p(U,\gamma,\{\sigma^\circ_n\})\right]} \tag{9-15}$$

The standard deviation on the direction solution $\bar{\gamma}$ is similarly computed. Finally, the standard deviation on the wind stress solution u^* is given in terms of $\sigma_{U_{19.5}}$ by Eq. (9-10). These computed 1-sigma standard deviations on u^*, $U_{19.5}$, and direction are contained in the basic geophysical record (see Table 8-1) in channels 1401-1800, 1801-2200, and 2601-3000, respectively.

As absolute measures of solution accuracies, these formally computed wind solution error standard deviations should not be taken too literally. They are derived assuming that (see Subsection 7.4.3) (a) the σ°-to-wind model function used to generate wind solutions accurately duplicates the real-world "true" model function to within a small (.7 dB) and random error, (b) the total noise on the σ° measurements is a random variable that is normally distributed in logarithmic (dB) units, and (c) the normalized standard deviation (NSD) on σ° computed by the sensor algorithms (see [3] and channels 3601-3800) accurately reflects the error in the sensor measurements -- which is assumed to be uncorrelated. The computed wind solution error levels are therefore realistic only to the extent that these assumptions are true. A prudent user of the data would probably employ these solution error measures primarily to discriminate relative, rather than to determine absolute, quality.

9.12 TELEMETRY STREAM BIT ERRORS

Random or sporadic errors occurring in the telemetry data bit stream offer another potential cause of spurious GDR wind solutions. These errors are broadly defined here as any that can occur and remain undetected at any of several operational stages after (and including) on-board recording that cause a quantity contained in a final PMDF, DOF, or DAF tape created by GSFC (which form the input to the JPL Seasat processing chain -- see Section 4) to have a value different from that generated by the spacecraft. Considerable effort was expended to implement schemes at the GSFC, IDPS, and ADF (see Figure 4-1)

processing levels to detect and mitigate the effects of such errors in the final derived geophysical parameters. In many cases, "problem" data was deleted (or marked for deletion) at the point of detection in units of entire minor or major frames (see Subsection 4.4.2.9) or even multiples of such frames. While no definitive error rate has yet been established for the overall Seasat telemetry data, various estimates have been as high as one bit in 10^4 -- a rather high rate indeed. Furthermore, there is no current estimate of the number of such errors that have passed through undetected into the SASS geophysical solutions.

On the positive side, very few anomalistic GDR wind solutions have been observed to date that can be directly traced back to bit errors in the telemetry. This is presumably due primarily to the data screening employed and, in particular, to the set of quality checks implemented into the SASS sensor algorithms that ask the basic question "Do the derived values for the σ° measurements, their uncertainties, and their locations make sense within the range of conditions expected for the operational characteristics of the instrument?" If the answer is "no" so that further processing of the offending σ°'s into geophysical solutions would probably yield erroneous winds, they are summarily rejected (see Subsection 9.8).

Naturally, the detectability of a bit error (or a "burst" of such errors) as well as the impact of such an error on a set of derived wind solutions is very dependent on its location within a telemetry block. An error in the lowest-order bit of a Doppler channel voltage measurement, for example, would probably have little effect on a final derived wind -- and would also most likely not be detected by either (1) quality checks at any processing level, or (2) a user of the data. It is hoped that bit errors that could result in the significant corruption of a wind solution are typically those very errors of such magnitude that they are either detected by the present data screening algorithms or, failing this, by examination of solution fields by the final arbiter -- the user himself.

SECTION 10
FACTS, OBSERVATIONS, AND OTHER HELPFUL HINTS

10.1 INTRODUCTION: ORBIT AND SWATH COVERAGE CHARACTERISTICS

The Seasat orbit was nearly circular, with an inclination of ∿108°, a period of ∿101 min, and an altitude of ∿800 km. The spacecraft circled the Earth 14-1/4 times a day with consecutive ascending equatorial sub-track crossings (longitude of ascending node relative to the rotating Earth) progressing westwardly with a mean separation of about 2800 km (∿25.1°). This results in equatorial crossings distributed around the globe approximately 470 km apart after any three-day interval. The ground-track was repeated (within a small tolerance) every 17 days for the time period between June 27, 1978 and August 27, 1978. During this phase of the mission, the equatorial crossings were spaced approximately 88 km apart after any 17-day interval. From August 27, 1978 to the mission termination on October 10, 1978, the orbit configuration was in a three-day-repeat mode in which the minimum equatorial crossing distance was 470 km. Approximately 95% coverage of the global ocean surface is possible with the SASS swath (see Subsection 3.4.3) in a 36-h period. For a double-sided SASS instrument mode, swath edges from successive orbits are separated by about 12° longitude at the equator and begin to overlap beyond about ±51° latitude. Swath latitude extremities can reach about ±78°. Over the course of the mission, an average of over 12,000 nadir- and primary-swath ocean-surface wind observations are derived from the (paired -- see Subsection 7.1.2) SASS sensor data per orbit.

The remainder of this section presents a small collection of facts and observations that will hopefully further assist the user in understanding and applying the SASS GDR data.

10.2 COUNT BREAKDOWN OF TOTAL SASS DATA SET BY POLARIZATION, SWATH REGION, AND ATTENUATION CORRECTION LEVEL

There are 15,910,267 wind solutions contained on the complete SASS mission set of 381 type I (see Subsection 1.6) GDR tapes. This includes a small redundancy of solutions since there is a data overlap of approximately 10 minutes on each tape (see Subsection 1.6.1). A breakdown of the complete solution set into subtotal counts for key solution-type categories generated by various

combinations of the primary sensor data attributes, i.e., (1) swath region, (2) polarization type, and (3) level of attenuation correction, is given in Table 10-1. Note, for example, that the total number (14,593,227) of primary (off-nadir) swath solutions is composed of 72.8% V-V polarization-pair data (i.e., both members of the solution-generating σ° pair are vertically polarized), 18.0% H-H data, and 9.2% cross-polarization (V-H or H-V) data. Also, note that only 27.1% of the primary swath data has been fully corrected for attenuation; i.e., both σ°'s in a solution pair have been corrected (with correction magnitudes less than the threshold-exceeded value -- see Subsection 9.5) by the attenuation algorithm, while 4.2% of the off-nadir solutions have been derived from σ° pairs composed of one corrected and one uncorrected measurement.

10.3 ALIAS-TO-ALIAS VARIATION IN VECTOR SOLUTION SPEEDS

The magnitudes of the four (or fewer) alias speeds can differ from each other by over 1 m/s for a given primary-swath solution, although the typical variation remains within ∿.5 m/s. In the absence of ground truth which could provide guidance for selecting a particular alias, the best wind-speed value to use is often the average of the alias speeds for a wind solution. Similar reasoning applies to the four or fewer u* alias friction velocity magnitudes derived for each off-nadir solution.

10.4 BENIGN SOLUTION RELATIVE PROBABILITIES

The relative probability values associated with each of the candidate aliases constituting a primary-swath wind vector solution (see Table 8-1, channels 3001-3400, and Subsections 7.4.6 and 8.3.7) should, for all practical purposes, be ignored. Despite the beckoning label descriptions, the contents of these channels will rarely assist the SASS data user, except by chance, in making the "correct" choice among the multiple alias solutions. Even if these probabilities were to demonstrate some small statistical degree of skill in removing ambiguities, there is apparently no means of predicting the specific solution circumstances that they could be successfully applied to. In addition, there is no preferential ordering implied by the particular ordering found for alias solutions contained within the four alias wind speed and direction channels (channels 1001-1400 and 2201-2600) in a geophysical record. That is, the "WIND DIR 1ST SOL" is, on the average, just as likely to be closest to the "true" wind direction as is any of the other aliases for a wind solution. (It is also just as likely to be farthest from the true direction.)

Table 10-1. Polarization-, Swath-, and Attenuation-Count Breakdown of Total SASS Data Set

- GRAND TOTAL 15,910,267[a]
  - TOTAL PRIMARY 14,593,227
    - TOTAL VV[b] 10,621,640
      - PORT 5,463,673
        - FULL ATTEN[c] = 0
        - 1/2 ATTEN[d] = 0
        - UNATTEN[e] = 5,463,673
      - STARBOARD 5,157,967
        - FULL ATTEN = 3,074,611
        - 1/2 ATTEN = 460,704
        - UNATTEN = 1,622,652
    - TOTAL HH 2,628,699
      - PORT 1,642,268
        - FULL ATTEN = 0
        - 1/2 ATTEN = 0
        - UNATTEN = 1,642,268
      - STARBOARD 986,431
        - FULL ATTEN = 492,319
        - 1/2 ATTEN = 90,580
        - UNATTEN = 403,532
    - TOTAL CROSS 1,342,888
      - PORT 659,003
        - FULL ATTEN = 0
        - 1/2 ATTEN = 0
        - UNATTEN = 659,003
      - STARBOARD 683,885
        - FULL ATTEN = 393,759
        - 1/2 ATTEN = 60,524
        - UNATTEN = 229,602
  - TOTAL NADIR 1,317,040
    - PORT 842,951
      - FULL/PARTIAL[f] ATTENUATION = 373,968
      - UNATTEN[g] = 468,983
    - STARBOARD 474,089
      - FULL/PARTIAL ATTENUATION = 314,391
      - UNATTEN = 159,698
- GRAND TOTAL 15,910,267
  - PRIMARY FULL ATTEN = 3,960,689
  - PRIMARY 1/2 ATTEN = 611,808
  - PRIMARY UNATTEN = 10,020,730
  - NADIR FULL/PARTIAL ATTEN = 608,359
  - NADIR UNATTEN = 628,681

[a]Numbers are total solution count for particular category over complete mission data set.
[b]Solutions derived from V-V polarization σ° pair.
[c]Solutions derived from σ° pair with both measurements corrected for attenuation.
[d]Solutions derived from σ° pair with one of the two measurements corrected for attenuation.
[e]Solutions derived from σ° pair with neither measurement corrected for attenuation.
[f]Nadir solutions derived from σ° group with one or more measurement corrected for attenuation. Recall (Subsection 7.1.2) that nadir solutions result from a "bin" of one or more measurements.
[g]Nadir solutions derived from a group of σ° measurements none of which are corrected for attenuation.

10.5 SENSE OF WIND SOLUTION DIRECTIONS

Wind directions on the GDRs are defined with the meteorological convention, i.e., in the "out-of" sense, and are measured clockwise from the north over the range 0°-360°. Thus, for an alias direction of 45°, the solution "wind" is blowing out of the northeast.

10.6 GEOCENTRIC WIND SOLUTION LOCATIONS

GDR solution location latitudes are given in the geocentric coordinate system, whereas most maps and geophysical location referencing is with respect to an implied geodetic coordinate system. The geodetic latitude at a location is the angle that the normal to the Earth reference ellipsoid at the location forms with the equatorial plane (see Figure 8-2): the maximum difference between the geocentric and geodetic latitudes (occuring at ±45° latitude) is .19°. For most applications where high-resolution wind locations are desired, GDR data users will want to convert the geocentric latitudes to the geodetic system. A simple form with which to make this conversion is given by Eq. (8-1).

10.7 GDR SUPPLEMENTAL GEOPHYSICAL RECORD

The SASS Supplemental Geophysical Record (SAGS) is discussed at some length in Section 8 (viz., Subsections 8.2.2.3, 8.2.2.4, 8.3.4.2, and 8.3.8). Essentially, the SAGS contains the paired sensor data ($\sigma°$'s and supporting parameters) used to generate, and organized in the same manner as, the (100) wind solutions contained in the corresponding Basic Geophysical Record (see Subsection 7.1.2, Cell Pairing). Geophysical data and all corresponding paired sensor data used in the wind inversion process to generate particular wind solutions may therefore be easily extracted from the two matched records. The SAGS record appears on the GDR almost exclusively for facilitating "inverse" investigations of geophysical data: particular wind solutions that appear to be pathological, or otherwise in need of further scrutiny or screening, can easily be traced back to their two $\sigma°$ measurement progenitors for a more detailed sensor-level study. Note that since $\sigma°$-pair polarization (V or H) information is contained exclusively in the SAGS record, this record must be "cracked" by any SASS data user who might, for example, desire to delete all cross-polarization (V-H or H-V) solutions from his application. Note further that a type III GDR tape copy that might be obtained from NOAA-EDIS does not contain the SAGS record.

10.8 ERRATIC SOLUTION ORDERING WITHIN GEOPHYSICAL RECORD

Time-tags and locations of successive wind solutions within a GDR geophysical record, as well as those crossing record boundaries, may appear to jump around erratically in a disconcerting manner. This is normal and, in fact, is a result of the cell pairing mechanism (see Subsection 7.2) that delineates solution candidate sensor measurement pairs and further prepares them for wind-extraction processing. The order in which this pairing occurs, which is somewhat random in space and time within a pairing "window" that moves along with the SASS swath, establishes the physical order of the resulting solutions within the geophysical records. Aside from this rather small-scale (high-frequency) "jitter," successive solution time-tags and locations move globally along with the window in an average sense, paralleling the window center to within a few minutes time and degrees location. Thus, the gradual intra- and inter-record trend is solution time-tags that increase chronologically and locations that follow the SASS swath.

If the use of the data involves the application of blocks of solutions extracted on a start- and end-time basis, the nonmonotonic time-tags add a slight complexity to the processing. If all relevant data is to be found, the block extraction mechanism must scan a GDR file 3-4 minutes, say, before and after what would otherwise appear to be the first and last solution within a time block. Similar logic also extends to the extraction of data for a fixed region. A full discussion on data ordering within the various record types contained in the SASS GDR will be found in Section 8.

10.9 MIXTURE OF NADIR AND PRIMARY SWATH SOLUTIONS WITHIN GEOPHYSICAL RECORD

Due to factors discussed in the previous subsection, nadir and off-nadir swath solutions are more or less randomly intermingled within a GDR record. A user can easily extract the off-nadir subset, say, by rejecting all solutions with incidence angle Θ_I less than 15°.

SECTION 11

MISSION OPERATIONS LOG

This section contains a listing of selected significant events that occurred during the Seasat mission. The list does not include each event of a series of repetitive operations such as SAR passes or SASS mode changes or ground-commanded heater cycles.

The operations log reproduced here starts with the engineering assessment phase of the mission. (The ascent sequence log is not included.) All instrument- and attitude-related events have been included.

GMT	REVOLUTION	EVENT
		ENGINEERING ASSESSMENT PHASE
184/14/13/51	94	ALT first turned on -- station down -- did not get data in real time (standby mode)
184/14/29/10	94	ALT off
184/16/43/06	95	ALT turned on (standby mode)
184/16/56/34	95	ALT turned off
184/19/12/49	96	ALT second turn-on (standby mode)
184/19/17/04	97	ALT data, T1*
184/19/22/14	97	ALT standby mode
184/20/56/00	98	ALT turned off
184/21/33/47	98	ALT third turn-on (standby mode)

*T1 refers to altimeter track mode one; similarly, for T2, T3 and T4.

GMT	REVOLUTION	EVENT
184/21/38/03	98	ALT data, T2, T3
184/21/42/15	98	ALT standby mode
184/23/06/53	99	SAR early turn-on #1
184/23/23/00	99	SAR turned off
185/00/01/00	99	ALT turned off
185/00/52/20	100	SAR early turn-on #2
185/01/01/43	100	SAR turned off
185/03/44/33	102	SMMR early turn-on #1
185/03/56/34	102	SMMR turned off. Turn-on not accomplished due to improper mode of the SMMR for accepting turn-on commands.
185/04/14/17	102	ALT fourth turn-on (standby mode)
185/04/18/39	102	ALT data, T4
185/04/26/17	102	ALT standby mode
185/05/56/00	102	ALT turned off
185/05/27/11	103	Rerun of SMMR early turn-on #1
185/05/31/00	103	SMMR turn-off; turn-off not accomplished
185/05/43/13	103	SAR early turn-on #3
185/05/53/53	103	SAR turned off

GMT	REVOLUTION	EVENT	
185/06/16/48	103	VIRR first electronics on	Turn-on and turn-off not accomplished
185/06/22/26	103	VIRR electronics off	
185/07/41/35	104	SMMR early turn-on #2	SMMR turn-on and turn-off not accomplished
185/07/50/40	104	SMMR turned off	
185/08/44/36	105	SAR early turn-on #4	
185/08/53/30	105	SAR turned off	
185/08/56/01	105	SMMR turn-off	
185/09/26/08	107	SMMR turn-on	
185/11/23/50	107	SMMR turn-off	
185/11/44/47	107	SMMR turn-on	
185/12/05/29	107	SAR early turn-on #5	
185/12/24/39	107	SAR turned off	
185/14/45/05	108	SMMR turn-off	
185/14/55/11	108	SMMR early turn-on #3	SMMR turn-on and turn-off not accomplished
185/17/15/50	108	SMMR turned off	
187/03/09/51	130	ALT fifth turn-on (standby mode) ALT turned on (quiet time)	
187/03/14/22	130	ALT data, T1, T2, T3, T4	
187/08/18/25	133	ALT standby mode	

GMT	REVOLUTION	EVENT
187/09/09/11	133	VIRR second turn-on
187/09/37/33	134	VIRR turn-off
187/12/00/01	135	ALT turned off
187/12/00/03	135	SMMR turn-on #4
187/12/57/02	136	VIRR electronics off
187/18/19/50	139	SASS enabled; Mode 1
187/21/47/24	141	SASS turn-on #1, Mode 4
187/23/11/26	142	SMMR turned off
187/23/23/55	142	SMMR turn-on #5
188/02/41/50	144	VIRR final turn-on
188/04/17/23	145	ALT final turn-on (standby mode)
188/04/21/44	145	ALT data, T1; start of scientific data
198/16/01/02	281	ALT +Y base plate temp went out of limits high
198/19/18/15	297	ALT commanded off due to high baseplate +Y temp
205/10/06/22	392	ALT heater bus off
205/10/07/35	392	ALT on (standby mode)
205/10/16/48	392	ALT data, T1

GMT	REVOLUTION	EVENT
205/21/27/30	398	SAR temp out of limits low
205/20/40	398	SASS temp below low limit
206/01/46/06	401	ALT heater bus on
206/02/50/00	402	ALT off
207/02/54/31	416	ALT on, 10% heater bus duty cycle (standby mode)
207/02/58/41	416	ALT data, T1
207/14/40/30	423	Initiate 15% heater bus duty cycle
207/17/20/	425	Initiate 20% heater bus duty cycle
214/	527	Initiate 15% heater bus duty cycle
215/08/34/40	534	Return to 20% heater bus duty cycle
220/08/54	605	Hit on attitude system (pitch and roll) (Sun interference in scan wheels)
220/17/10/15	610	No ALT data to 220/18/13/10
222/20/20/07	641	VIRR electronics shut off (approaching detector upper temp limit)
225/14/51/34	681	VIRR electronics turned on
		MANEUVER PHASE
227/01/10/00	701	Command SASS standby
227/01/10/30	701	Turn SASS off

GMT	REVOLUTION	EVENT
227/03/22/19	702	ALT off
227/07/41/08	705	Maneuver #1 (Cal burn No. 1)
227/10/20/13	707	ALT on (standby mode)
227/10/28/26	707	ALT data, T1
227/10/29/02	707	Enable SASS high voltage power supply
227/10/33/22	707	SASS on, operating mode 1
230/01/08/00	744	Command SASS standby
230/01/08/30	744	Turn SASS off
230/03/52/21	746	ALT off
230/07/46/58	748	Maneuver #2 (Orbit adjust No. 1)
230/09/29/13	749	ALT standby
230/09/37/26	749	ALT data, T1
230/09/39/32	749	Enable SASS high voltage power supply
230/09/42/52	749	SASS on, operating mode 1
235/09/16/19	820	ALT standby
235/09/20/36	820	Maneuver #3 (Cal burn No. 2) (Note: SASS remained on during this maneuver.)
235/12/54/07	823	ALT data, T1

GMT	REVOLUTION	EVENT
238/07/05/01	862	ALT standby
238/08/19/07	863	Select SASS standby
238/08/20/08	863	Turn SASS off
238/09/22/08	863	Maneuver #4 (Orbit adjust No. 2)
238/11/04/19	864	Enable SASS high voltage power supply
238/11/07/49	864	SASS on, operating mode 1
238/11/17/14	864	ALT data, T1
240/07/23/25	891	VIRR scan motor drive failed
240/08/10/00	891	ALT transmitter (TWT) auto shut down due to low S/C bus voltage
240/13/40/33	895	ALT standby
240/13/44/08	895	Heater bus cycle to 60%
240/16/32/32	896	ALT off due to low temp
240/17/03/00	897	First attempt to restart VIRR (See LMSC 90-day report)
242/02/45/00	917	Begin 20% heater duty cycle
243/07/03/00	933	Begin 25% heater duty cycle
243/13/38/44	937	Begin 30% heater duty cycle
243/18/39/17	940	Begin 35% heater duty cycle

GMT	REVOLUTION	EVENT
244/03/56/38	946	Begin 40% heater duty cycle
244/15/03/07	953	ALT standby
244/16/47/08	954	ALT data, T1, for TWT checkout (OK)
244/16/55/01	954	ALT standby
245/21/48/00	971	ALT 15% heater duty cycle
247/21/57/15	1000	Begin 20% heater duty cycle
248/23/08/15	1015	Begin 10% heater duty cycle
249/01/44/20	1016	ALT data, T1 (50% duty cycle)
249/21/44/24	1028	ALT 60% duty cycle
250/22/39/04	1043	ALT standby, due to Engineering Model Receiver failure
253/01/07/30	1073	Select SASS standby
253/01/08/01	1073	SASS off
253/01/10/22	1073	Maneuver #5 (Orbit trim No. 1)
253/01/23/30	1073	SASS on, operating mode 1
253/02/30/52	1074	ALT data, T1 } Bermuda overflt #1
253/04/32/03	1075	ALT standby } Bermuda overflt #1
254/20/08/30	1099	VIRR on for approximately 10 s
254/22/22/00	1100	VIRR on 10 s

GMT	REVOLUTION	EVENT
255/06/54/44	1105	VIRR motor started
256/00/25/35	1115	VIRR motor failed again
256/00/28/47	1115	VIRR motor start attempt (unsuccessful)
256/02/43/38	1117	ALT data, T1 } Bermuda overflt #2
256/04/07/01	1118	ALT standby } Bermuda overflt #2
256/17/38/14	1126	ALT data, T1 } Gulf of Alaska overflt
256/17/46/01	1126	ALT standby } Gulf of Alaska overflt
258/00/06/24	1144	ALT data, T1 (but test mode 1 over major land)
258/16/45/00	1154	VIRR motor on 20 s
259/19/24/00	1170	VIRR motor on 20-30 s
261/10/21/00	1193	Begin 20% heater bus cycle
265/13/46/00	1252	Start ALT track 4 test 1 execute from memory
265/13/46/01	1252	No ALT data
265/13/55/32	1252	ALT data, T1
265/18/13/00	1255	Start ALT track 4 test 2 start at Goldstone, end at Fairbanks
265/18/13/01	1255	No ALT data to 265/18/21/11
265/18/21/11	1255	ALT data, T1
268/00/15/10	1287	Start ALT modified operations (Track mode 1 over major land and track mode 4 with modified acquisition offset everywhere else)

GMT	REVOLUTION	EVENT
273/22/37/30	1372	SMMR encoder A off; encoder B on
283/02/30/36	1502	No ALT, SASS, SMMR or VIRR data
283/03/12/01	1503	Short occurred in electrical power subsystem
283/04/08/27	1503	Last contact

REFERENCES

[1] Brown, J.W., Introduction to the Seasat Algorithm Development Facility, JPL Internal Document 622-98, Pasadena, CA, November 29, 1978.

[2] Brown, J.W., et al., "Seasat Low-Rate Data System," Science, Vol. 204, pp. 1407-1408, June 29, 1979.

[3] Boggs, D.H., Algorithm Development Facility Scatterometer Sensor Algorithm Specifications, JPL Internal Document 622-231, Pasadena, CA, May 1981.

[4] Klose, J.C., Seasat Node Tables and Osculating Orbital Elements, JPL Internal Document 622-215, Pasadena, CA, December 18, 1979.

[5] Porche, W.D., Detailed Accountability of Seasat Data and Data Gaps, JPL Internal Document 622-221, Pasadena, CA, September 15, 1980.

[6] Kitsiz, S.N., Seasat Instrument Data Processing System Functional Specifications, Vols. I and II, JPL Internal Document 622-14, Rev. 1, Pasadena, CA, March 1, 1978.

[7] Klose, J.C., Seasat-A Sensor Data Record Tape Specification: Interface Control Document and Telemetry Dictionary, Rev. A, JPL Internal Document 622-57, Pasadena, CA, May 1, 1979.

[8] NASA Headquarters, "Earth and Ocean Physics Applications Program," Vol. I, Executive Summary, National Aeronautics and Space Administration, Washington, D.C., September 1972.

[9] Seasat-A Mission Specification, JPL Internal Document 622-4, Pasadena, CA, May 6, 1977.

[10] Bracalente, E.M., Boggs, D.H., Grantham, W.L., and Sweet, J.L., "The SASS Scattering Coefficient σ° Algorithm," IEEE J. Oceanic Eng., Vol. OE-5, No. 2, pp. 145-154, April 1980.

[11] Born, G.H., Wilkerson, J.C., and Lame, D.B., Seasat Gulf of Alaska Workshop Reports, Vol. I, JPL Internal Document 622-101, Pasadena, CA, 1979.

[12] Barrick, D.W., Seasat Gulf of Alaska Workshop II Report, JPL Internal Document 622-107, Pasadena, CA, January 1980.

[13] Businger, J., et al., Seasat-JASIN Workshop Report, Vol. I, JPL Publication 80-62, Pasadena, CA, 1980.

[14] Black, P., and Wilkerson, J.C., Seasat Storms Mini-Workshop Report, JPL Internal Document, 622-210, Pasadena, CA 1979.

[15] Njoku, E.G., Christensen, E.J., and Cofield, R.E., "The Seasat Scanning Multichannel Microwave Radiometer (SMMR): Antenna Pattern Corrections—Development and Implementation," IEEE J. Oceanic Eng., Vol. OE-5, No. 2, pp. 125-137, April 1980.

[16] Johnson, J.W., et al., "Seasat-A Satellite Scatterometer Instrument Evaluation," IEEE J. Oceanic Eng., Vol. OE-5, No. 2, pp. 138-144, April 1980.

[17] Grantham, W.L., et al., "An Operational Satellite Scatterometer for Wind Vector Measurements Over Oceans," NASA TMX 72672, March 1975.

[18] Skolnik, M.I. (ed.), Radar Handbook, McGraw-Hill, New York, NY, 1970.

[19] Fischer, R.E., "Standard Deviation of Scatterometer Measurements From Space," IEEE Trans. Geosc. Electron., Vol. GE-10; pp. 106-113, April 1972.

[20] Njoku, E.G., Stacey, J.M., and Barath, F.T., "The Seasat Scanning Multichannel Microwave Radiometer (SMMR): Instrument Description and Performance," IEEE J. Oceanic Eng., Vol. OE-5, No. 2, pp. 100-115, April 1980.

[21] Swanson, P.N., and Riley, A.L., "The Seasat Scanning Multichannel Microwave Radiometer (SMMR): Radiometric Calibration Algorithm Development and Performance," IEEE J. Oceanic Eng., Vol. OE-5, No. 2, pp. 116-124, April 1980.

[22] Moore, R.K., Birrer, I.J., Bracalente, E.M., Dome, G.J., and Wentz, F.J., "Evaluation of Atmospheric Attenuation From SMMR Brightness Temperature for the Seasat Satellite Scatterometer," J. Geophys. Res., Vol. 87, No. C5, pp. 3337-3354, April 30, 1982.

[23] Dome, G.J., Moore, R.K., Birrer, I.J., and Van Sickel, K., "Use of a Satellite Multifrequency Radiometer to Determine Attenuation Suffered by a Satellite Radar," presented at the AGARD Conference, Propagation Effects in Space/Earth Paths, London, May 1980.

[24] Wu, S.T., and Fung, A.K., "A Theory of Microwave Apparent Temperature Over the Ocean," NASA Contractor Report CR-2329, November 1973.

[25] Dome, G.J., "Oceanic Wind Vector Determination Using Seasat Satellite," Doctor of Engineering Thesis, University of Kansas, Lawrence, Kansas, 1980.

[26] Van Sickel, K., "A Technique for Correcting Scattering Coefficient Measurements Performed Within a Lossy Atmosphere," Master's Thesis, University of Kansas, Lawrence, Kansas, 1978.

[27] Birrer, I.J., and Dome, G.J., "SASS/SMMR Co-Location Algorithm," Remote Sensing Laboratory, The University of Kansas Center for Research, Inc., TM 343-3, February 1980.

[28] Moore, R.K., and Fung, A.K., "Radar Determination of Winds at Sea," Proc. of IEEE, Vol. 67, No. 11, pp. 1504-1521, November 1979.

[29] Barrick, D.E., "Wind Dependence of Quasi-Specular Microwave Sea Scatter," IEEE Transactions on Antennas and Propagation, Vol. AP-22, No. 1, pp. 135-136, January 1974.

[30] Wentz, F.J., "A Two-Scale Scattering Model With Application to the JONSWAP '75 Aircraft Microwave Scatterometer Experiment," NASA Contractor Report-2919 under Contract NAS1-14330 for Langley Research Center, Hampton, VA, December 1977.

[31] Jones, W.L., Wentz, F.J., and Schroeder, L.C., "Algorithm for Inferring Wind Stress From Seasat-A," AIAA J. Spacecraft and Rockets, Vol. 15, No. 6, pp. 368-374, December 1978.

[32] Schroeder, L.C., et al., "The Realtionship Between Wind Vector and Normalized Radar Cross Section Used to Derive Seasat-A Satellite Scatterometer Winds," J. Geophys. Res., Vol. 87, No. C5, pp. 3318-3336, April 30, 1982.

[33] Wentz, F.J., "Estimation of the Sea-Surface's Two-Scale Backscatter Parameters," NASA CR-145255, Langley Research Center, Hampton, VA, March 1978.

[34] Dome, G.J., Fung, A.K., and Moore, R.K., "An Empirical Model for Ocean Radar Backscatter and Its Application in Inversion Routine to Estimate Wind Speed and Direction Effects," Proc. URSI Comm. F, La Baule, France, April 28-May 6, 1977.

[35] Pierson, W.J., Cardone, V.J., and Greenwood, J.A., "The Application of Seasat-A to Meteorology," City University of New York Tech. Report, New York, NY, August 1974.

[36] Wentz, F.J., "Documentation for Program WINVEC: Computation of Statistics on the Sea-Surface Friction Velocity and Wind Direction," Technical Report 78-001 under JPL Contract 954942, January 16, 1978.

[37] Jones, W.L., et al., "Evaluation of Active Microwave Remote Sensing of Oceanic Wind Vector: Results of the Seasat JASIN Workshop," J. Geophys. Res., to be published in special Seasat issue, 1982.

[38] Jones, W.L., et al., "The Seasat-A Satellite Scatterometer: The Geophysical Evaluation of Remotely Sensed Wind Vector," J. Geophys. Res., Vol. 87, No. C5, pp. 3297-3317, April 30, 1982.

[39] Boggs, D.H., The Seasat Scatterometer Model Function: The Genesis of SASS1, JPL Internal Document 622-230, Pasadena, CA, March 3, 1981.

[40] Wurtele, M.G., "Wind Direction Alias Removal Studies of SEASAT Scatterometer-Derived Wind Fields," J. Geophys. Res., Vol. 87, No. C5, pp. 3365-3377, April 30, 1982.

[41] Wentz, F.J., "The Effect of Azimuth Angle Error on the SASS Wind Vectors," NASA Technical Report 030681 under Contract L18134B, March 6, 1981.

[42] Halberstam, I., "Some Considerations in the Evaluation of Seasat-A Scatterometer (SASS) Measurements," J. Physical Oceanography, Vol. 10, pp. 623-632, April 1980.

REFERENCES (Contd.)

[43] Cardone, V.J., Specifications of the Wind Distribution in the Marine Boundary Layer for Wave Forecasting, New York University Report TR 69-1, 1969.

[44] Kondo, J., "Air-Sea Bulk Transfer Coefficients in Diabatic Conditions," Boundary-Layer Meteorol., Vol. 9, pp. 91-112, 1975.

[45] Boggs, D.H., and Woiceshyn, P.M., "SASS GDR Calculation of u+ from $U_{19.5}$," JPL IOM 335.6-44, June 23, 1980.

[46] Brown, R.A., and Liu, T., "An Operational Large Scale Marine Planetary Boundary-Layer Model," J. Appl. Meteorol., in press, 1982.

[47] Halberstam, I., "Verification Studies of Seasat-A Satellite Scatterometer (SASS) Measurements," J. of Geophy. Res., Vol. 86, No. C7, pp. 6599-6606, July 20, 1981.

[48] Pierson, W.J., and Salfi, R.E., "The Theory and Data Base for the CUNY SASS Wind Vector Algorithm, JPL Report under Contract 954411 (Including Appendices A through H), City University of New York, NY, 1978.

[49] Pierson, W.J., "The Measurement of Synoptic Scale Winds, J. Geophys. Res., to be published in special Seasat issue, 1982.

[50] Brown, R.A., et al., "Surface Wind Analyses for Seasat," J. Geophys. Res., Vol. 87, No. C5, pp. 3355-3364, April 30, 1982.

[51] Tredor, A.J., Seasat Final Report: Volume IV. Attitude Determination, JPL Publication 80-38, Pasadena, CA, July 1, 1980.

[52] Moore, R.K., and Fung, A.K., "Radar Determination of Winds at Sea," Proceedings of the IEEE, Vol. 67, No. 11, pp. 1504-1521, November 1979.

6192